UNIVERSIDADE DE LISBOA
FACULDADE DE CIÊNCIAS

Ciências
ULisboa

Photovoltaic Potential in Building Façades

Doutoramento em Sistemas Sustentáveis de Energia

Sara Regina Teixeira Freitas

Tese orientada por:
Professor Doutor Miguel Centeno da Costa Ferreira Brito
Professora Doutora Paula Maria Ferreira de Sousa Cruz Redweik

Documento especialmente elaborado para a obtenção do grau de doutor

2018

UNIVERSIDADE DE LISBOA
FACULDADE DE CIÊNCIAS

Ciências
ULisboa

Photovoltaic Potential in Building Façades

Doutoramento em Sistemas Sustentáveis de Energia

Sara Regina Teixeira Freitas

Tese orientada por:
Professor Doutor Miguel Centeno da Costa Ferreira Brito
Professora Doutora Paula Maria Ferreira de Sousa Cruz Redweik

Júri:
Presidente:
- Doutor João Manuel de Almeida Serra, Professor Catedrático, Faculdade de Ciências da Universidade de Lisboa

Vogais:
- Doutor Wilfried Van Sark, Associate Professor, Faculty of Geosciences da Utrecht University (Holanda)
- Doutor Francesco Frontini, Researcher, Department for Environment Constructions and Design da University of Applied Scienced and Arts of Southern Switzerland (Suiça)
- Doutora Maria João Rodrigues, Diretora Técnica-Financeira, Associação Lisboa E-nova – Agência de Energia e Ambiente de Lisboa, na qualidade de individualidade de reconhecida competência na área científica
- Doutor Miguel Centeno da Costa Ferreira Brito, Professor Auxiliar, Faculdade de Ciências da Universidade de Lisboa (orientador)

Documento especialmente elaborado para a obtenção do grau de doutor

Fundação para a Ciência e Tecnologia, SFRH/BD/52363/2013

2018

ACKNOWLEDGMENTS

The research presented in this dissertation was possible thanks to the framework and support from the MIT Portugal Program on Sustainable Energy Systems and the funding received from the Portuguese Science Foundation (FCT), under the doctoral grant SFRH/BD/52363/2013.

I also acknowledge: Fundação Calouste Gulbenkian, for the Incentive to Research Award I received in 2014; Fundação Luso-Americana para o Desenvolvimento, for the scholarship that allowed me to visit and present my work at JPL/NASA (California); Project UID/GEO/50019/2013 - Instituto Dom Luiz and Project PTDC/EMS-ENE/4525/2014 – PVCITY, for the financial support. I am also grateful for being part of Project Project MITP-TB/CS/0026/2013 – SUSCITY, in the scope of which I developed part of my research at the MIT (Boston), and Project ED2050-M-05-USS - Urban Sun Skins, which allowed me to work at HEPIA (Geneva) for 3 weeks.

My supervisor Miguel Brito, for the endless motivation, inspiration and vital support. For inciting me to face challenges right in the eye, to constantly seek self-improvement and to be creative in the resolution of the many Columbus' eggs I have faced during the last 4 years.

My co-supervisor Paula Redweik, for her support and kind words, and for sharing SOL model's code and introducing me to its workflow.

Carlos Rodrigues and Antonio Joyce from LNEG for providing the electricity production data from the Solar XXI PV façade used in the validation of the SOL model.

EDP Distribuição for providing the load demand data associated to the distribution power transformers in Lisbon.

MIT Portugal SES program coordinator in FCUL João Serra, for his support during the 1st year advanced course and in financial and travel matters, and MIT Portugal communications director Sílvia Castro, for sharing my humble achievements with the media.

Christoph Reinhart, for the stimulating lectures and discussions during my visit to the Sustainable Design Lab (MIT), and his team of inspirational, hardworking and kind individuals.

Gilles Desthieux and Claudio Carneiro, for sharing their experiences as senior researchers and for engaging in fruitful discussions during my visit to HEPIA.

MSc students with whom I explored dark waters and deepened my knowledge: André Cristóvão, Ana Barros, João Segadães, Inês Martinho, Sérgio Guimarães, Bernardo Tavares and Sofia Ganilha.

Ex- and current openspace colleagues: Mário Pó, Ivo Costa, Joana Baptista, Rodrigo Silva, Raquel Figueiredo, Pedro Nunes, Ângelo Casaleiro, Rita Montes, José Silva, Rita Almeida, Filipe Serra, David Pera. One does not simply forget all the funny moments, engaging discussions, absurd situations, outreach preparation, sweet pastry and tea time, outdoor lunches, adventures abroad,…

Aos que têm alimentado a minha criatividade musical e performativa, a minha imaginação, sem a qual tudo seria muito menos interessante: os Monolith Moon, o Grupo Coral Stravaganzza, o Gonçalo Antunes e os PSI.

Ao João e à Paula, pela partilha, a humildade, e por me guiarem no caminho do ashtanga yoga, a cola que une e me faz compreender tudo o resto.

À Daniela Fonte, pela amizade intemporal, pelo apoio constante aos meus projetos científicos e artísticos. Pelos bons momentos de gulodice!

À família emprestada, Pires e Gamito, junto dos quais o tempo parece parar. A boa vontade não se agradece, mas a minha gratidão pela amizade e pelas boas memórias é imensa.

Aos meus pais e irmão, pelo amor incondicional, por estarem sempre presentes nos bons e maus momentos e pelos valores que me têm transmitido ao longo da vida.

Ao Carlos, por tudo.

E ao universo que, de algum modo, parece conspirar…

ABSTRACT

Consistent reductions in the costs of photovoltaic (PV) systems have prompted interest in applications with less-than-optimum inclinations and orientations. That is the case of building façades, with plenty of free area for the deployment of solar systems. Lower sun heights benefit vertical façades, whereas rooftops are favoured when the sun is near the zenith, therefore the PV potential in urban environments can increase twofold when the contribution from building façades is added to that of the rooftops. This complementarity between façades and rooftops is helpful for a better match between electricity demand and supply.
This thesis focuses on: i) the modelling of façade PV potential; ii) the optimization of façade PV yields; and iii) underlining the overall role that building façades will play in future solar cities.

Digital surface and solar radiation modelling methodologies were reviewed. Special focus is given to the 3D LiDAR-based model SOL and the CAD/plugin models DIVA and LadyBug. Model SOL was validated against measurements from the BIPV system in the façade of the Solar XXI building (Lisbon), and used to evaluate façade PV potential in different urban sites in Lisbon and Geneva. The plugins DIVA and LadyBug helped assessing the potential for PV glare from façade integrated photovoltaics in distinct urban blocks.
Technologies for PV integration in façades were also reviewed. Alternative façade designs, including louvers, geometric forms and balconies, were explored and optimized for the maximization of annual solar irradiation using DIVA. Partial shading impacts on rooftops and façades were addressed through SOL simulations and the interconnections between PV modules were optimized using a custom Multi-Objective Genetic Algorithm.
The contribution of PV façades to the solar potential of two dissimilar neighbourhoods in Lisbon was quantified using SOL, considering local electricity consumption. Cost-efficient rooftop/façade PV mixes are proposed based on combined payback times. Impacts of larger scale PV deployment on the spare capacity of power distribution transformers were studied through LadyBug and SolarAnalyst simulations. A new empirical solar factor was proposed to account for PV potential in future upgrade interventions. The combined effect of aggregating building demand, photovoltaic generation and storage on the self-consumption of PV and net load variance was analysed using irradiation results from DIVA, metered distribution transformer loads and custom optimization algorithms.

SOL is shown to be an accurate LiDAR-based model (nMBE ranging from around 7% to 51%, nMAE from 20% to 58% and nRMSE from 29% to 81%), being the isotropic diffuse radiation algorithm its current main limitation. In addition, building surface material properties should be regarded when handling façades, for both irradiance simulation and PV glare evaluation. The latter appears to be negligible in comparison to glare from typical glaze/mirror skins used in high-rises.
Irradiation levels in the more sunlit façades reach about 50-60% of the rooftop levels. Latitude biases the potential towards the vertical surfaces, which can be enhanced when the proportion of diffuse radiation is high. Façade PV potential can be increased in about 30% if horizontal folded louvers becomes a more common design and in another 6 to 24% if the interconnection of PV modules are optimized.
In 2030, a mix of PV systems featuring around 40% façade and 60% rooftop occupation is shown to comprehend a combined financial payback time of 10 years, if conventional module efficiencies reach 20%. This will trigger large-scale PV deployment that might overwhelm current grid assets and lead to electricity grid instability. This challenge can be resolved if the placement of PV modules is optimized to increase self-sufficiency while keeping low net load variance. Aggregated storage within solar

communities might help resolving the conflicting interests between prosumers and grid, although the former can achieve self-sufficiency levels above 50% with storage capacities as small as 0.25kWh/kW_{pv}. Business models ought to adapt in order to create conditions for both parts to share the added value of peak power reduction due to optimized solar façades.

KEYWORDS: solar potential; urban environment; building façades; BIPV; electricity grid

RESUMO

As reduções continuas e consistentes no custo dos sistemas fotovoltaicos registadas nos últimos anos têm estimulado o interesse em aplicações com orientações e inclinação que não as ótimas. Este é o caso das fachadas dos edifícios, que possuem uma vasta área livre e disponível para a instalação de sistemas de energia solares. Do ponto de vista da geração de eletricidade via fotovoltaico, alturas solares menores são mais benéficas para as superfícies verticais nos edifícios, como as fachadas, enquanto que os telhados, horizontais ou inclinados, irão produzir mais quando o sol estiver mais próximo do zénite. Deste modo, o potencial solar fotovoltaico no meio urbano pode aumentar em duas vezes quando à produção pelos telhados se junta a contribuição das fachadas dos edifícios. Esta complementaridade entre fachadas e telhados permite uma maior facilidade de ajuste entre o perfil de consumo e o perfil de fornecimento de eletricidade nos edifícios e nas cidades.
A tese desenvolvida na presente dissertação foca-se, assim, em: i) explorar ferramentas para a modelação do potencial solar fotovoltaico nas fachadas dos edifícios; ii) testar formas alternativas de otimizar os ganhos de sistemas fotovoltaicos em fachada; e iii) salientar o papel fundamental que as fachadas solares irão desempenhar nas cidades do futuro.

Diversas metodologias para a construção de modelos digitais de superfície urbanos e para a simulação da radiação solar nesses contextos foram revistas. Atenção especial é dada ao modelo tridimensional SOL, baseado em dados LiDAR, e aos plug-ins DIVA e LadyBug, para o software CAD Rhinoceros 3D. O primeiro sofreu um processo de validação através da comparação com medidas de produção elétrica feitas no sistema fotovoltaico integrado na fachada do edifício Solar XXI, localizado no Lumiar, em Lisboa. Este modelo foi depois utilizado para avaliar o potencial fotovoltaico em várias zonas urbanas em Lisboa e também em Genebra, na Suíça. As outras duas ferramentas, baseadas do método *raytracing* com as propriedades físicas dos materiais implementado em Radiance, serviram, numa primeira fase, para avaliar potenciais impactos visuais nos espaços exteriores consequentes da reflexão da luz por módulos fotovoltaicos instalados em fachadas.
Tecnologias existentes no mercado e protótipos de produtos fotovoltaicos para fachadas foram igualmente revistos. Designs de elementos alternativos para fachadas, incluindo palas fixas horizontais e verticais e formas geométricas tridimensionais foram exploradas e as suas dimensões otimizadas para que a coleção anual de radiação solar fosse máxima. Foram também estudadas as dimensões otimizadas de varandas contendo painéis bifaciais sujeitos à radiação refletida por diferentes materiais nas envolventes. O plugin DIVA foi usado nestes estudos. No passo seguinte, averiguaram-se as consequências negativas do sombreamento parcial em sistemas fotovoltaicos em telhados e fachadas teste, através de simulações realizadas pelo modelo SOL. Um algoritmo genético multi-objectivo foi proposto como uma possível metodologia para alcançar uma solução com custo-benefício opimo para a localização dos módulos fotovoltaicos e como devem ser ligadas as strings sujeitos a sombreamento parcial.
A contribuição de fachadas fotovoltaicas para o potencial solar foi quantificada em duas localidades distintas em Lisboa usando simulações pelo modelo SOL, considerando o perfil de consumo de eletricidade no local. Várias percentagens de telhado/fachada com um bom compromisso entre produção e custos de investimento são propostas com base no tempo de retorno financeiro. Numa última fase, foram estudados os impactos adversos que uma penetração fotovoltaica a grande escala pode ter nos equipamentos da rede de distribuição elétrica, nomeadamente na capacidade de os transformadores locais receberem toda a eletricidade excedente produzida pelos sistemas fotovoltaicos. A ferramenta SolarAnalyst foi aqui utilizada para simular a irradiação nos telhados, enquanto que nas fachadas a irradiação foi obtida através do plugin LadyBug. Foi proposto um fator

solar empírico que seja incorporado nas metodologias de substituição de transformadores antigos ou no dimensionamento de novos equipamentos para zonas urbanas em construção. O efeito combinado da agregação dos consumos de eletricidade, da produção agregada de telhados e fachadas e do armazenamento agregado de vários edifícios no nível de autoconsumo foi analisado em detalhe. A variância de carga na rede elétrica foi também incluída no estudo dada a existência de dados reais de consumo a nível dos transformadores de dois bairros em Lisboa. Também aqui foi utilizado o plugin DIVA para simular a irradiação solar horária em todas as superfícies dos edifícios.

O modelo SOL mostrou-se razoavelmente exato, tendo em conta as limitações impostas pela natureza dos dados LiDAR. Foram alcançados Erros Viés Médios normalizados na ordem de 7% a 51%, Erros Absolutos Médios normalizados entre 20% e 58% e Raízes do Erro Quadrático Médio de 29% a 81%. A principal limitação da versão atual deste modelo deve-se ao algoritmo de radiação difusa ser isotrópico. Por outro lado, percebeu-se que as propriedades físicas dos materiais constituintes das superfícies dos edifícios devem ser levadas em conta quando se analisam as fachadas, tanto em termos da irradiação como no potencial de encadeamento visual. O ultimo, porém, aparenta ser pouco significativo em comparação com outros materiais típicos de construção como envidraçado e espelho, muito comuns em arranha-céus.
Os níveis de irradiação nas áreas mais iluminadas das fachadas podem alcançar até 50-60% dos níveis calculados para os telhados, nas cidades analisadas. Um viés positivo existe à medida que o aumento da latitude se traduz num maior potencial solar nas superfícies verticais face às horizontais ou pouco inclinadas. Este efeito é ligeiramente amplificado se as condições atmosféricas no local forem propicias à ocorrência de céus cobertos e, portanto, a fração de radiação difusa for elevada. Por outro lado, o potencial fotovoltaico nas fachadas pode aumentar também por meio do design alternativo que, contemplando módulos fotovoltaicos integrados em palas fixas horizontais, pode chegar aos 30%. Uma otimização do posicionamento dos módulos e das interligações em strings pode contribuir com mais 6% a 24% de ganhos (ou perdas evitadas) no sistema.
No ano 2030, se a eficiência dos módulos fotovoltaicos convencionais alcançar os 20%, será possível obter tempos de retorno financeiro do investimento na ordem dos 10 anos, se um misto de 40% da área nas fachadas e 60% da área dos telhados numa cidade for ocupado por sistemas solares. Nos anos seguintes, a manter-se essa tendência de redução de custos e aumento da eficiência, a introdução de sistemas fotovoltaicos a grande escala será impulsionada. Apesar de as fachadas permitirem alargar o período de produção e, portanto, um melhor ajuste da geração ao perfil de consumo local, a rede elétrica atual revela-se incapaz de suportar a injeção de produção excedente dos trilhados orientados a sul e da vasta área de fachada num cenário 100% penetração fotovoltaica, o que pode levar a instabilidade na rede. Este desafio pode ser resolvido recorrendo a uma otimização da localização de cada modulo fotovoltaico nas superfícies dos edifícios de modo a aumentar o autoconsumo e a minimizar a variância de carga na rede. Sistemas de armazenamento de eletricidade agregados ao nível de comunidades solares poderão aliviar o conflito de interesses entre prosumidores e a entidade reguladora da rede, apesar de ser possível aos primeiros obter níveis de autoconsumo acima dos 50% sem qualquer capacidade de armazenamento, ou alguma na ordem dos 0.25kWh/kWpv. Modelos de negócio alternativos terão que ser criados ou os atuais terão que se adaptar de maneira a serem criadas condições que permitam a ambas as partes partilhar do valor acrescentado consequente de um pico de potencia na rede reduzido graças às fachadas fotovoltaicas.

PALAVRAS-CHAVE: potencial solar; meio urbano; fachadas de edifícios; BIPV; rede elétrica

CONTENTS

LIST OF FIGURES

LIST OF TABLES

NOMENCLATURE AND ABBREVIATIONS

Parameter/index	Description
3DCM	3D city model
A_{build} [m^2]	Total available area on all roof and façade surfaces
A_{foot} [m^2]	Total building footprints area
A_f [m^2]	Total installed PV area in the façade
A_r [m^2]	Total installed PV area in the rooftop
A_s [m^2]	Area of surface s
AC	Alternating current
AL [-]	Losses due to angle of incidence
ALS	Aerial laser scanning
AVF	Anisotropic view factor
a_r [-]	Empirical angular losses coefficient
a-Si	Amorphous silicon
B_{bat} [kWh/kW$_{pv}$]	Storage capacity
B_{exp} [kWh]	Electricity stored in the battery that was exported to the grid
B_{sc} [kWh]	Electricity stored in the batteries that supplies for the loads
$B_{soc,f}$ [kWh]	Ending of cycle battery energy state of charge
$B_{soc,i}$ [kWh]	Beginning of cycle battery energy state of charge
BIM	Building Information Modelling
BAPV	Building applied photovoltaics
BIPV	Building integrated photovoltaics
b [-]	Block/building index
C_0 [€]	Initial investment cost
C_{bat} [€/kWh]	Unitary cost of the battery
$C_{diversity}$ [-]	Simultaneity coefficient for consumption
C_i [€]	Inverter cost
C_m [€/m^2]	Cost of conventional c-Si PV module
C_{om} [€]	Operation and maintenance costs
$C_{pv,f}$ [€]	Cost of the PV installation for the façade
$C_{pv,r}$ [€]	Cost of the PV installation for the rooftop
C_{rate} [kW/kWh]	Charging rate relative to maximum battery capacity
C_{rep} [€]	Replacement costs of the storage
C_s [€/m]	PV string wiring cost
C_{syst} [€]	PV system investment cost
C_y [€]	Cash flow in year y
CAD	Computer-aided design
CFD	Computational fluid dynamics
CIE	International Commission on Illumination
CIGS	Copper indium gallium (di)selenide
CPV	Concentrating photovoltaics
c-Si	Crystalline silicon
dg [%/year]	Degradation rate for PV
Dir_{horiz} [kWh/m^2]	Direct horizontal irradiation
Dir_{norm} [kWh/m^2]	Direct normal irradiation
Dir_{vert} [kWh/m^2]	Direct vertical irradiation
Dif_{horiz} [kWh/m^2]	Diffuse horizontal irradiation

Dif_{vert} [kWh/m^2]	Diffuse vertical irradiation
DC	Direct current
DIVA	Design Iterate Validate Adapt
DSM	Digital surface model
DSSC	Dye-sensitized solar cells
DTF	Diffuse tilt factor
DUM	Digital urban model
E_{dem} [kWh]	Electricity demand
E_{imp} [kWh]	Electricity purchased from the grid
E_{syst} [kWh/year]	PV System anual electricity yield
e_p [€/kWh]	Grid single tariff
e_s [€/kWh]	Retail electricity market prices
F_{dif}[-]	Transposition factor for diffuse irradiation
F_{ref} [-]	Transposition factor for ground reflected irradiation
F_{PV} [-]	Solar factor for transformer sizing
F_{safety} [-]	Safety margin for power transformer capacity
FCUL	Faculdade de Ciências, Universidade de Lisboa
G_{horiz} [kWh/m^2]	Global horizontal irradiation
G_{ref} [kWh/m^2]	Reference global irradiation
G_{tilted} [kWh/m^2]	Global irradiation in the tilted plane
G_{vert} [kWh/m^2]	Global vertical irradiation
GA	Genetic algorithm
GIS	Geographic information system
GUI	Graphical user interface
g_{horiz} [-]	Normalized ratio between façade and horizontal rooftop electricity production
g_{optim} [-]	Normalized ratio between façade and optimal rooftop electricity production
h [h]	Hourly time step index
H [h]	Total number of hours
HPC	Holographic planar concentrator
i [-]	Inverter index
inf [%]	Inflation rate
k_D [-]	Diffuse fraction
L [years]	System lifetime
L_{bat}[years]	Battery lifespan
LiDAR	Light detection and ranging
LoD	Level of detail
LSC	Luminescent solar concentrator
L_c [m]	Length of PV string wiring
m [-]	PV module index
MAE	Mean absolute error
MBE	Mean bias error
MLS	Mobile laser scanning
MOGA	Multi objective genetic algorithm
N_b [-]	Total number of surfaces in Block b
NLV	Net load variance
$NOCT$ [°C]	Nominal operating cell temperature
n_{bat} [-]	Number of batteries
nMAE	Normalized mean absolute error
nMBE	Normalized mean bias error

nRMSD	Normalized root mean squared deviation
nZEB	Net zero energy building
OGC	Open geospatial consortium
OPV	Organic photovoltaics
O&M	Operation and maintenance
$P_{contract}$ [kW]	Customer contracted power
P_{demand} [kW]	Local aggregated power demand
P_{GAP} [kW]	Transformer spare power
P_{over} [kW]	Transformer oversized power capacity
P_{PT} [kVA]	Nominal power transformer capacity
P_{ref} [W/m^2]	Nominal PV module power
$P_{storage}$ [kW/kW$_p$]	Local aggregated storage capacity
PT	Power transformer
PV	Photovoltaic
PV [kWh]	PV generated electricity
PV_i [kWh]	PV electricity yields by inverter i
PV_m [kWh]	PV generated electricity by module m
PV_{bat} [kWh]	PV produced electricity that charges the storage bank
PV_{exp} [kWh]	PV produced electricity that was exported to the grid
PV_{sc} [kWh]	Self-consumed PV generated electricity
PVCC	Photovoltachromic cells
p_{PV} [kW/m^2]	PV peak power density
p-Si	Polycrystalline silicon
$RMSD$	Root mean squared deviation
r [%]	Opportunity cost of capital
$ramp$ [kW/h]	Hourly ramp rate
S [-]	PV string index
SC [%]	Self-consumption rate
SOC_{max} [%]	Maximum state of charge relatively to the nominal battery capacity
SOC_{min} [%]	Minimum state of charge relatively to the nominal battery capacity
SOL	Solar out of LiDAR
SRA	Simplified radiosity algorithm
SS [%]	Self-sufficiency rate
ST	Solar thermal
SVF	Sky view factor
s [-]	Surface index
TLS	Terrestrial laser scanning
TMY	Typical meteorological year
T_a [°C]	Ambient temperature
T_m [°C]	Temperature of module m
T_{ref} [°C]	Reference ambient temperature
VSC	Vertical sky component
XML	Extensible markup language
y [year]	Yearly time-step
z [°]	Sun zenith angle
α_{horiz} [-]	Ratio between façade and horizontal rooftop electricity production
α_{optim} [-]	Ratio between façade and optimal rooftop electricity production
β [°]	Surface tilt
γ [%/°C]	Power correction factor for PV module temperature

Δ_η [%]	Temperature coefficient for efficiency
δ [°]	Earth's declination
η_c [%]	Charge efficiency
η_d [%]	Discharge efficiency
η_i [%]	Inverter efficiency
η_r [%]	Average reference efficiency for c-Si solar panels
θ [°]	Angle of incidence of the sun rays
ρ [-]	Foreground albedo
φ [°]	Surface azimuth
ψ [°]	Latitude
ω [°]	Hour angle

1. INTRODUCTION

In an Era of considerably high electricity demand in urban environments, instigated by the continuous growth of the world's population and a consistent migration of people from rural areas to large cities, the use of Earth energy resources such as coal, oil and gas has produced severe impacts at the environmental, political and economic levels. The negative outcomes from burning fossil fuels have gradually become more perceptible by the public in general, who acknowledge the need for non-polluting and renewable energy technologies to tackle global warming. In this sense, solar photovoltaics (PV) has emerged not only as a renewable solution, that is free of emissions during operation, but also as a key player in the future of the electricity supply chain.

1.1 Background and motivation

The light that comes from the sun and reaches our planet may be described as a flux of particles called photons, which can be decomposed into their spectral distribution as a function of the wavelength. Solar spectral irradiance is similar to that of a black body at 5900K, but before it reaches the surface of the Earth it is absorbed in several wavelength bands by the different atmospheric constituents (Valley, 1965). Figure 1.1 compares the spectral irradiance of a sun-equivalent blackbody with the solar spectral irradiance outside the atmosphere and after being absorbed by the ozone layer (visible region), oxygen (near infrared), water vapour and carbon dioxide (near/far infrared). The energy of a photon decreases with wavelength, thus an energy technology that makes use of solar radiation ought to preferably operate in the wavelengths associated to higher solar spectral intensities, i.e. around 500nm.

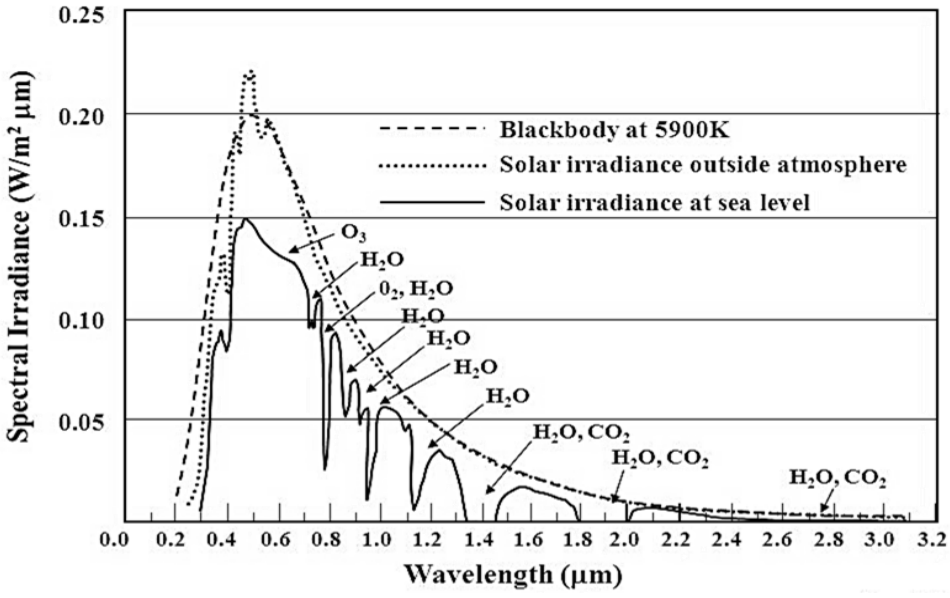

Figure 1.1 – Spectral irradiance of: a 5900K blackbody, the sun light outside Earth's atmosphere and at sea level (Valley, 1965).

A solar PV cell produces a current and a voltage when light shines on it. The material responsible for the absorption of light is usually a semiconductor, within which the photon increases the energy state of an electric charge which is collected by electric contacts and, then, fed into an external circuit to supply the load (Green, 1982). Every material has its quantum efficiency (i.e. the ratio of energy carrying electrons by the number of photons incident on the solar cell), which combined with the

incident light spectral distribution determines how much power can be produced. The efficiency of a PV cell is a measure to characterize how much power can be generated by unit area under a reference solar spectrum, allowing the comparison among different cell technologies.

In the last four decades, the efficiency of PV cells has increased significantly, with efficiency records being overcome year after year, although the quantum limits have almost been reached. The most relevant PV technology is based on crystalline silicon clear market leader due to many factors including its relative high efficiency, the processing technology spill over from the semiconductor industry, the abundance of silicon in the Earth's crust (in the form of silica) and, in an earlier development phase, to the use of leftovers from the production of high purity materials for the electronics industry. The manufacturing costs have also been dramatically reduced, especially with economies of scale after most of the industry has moved to Asia (Meza, 2016). The most efficient cells are multijunction, a tandem of layers of different semiconductor making use of different wavelength ranges, but encompass high-priced and complex assemblies. On the other hand, emerging technologies such as perovskites have achieved recently efficiencies comparable to silicon technologies. Thin-film PV cells such as CIGS and CdTe are also interesting but avoidable given the use of toxic and rare materials.

Thanks to the interconnection of cells in modules, PV power plants can be installed in a fairly simple way, especially if mature PV technology such as silicon-based modules is used. The sizing of PV systems must be thoroughly planned given the interconnection possibilities between modules. Due to the relatively high current produced by a single silicon PV cell, modules are usually connected in series (i.e. strings) so that their voltages can be added. The main limitation from this practice is that an individual shaded or faulty cell can cause current mismatch throughout the whole PV string, compromising its electricity production, since it will not operate at its maximum power point.

Large PV power plants are often installed in open field areas, making use of ground area that otherwise would not be used. These plants can be utility-scale and feature nominal generation capacities of the order of the megawatt. However, even if the estimated total land area required to run the world solely on solar is relatively small - about the size of Spain according to (Harrington, 2015) - that area would expand quickly once service roads, operational facilities and transmission lines were incorporated. PV power plants must also be distributed over a wide area to avoid production breaks caused by weather events such as storms and cloudy skies and reduce transmission losses in the grid from the point of production to the point of consumption. Large utility-scale PV plants encompass other limitations such as a more intricate legal framework associated to permitting, environment clearance and land sitting, additional costs with grid assets upgrade/expansion, greater impacts on grid stability as PV penetration increases (Shah, 2011), vast water requirements for wet cooling systems and impacts on wildlife (Anthony, 2010).

Distributed PV plants have been acquiring special interest. Smaller PV plants can be found in the periphery of urban areas, as well as integrated in buildings. The latter are generally deployed by building owners' initiative, seeking to lower their electricity bill while becoming more independent from the grid and resilient in case of power outages. As solar becomes more affordable and efficient, with rooftop PV competing with most of the conventional technologies such as coal, gas and nuclear (Lazard, 2017), citizens pursue electricity self-sufficiency through their own PV, gradually prompting the decentralization of electricity production in the urban context.

The integration of solar systems into the urban environment is not always free of obstacles, especially because the position of the sun changes during the day and the year. The sun has an apparent movement in the sky associated to the movements of rotation and translation of the Earth. Its position in the sky is characterized by the azimuth and zenith angles whose change leads to variations in the incidence angle of the solar rays onto the surfaces. Therefore, depending on the end-use of the energy system, a fixed PV system must be installed with the appropriate orientation and inclination, which depend on the geographic location and topography. Usually, in most fixed applications, the modules

are facing the equator (facing south if in the northern hemisphere), in an attempt to gather more radiation around solar noon (i.e. when solar radiation is more intense), and tilted at angles close to plus 15° of the local latitude (Stein, 2000), to ensure absorption of solar rays at times of the year when the sun reaches lower zeniths, i.e. in the winter.

In general, the installation of a solar system on buildings is made preferentially on rooftops, which represent areas with great solar exposure and more free space, allowing the use of mounting structures to attain the optimum inclinations and orientations, which may be different from those of the rooftop itself. Building façades, on the other hand, typically vertical, do not at first seem good candidates for solar applications – for moderate latitudes the sun is high in the sky most of the time, so a solar panel installed on a façade produces less per unit area than it would if optimally tilted. Nonetheless, façade area in modern urban agglomerates is far greater than the rooftop area, thus the combined production from PV façades can represent a relevant fraction of the solar potential of a city.

The solar potential of façades becomes interesting with the decrease in the cost of PV modules. Not long ago, PV modules were very expensive, preventing their deployment on buildings in less-than-optimal conditions. However, as prices dropped dramatically - 4 times cheaper in about a decade (Wirth, 2017) - installation of PV systems in less than optimum conditions is now a viable investment in many parts of the world, making it more attractive to install panels not only on the best spots of a building but also on the remainder available area. Furthermore, although solar irradiance is higher around noon, the electricity demand profile in urban areas does not follow the solar resource availability –peak demand seldom occurs around noon. In the case of typical residential areas, if most of the electricity into the grid was from rooftop solar PV, it would be null at night, scarce in the morning and in the afternoon, and excessive around noon. Thus, another possible benefit of PV on façades is that the range of orientations throughout the city would allow for different peaks of production at different times of the day (i.e. a south-facing façade produces more at noon, an east-facing façade produces more in the morning and those facing west produce more in the afternoon), contributing to a better match between the production and the demand. There might be other minor gains from PV façades such as the minimization of the accumulation of dirt, dust and snow in vertically mounted panels, avoiding optical losses.

Façades in the built context, however, do not always gather the conditions for the suitable installation of PV panels. The most frequent difficulties are related to dynamic phenomena such as shading caused by adjacent buildings, trees and other urban structures. Due to the apparent movement of the sun throughout the day, shadows cast by obstructions also vary, which can dramatically reduce the attractiveness of a façade area for PV applications. Hence, it is of critical importance to evaluate the solar potential at a certain area in the early stage of the system and/or building design. Currently, there are computational numeric models capable of characterizing the urban surfaces and simulate PV production in a physically-based way, considering the interaction between light and surface materials in simple and complex façade layouts. These tools produce valuable information on the PV potential of building façades, which is paramount for urban planning and decision making towards more sustainable urban environments.

1.2 Thesis outline

The purpose of this thesis is to explore the potential of photovoltaics on façades. The core research questions, listed below, encompass three challenges: the assessment of the potential of PV façades (I), followed by the optimization of the realization of that potential (II) and the overall role that PV façades can play in the city scale (III). Table 1.1 indicates the Chapters addressing each one.

I. How to **model** façade solar potential in an urban context?
II. How to **optimize** the solar potential of façades?
III. What is the **role** of building façades for the solar potential of a modern city?

Table 1.1 – Research questions distribution by Chapters.

Research questions	Chapter 2	3	4	5	6	7	8
I	✔	✔					
II			✔	✔	✔		✔
III		✔			✔	✔	✔

This thesis builds on several of the articles published in international scientific journals and conference proceedings in the course of the research presented in this document. A chronologic list of these publications follows:

Publications in international peer reviewed journals

- Freitas, S., Catita, C., Redweik, P., Brito, M.C. "Modelling solar potential in the urban environment: State-of-the-art review". Renewable and Sustainable Energy Reviews, Volume 41, Jan 2015, 915–931. DOI: 10.1016/j.rser.2014.08.060
- Freitas, S., Serra, F., Brito, M.C. "PV layout optimization: string tiling using a multi-objective genetic algorithm". Solar Energy, Volume 118, Aug 2015, 562–574. DOI: 10.1016/j.solener.2015.06.018
- Brito, M. C., Freitas, S., Guimarães, S., Catita, C., Redweik, P. "The importance of façades for the solar potential of a city". Renewable Energy, Volume 111, Oct 2017, 85–94. DOI: 10.1016/j.renene.2017.03.085
- Freitas, S., Reinhart, C., Brito, M. C. "Minimizing storage needs for large scale photovoltaics in the urban environment". Solar Energy, Volume 159, Jan 2018, 375-389. DOI: 10.1016/j.solener.2017.11.011
- Freitas, S., Santos, T., Brito, M. C. "Impact of large scale PV deployment in the sizing of urban distribution transformers". Renewable Energy, Volume 119, Apr 2018, 767-776. DOI: 10.1016/j.renene.2017.10.096

Publications in conference proceedings

- Freitas, S., Brito, M.C., "Maximizing the Solar Photovoltaic Yield in Different Building Façade Layouts". 31st EUPVSEC, Set 2015, Hamburg, Germany. DOI: 10.4229/EUPVSEC20152015-6AV.5.6
- Freitas, S., Serra, F., Brito, M.C., "Multi-objective genetic algorithm for the optimization of a PV system arrangement". ISES Solar World Congress, Nov 2015, Daegu, South Korea. DOI: 10.18086/swc.2015.05.16
- Freitas, S., Brito, M. C., Catita, C., Redweik, P., "Potential solar nas cidades". Presentation/paper at the VI Congresso Brasileiro de Energia Solar, Apr 2016, Belo Horizonte, Brazil
- Freitas, S., Cristóvão, A., Silva, R., Brito, M.C., "Obstruction surveying method for PV applications in urban environments". 32nd EUPVSEC, Jun 2016, Munich, Germany. DOI: 10.4229/EUPVSEC20162016-6AV.5.18

- Freitas, S., Brito, M.C., "Bifacial PV integrated on building balconies". 32nd EUPVSEC, Jun 2016, Munich, Germany. DOI: 10.4229/EUPVSEC20162016-6DO.8.1
- Freitas, S., Santos, T., Brito, M.C., "Sizing of urban distribution transformers in a neighbourhood with PV generation and energy storage". 33rd EUPVSEC, Sep 2017, Amsterdam, The Netherlands. DOI: 10.4229/EUPVSEC20172017-6BV.3.95
- Freitas, S., Brito, M.C., "Validation of a façade PV potential model based on LiDAR data". 33rd EUPVSEC, Sep 2017, Amsterdam, The Netherlands. DOI: 10.4229/EUPVSEC20172017-6DO.11.6
- Freitas, S., Brito, M.C., "The contribution of façades to the PV potential for sites with high diffuse fraction". 33rd EUPVSEC, Sep 2017, Amsterdam, The Netherlands. DOI: 10.4229/EUPVSEC20172017-6BV.3.67

Publications in national magazines

- Magarreiro, C., Freitas, S., Brito, M.C., (2016). "Radiação e energia solar". Gazeta de física, Vol. 39 – N1/2, pages 57-59
- Rodrigo A. Silva, Vera Reis, Ângelo Casaleiro, Sara Freitas e Miguel C. Brito (2016). "Dimensionamento de sistemas fotovoltaicos em autoconsumo residencial: a lei dos pequeninos". Renováveis magazine, Vol. 28, pages 28-29

2. MODELLING URBAN SOLAR POTENTIAL

Cityscapes propagating vertically provide a complex environment where solar radiation is unevenly distributed. Dynamic shading is almost ubiquitous in building surfaces. The ability to portray these phenomena is essential when it comes to modelling the solar potential in cities. Radiation algorithms scripted in numerical computing software or coupled with GIS tools and CAD software are useful to evaluate such complex effects. On the other hand, it is also necessary to develop the tools for reliable representation of the city terrain, building structures, vegetation and urban equipment, which can be accomplished through a digital surface model or described in a semantic way. As always, models must compromise between accuracy and computation time.
In this Chapter, an overview of digital surface and solar radiation modelling is provided, followed by a thorough revision of solar potential models, from the simplest 2D to the state-of-the-art able to handle façade solar potential. Web-based solar maps to communicate the benefits of solar energy to the public are also briefly addressed. [1]

2.1 Introduction

The sun represents a clean and plentiful source of energy. Solar energy will be a key player in future energy systems, thanks to technological improvements, consistent reduction of costs and increasing public awareness and acceptance. The modularity nature of photovoltaics (PV) and solar thermal (ST) collectors facilitates their deployment in the urban environment, while prompting the decentralization of electricity and heat production, which is a cornerstone of the Nearly Zero Energy Buildings (nZEB) concept, i.e. buildings that become almost independent from the electrical grid due to a systematic integration of renewable energy sources and building designs that maximize natural ventilation, daylighting, etc. (Torcellini et al., 2006)(Marszal et al., 2011)(Karlessi et al., 2017).
The built environment, however, is not everywhere suitable for solar energy applications. While in non-urban locations the constraints to energy yields are mostly related to unfavourable meteorological conditions, in cityscapes the limited available area and obstructions to the incoming sunlight also limit the solar energy harvesting. Therefore, the local solar resource must be assessed to evaluate the system technical and economic feasibility before its deployment. The methods to do so will depend on the end-goals and the level of detail required: whereas a straightforward estimate by simple and generalist methods is a usual practice for small scale rooftop installations, a complete parish- or city-scale study must account for intricate shading events, which asks for more sophisticated approaches. When vertical surfaces such as building façades are regarded, the physical properties of the surrounding materials become relevant for the solar irradiance distribution, thus the selection of the solar potential model ought to be carefully done.
The choice of models also depends on the questions being addressed. In (Izquierdo et al., 2008), a hierarchical approach with gradual restrictions is defined for the use of a specific renewable resource such as the solar radiation. The first one concerns the physical potential, i.e. the maximum solar irradiation level in a certain area. The second level regards the geographic potential that can be determined by restricting the locations where solar energy systems can be deployed. The next level, the technical potential, accounts for the technical characteristics of the equipment used in the

[1] Chapter includes work published on:
- Freitas, S., Catita, C., Redweik, P., Brito, M.C. "Modelling solar potential in the urban environment: State-of-the-art review". Renewable and Sustainable Energy Reviews, Volume 41, Jan 2015, 915–931, doi:10.1016/j.rser.2014.08.060
- Magarreiro, C., Freitas, S., Brito, M.C. "Radiação e energia solar". Gazeta de física 2016, Vol. 39 – N1/2, 57-59

conversion of energy from solar radiation. Further levels are defined, such as the economic potential and the social potential, to deal with the deployment prospects.
Figure 2.1 summarizes the sequential approach for the estimation of the physical and geographic solar potential. Data concerning the urban features of interest and their surroundings is an input that can be obtained through different techniques, according to the scale and the required analysis detail. Weather data-series are also needed; they are usually derived from long-term measurements in ground-based meteorological stations or from satellite data. The available data might restrict the solar radiation models that can be employed. These aspects will be explored in Sections 2.1 and 2.2.

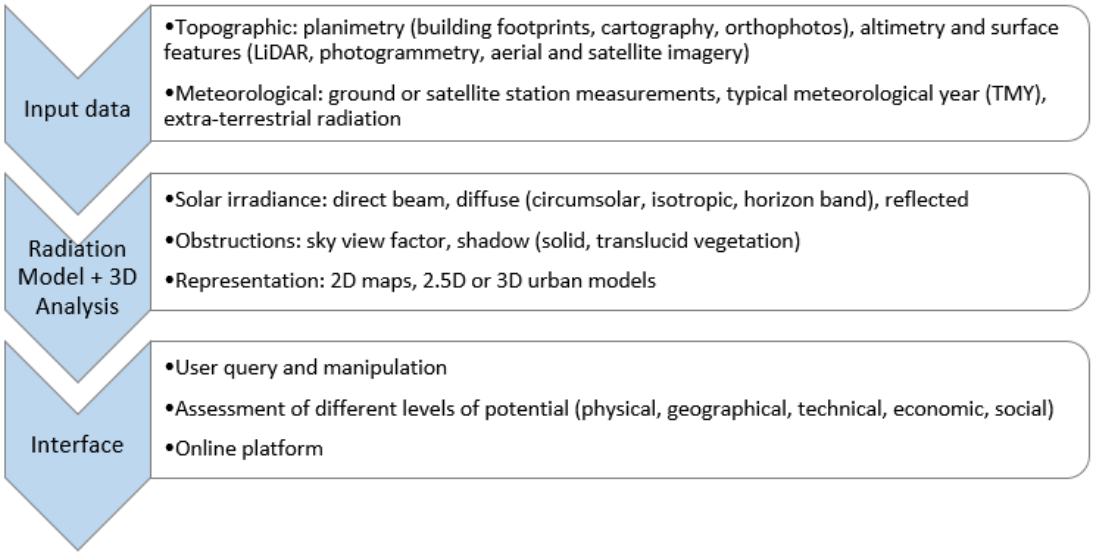

Figure 2.1 – Steps and options involved in the assessment of solar potential at a certain location.

Earlier solar potential models were only capable of computing the physical potential in non-urban scenarios, individual rooftops or 2D elementary digital geometries (addressed in Section 2.3). Improvement of computer power and advanced modelling techniques allowed for faster estimation and visualization of the cityscape solar geographical and technical potential using more sophisticated approaches (detailed in Section 2.4), which facilitates the dissemination of solar energy systems to the citizens, namely in the form of solar radiation interactive maps available online (Section 2.5). The policy-making process may also benefit from these tools, which can produce information on the available energy resources of a country (Ramachandra and Shruthi, 2007) or map a city's most interesting areas for the installation of solar systems. Studies such as these can support the implementation of energy measures or establish a framework for long-term energy supply and demand strategies, as presented in (Koo et al., 2014).

2.1 Digital Urban Models

Different models have been created to evaluate the solar resource and energy potential in the urban context. One key element in these models is the digital representation of the buildings, and optionally the terrain, trees and other urban equipment.
Any digital surface model (DSM) – i.e. a digital urban model (DUM) or a 3D city model (3DCM), when addressing urban environments - can be represented in different Levels of Detail (LoD), according to the purpose of the analysis. The concept of LoD as per the CityGML reference (Nouvel et al., 2013) encompasses 5 levels, from 0 to 4: the lowest LoD contains only the representation of the footprint, while LoD 1 features buildings represented by basic parallelepipeds, LoD 2 includes the slope of

rooftops, LoD 3 has modelled façades elements and the highest LoD features the indoor spaces. Recently, additional LoDs were proposed to avoid ambiguities (Biljecki et al., 2014), extending the levels of detail up to 10 categories.
The construction of a DUM or 3DCM can be done through the following techniques:

i) FOOTPRINTS

This type of data consists on the delineation of buildings and related structures, usually in the form of vector lines or polygons. They can be stored in shapefiles, when associated with Geographical Information Systems (GIS), or layers, in the case of Computer-aided Design (CAD) software. The largest source of footprints is OpenStreetMaps (OpenStreetMap contributors, 2017), a free database were users can copy, distribute, transmit and adapt their data (without guarantee of correctness).
Building footprints are commonly employed in 2D applications, such as the study of flat rooftop solar potential, but can also be used in 3D models. In this case, the footprints must be extruded to the heights of the respective buildings to create simple and flat geometries (i.e. a 2.5D model), which can later be enhanced with further details such as the modelling of façade and rooftop architectonic elements.

ii) ARCHETYPES

Building archetypes are theoretical buildings created by a composite of several characteristics found within a category of buildings with similar attributes. A complete city model can be constructed by populating a terrain model with multiple archetypes of different buildings.

iii) PHOTOGRAMMETRY

The tri-dimensional space can be reconstructed from bi-dimensional images using vertical aerial photographs from satellites, airplanes or drones. These images are taken with a degree of overlap that, due to the different perspectives, originate a perception of the three dimensions, allowing the measurements of elevation in a rigorous way. The data acquisition process has been facilitated by the use of drones because it is a more affordable option that allows flights at lower altitude, thus avoiding cloud cover while producing images with higher spatial resolution.

iv) LiDAR

Another option that has become popular in studies of large urban areas is Light Detection And Ranging (LiDAR). This type of survey consists on spatially contiguous measurements of the urban form. The LiDAR system in the aircraft emits a laser pulse and records the time taken for that same pulse to return to a sensor. Accurate distances can be computed using the time of return of the signal. Since the location of the sensor is known, the LiDAR data can then be used to map the position and height of objects in its scanning range (Tooke, 2014). The result is a 3D point cloud entailing a large set of points with assigned x, y and z coordinates that can be used as is or further manipulated: resampled to a lower resolution, input to produce surfaces by Delaunay triangulation, etc.
LiDAR sensors can be ground-based, Terrestrial Laser Scanning (TLS), or moving sensors that are mounted either on aircraft, Airborne Laser Scanning (ALS), or ground vehicles, Mobile Laser Scanning (MLS). Large scale urban environment is usually surveyed using ALS, however, the representation of vertical elements and the storage of their information is a challenge as the data acquisition is done from above and parallelly to the ground, the third-dimension attribute of vertical elements may not be properly grasped, which embodies discontinuities in a 2.5D model. It can, although, be derived by filling the holes between the ground and the rooftop points, when information on building façades is required (Redweik et al., 2011), or by a complementary MLS. Still, a proper treatment of MLS data is essential since only the surfaces that are facing the street can be surveyed and point collection might

be incomplete due to trees, window curtains and other objects non-transparent to the laser wavelength (Jochem et al., 2011).

Although the advancements in remote sensing have provided elevation data to generate 3D city models of many cities of the world, there are still many unchartered cities. (Biljecki et al., 2017) present a method to quickly obtain 3D models in LoD1 in places where elevation measurements are scarce, but there is plenty of footprints from governments and volunteered geoinformation.

2.2 Empirical Solar Radiation Models

The availability of solar energy arriving on a location may be assessed through the measurement of the solar irradiance (incoming solar power density) and/or insolation (solar irradiance integrated over time) by fully instrumented ground weather stations or derived from satellite images (Iqbal, 1983). In the latter, the beam irradiance is usually constructed by knowing the Linke turbidity factor and performing data fitting techniques, while the diffuse portion is the product of a diffuse transmission function at zenith and a diffuse angular function (Rigollier et al., 2000). Here emphasis will be given to ground measurements, the most common approach in modelling urban solar potential. Meteorological stations generally measure global and/or diffuse irradiance on the horizontal plane and/or direct normal (or beam) irradiance, related through the following expression:

$$G_{horiz} = Dir_{horiz} + Dif_{horiz} = Dir_{norm} \cos Z + Dif_{horiz} \, , \tag{2.1}$$

where G_{horiz} is the global horizontal irradiance, Dir_{norm} is the direct normal irradiance, Dif_{horiz} is the diffuse horizontal irradiance and Z is the sun's zenith angle.

Long-term data series from ground stations allow the estimation of the irradiance that reaches other tilted surfaces employing geometrically-based formulations. These are suited either to clear sky conditions or to overcast conditions, as long as cloud cover is considered (Angelis-Dimakis et al., 2011). The classic method to determine global irradiance on a tilted surface, G_{tilted}, relies on previous knowledge of its components and can be evaluated through the following expression:

$$G_{tilted} = Dif_{horiz} F_{dif} + \rho G_{horiz} F_{ref} + Dir_{norm} \cos\theta \, , \tag{2.2}$$

where F_{dif} and F_{ref} are, respectively, the transposition factors for diffuse and ground reflection, ρ is the foreground albedo and θ is the angle of incidence of the sun rays on the tilted plane. This angle can be assessed using the trigonometric relation (Duffie and Beckman, 2013):

$$\begin{aligned} \cos\theta = {} & \cos\delta \sin\beta \sin\gamma \sin\omega + (\cos\varphi \cos\beta + \sin\varphi \sin\beta \cos\gamma) \cos\delta \cos\omega + \\ & (\sin\varphi \cos\beta - \cos\varphi \sin\beta \cos\gamma) \sin\delta \, , \end{aligned} \tag{2.3}$$

where δ is the declination angle, γ is the site's latitude, β is the surface tilt, ω is the hour angle and φ is the surface azimuth.

Whereas the transposition of the direct component is rather simple, the same does not hold for diffuse and ground-reflected radiation. Figure 2.2 illustrates the two critical unknowns in Eq. (2.2), F_{dif} and F_{ref}. If the incoming diffuse radiation is assumed isotropic, Eq. (2.4) and (2.5), they take the same value whether radiation comes from the ground, sky or environments.

$$F_{dif} = \frac{1 + \cos\beta}{2}, \tag{2.4}$$

$$F_{ref} = \frac{1 - \cos\beta}{2}. \tag{2.5}$$

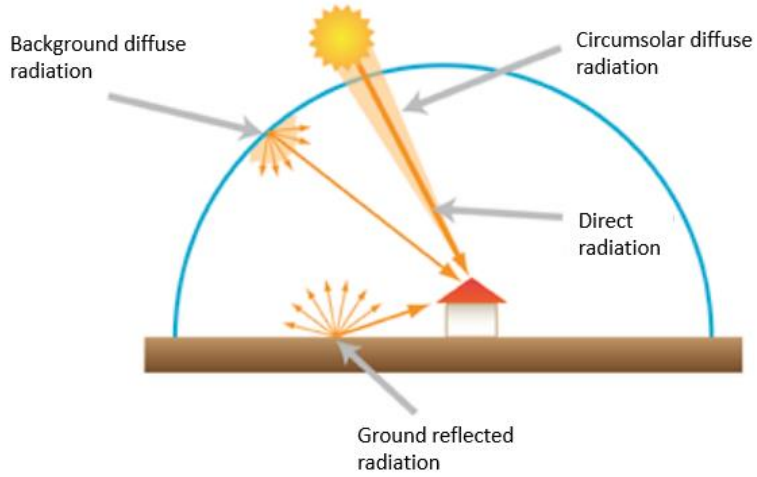

Figure 2.2 - Schematic representation of the radiation reaching a tilted surface by the sky anisotropic concept, including the anisotropy of the ground reflected component. It is important to note that the sky diffuse component may as well not be perfectly isotropic. (Adapted from Magarreiro et al., 2016).

If the diffuse component is considered anisotropic, varying with its origin and the physical properties of surrounding features, the transposition factors need to be adapted. The specularity of reflections may also be defined. Another often disregarded component is the diffuse circumsolar radiation, which refers to light that, to an observer on the ground, appears to originate from the region around the sun. This component is highly dependent on the percentage of haze, but can also vary when the solar disc is partially obstructed.

The simplest empirical radiation model is that of Liu and Jordan (Liu and Jordan, 1960). This model considers diffuse radiation to originate from the entire visible sky. The global solar radiation aggregates only three components: direct beam, isotropic diffuse and diffusely reflected from the ground. More realistic models consider anisotropic diffuse radiation, such as the Hay model (Hay, 1979) that defines an anisotropy index, assuming linearity of the isotropic and circumsolar contributions to the diffuse radiation on a tilted plane. The Perez model (Perez et al., 1987) is perhaps the most popular radiation model. It incorporates a geometric description of the sky hemisphere superimposing a circumsolar disc and horizon band on an isotropic background. Multiple coefficients derived from statistical regression analysis allow a parametric representation of the solar radiation. This configuration accounts for forward scattering by aerosols and multiple Rayleigh scattering and retro-scattering near the horizon, two consistent anisotropic effects in the atmosphere. The reflected radiation component is still treated as incoming from adjacent Lambertian diffusers. More recently, a new model reported in (Yao et al., 2016) outperformed the Perez and other models by introducing a third diffuse radiation component, the orthogonal diffuse radiation. It is worth noting that this model is calibrated to subtropical monsoon climate zones.

Choosing the proper radiation model for a certain application is not trivial, since diversity is great among literature. A comparison of 12 models for estimating total solar radiation on south and west facing tilted surfaces was conducted in (Noorian et al., 2008) were both original and simplified Perez (Perez et al., 1986)(Perez et al., 1990) and Hay (Hay, 1979) models compared well to data from pyranometers. (Mondol et al., 2008) tested the effect of 12 different combinations of diffuse-global correlations and tilted surface radiation models, concluding that Perez performs best in comparison to other anisotropic models, although the prediction of PV generation was more accurate with isotropic models. (Evseev and Kudish, 2009) compared global solar radiation predictions on a south-oriented surface tilted at 40 degrees as a function of four different types of sky conditions. Here, Ma–

Iqbal model (Ma and Iqbal, 1983) performs best under all sky, clear and partially cloudy conditions, whilst Muneer model (Muneer et al., 2004) gives the best results for cloudy sky. In (Gueymard, 2009), Gueymard takes 10 transposition models, with optimal or suboptimal input data, against global radiation measured on south-facing planes at 40 degrees, vertical planes and on a 2-axis tracker. The author found that for suboptimal input Hay (Hay, 1979), Reindl (Reindl et al., 1990a) and Skartveit (Skartveit and Asle Olseth, 1986) models deliver better outputs. However, for ideal input and conditions the results from anisotropic models fall within the instrumental uncertainty, with Gueymard (Gueymard, 1987) and Perez (Perez et al., 1990) models performing best. On the other hand, for ideal input and all-sky conditions Reindl (Reindl et al., 1990a) featured the overall best performance and gave noteworthy results for vertical surfaces, which are very sensitive to inaccuracies in the ground reflected radiation.

The ability to portray different sky conditions with detail plays an important role on the success of the transposition models. (Grigiante et al., 2011) introduced the definition of *octas* sky covered conditions as an empirical evaluation of the sky brightness based on experimental data. The global horizontal real sky irradiance determined using an improved version of Bird's clear sky model (Bird and Hulstrom, 1981), which encompassed atmospheric parameters such as a cloud cover factor specifically defined for the studied location. A comparison with global radiometer measurements from a mountainous area featured an overestimation of 2.16%, a fine result, but an approach on the global radiation incident on vertical surfaces may change these figures. (Li et al., 2013) estimates the vertical sky irradiance based on the 15 standard skies adopted by the International Commission on Illumination (CIE), which cover the whole probable spectrum of skies in the world. Six pyranometers were used to carry out the measurements of global and diffuse irradiance on a horizontal surface and the global irradiance on the vertical planes facing north, east, south and west. Solar irradiance was estimated with RMSE values between 17.9% and 19.8% through the CIE standard skies method.

An exhaustive review of a total of 26 transposition models is presented in (Yang, 2016). Models were arranged, discussed and validated using 18 case studies from 4 sites. The comparison revealed the best performing (families of) models: Perez, Muneer, Hay and Gueymard; although no universal champion model could be identified. The author also highlights that most transposition models struggle for vertical surfaces, since the foreground albedo is a crucial modelling parameter. This observation is confirmed by the benchmark of 30 models presented in (de Simón-Martín et al., 2017), which focuses on the estimation of diffuse solar irradiance on building façades under all sky conditions. Models ranging from classical semiphysical to the newest non-parametric models were classified according to their characteristics and evaluated against measurements from high precision pyranometers placed on vertical positions facing the four cardinal directions. The non-parametric Multi-Layer Perceptron model obtains the best results, whereas the Perez with local optimized coefficient is the best among the parametric group.

2.3 Context of Computational Solar

Real topographies and urban landscapes involve more than one single surface, hence physically-based solar radiation formulations alone cannot compute radiation in particular when there are changing obstructions. Such analysis can only be conducted employing computational tools that couple empirical solar radiation formulations with the digital description of the site's context. It is relatively simple to determine the reduction of the direct radiation. However, the variation of the diffuse radiation is a major challenge, not just because of its anisotropic nature but also due to the different materials that constitute the surroundings – especially for vertical surfaces.

The sky view factor (SVF) was introduced to quantify obstructions resulting either from 'self-shadowing' by the slope itself, known as shading, or from adjacent terrain or elements, called shadowing (Dubayah and Rich, 1995). It represents the solid angle of the visible celestial hemisphere normalised by the solid angle of the total celestial hemisphere, i.e. only the geometrical aspect of the available sky radiation is considered. A procedure to calculate the SVF is suggested in (Tregenza, 1987), where the division of the sky hemisphere into small segments or sky zones is proposed, each with similar solid angles. From this work, the CIE recommended the use of a hemisphere evenly-distributed in 145 virtual light sources. Many other different sky subdivision strategies can be applied, some of which are illustrated in Figure 2.3.
SVF is time independent unless significant changes occur in the surroundings, which is fairly probable in the urban environment. (Littlefair, 1998) reviews a range of tools to predict solar access in obstructed urban situations, including simple angular criteria, sun path diagrams, solar gain indicators and solar envelopes, among others. (Ratti and Richens, 2004) assume that the whole sky hemisphere is represented by a large number of disperse light sources, and propose the estimation of the SVF of a particular point by knowing the number of times that a point has been lit and the total number of times it could have been lit.

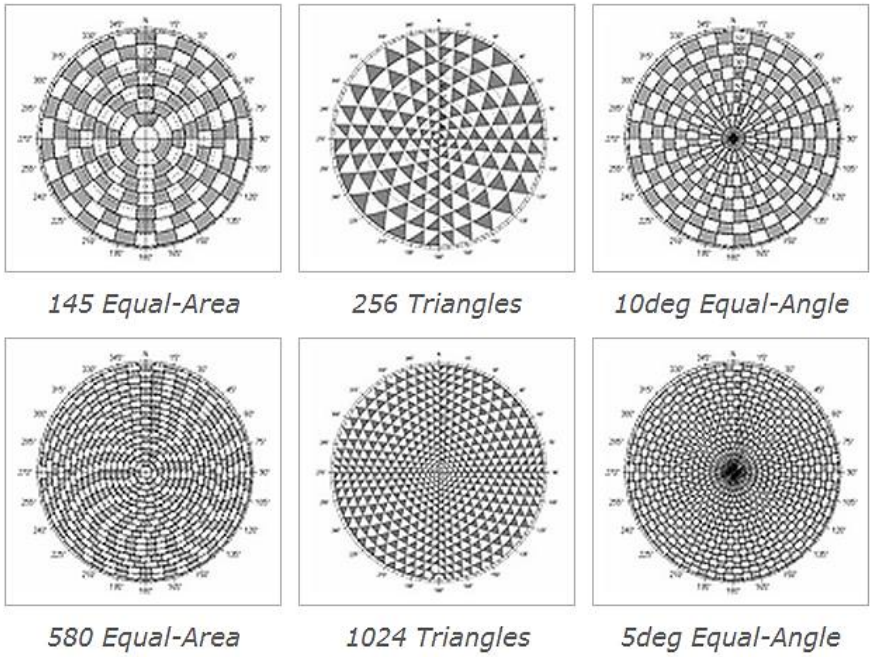

Figure 2.3 – Variety of sky division strategies to calculate SVF (Marsh, 2011).

In a vertical façade point, the SVF is lower than 0.5, since only half of the sky dome is visible. (Rakovec and Zakšek, 2012) explore different rationale for estimating diffuse radiation on a tilted surface, proposing a Diffuse Tilt Factor (DTF) which involves the integration of two different radiances over the two appropriate proportions of the solid angle. The DTF depends on the ratio of ground/sky brightness, which means that more diffuse radiation will reach the surface if the surface tilt is high and the sky is brighter than the ground. (Ramírez-Faz et al., 2015) study the SVF on vertical surfaces that have a high level of obstruction, proposing the calculation of the vertical sky component (VSC) through adequate projections for vertical planes based on fish-eye photographs. (Ivanova, 2013) modified the anisotropic model of Muneer (Muneer, 2004) to predict the background sky diffuse radiance falling onto building wall modelled as rectangular cuboids, under clear and overcast skies, by defining a new anisotropic view factor (AVF).

A modest list of reviewed computational tools is presented in the next pages. This group of tools comprises the pioneer software developed for solar potential assessment, mostly for small-scale studies. Some early conceptual tools and auxiliary software packages are also included.

i) GOSOL

One of the first energy simulation software, developed between 1982 and 2013 (Goretzki, 2013), is based on a model of a whole housing scheme and can analyse energy balance on particular surfaces. Shading patterns can be visualised and an outline of obstructions on a sun path diagram can be produced graphically, pointing out the times of day and year when the sun shines on a particular area of the urban model. GOSOL includes vegetation and climate characteristics. It was designed and hence it is the most suitable for building data source of german housing types with restricted energy consumption, such as passive buildings.

ii) SHADOWPACK

Created by Peckham (Peckham, 1990), SHADOWPACK includes a CAD interface developed to facilitate modest shading studies, for the direct component of solar radiation received by surfaces, which can be plotted as contour maps. View of the site can also be generated with the shadows at any particular time of day and year.

iii) ATM

The first topographical solar model was the Atmospheric and Topographic Model (Dubayah, 1992) which was a collection of UNIX-based tools and raster based programs within an image processing framework, not explicitly implemented within a GIS.

iv) SOLEI-32

Introduced by Miklánek and Mészároš in 1993, with a last update in 2002 (Mészáros et al., 2002), Solei-32 calculates potential energy yield from slopes with different orientations, daily solar irradiation, insolation duration and sunrise time and analyses shadow from surrounding topography and vegetation. The inputs include elevation data, cloudiness information, albedo and turbidity values. First developed for DOS environment, the later version of the model was reprogrammed into the operating system Windows with Fortran programming language.

v) SOLARFLUX

This tool was implemented in the ArcInfo and Grid GIS platform, providing access to a broad range of GIS capabilities (Hetrick et al., 1993). Through the input of a topographic surface, in the form of a grid of elevation values, latitude and atmospheric transmission values, SolarFlux delivers total direct and diffuse radiation, direct sun duration, SVF and fisheye projections of sky obstructions, with flexible temporal and spatial resolutions. The reflected radiation is not considered. It features a *hillshade* function that can be used to simulate topographic shading (Rich et al., 1995) and simulate plant canopies, when integrated with the program Canopy.

vi) SRAD

This model was developed in (Gallant and Wilson, 2000) to evaluate circumsolar radiation derived from within 5 degrees of the direct solar beam and the isotropic portion of the diffuse component. It also generates monthly average cloudiness and sky view factor values, short- and long-wave radiation components, the net irradiance, surface and air temperatures from inputs such as latitude, surface slope and aspect, monthly averaged atmospheric transmission or sunshine fraction, ground albedo, topographic shading and vegetation classification.

vii) SOLAR ANALYST

The Solar Analyst (Fu and Rich, 1999) was developed as an ESRI ArcView extension. The radiation method consists in a geometrical approach that splits the sky into different sectors, defined by pairs of zenith and azimuth coordinates. Considering either a uniform overcast sky, with the same incoming diffuse radiation from all sky directions, or a standard overcast sky, where diffuse radiation flux varies with zenith angle, this model computes a set of radiation maps, fisheye views and a viewshed analysis similar to SolarFlux (Rich et al., 1995). It is also a very flexible model in terms of temporal and spatial resolution. Solar Analyst has been featured in many studies of solar potential (Wiginton et al., 2010)(Faessler, 2010)(Mendes, 2010)(Brito et al., 2012).

viii) R.SUN

Conceptually motivated by the satellite-based ESRA model (Rigollier et al., 2000), r.sun was developed as a clear-sky GRASS GIS-based model (Hofierka, 1997), later improved (Hofierka et al., 2002), to overcome the limitations of some of the previously discussed models: Solei-32 (Mészáros et al., 2002), SolarFlux (Rich et al., 1995), SolarAnalyst (Fu and Rich, 1999) and SRAD (Gallant and Wilson, 2000). The r.sun model uses raster maps of the terrain, latitude, turbidity and clear-sky index in order to produce irradiance and irradiation raster maps, reflectance and shadow maps for horizontal or inclined surfaces, and relies on diffuse transmission and altitude functions. Reflected ground radiation is considered isotropic and it is calculated from the fraction of visible ground. It is fit to overcast and clear-sky conditions. It may run in instant time mode or daily mode, that can be used separately or in combination to provide estimates for any desired time step or interval. r.sun is optimized for European climate conditions, being the PVGIS online database (Suri et al., 2005) its most notable application, also employed in an early GIS tri-dimensional study of the rooftop solar potential of a small city (Hofierka and Kaňuk, 2009).

ix) RADIANCE

This software employs a light backward ray-tracing algorithm based on the physical behaviour of light in a volumetric 3D model, including complicated curved geometries with different reflectance and specular properties (Ward, 1994). It is extensively validated and successfully used in applications related to solar potential in building roofs and façades for electricity generation and daylighting analysis (Compagnon, 2004). Another early example of application of Radiance is the work of Robinson (Robinson, 2006), who showed that the relation between SVF and irradiance is not linear, as it depends on the different materials, geometry of the street canyons, etc. More recently, (Fath et al., 2015) used Radiance to evaluate the economic potential of PV in urban areas. Given that Radiance is a powerful tool for evaluating the light distribution in indoor and outdoor spaces, architects and designers were the first to benefit from its implementation within several CAD interfaces such as Autodesk Ecotect Analysis (Ecotect, 2010), DIVA4RHINO (Jakubiec and Reinhart, 2011), among others. A database with material properties for lighting simulations with Radiance is freely available (Jakubiec and Balakrishnan, 2015).

x) DAYSIM

Daysim is a validated Radiance-based daylighting analysis program (Reinhart and Walkenhorst, 2001) that employs a daylight coefficient method (Mardaljevic, 2000) based on ray-trace calculations and the Perez all-weather sky model (Perez et al., 1993). The workflow of Daysim consists on generating an annual illuminance profile at each point in and around the digital model of the buildings, followed by a ray-trace operation, which takes a 145 segments sky dome and 3 ground segments, and a second raytracing run with approximately 65 direct solar positions distributed along the annual solar path. By

tracing backwards from the simulation sensor points, each sky segment and solar position is weighed relative to its contribution to each point in the scene (Reinhart, 2011). Contextual shading and reflections are, therefore, considered. Typical climate data series are usually input and any incremental time step is allowed. Currently, Daysim is part of the package for energy simulation in a variety of CAD plug-ins including Autodesk Ecotect Analysis (Ecotect, 2010), DIVA4RHINO (Jakubiec and Reinhart, 2011) and LadyBug (Roudsari and Pak, 2013).

xi) ALBEDO CALCULATOR/VIEWER

These are two associated graphical user interface-based applications that provide simulation of albedos within 3D urban structures, considering perfect isotropic return from multiple reflections and shading in the urban canopy (Chimklai et al., 2004). Albedo viewer consists of a web application that offers access to a database of instantaneous calculations of albedo. Comparison with literature and observations reveal that calculated albedo is positively biased when the sun is low in the horizon, probably due to the isotropic assumption.

xii) CUMULATIVE SKY

The Cumulative Sky approach is a method introduced in (Robinson and Stone, 2004) to produce annual irradiation results from a single simulation. It was included in Radiance (Ward, 1994) as a module called GenCumulativeSky and consists on the sky division discussed in (Tregenza, 1987), in which each of the 145 patches subtends a similar solid angle. The all-weather Perez model (Perez et al., 1993) is then used to predict the global irradiance at the centroid of these patches, achieving an elegant balance between computational accuracy and efficiency. This module has become common within recent energy simulation tools such as (Dogan and Reinhart, 2017) and (Roudsari and Pak, 2013).

xiii) SRA

Proposed in (Robinson and Stone, 2005), the Simplified Radiosity Algorithm was developed and applied to predict shortwave irradiance, interior illuminance and longwave irradiance in an urban setting. The solar radiation model accounts for the effects of obstructions in reducing direct and anisotropic diffuse radiation and contributing reflected radiation. On the other hand, the longwave model considers obstructions to an isotropic sky, emissions from these obstructions and from the ground, possibly covered with vegetation. The sky vault is split into 145 divisions (Tregenza, 1987) and the all-weather Perez model (Perez et al., 1993) is used to define the luminance from each one of them. SRA results compared well to simulations done with Radiance (Ward, 1994).

2.4 Urban-scale Solar Potential Models

The assessment of the building façades solar potential in the urban environment requires more sophisticated methods to perform full 3D radiation operations in the intricate digital surface model. Moreover, the management of numerical results and their visual representation might not be trivial. A high degree of user-friendliness is desirable for large-scale solar potential models, which changes with the number of software tools that are required to perform different tasks within a complete analysis. The associated input/output data format and the user interface also contribute to a successful dissemination of these models among users and research community.

In the following Sub-sections, the state-of-the-art solar potential models able to deal with building façades are chronologically described, grouped by GUI-based (2.4.1), GIS-based (2.4.2), Customized (2.4.3), CAD/plugin-based (2.4.4), BIM-based (2.4.5) and CityGML-based (2.4.6) model categories.

2.4.1 GUI-based

Graphical User Interface-based models encompass a program where most of the solar potential modelling steps can be carried on. These are typically very user-friendly options since most of the functionalities are concentrated in one single software. Examples of such models are TOWNSCOPE and SOLENE.

i) TOWNSCOPE

TOWNSCOPE II was a follow-up of the earlier model CAM.UR (Computer Aided Management System for Urban Renewal) developed in the 80s. It was developed to support solar access decision-making in a sustainable urban design perspective within the POLIS project 1996-1998. It was applied to a number of case studies, including the LISBOA'98 international exhibit, in Portugal, and a central urban located open space, the place Saint-Lambert, in Belgium (Teller and Azar, 2001). The software consists on 3D urban information system coupled with solar evaluation tools, morphological and wind risk analysis tools. 3D volumes are represented as 3D point, polyline, border, face and volume, applying a triangulation to define ground and other irregular surfaces, however holes may not be described. The 3D objects can be acquired either via CAD software or direct data acquisition tools.

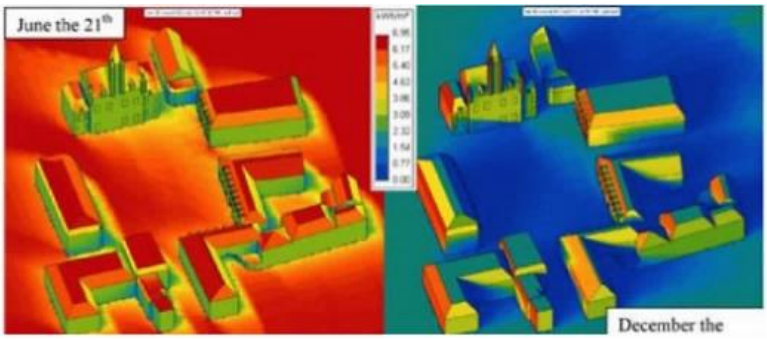

Figure 2.4 – Example of an insolation analysis in the summer and winter as seen in Townscope (Teller and Azar, 2001).

Data-processing tools calculate clear-sky hourly direct, diffuse and reflected solar radiation on any point or face defined by the user from latitude, altitude, humidity and turbidity information, or more precise meteorological data, if available. Direct component calculations are based on analytical geometry equations made on the sphere, considering partial solar masks, through transmissivity and diffusion factor applied to the volumes, and possible density of foliage. Diffuse radiation is assumed to be isotropic, to which SVF and a sky component factor based on the CIE standard overcast conditions are calculated. Reflected radiation is computed from surrounding faces considering view factors, isotropy and one inter-reflection. Specularity is not included. The masks of shade and sunshine duration can also be evaluated for any specified point through stereographical projections. This tool can also evaluate human thermal comfort in an urban open space and perform sky opening, view lengths and visibility analysis. A newer version of the software is commercially available (Azar, 2013).

ii) SOLENE

To overcome some limitations of the existing tools, such as restrictive conditions about the input geometry, limited sky conditions, and a separate approach for indoor and outdoor spaces, a set of numerical models for the simulation of natural light in the urban morphologies (Figure 2.5) was created and named SOLENE (Miguet and Groleau, 2001). It relies on the solar constant value, altitude, eccentricity, air mass, turbidity, 3D meshed geometry of the scene, the nature of the surface materials and their physical parameters to compute radiation in small sets of buildings and streets. The sky vault

is divided in patches to account for anisotropic distribution of the sky diffuse radiation, employing the all-weather Perez model (Perez et al., 1993), with further implementation of CIE overcast and clear skies. Emphasis is given to the processing of transparencies and using a multi-reflection method.

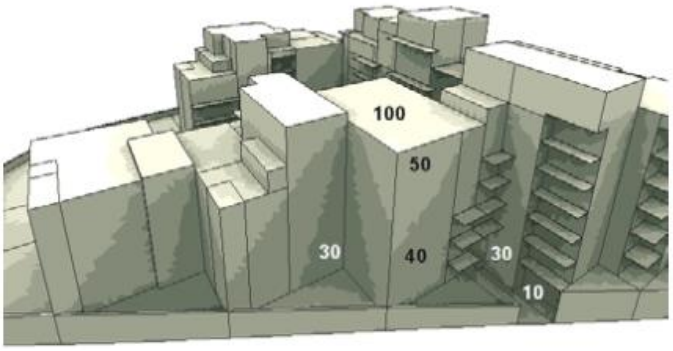

Figure 2.5 – Distribution of daylight availability in an urban setting computed by SOLENE (Miguet, 2007).

A newer version of the software, SOLENE-microclimate (Morille et al., 2015) splits the radiation spectrum into solar radiation and infrared thermal radiation to perform dynamic simulations of the evolution of surface temperatures. It is also able to perform Computational Fluid Dynamic (CFD) analysis and multizone building nodal network modelling to fully evaluate building energy consumption.

2.4.2 GIS-based

When an algorithm runs solely inside a GIS platform, large sets of information can be manipulated and heavy solar potential calculations performed on them, although some GIS programs still do not handle full 3D operations. In this Sub-section, the models employing v.sun, gvSIG and SURFSUN3D are described.

i) V.SUN

The v.sun module (Hofierka and Zlocha, 2012) is a free open-source program created specifically for vector-based data. It is implemented within GRASS GIS and it is based on the r.sun model (Hofierka et al., 2002), with a new calculation technique based on the combined vector-voxel (Alias and Pilouk, 2008) approach to process 3-D vector data representing complex urban environments. Solar radiation analysis comprises beam, diffused and reflected radiation, for clear- or real-sky conditions, and the results are saved to an attribute table of polygon elements. The shadowing effects of surrounding objects are considered using an exclusive algorithm considering the effects of neighbouring buildings: given partial shading on some façades or roofs, the original 3-D polygons representing those surfaces are segmented to smaller elements if spatial variation of attributes such as solar radiation are accounted for. A perpendicular projection of segmentation polygons to the solar ray vector is calculated either using a voxel bit mask or a projection technique. Radiation reduction due to vegetation canopy can also be implemented in the v.sun model through voxels representing an attenuation factor.

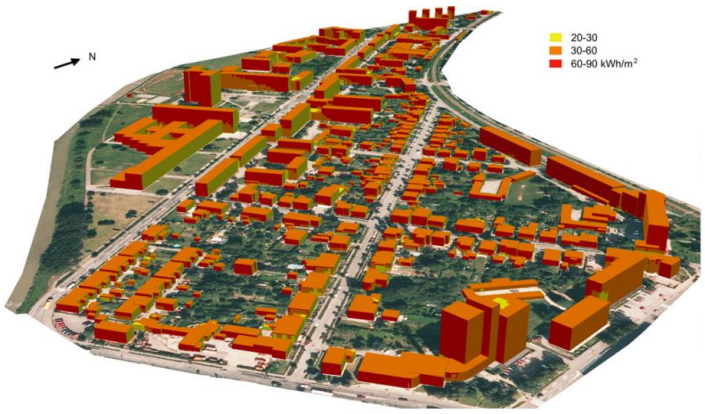

Figure 2.6 - Global clear-sky solar irradiation for the month of January, as represented by v.sun (Hofierka and Zlocha, 2012).

The applicability of the model was demonstrated for the urban area of Presov, Slovakia (Figure 2.6). Smaller voxel size provides more spatial details and higher estimation accuracy but calculation time is inversely affected, hence, the 3D city model of this sample area was represented in LoD1, as a compromise between accuracy and execution time.

ii) GVSIG

The method proposed in (Esclapés et al., 2014) relates variables of solar irradiance with urban geometry to estimate the insolation and solar irradiance in the urban fabric. The code is written in Java and has been designed to run with several libraries of the open source gvSIG. However, there is still no graphical interface, hence only preformatted input and output files work with this tool. This is the first GIS-based method specifically developed for the study of façade integrated PV potential in bulky areas (Figure 2.7). The model can calculate the usable surface area for the installation of PV systems, potential energy generation and corresponding avoided CO_2 emissions. Several other files are generated, containing 3D cartography data associated with annual and monthly insolation, solar irradiance, losses related to shading, orientation and inclination.

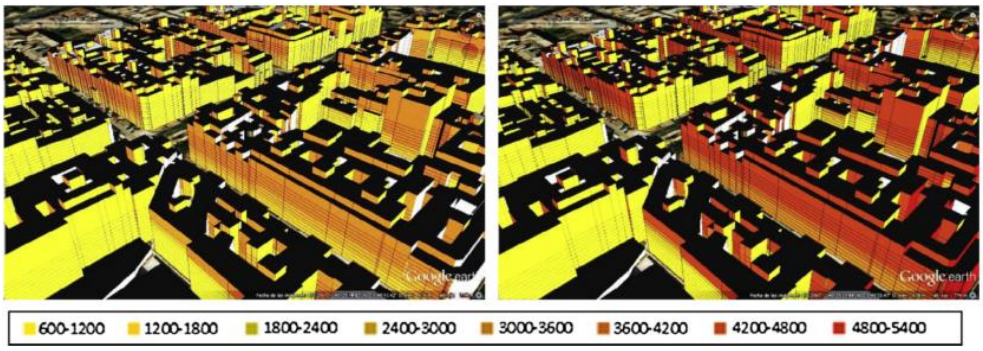

Figure 2.7 – Comparison between the irradiation on the vertical plane and for an optimal inclination, modelled in (Esclapés et al., 2014).

iii) SURFSUN3D

In (Liang et al., 2015) the efficient computation with Compute Unified Device Architecture (CUDA)-accelerated shadow casting and GPU-based parallel computing are explored to evaluate the irradiation levels in georeferenced 3D buildings. Thanks to the significant achieved speedup, the calculations run on-demand and their results can be visualized in real-time through surface mapping techniques, which transform 3D surfaces into 2D raster maps, thus facilitating conventional GIS operations and real-time rendering. The algorithm is based in the r.sun model (Hofierka, 1997) and performs radiation calculations on a cell-by-cell basis. Users can query the space by numerically specifying a region of

interest or by interactively identifying an individual building through mouse actions. The orientation and tilt of hypothetical rooftop PV systems can be adjusted to simulate their irradiation, when a building is selected, which is promptly shown in line plots.

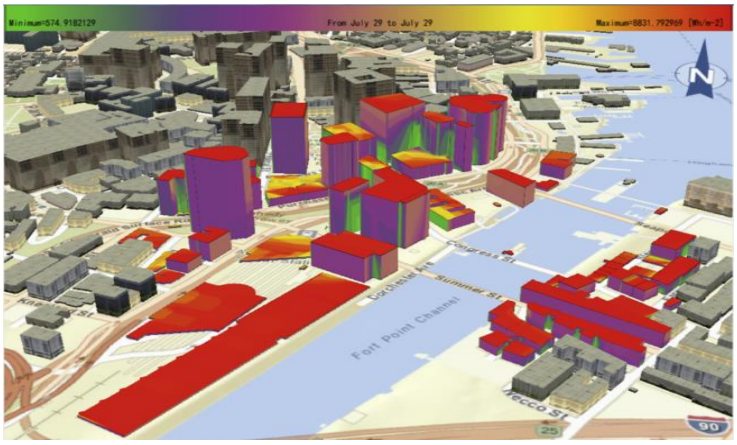
From July 29 to July 29
N
Fort Point Channel
Summer St
Lincoln St
Kingston St
Arch St
Atlantic Ave
Pearl St
Purchase St
Franklin St
Devonshire St
Milk St
Broad St
Water St
Congress St
Oliver St
Hawley St
Federal St
Post Office Sq
Devonshire St
Kilby St
Batterymarch St
Central Wharf

To overcome the discontinuity in the third dimension associated with the LiDAR data, the model works with façades sliced at regular height levels, every 3 meters, which approximately represents the typical height of a floor. However, those slices are not discretized in the horizontal dimensions, thus only one irradiation value is assigned to an entire façade slice (Figure 2.9). The estimated energy generation is obtained by multiplying the global irradiation incident on a given roof section by the installed power of a given PV panel and a performance ratio. Solar thermal evaluation was also performed.
The first version of this model was used to estimate the solar potential in the city of Geneva, Switzerland. An updated version of this model, yet to be published, features several improvements on the spatial resolution, which now has the same detail for façades and rooftops, and the execution time, which was significantly reduced since the whole code was re-written to Java and cloud computing allowed.

ii) SOL

Solar Out of LiDAR (SOL) is an algorithm written in Matlab environment for the assessment of solar potential in the urban environment at any point of an urban landscape regardless of its location on a roof, ground or façade (Redweik et al., 2011). The methodology starts from a geo-referenced LiDAR data cloud, re-sampled for a 1x1m^2 raster. Pixels with a slope greater than 72° are considered vertical walls or façades. Local typical meteorological year (TMY) data set, featuring hourly mean horizontal, direct and diffuse irradiation averaged over 30 years is used. To determine the irradiance on tilted surfaces, a geometrical approach based on the position of the sun is employed, although, solar constant radiation models could be used instead.
At every instant, a shadow algorithm takes each point of the DSM, thus including trees, as a shadow caster along the line opposite to the direction of the sun. If this line is interrupted, i.e. when a DSM cell along that line features a Z value lower than the shadow line at that position, the pixel is in shadow and receives the attribute 0, otherwise receives 1, creating a binary map. The SVF method (Ratti and Richens, 2004) includes a non-uniform disposition of sky light sources, with higher density in the zenith for portraying the circumsolar diffuse irradiation. Points in façades correspond to hyperpoints, which aggregates several points with the same XY but different Z coordinates. Since a hyperpoint in a façade can be totally in shadow, partially in shadow or totally sunlit, the SVF algorithm must treat each single point individually. The application of the model to the Faculty of Science of the University of Lisbon (FCUL) campus (Redweik et al., 2013)(Catita et al., 2014), the first study which conveniently addressed building façade solar potential in the urban scale (Figure 2.10), showed façades show smaller seasonal variations than rooftops.

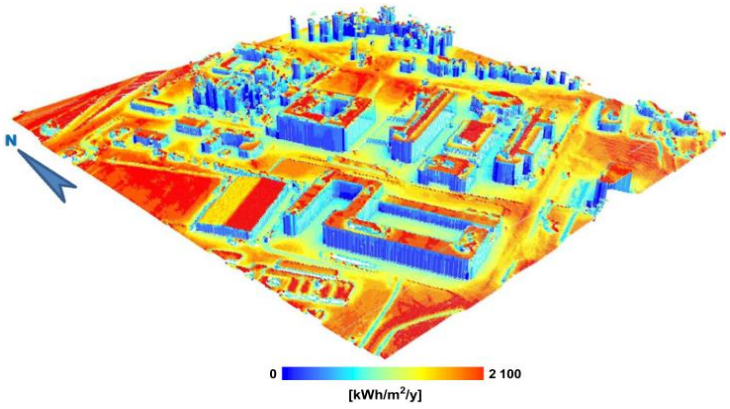

Figure 2.10 - Annual global radiation over façades, roofs and ground as computed by SOL (Catita et al., 2014).

iii) JAKUBIEC AND REINHART

The model described in (Jakubiec and Reinhart, 2013) employs the validated Radiance/Daysim backward-raytracing daylight simulation engines (Reinhart, 2011; Ward, 1994) on a LiDAR-derived 3D representation of the city of Cambridge, USA. Using GIS datasets from the city, buildings and ground were separated into two categories of points, for posterior Delaunay triangulation. The result was converted into a Radiance compatible format. Building walls were considered Lambertian diffusers with 35% reflectance, whereas the surrounding landscape was attributed a diffuse reflectance of 20%. The reflectance and absorptivity values for rooftops were calibrated according to their surface material. For simplicity, slopes that exceeded 60° were considered vertical surfaces or walls.

All-weather Perez sky model and the cumulative sky approach were employed in irradiation simulations (Figure 2.11) performed at an hourly time-step with over a 1.5m^2 light sensor grid. Hourly averaged global horizontal irradiation and air temperature from a nearby weather station were input. Direct beam component was sampled for each ray reflection, considering up to two ambient reflections from direct solar radiation and one reflection from diffuse sky radiation from the environment.

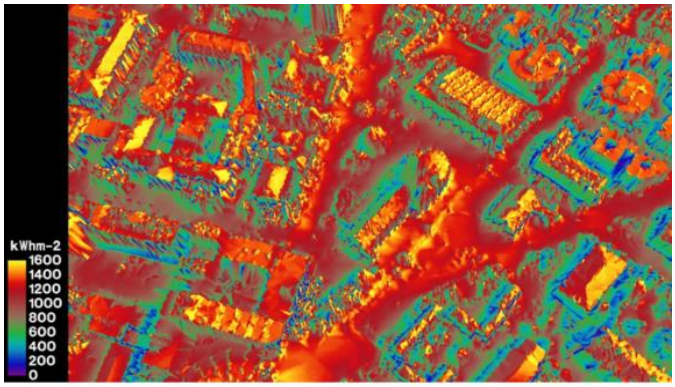

Figure 2.11 - Annual irradiation for a surface model with detailed rooftops (Jakubiec and Reinhart, 2013).

Hourly energy production from PV systems was also simulated, based on the calculation of the sol–air temperature (i.e. the air temperature near urban rooftops, accounting for the effects of convection and absorptivity on the surfaces, plus the ambient temperature). The panel temperatures were calculated using the NOCT (Nominal Operating Cell Temperature) model and a derating factor based on temperature correction. This method was validated against real rooftop PV systems, achieving errors around 4% in the annual estimated production for the years 2008 to 2011, which is smaller than inter-annual variations in predictions for PV electrical generation from SolarAnalyst and r.sun.

iv) SORAM

SORAM is described in (Erdélyi et al., 2014) and specifically addresses the computation of direct and diffuse solar radiation incident on a sloping PV cell in an urban environment. The decomposition model (Reindl et al., 1990b) is used to convert global horizontal radiation to direct and diffuse radiation and the direct radiation is determined with a ray-tracing algorithm considering the model of (Duffie and Beckman, 2013) and (Muneer, 2004). The Perez model (Perez et al., 1990) is refined with a ray-tracing algorithm to convert diffuse radiation from a patch in the sky to a specific ray. SORAM computes dynamic 3D shading from urban obstacles, such as buildings or trees. However, no reflected radiation is considered in this model and the third dimension is treated as slices (Figure 2.12).

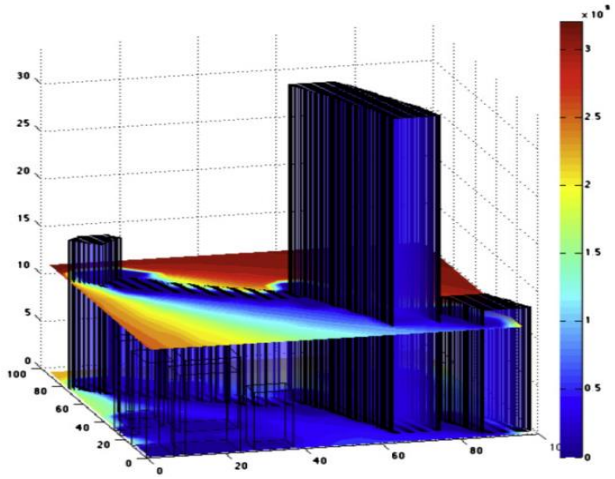

Figure 2.12 - SORAM simulation of global radiation distribution at heights of 0 m and 11.3 m (Erdélyi et al., 2014).

A validation attempt was conducted using empirical measurements from two pyranometers installed in a sample area: one facing southeast and the other southwest, but both slightly tilted. The edges of the sampled buildings were introduced based on Google Maps images and the obstacles, such as surrounding buildings and trees, were approximated by voxels. Results show that SORAM overall performance is better than the standard Perez model.

v) SEBE

The model SEBE, described in (Lindberg et al., 2015), is able to estimate solar irradiance on roofs and building walls of high resolution DSM, including vegetation. Hourly data of global solar radiation is used as meteorological input information to the decomposition model of (Reindl et al., 1990b). A cumulative sky approach is followed using sky vault division with 145 patches of similar solid angles, thus the position of the sun is derived and added to the centroid of the closest patch to distribute the direct component. The diffuse radiation component is redistributed based on the all-weather model of Perez (Perez et al., 1993). The model was evaluated for tilted roofs and walls in the city of Göteborg, Sweden, proving itself a computational efficient tool. Overall, SEBE is very similar to SOL (Redweik et al., 2013), but presents several improvements including considering anisotropic diffuse radiation and reflected radiation and faster calculations, with only 145 sky divisions and no SVF computation. It is intended to incorporate SEBE into an urban climate planning tool, available as a plugin in QGIS.

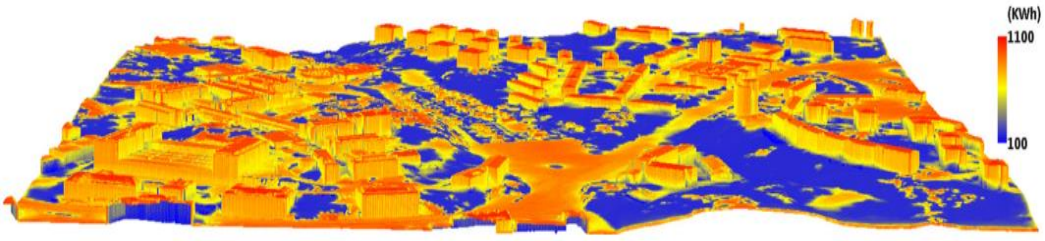

Figure 2.13 – Example of the 3D visualisation of the shortwave irradiance computed by SEBE model (Lindberg et al., 2015).

2.4.4 CAD/plugin-based

Some models that work as non-essential components on a hosting Computer-aided Design (CAD) software are described in this Sub-section. The main advantage of these methods is that they explore

the flexible and advanced 3D modelling functionalities of the CAD, occasionally including parametric design possibilities (Amado and Poggi, 2014; Anton and Tănase, 2016), coupled with dedicated energy models. Examples of these tools are Ecotect, DIVA, Skelion and LadyBug.

i) ECOTECT

Ecotect was developed by Square One Research and acquired by Autodesk in 2008, and it has been commercially available since then, although it has been discontinued in 2016 and replaced by Revit (Autodesk Inc, 2017), a Building Information Modelling (BIM) software. Ecotect was the combination of numerous detailed analysis functions with a highly visual and interactive display presenting analytical results directly within the context of the 3D model. Ecotect followed a split-flux model of daylighting, featuring several applications, such as solar radiation on windows and surfaces showing differential incident radiation (Figure 2.14) calculated over any period using longitude, latitude and climate file as inputs. It also displays the position of the sun and its path relative to the input model at any date, hour and location. The behaviour of sunlight passing through windows and moving around within a space can be visualized, and daylight factors and illuminance levels at any point can be calculated (Ecotect, 2010). The final results can be assigned to the objects in the model as attributes. Although this tool has been widely used for solar access studies, a comparison with measurements conducted in (Vangimalla et al., 2011) shows that Ecotect cannot be used for accurate simulations of thermal loads and illuminance levels.

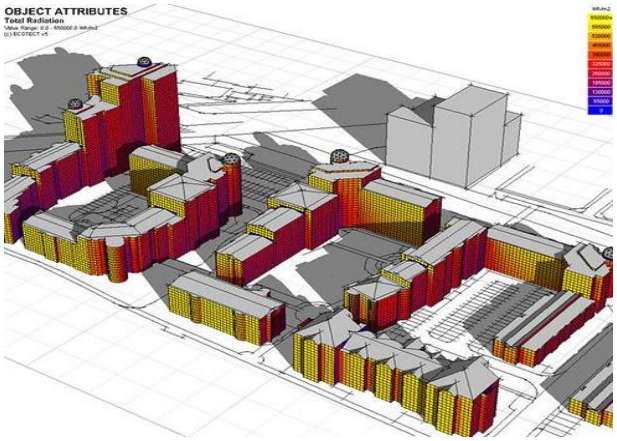

Figure 2.14 – Global radiation over the façades of a urban 3D model as presented by Ecotect (Ecotect, 2010).

ii) SKELION

Skelion (Skelion, 2013) was created in 2011 as a plug-in for the former Google SketchUp, now Trimble Sketchup. This plug-in simulates the electrical output power of a group of PV components incorporated to a 3D model. Solar obstructions can be projected over the roof with a distance/height or a solstice shadow criterion to determine the area that accomplishes the required feasibility levels. Geo-referenced buildings and terrain models can be imported from Google Earth. Solar radiation and the subsequent electrical PV production estimates are acquired from the PVGIS (Suri et al., 2008), or from PVWatts (Marion et al., 2001), depending on the site's location. When using PVWatts, Skelion further calculates the shade derating factor, the percentage of solar energy available for each panel considering shadows. If modelled, trees are considered as solid shadow casters. The output is delivered as reports containing the system components and energy yield, arranged either by face, or by groups with the same component, slope and aspect, or by arrays. The production levels can be visible in the sketch, although the irradiation levels are not shown. Nevertheless, such visualization

and further functionality in terms of PV simulation is available in its competitor plug-in Archelios Pro (Trimble, 2016).

Figure 2.15 – Implementation of rooftop solar PV using Skelion (Skelion, 2013).

iii) DIVA

This environmental analysis plug-in is incorporated within both Rhinoceros 5.0 (McNeel, 2016) and its graphical algorithm editor Grasshopper (Davidson, 2017). The first version of the plug-in worked only in Rhinoceros (Jakubiec and Reinhart, 2011), but its Grasshopper version has recently been released with improved functionality (SolemmaLLC, 2016). The first version of DIVA was employed in (Kanters et al., 2014) to estimate the energy production from solar thermal collectors and PV panels, in a workflow called Fassades. DIVA is based on the validated daylighting and thermal simulation engines Radiance (Ward, 1994), Daysim (Reinhart, 2011) and Energy Plus (Crawley et al., 2001). This plug-in allows for a series of environmental performance evaluations of individual buildings and urban landscapes, including Radiation Map analysis, which consists on the selection of the geometries of interest and the input of several details such as analysis period, time step, location, typical meteorological year weather file, grid resolution. etc., and the output of irradiation values for each grid element from an hourly to an annual basis.

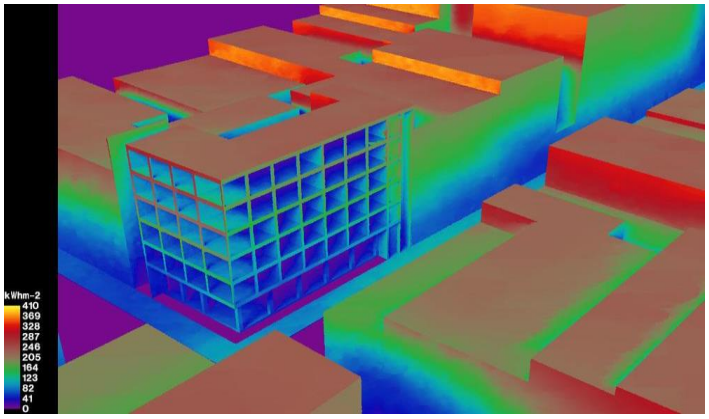

Figure 2.16 – DIVA typical false colour visualization of irradiance results (Jakubiec and Reinhart, 2011).

DIVA will be used extensively in this thesis, in particular in chapters 3, 4 and 8. A more detailed operational description is provided in sub-sections 3.2.3 and 4.4.1.

iv) LADYBUG

This plug-in (Roudsari and Pak, 2013) also works within the CAD software Rhinoceros3D (McNeel, 2016), through the capabilities of its integrated graphical algorithm editor Grasshopper (Davidson,

2017), and AutoDesk Revit (Autodesk Inc, 2017), through Dynamo (Autodesk Inc, 2016). Similarly to DIVA (SolemmaLLC, 2016), LadyBug is based on Radiance (Ward, 1994) and several EnergyPlus (Crawley et al., 2001) validated models to perform a very complete set of energy simulations and environmental analysis, but it is an open-source tool with freely editable Python code. It has far more functionalities than DIVA, which makes it slightly harder to master, and it is more unstable. The plug-in package usually includes HoneyBee, a set of components that focus on the thermal modelling and energy systems simulation. More recently, a third part has been added to the plug-in to perform CFD analysis, called Butterfly (Roudsari, 2017).

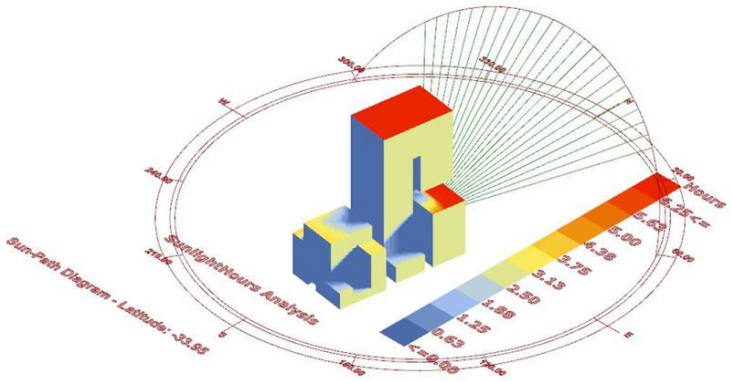

Figure 2.17 – Example of sunlight hour analysis over a 3D model using LadyBug (Roudsari and Pak, 2013).

2.4.5 BIM-based

Building Information Modelling (BIM) software is an upsurging technology that integrates a 3D building model with building information from the building model's database through the lifecycle of the building. The generation and management of the virtual representation of a building/facility, allows architects to explore different design concepts in a short period of time. One of the features of BIM is that the building geometry can be extracted to enable energy simulation and analysis, such as solar exposure, rainwater harvesting, recycled content, etc. When the conceptual design has been finalized, the BIM model can undergo further development into the schematic design and design development stage (Kuo et al., 2016).

i) REVIT

Revit (Autodesk Inc, 2017) is a 4D BIM software, which means it has tools to plan and track various stages in the building's, from concept to construction and later maintenance and/or demolition. Revit does not feature Rhinoceros 3D's ability to manipulate an object's individual polygons and surface fitting techniques. In this sense, its Solar Analysis (Egger, 2016) plug-in has similar energy simulation features to DIVA and LadyBug, although less developed. Its solar radiation analysis outputs direct and diffuse solar irradiation, as well as the amount that is absorbed, reflected and/or transmitted through the building surfaces. It is possible to assess PV potential of all the surfaces in the building model (either rooftops or façades) and explore the impact and interaction between several design variables that affect the PV potential. Like Grasshopper works on objects in Rhinoceros 3D, the same kind of directly programming the behaviour of hosted components through a drag and drop node interface is possible in Revit through Dynamo (Autodesk Inc, 2016). Deeper solar and PV potential can thus be estimated using LadyBug's version for Dynamo.

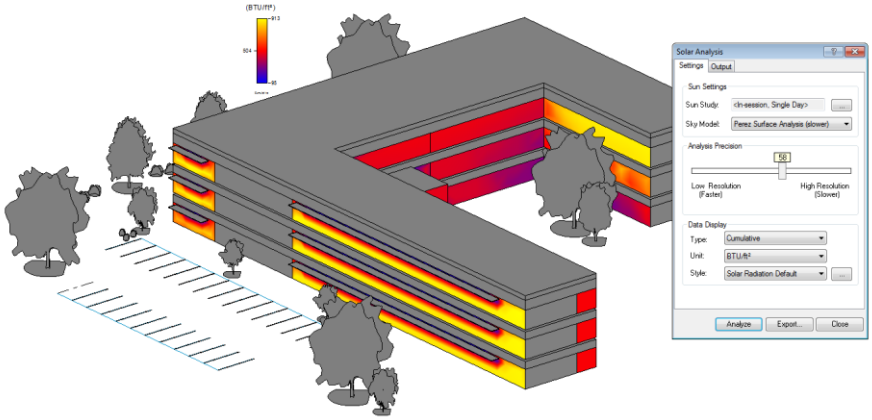

Figure 2.18 – Solar irradiation for the façade surfaces of a 3D building model as represented by Solar Analysis plug-in for Revit (Egger, 2016).

According to reviewed literature (Ning et al., 2017)(Ning et al., 2018)(Habibi, 2017), Revit is, currently, the most used BIM software to assess solar potential in buildings and evaluate design alternatives.

ii) PVSITES

In the scope of the PVSites European project, a software suite based on the BIMsolar platform (BIMsolar, 2018) was created to allow users to model and evaluate building integrated PV projects in terms of architectural design, energy production, thermal impacts and light transmission. It consists of an either online or offline user-friendly interface for importing building 3D models, selecting the project location and respective weather data, raytracing for irradiance calculations and visualization of results on all surfaces of the model. Simulation of PV performance and financial analysis can be carried out through the import of existing PV module templates or assisted self-design of products. Inverters and module/string interconnections can be automated or manual (PVsites, 2017).

Figure 2.19 – Example of irradiance on a custom project and simulation of a rooftop PV system (PVsites, 2017).

The software official release is scheduled for early 2019, but its current beta version is available for free. The updated version will contain further functionalities, such as an extensive built-in database of PV products, the modelling of energy storage systems with energy management strategies and optical and thermal simulation of glazing products.

2.4.6 CityGML-based

CityGML is an eXtensible Markup Language (XML)-based open data model for the storage and exchange of virtual 3D city models, issued by the Open Geospatial Consortium (OGC). It provides a basis for 3D geospatial visualization, analysis, simulation and exploration tools (Nouvel et al., 2013). Some models which work with CityGML standard are presented next.

i) CITYSIM

CitySim is an update of the SUNtool that goes beyond solar radiation analysis (Robinson et al., 2009). This tool simulates and optimises hourly building-related resource flows, requiring site location and associated climate data definition, adjustment of default datasets for the types and age categories of the buildings in the 3D model, and the description of energy supply and storage systems to be modelled. The scale of the case-study can range from a few buildings to the city large-scale. Several core algorithms provide different functionality to the tool: thermal model based on a resistor-capacitor network; shortwave irradiance; occupant behaviour; heating, ventilating and cooling systems and energy conversion systems. Regarding the radiation model, it is specifically based on the SRA algorithm (Robinson and Stone, 2005) to compute the short-wave radiation. The all-weather Perez (Perez et al., 1993) and 145 sky divisions are also used in this software.

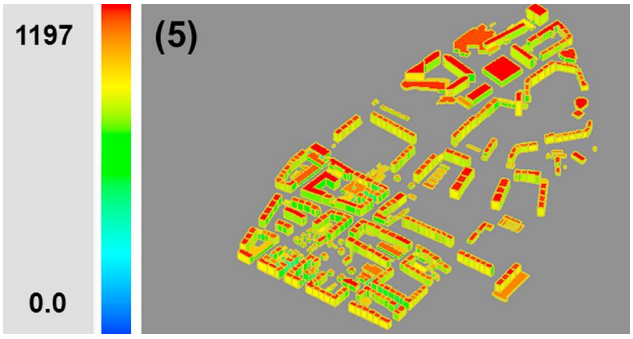

Figure 2.20 - Annual solar irradiation [kWh/m^2] estimated using CitySim (Mohajeri et al., 2016).

Although, more recent versions of CitySim make it a very complete and powerful urban planning tool, it requires the use of external programming scripts to access data stored in databases to create an essential input XML file, which must contain the geometric description of the urban scene together with attributes that relate to each of the core models. In (Mohajeri et al., 2016) this approach was taken to evaluate hourly active and passive solar gains associated with rooftops and façades from 11418 buildings in the city of Geneva, Switzerland. A gateway between CitySim and CityGML is presented in (Coccolo et al., 2016).

ii) SIMSTADT

Firstly introduced in (Nouvel et al., 2015), SimStadt builds upon the flexible spatio-semantic data structure for 3D geospatial visualization, multi-domain analysing, simulation and exploration CityGML reference. It consists on a platform to support the creation of energy strategies for cities, with a variety of multi-scale energy analyses, and the development and test of new simulation algorithms and new data sources.

For the solar potential analysis, hourly or monthly weather data can be imported from different online/software databases or weather data files. The computation of solar irradiation on each building boundary surface is possible under different radiation models, according to the required level of detail and accuracy: Hay sky model (Hay, 1979), if the building can be treated as an insulated object; a ray-casting algorithm coupled with the Hay model and an average urban albedo, if surrounding

obstructions must be considered; and SRA (Robinson and Stone, 2005) coupled with the Perez sky model (Perez et al., 1993), if both shadowing and reflection effects are compulsory for the study.

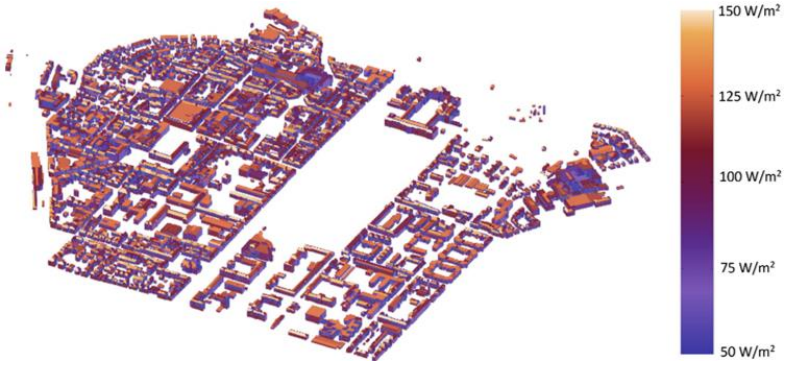

Figure 2.21 - Radiation map simulated using SimStadt (Romero Rodríguez et al., 2017a).

In (Romero Rodríguez et al., 2017a) the large-scale solar technical and economic potentials in the Ludwigsburg County, Germany, were evaluated using SimStadt (Figure 2.21). Although reducing the accuracy of the procedure, the Hay model was chosen with shadowing reduction factors to account for irradiation losses due to the surroundings. The authors have recently developed tiling strategies to reduce the computational time (Romero Rodríguez et al., 2017b) and allow for the implementation of the more reliable radiation model option. Such improvements help to making the large scale more valuable.

iii) BREMER ET AL.

(Bremer et al., 2016) explore several data representation types of multiple scales to model solar irradiation. The focus lies on a new kind of 3D spatial sampling combined with multi-scale geometrical object representations. A texture mapping approach is used for object sampling on the 3D city models. Contrarily to voxel-intersection and Delaunay-subdivision methods, a decrease in cell sizes does not exponentially increase file sizes. Therefore, querying data set with high resolution becomes feasible. This novel technique can produce accurate full 3D irradiation results with similar computational effort as a 2.5D assessment. The output consists on either a COLLADA or CityGML data structure. It is highlighted that efficient and intuitive dissemination of the results can be achieved when 3D models are included into Web Mapping Services (WMS) of cities or into commercial systems such as GoogleEarth.

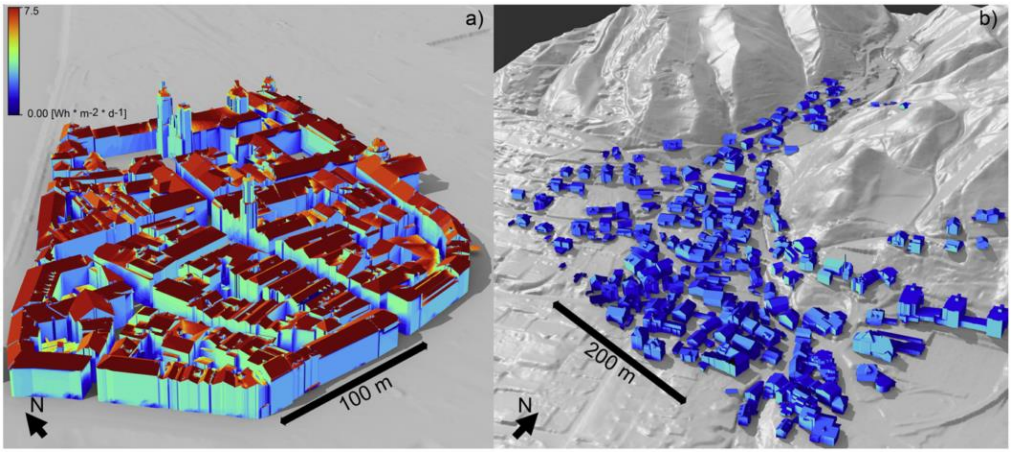

Figure 2.22 - Direct irradiation over two city models for the 15th of June (left) and the 15th of January (right) calculated using the methodology in (Bremer et al., 2016).

The city of Innsbruck, Austria, was the case-study for testing this methodology, where the contribution of vertical features is highlighted (Figure 2.22). Still, some improvements are needed, specifically at the level of vegetation influence on solar radiation, reflected radiation, surface albedos and atmospheric turbidity information will also complete the modelling setup.

Many other tools exist for assessing all the levels of potential for solar applications in buildings and cities. A thorough review of around 200 tools for radiation, daylight and thermal energy simulation can be found in (Jakica, 2017), as well as a comprehensive table summarising their relevant functionalities.

2.5 Online solar maps

It is unquestionable that solar potential assessment methods are powerful tools to help in the resolution of field-related issues. However, one thing is the visual representation of the outcomes of a particular study; another thing is the possibility of disseminating large-scale results to the general public, who might be unacquainted with the theory behind the tools. This goal can be achieved through online solar maps, web-based interfaces that visually represent the solar potential at a specific location whilst providing on-demand information such as annual solar irradiation, estimated solar system size, solar electricity generation estimates, etc. Solar maps should be user-friendly tools to instruct the users about the benefits of solar energy technologies and their associated benefits.
Reviews of solar maps existing in the United States can be found in (Dean et al., 2009) and, more recently, in (Fish and Calvert, 2017). There are no online solar maps that include building façades. Some of the most relevant rooftop solar potential maps will be described: PVGIS, PVWatts, Mapdwell Solar Systems and Google Project Sunroof.

i) PVGIS

The well-known PVGIS database (Huld et al., 2005) allows the visualisation of solar radiation data for Europe, Africa and South-West Asia, with a spatial resolution of 1km. The tool uses the r.sun model with ground-based measurements for Europe (1981–1990 data) and Africa (1985-2005 data) and includes shadows due to the terrain. The interface allows the user to input nominal PV peak power, orientation and inclination, mounting type, technology used, among other features. The visible horizon can also be outlined; thus, estimations can be made for an urban façade system. The output includes optimum panel inclination for a given location, monthly and yearly global irradiation maps, daily irradiance profiles, climatic parameters and potential PV production, considering ambient temperature.
This solar map also lets the user choose between the older or a more recent solar database, based on CM-SAF satellite data, i.e. solar irradiance data derived from instruments on board the Meteosat satellites. Although mountain areas may still incorporate a significant level of uncertainty, the newer database has a minimum bias deviation (MBD) of +2%, whereas the older has +5% (Huld et al., 2012).

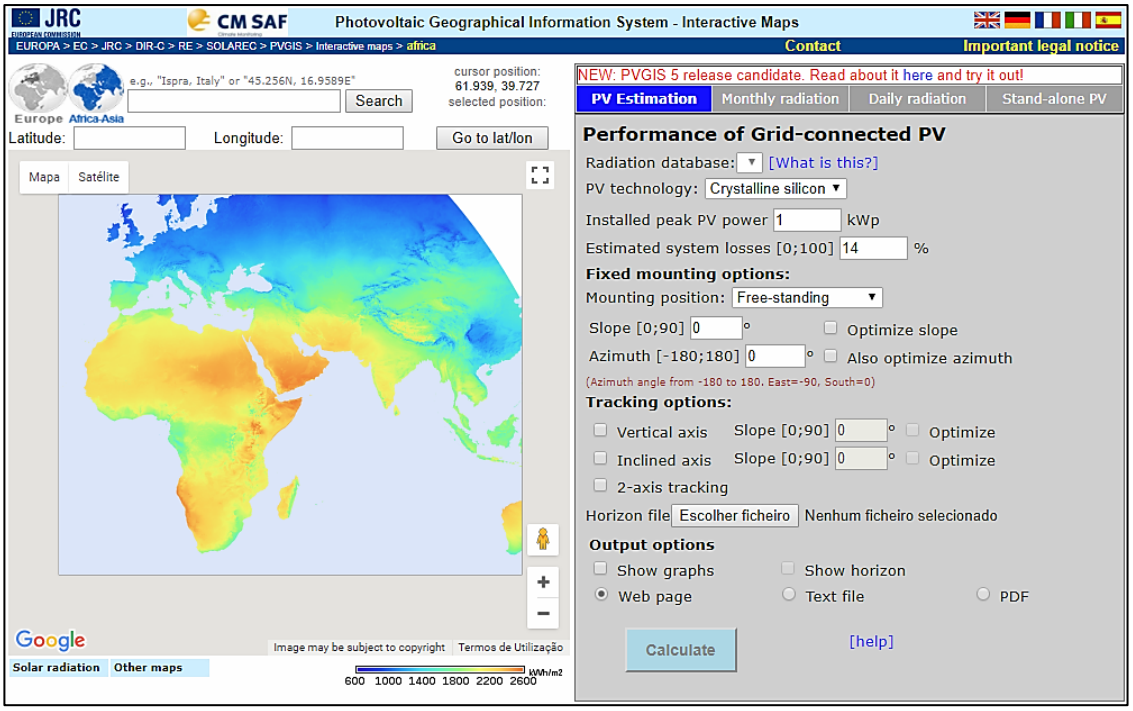

Figure 2.23 – Global horizontal radiation as presented by PVGIS database and its graphical user interface (JRC EC, 2014).

ii) PVWATTS

The solar mapping tool PVWatts (Marion et al., 2001) was firstly available for locations in the United States. It combines data from the second TMY dataset with a 40km^2 spatial resolution topographic model, and employs the PVFORM calculator (Menicucci and Fernandez, 1989) and the Perez anisotropic diffuse model (Perez et al., 1993) to estimate annual PV production, and its economic value. A newer version of the tool (NREL, 2017) extends the model to any location in the world, allowing users to delimitate the rooftop of interest after searching for any address, postal code or geographical coordinates. Additional information such as local electricity costs, tilt and surface azimuth, tracking mode, DC rating and a de-rating factor can also be stipulated to estimate monthly energy production.

The new version of PVWATTS also incorporates In My Backyard (IMBY, 2013), another tool to access PV potential with a map-based interface that allows the user to specify an address or manually select a rooftop. An hourly satellite-derived dataset with a spatial resolution of 10km was used to calculate the solar resource. Using the DSIRE database of renewable incentives and taxes (N.C. Clean Energy Technology Center, 2017), it estimated the electricity produced by a PV system over a year, including hourly AC output, its value, payback and contribution to the load profile. It was discontinued and incorporated into the new version of PVWatts.

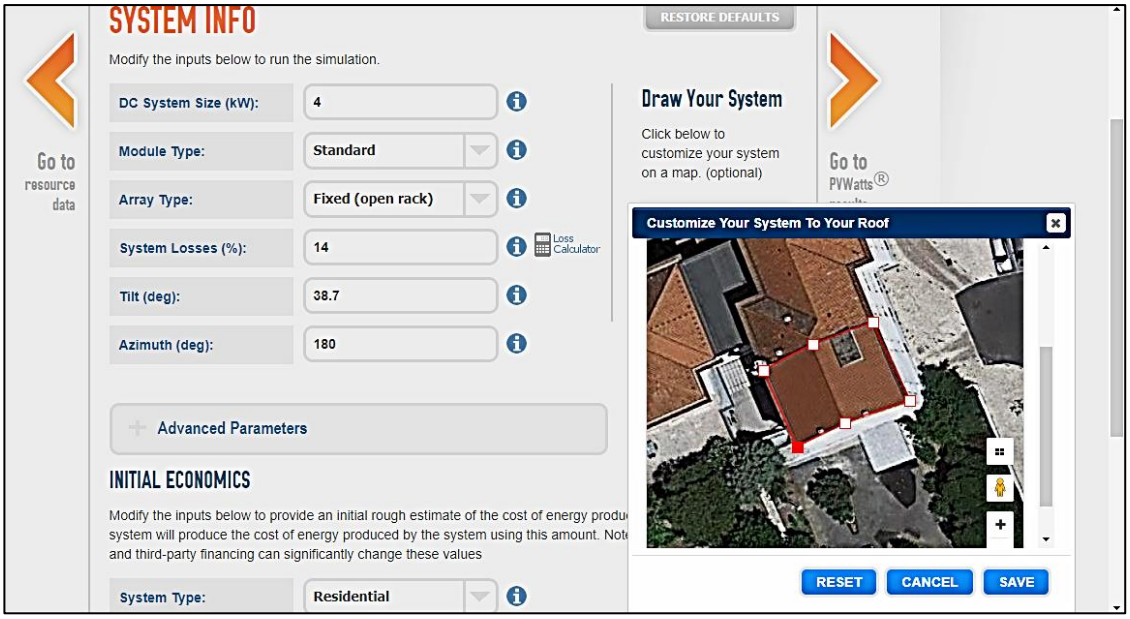

Figure 2.24 – PVWATTS user interface for rooftop PV systems costumization (NREL, 2017).

iii) MAPDWELL SOLAR SYSTEMS

Mapdwell Solar Systems developed online solar maps for Cambridge, created under the scope of (Jakubiec and Reinhart, 2013), and Washington DC. Both maps include building rooftops and structures and tree foliage derived from high-resolution LiDAR data. The user can search for an address or manually select the rooftop of interest and/or change its size. For a queried rooftop, results include financial, technical and environmental information such as installed peak power, costs to owner, monthly revenue, payback period and carbon offset, measured in trees per year. A colourmap code also helps visualizing roofs defined as "poor", "average", "good" and "optimal" or not available at all. A ±3-5% margin of error is stated, attributed to inaccuracies due to partial sample obsolescence, excess of vegetation or non-modelled obstructions, incomplete or corrupted databases, incomplete or corrupted GIS layers, or undetectable partial obstructions based on survey resolution.

Figure 2.25 – User interface in Mapwell Solar Systems for assessing cost and revenue from a costumized PV rooftop (Mapdwell, 2017).

iv) GOOGLE SUNROOF

This project was launched in 2015 and informs users of their rooftop solar potential from the address (Google, 2017). The model accounts for historical weather patterns, the location of the sun throughout the year, the geometry of the roof, and shading from nearby objects such as trees and buildings. An estimate of potential household electricity savings over the term of a 20-year lease is created, which can be refined if further electricity bill information is provided and different financing options are chosen. Project Sunroof works by using high-resolution aerial imagery from Google, Google Maps, 3D models and machine learning to estimate solar generation potential accurately and at large scale. After a launch phase for a few US cities, its coverage is being extended, reaching about 60 million rooftops in the United states and around 7 million roofs in Germany (E.ON Solar, 2017).

Figure 2.26 – Sunlight hour levels on rooftops as presented by Google Sunroof (Google, 2017).

2.6 Discussion

Although enhanced computer power has triggered considerable advancement in the modelling of solar potential in cityscapes, there are still many challenges that require further research and development. Firstly, the reliability of the methods should not be compromised by differences in the accuracy of the inputs. Taking PVGIS as an example, its major source of uncertainty comes from the quality and the spatial distribution of parameters such as atmospheric turbidity, ozone, water vapour, aerosol optical depth, which may not adequately match the DSM resolution (Suri et al., 2008). On the other hand, using data from different periods, as well as differences in accuracy between interpolation from ground station and satellite measurements, might also increase uncertainty. Of course, higher temporal and spatial resolution are always desirable, but its impacts, in terms of computing time and propagation of errors, must be carefully weighted.

Further challenges arise from the representation of the surfaces in the modelled scene. In the case of simpler models, a critical limitation is the disregard of surface slope and/or aspect, whilst other models consider those properties in the form of flat surfaces, which means that features such as chimneys, air-conditioning units and other structures are left out. In this sense, façade elements such as windows and balconies also lack proper representation, which can only be achieved through manual modelling, labour intensive acquisition procedures and/or machine learning techniques.

LiDAR data-based models also present limitations, especially when building façades are concerned. (Redweik et al., 2011) points out modelling errors in façades that are very close to each other, attributing this circumstance to multi-path effects in the LiDAR survey. Outdated LiDAR data may also

lead to less reliable results. Conversely, due to its complexity, vegetation is often unsuitably modelled as solid shadow casters, if not disregarded. It may be noted that (Tooke et al., 2012) reports that a 18% underestimating of direct irradiance arises from the representation of trees as opaque objects and (Zhang et al., 2015) highlight this overestimation in winter time. Gap fraction method is presented in (Jakubiec and Balakrishnan, 2015) as a method to model the trees geometrically and their corresponding Radiance material definition, and the luminance method, to determine the transmittance coefficients of the trees. Nevertheless, further research is still needed in this area.

As far as GIS tools are concerned, currently *en vogue* as they bring together complementary knowledge, CityGML (Nouvel et al., 2013) is indeed the state-of-the-art standard that allows performing spatial and attribute query and manipulation in such environments, as well as effective sharing of models and results. Other options under development include the commercially available Esri City Engine, combined with analysis tools implemented in ArcGIS. In this case, the development of databases that handle 3D geometries, such as Postgis or Oracle, and 3D spatial query languages, e.g. spatial Structured Query Language (SQL), would be needed. Through SQL, the open source PostGIS can be integrated within a GIS tools for visualization through applications such as GLOBE or Horao (Oslandia, 2014). With GIS fully able to handle 3D analysis, it will be of interest to create solar maps including building façade solar potential, with online interfaces and sophisticated interactive features to enhance the visibility of the environmental, economic and visual impacts of their choices.

Some of the reviewed solar potential models still adopt simplistic isotropic characterization of diffuse radiation, as a compromise between acceptable results with reasonable computation effort. Thus, the use of programs such as Radiance is advised when the study requirements involve detail and high quality, since these are the most appropriate light propagation engines to perform simulation with anisotropic distribution and specular effects, including inter- and multi-reflections in complex environments. However, the complexity and spatial resolution of the urban digital representation paired with detailed models of solar radiation increase the computational requirements. The programming language used in the scripts/software may also have an influence in the overall execution time. Parallel computing has become common practice, usually performed using multi-core processors in one single computer or a cluster of standalone machines connected by a network. An alternative approach consists on the identification of representative portions of an urban layout, in terms of their form and energy exchanges, as proposed in (Dogan and Reinhart, 2017), where a “shoeboxer” method facilitates large-scale urban simulations and is applicable in urban design, planning and other geospatial energy analysis scenarios.

The conversion of solar radiation to electricity and/or hot water production can be estimated within the model itself or calculated using the results of the model through another software. The user can skip the solar potential modelling and jump directly into the energy systems simulation, using, for instance, specialized software or scripts such as the standalone PVsyst, PVlib for MatLab and BuildsysPro for Modellica, to simulate solar PV in all its features. When converting irradiation to energy generation, it is essential to provide and account for ambient temperature and/or module temperature. For solar thermal potential the analysis must entail estimates of local hot water demand, e.g. from population distribution, as the conversion efficiency depends on demand (Quiquerez, 2012).

Despite the extensive validation of empirical radiation models, a full 3D solar potential model requires renewed validation procedures. This requires the accumulation of a significant amount of case studies since outcomes are site, materials and technology dependent due to the complex light phenomena involved. These efforts are somewhat hindered by the lack of measured data. Measurement systems (e.g. pyranometers) are seldom installed in urban scenarios and (monitored) building integrated PV systems are difficult to find. It is expected that, as solar energy becomes more attractive, more research will be conducted in this area and people will get more incentives to invest in solar systems and to share their production data.

Most modelling tools only address one specific issue; however, attentions are turning to holistic approaches to model urban energy systems while taking into account the consumption patterns and behaviour of citizens. Furthermore, beyond solar PV or thermal, there can be other options that may alter the optimal building design or urban configuration, such as access to natural daylight, natural ventilation, outdoor thermal comfort, streets walkability, etc. Urban solar potential models are but one of the many possible bridges to the nascent field of urban building energy modelling (Reinhart and Cerezo Davila, 2016). Such models are key tools for the dissemination of renewable energy deployment in urban environments among the general public and to provide decision makers and urban planners trustworthy knowledge to drive cities closer to the nZEB goal.

2.7 Conclusion

Reviewing the state-of-the-art tools for modelling the solar potential clarified that this is a complex area of research, which, in its earlier times, was mainly done by experts with strong mathematics and physics background. Almost 40 years later, multidisciplinary teams worldwide started to join efforts to couple sophisticated numerical approaches with modern cloud computing and processing power.

A solid trend in urban solar energy potential studies is the use of GIS-based models, and more recently CAD and BIM-based models. The former are known for their associated databases, data interoperability and large-scale spatial analysis functionalities, whereas the latter, which can also manipulate GIS datasets, concentrate advanced 3D modelling and energy systems simulation components in a single software. Nevertheless, the ideal tool would be a mix of the urban-scale processing power of GIS when coupled with CityGML (p.e. SimStadt model) and the parametric design and simulation options of CAD graphical algorithm editors (p.e. Grasshopper, Dynamo).

The major limitations of current models and tools have been discussed. The most relevant enhancements yet to be made concern improved data quality, more detailed diffuse radiation algorithms, upgraded energy conversion modelling, full 3D analysis and city-scale online mapping (i.e. including building façades and vertical elements), comprehensive manipulation, query and visualization, and overall model validation, which is paramount for model reliability. User-friendliness is also desirable, however it may mislead users that are less familiar with the fundamental concepts.

The study of solar potential of façades for electricity generation goes back almost two decades (Vartiainen, 2001), with the, still operational, Mataro public library (Lloret et al., 1995) being one of the earliest examples of vertical installation of PV panels in a building. However, only recently it could be numerically quantified employing more modern techniques: in (Hachem et al., 2011), using SketchUp to model input buildings for EnergyPlus (Crawley et al., 2001),and in (Brito et al., 2017), using LiDAR data and the model SOL (Redweik et al., 2013).

Façade potential enabled tools stand out for allowing detailed analysis of irradiation over those surfaces and their subsequent use for more than just visualization purposes. At the level of radiation calculations on façades, the customized tools presented in Carneiro et al. and SORAM and the GIS gvGIS, regardless of the implemented radiation model, are somewhat limited given their regular sliced façades approach that loses definition by aggregating the solar potential of different portions of the façade in a single value. Townscope and Solene are high surface spatial resolution GUI tools adequate for up to the neighbourhood scale. Their specific native functions for evaluating solar potential are usually non-editable, which might prevent further use of results. Large-scale façade solar potential can be achieved using LiDAR data and GIS models such as v.sun and customized ones such as SOL and SEBE that recreate vertical surfaces from elevation data. These might require parallel computing and simplifications to compute results in a timely manner. The tool SURFSUN3D achieved a significant improvement with GPU acceleration, being able to create detailed façade potential georeferenced

representations on-demand. Promising tools encompass parametric modelling and editing of building geometries coupled with energy simulation features, including DIVA and LadyBug, which allow for simulating the building performance with several design alternatives as a function of façade solar potential. In the latter, the user is free to adapt its source code, create new functions and share with other users, which prompts faster development of the tool. The combination of LadyBug with the BIM and semantic database functionalities of Revit can be considered the top state-of-the-art for façade solar potential modelling in the life cycle of the building. Yet, it is unable to easily scale up from a few buildings to the citywide context. Non-BIM models based on CityGML, such as SimStadt and Bremer et al., are also on the top state-of-the-art, since they feature complex radiation models, effortless computation for high spatial coverage and stablish relationships between the different elements represented.
Some of the revised models can help professionals of diverse fields evaluating the solar energy potential of their projects, even without having deep knowledge on the physics behind it or advanced programming skills. When solar potential models evolve into online maps, estimating the revenue from a building applied solar system becomes assessible to all citizens, decision makers and local authorities, who might not be acquainted with solar radiation formulations neither have solar energy systems background.

In this thesis, three of the revised models will be employed: SOL, DIVA and LadyBug. The first will be validated against measured production data from an urban façade PV system (chapter 3), used in the assessment of the large-scale PV potential in several neighbourhoods in Lisbon and Geneva (chapter 3 and 6), and some of these results will be input to PV string arrangement optimizations (chapter 5). The other two will be used to evaluate different methodologies for constructing a DSM for PV potential estimation (chapter 3), to analyse the potential for glare events from façade PV systems in urban settings (chapter 3), to determine solar irradiation over unconventional façade layouts (chapter 4), to calculate the hourly PV production into the electricity grid in a large urban area (chapter 7) and to investigate the optimal placement of PV in a solar community (chapter 8).

3. PV POTENTIAL IN THE VERTICAL PLANE

Buildings offer large areas available for the deployment of solar energy technologies. Photovoltaics is often considered for installation on the many rooftops available in cities. But façades, which in tall buildings feature larger areas than rooftops, are usually disregarded due to their non-optimal inclination. The assessment of the solar potential of façades requires dedicated tools which require empirical validation. These tools may then be used to estimate the solar potential of urban regions with different morphologies and climates. The impacts of photovoltaic façades on the outdoor environment may also be perceived as an obstacle to its dissemination and therefore ought to be evaluated.
In this Chapter, different solar potential models are used, each one adequate to the scale of the problem that is addressed: first, the 3D model SOL is validated against measurements from a real façade integrated photovoltaic system and then used to evaluate the role of solar façades in different urban contexts. Then, the plugin DIVA is used to compare different methodologies for DSM construction and, together with LadyBug, to assess potential glare from façade integrated photovoltaics in distinct urban blocks. [2]

3.1 Introduction

In 2015, almost 54% of the world's population was urban (The World Bank, 2017). The growth in the number of people living in cities led to an increase in the urban electricity demand, mostly covered by fossil fuel combustion in utility scale power plants. Albeit waste electricity reduction due to increasing energy efficiency of household appliances, industrial machinery, public lighting, etc, it is crucial to explore new clean ways of electricity generation, using local resources and not contributing to climate change. In this sense, the deployment of PV systems in the built environment appears not only as promising but also as a logical solution, since the solar resource is abundant in most densely populated cities.
Conventionally, solar PV modules are installed to maximise the yearly electricity generation. In the urban environment, building rooftops are usually the main candidates to host PV systems. Pitched rooftops can integrate PV modules with tilt and aspect angles that increase their exposure to the sunrays while horizontal rooftops feature substantial free space and easy access. The solar potential of rooftops has been thoroughly explored in the literature (Assouline et al., 2017) and put into practice in many locations in the last two decades: the installation of PV panels and/or thermal collectors on rooftops of buildings has become common practice and part of many modern cityscapes.
However, as urban agglomerates develop vertically, the available area for PV deployment on rooftops becomes scarcer. High population density leads to high electricity density (kWh/footprint m^2). Furthermore, centralized air conditioning units, recreational structures, gardens/urban farms and car parking lots are examples of rooftop uses that might invalidate the PV systems on the tops of the buildings. Thus, vertical surfaces of buildings should not be disregarded, despite their non-optimal

[2] Chapter includes work published on:
- Freitas, S., Brito, M. C., Catita, C., Redweik, P., "Potencial solar nas cidades". VI Congresso Brasileiro de Energia Solar, Apr 2016, Belo Horizonte, Brazil
- Freitas, S., Cristóvão, A., Silva, R., Brito, M.C., "Obstruction surveying methods for PV applications in urban environments". 32nd EUPVSEC, Jun 2016, Munich, Germany. doi:10.4229/EUPVSEC20162016-6AV.5.18
- Freitas, S., Brito, M.C., "Validation of a façade PV potential model based on LiDAR data". 33rd EUPVSEC, Sep 2017, Amsterdam, The Netherlands, doi: 10.4229/EUPVSEC20172017-6DO.11.6

inclination, because façades feature larger available area than rooftops and usually face at least 2 different orientations.

A vertical solar PV system will intersect direct solar irradiation differently from a horizontal or an optimally tilted system, during the day and throughout the year. In the earlier and last hours of the day, the position of the sun in the sky is closer to the horizon, which means that sunlight will reach vertical surfaces more perpendicularly, increasing the collection of solar radiation and corresponding electricity production from a PV façade, as illustrated in Figure 3.1 a). Conversely, a tilted rooftop PV system will generate more electricity around noon, when the sun is located near the zenith, as shown in Figure 3.1 b). The same illustrations are valid when comparing summer and winter time PV generation: due to the varying solar declination, the solar path in the sky is closer to the horizon during winter, with higher solar elevations in the summer. In winter, the contribution from PV systems installed in façades is expected to match, or surpass, the rooftop's.

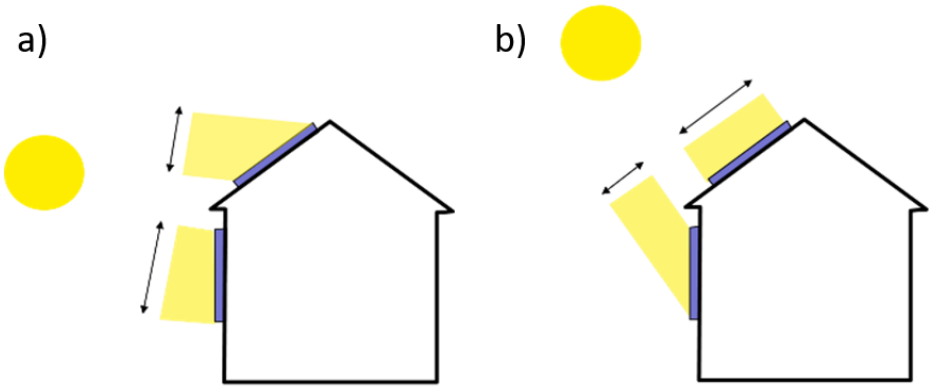

Figure 3.1 – Incidence of direct sunlight in vertical façades and tilted rooftops in: a) morning/afternoon; and b) around noon.

3.2 Assessing PV potential of façades

SOL consists of a customized algorithm scripted in MatLab (sub-section 2.4.3 - ii) for the reconstruction of vertical surfaces in a LiDAR-derived DSM and subsequent irradiation analysis using a local typical meteorological year data set. The core routine in this model regards the shadow/SVF algorithm, which consists on taking each DSM point as a shadow caster along the line opposite to the direction of the sun (represented by one of the pixels in the sky dome division). As long as this line is not interrupted, i.e. whenever a DSM cell along that line features an elevation value lower than the shadow line at that position, the pixel is shaded. Whereas shadow maps are produced hourly, the SVF routine runs only once, since it is not time dependent. It consists on calculating the fraction between the number of sky divisions that are visible from each DSM point perspective over the total number of divisions (originally 1082, but latter updated to 400). The distribution of sky pixels is equiangular, meaning that those are more concentrated near the zenith.

In the following Sub-sections, the model SOL, developed in the Faculty of Science of the University of Lisbon (FCUL), will first be subject of a validation procedure (3.2.1) and then used to study in detail the PV potential of different neighbourhoods in Lisbon, Portugal, and Geneva, Switzerland (3.2.2). Moreover, the plugin DIVA will be introduced in the last sub-section to compare results from a footprint-based with a LiDAR-based DSM (3.2.3).

3.2.1 Validation of SOL model

The validation process of the SOL model has two parts: first, the sky view factor algorithm in SOL is validated through fisheye photographs, and second, the whole model is validated against electricity production records from a real façade PV system.

i) Sky View Factor validation

To estimate the solar PV potential in all points of a building, neighbourhood or a whole city, the elements that might obstruct the sun and the sky must be considered. As seen in Section 2.3, the SVF is the parameter used to describe the degree of obstruction of the sky.

The SOL SVF method is validated against SVF estimation using the standard photographic method for the evaluation of sky obstruction (Holmer et al., 2001) [3]. An Olympus SP-350 photographic camera was used with a Nikon FC-E8 fisheye converter, a fisheye lens commonly used to capture the entire surroundings of a shooting place (Grimmond et al., 2001; Unger, 2009), and known for its 180 degree hemispheric view, depicting the full horizon skyline with great quality. The photographs were taken at 1.20m height using a tripod in different places at the FCUL campus Figure 3.2, including some vertical façade points.

Figure 3.2 - Location of the 13 shooting places in FCUL campus. Points 1, 3 and 4 belong to a façade (Freitas et al., 2016a).

After the collection of the photos, the corresponding SVF values were estimated using the SkyViewFactor Calculator software (Lindberg and Holmer, 2010), a tool that allows the upload of single fisheye photographs to estimate the SVF using two different methods: the annulus method (Johnson and Watson, 1984) and the pixel-based method introduced in (Holmer et al., 2001). The SkyViewFactor Calculator allows small adjustments to images, such as corrections to the skyline delineation in case the software misses part of it or does improper recognition of non-sky pixels. This is an important feature, since some of the photos (Figure 3.3) were taken under clear-sky conditions, instead of overcast and homogeneous sky as recommended in (Chapman et al., 2002).

[3] An alternative method for the experimetnal estimation of SVF using the quality of GPS signal was also explored in Freitas et al., 2016a and in the MSc thesis (Cristóvão, 2016).

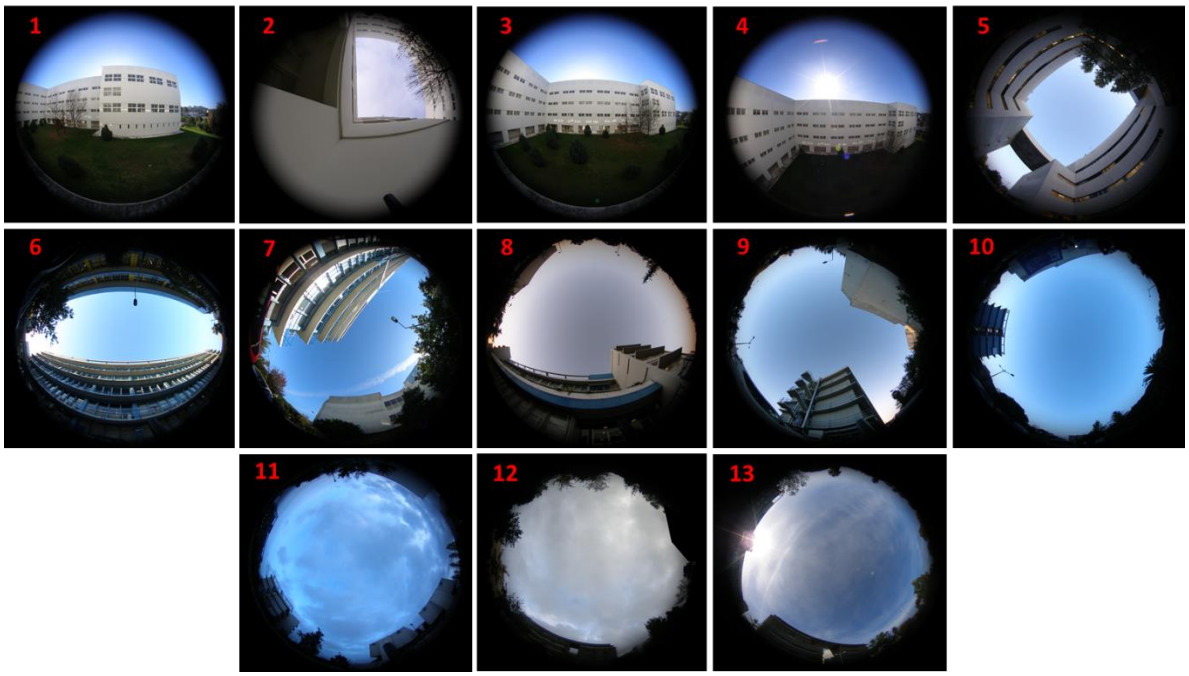

Figure 3.3 - Fisheye photographs taken in the 13 shooting places in FCUL campus (Freitas et al., 2016a).

The SVF values for the area under analysis were computed by the SOL model using a 1m^2 spatial resolution digital surface model derived from LiDAR data produced in 2006. To ensure that the coordinates for the extraction of the SVF values from the maps produced by SOL match the locations of the photographs, the SVF value of the chosen cell coordinates were averaged over the eight neighbouring cells' SVF.

The number of sky vault divisions considered by the SVF algorithm was optimized. The original source code considers 1081 divisions but has been shown to be very time consuming. Hence, sky vaults with 400, 290 and 145 divisions were also tested (Figure 3.4).

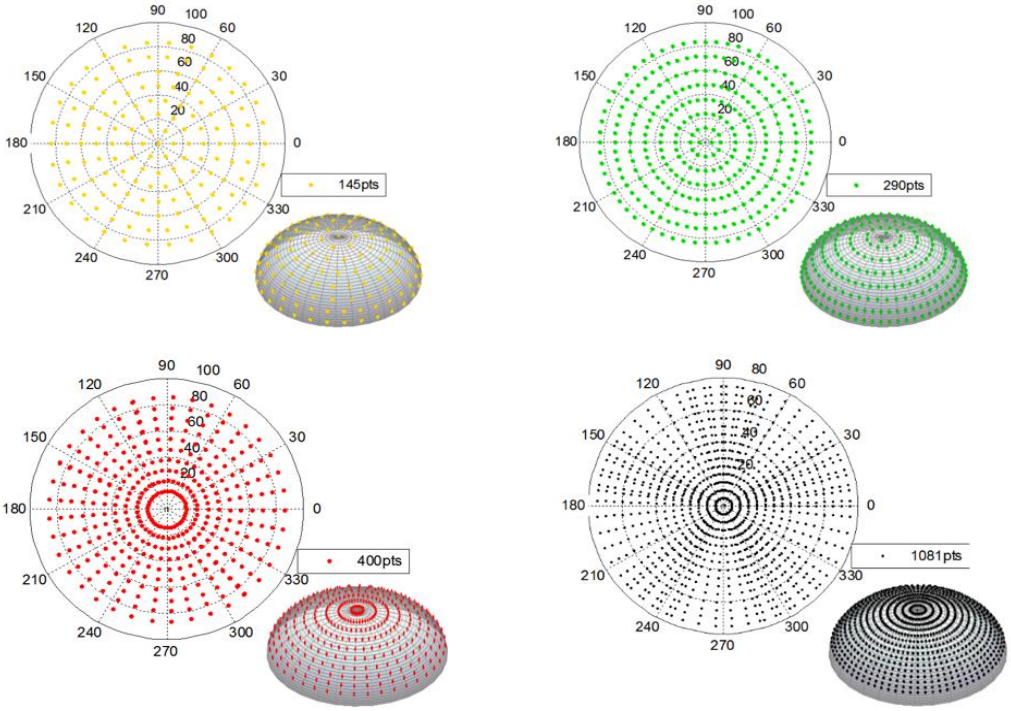

Figure 3.4 - Four sky vaults studied: 145, 290, 400 and 1081 divisions (Freitas et al., 2016a).

Figure 3.5 presents the SVF values obtained using SOL and the fisheye photographs. It can be noted that the SVF values for the lower and intermediate floors of the building façade (places 1 and 3) and in the ground-level corner (place 2) are significantly overestimated by SOL. Open field areas (places 11 – 13) and wide streets (places 8 – 10) achieve good accuracy. However, the method seems to fail when buildings and vegetation start to fill the near horizon (places 2, 6 and 7).

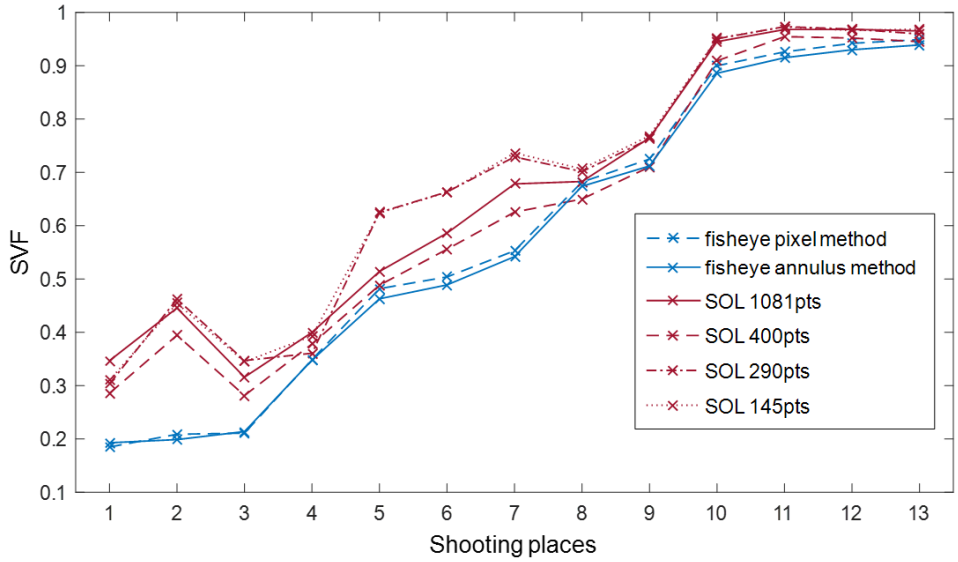

Figure 3.5 - SVF values obtained with 4 different sky vaults in comparison with the fisheye photographs processed with the annulus and the pixel methods (Freitas et al., 2016a).

Places 4 and 5 feature unexpected accurate SVF values. Since place 4 is on a vertical façade, an overestimation in the order of that is verified for places 1 and 3 was expected. Place 4 corresponds to the top floor of the building, which might indicate that the DSM is either producing a wrong building height or there are elements being incorrectly represented. On the other hand, the SVF calculated for place 5 should be underestimated by SOL due to the hole that exists in the façade (Figure 3.3) which is closed in the DSM representation (because vertical façade points are derived from the terrain and building heights), thus a smaller amount of sky should be visible. The presence of tall trees obstructing part of the sky (probably were not as tall as when the LiDAR assessment was carried out in 2006) might balance out the effect.

Another interesting observation relates to the similar accuracy that is observed for the four sky vaults in most cases, except for places 2, 5 and 6. Sky models with 145 and 290 divisions do not show noteworthy differences between them, which is not surprising given that one has only twice the number of divisions of the other. The main difference from the 145 and 290 pair to the 400 and 1081 pair is that the number of divisions per zenith band is kept the same in the latter, which means that for places such as 6 and 7 the SVF will always be overestimated relatively to the fisheye photographic reference when 145 and 290 sky models are used. This might be due to the SkyViewFactor Calculator algorithm, which also employs a distribution of pixels/divisions with constant number of divisions per zenith band.

Overall, a sky with 400 divisions emerges as an optimal option, with accurate results with acceptable computation time. Results validate the SOL sky view factor algorithm but highlight the limitations of LiDAR-derived DSM representation.

ii) PV potential validation

The full validation of the 400 sky divisions version of the SOL model was done using measured data from a PV system integrated in the south-facing façade of the Solar XXI building (Figure 3.6), located

in Lisbon, Portugal (38.7723037 N, 9.177954 W). The PV system has a peak power of 12.16kW provided by 76 p-Si modules connected to 3 inverters. The modules are installed vertically as a double skin façade, i.e. with an air gap between modules and the wall, to provide cooling or heating to the indoor spaces (Rodrigues, 2008).

Figure 3.6 - Façade integrated PV system in the Solar XXI building, in LNEG, Lisbon (Freitas and Brito, 2017a).

The experimental datasets for the months of June and November of 2012 comprise electricity production (Wh), power (W), direct (DC) and alternating (AC) voltage and current grouped by inverter (as shown in the schematic layout presented in Figure 3.7), irradiance on the vertical plane of the façade (W/m^2) (Figure 3.8) and module and ambient temperature (°C) (Figure 3.9), all with a time step of 15min. Hourly global and diffuse horizontal irradiation (Wh/m^2) measured on a nearby weather station (Figure 3.8) were also used as input to the model SOL to estimate the solar irradiation on a 1x1m^2 resolution Digital Surface Model (DSM) of the area. For the sake of readability, and since the data for 2013 is qualitatively similar to 2012, this discussion only addresses the data for 2012.

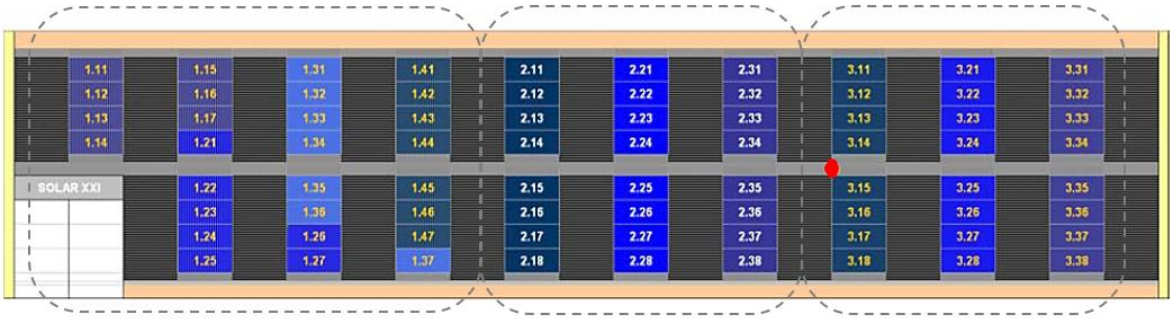

Figure 3.7 - Distribution of modules in the façade and interconnections of the strings to the respective inverter (Rodrigues, 2008), and the location of the radiation sensor (red dot).

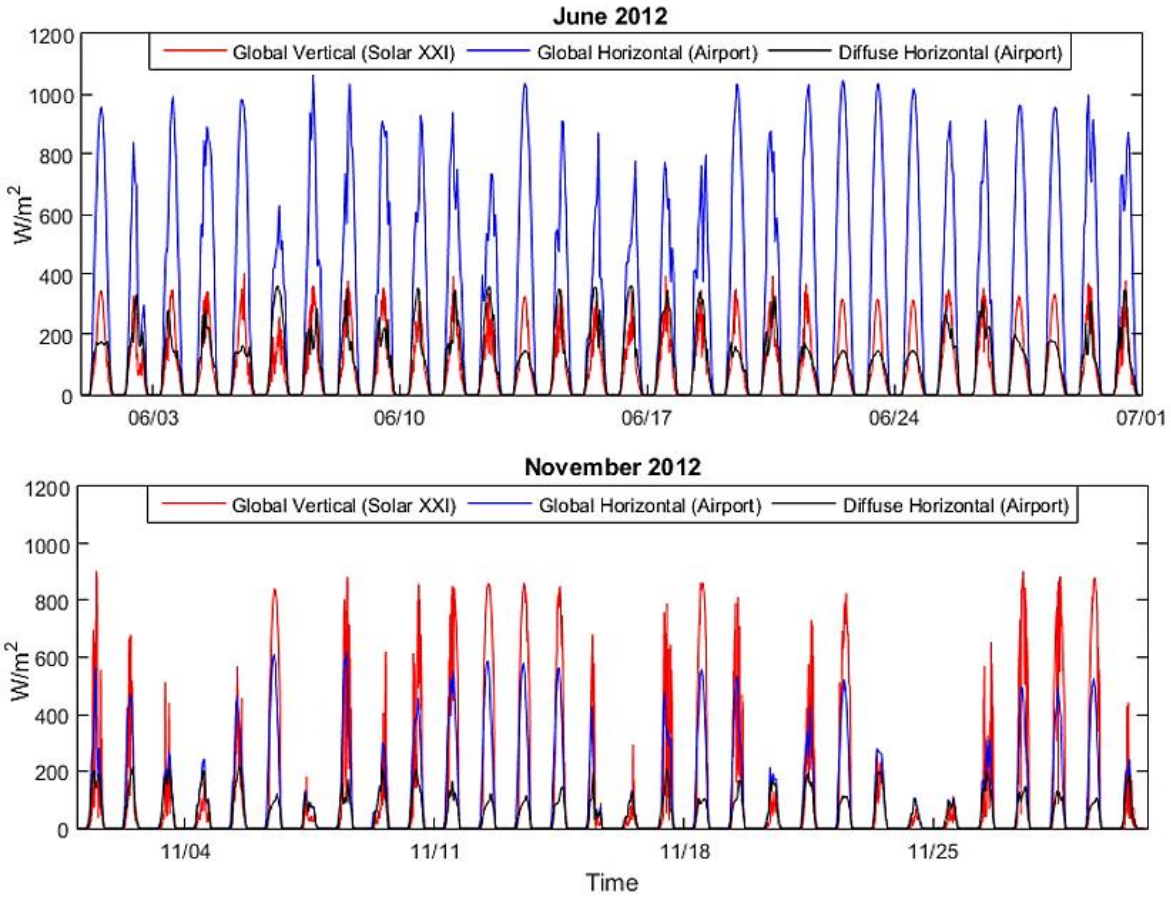

Figure 3.8 – Global vertical (red), global horizontal (blue) and diffuse horizontal (black) irradiances for the months of June (top) and November (bottom) of 2012.

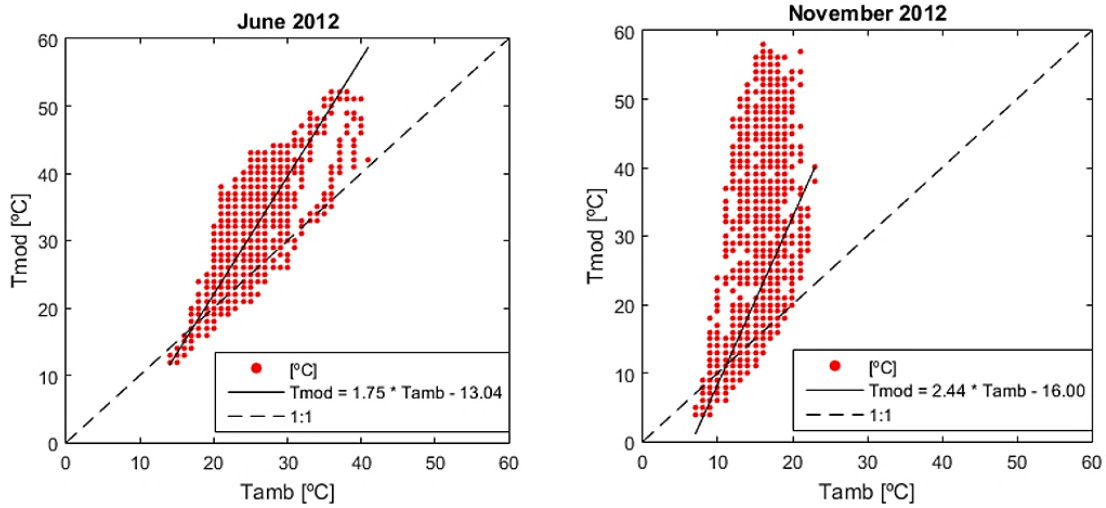

Figure 3.9 – Scatter plots of the recorded module temperature against ambient temperature, and respective linear regression, for the months of June (left) and November (right) of 2012.

Due to lower sun paths, the global vertical irradiance surpasses the global horizontal irradiance in the winter month, reaching 900W/m^2 around solar noon (Figure 3.8, top). Most days in the summer month correspond to clear sky days, with few partially cloudy hours. In the winter the variability is higher (Figure 3.8, bottom). In 2012, the amplitude of ambient temperatures ranged between 13°C and 41°C in June, and between 7°C and 23°C in November. This parameter has direct influence on the

temperature of the modules, but the effect of irradiance is more pronounced, as observed in Figure 3.9.

Hourly solar irradiance results were produced for all sample surfaces using SOL. Façade points corresponding to the Solar XXI façade were manually extracted (Figure 3.10). Those points in the approximate position of modules were assigned the respective string/inverter number. Comparison between the sensor measured irradiation and SOL calculated irradiation for the sensor location shows a slight underestimation in summer and considerable dispersion in winter (Figure 3.11).

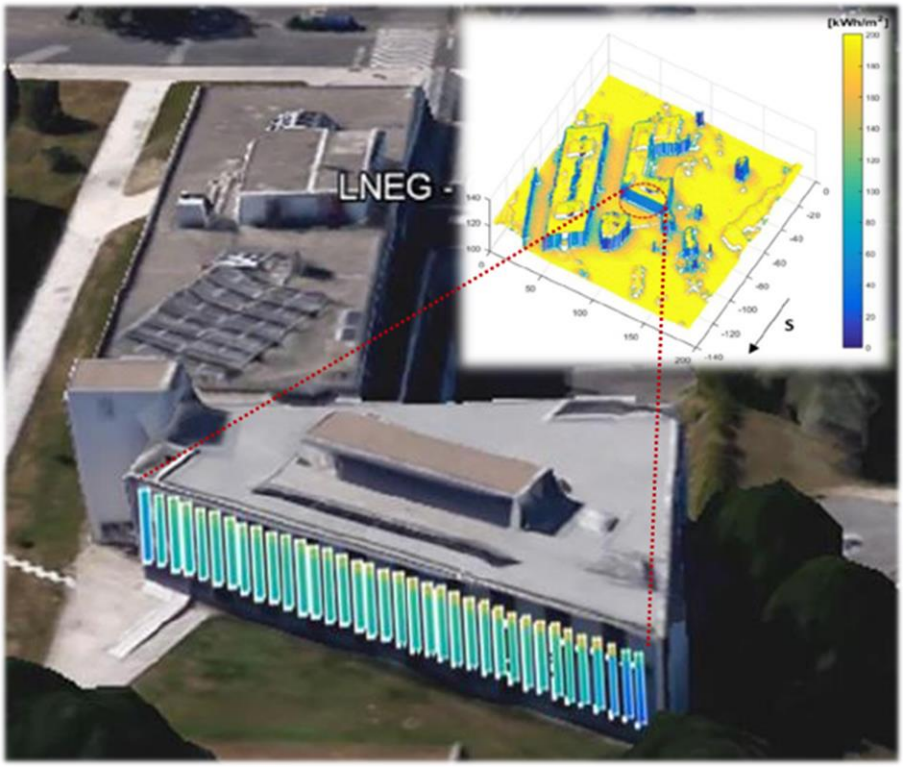

Figure 3.10 - Cumulative solar irradiation estimated for the month of June 2012 (inset) and the façade points superimposed over a Google Earth view of the building (Freitas and Brito, 2017a).

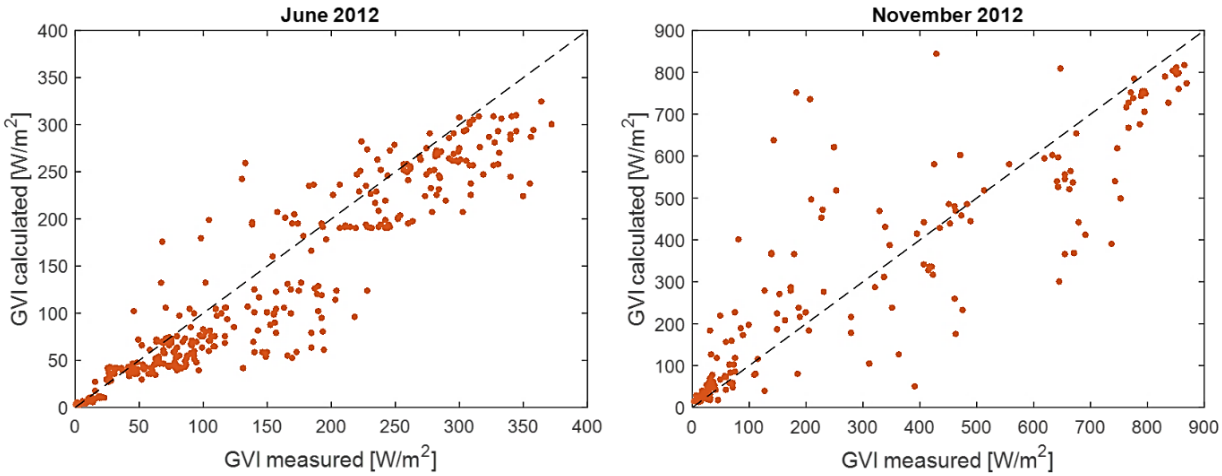

Figure 3.11 – Global vertical irradiation measured by the sensor against results produced by SOL in an approximate position, for June (left) and November (right).

Using the SOL output solar radiation for each module, the hourly PV production of each module (PV_m) was estimated through the following expression (Marion, 2002):

$$PV_m = P_{ref}\frac{Dir_{vert,m}AL + Dif_{vert,m}}{G_{ref}}\left[1+\gamma\left(T_m - T_{ref}\right)\right], \quad (3.1)$$

where P_{ref}=160W/m² is its nominal power, $Dir_{vert,m}$ and $Dif_{vert,m}$ are respectively the direct and diffuse vertical irradiance estimated for the module m's position, and AL is a fraction to account for the angular losses (c.f. below) due to the effect of the angle of incidence in the direct component of solar radiation, G_{ref}=1000W/m², T_m is the estimated module temperature, T_{ref}=25°C and γ is the power correction factor due to the PV module temperature. One can set γ=0 if the effect of temperature is to be neglected and γ=-0.5%/°C (BP_Solar, 2006) when it is considered.
The hourly temperature of the PV modules was calculated according to:

$$T_m = T_a + \frac{NOCT - 20^oC}{800\ \mathrm{W/m^2}}G_{vert,m}, \quad (3.2)$$

where T_a is the ambient temperature and $NOCT$ is the nominal operating cell temperature, which was reported to be higher (56°C (Rodrigues, 2008)) than the manufacturer data (47°C (BP_Solar, 2006)) due to the integration in the façade.
Following (Martin and Ruiz, 2001), the factor for the angular losses, AL, is estimated by:

$$AL = \frac{1 - e^{-\frac{\cos\theta}{a_r}}}{1 - e^{-\frac{1}{a_r}}} \quad (3.3)$$

where θ is the hourly angle of incidence of the sun rays in the plane of the façade (output by the model *SOL*) and a_r=0.159 is an empirical angular losses coefficient for p-Si modules (Martin and Ruiz, 2001). When the angle of incidence effect is neglected, AL can be set to 1. This factor becomes relevant for angles of incidence above 70°. The angle of incidence effect for the diffuse irradiation was disregarded since it is more significant when PV module tilt angles are small (Marion, 2017).
Following the string arrangement in Figure 3.7, the hourly PV production by inverter (PV_i) was computed considering that the total production of each string (S) is determined by the lowest producing module, Eq. (3.4). This method portrays the partial-shading effect in the strings in a conservative way.

$$PV_i = \eta_i \sum_1^{Ni} min\left(PV_{m,Si}\right)n_{Si} \quad (3.4)$$

where η_i=94% (Rodrigues, 2008) is the inverter DC/AC efficiency, Ni is the total number of strings connected to inverter i, $PV_{m,Si}$ is the production of module m belonging to string S connected to inverter i and n_{Si} is the total number of modules in that string.
To assess the impact of temperature and angular losses in the model results, the PV production was estimated from the model SOL radiation output and Equations (3.1) - (3.4) using three different settings: i) without considering temperature and incidence angle losses; ii) considering the effect of temperature but no angular losses; and iii) with both. Results from these three settings were compared against the measurements and performance errors calculated: the mean bias error (MBE, Eq. (3.5)), which measures the systematic deviations; the mean absolute error (MAE, Eq. (3.6)), which quantifies negative and positive deviations equally; and the root mean square error (RMSE, Eq. (3.7)) that weights the larger deviations. Errors were normalized by measured PV power.

$$nMBE = \frac{\frac{1}{H}\sum_{h=1}^{H}\left(PV_{i(h)} - PV_{i,meas(h)}\right)}{\frac{1}{H}\sum_{h=1}^{H}PV_{i,meas(h)}}, \quad (3.5)$$

$$nMAE = \frac{\frac{1}{H}\sum_{h=1}^{H}\left|PV_{i(h)} - PV_{i,meas(h)}\right|}{\frac{1}{H}\sum_{h=1}^{H} PV_{i,meas(h)}}, \quad (3.6)$$

$$nRMSE = \frac{\sqrt{\frac{1}{H}\sum_{h=1}^{H}\left(PV_{i(h)} - PV_{i,meas(h)}\right)^2}}{\frac{1}{H}\sum_{h=1}^{H} PV_{i,meas(h)}}, \quad (3.7)$$

where H is the total number of hours and $PV_{i(h)}$ and $PV_{i,meas(h)}$ are respectively inverter i's estimated and measured output in hour h.

Figure 3.12 compares the estimated PV production against the experimental records. It is clear that electricity generation reached higher levels in the winter month, as lower sun elevation leads to closer to normal incidence on the façade. The level of scattering is lower in summer, due to fewer cloud cover events. The model overestimates PV generation in both months.

When the effect of temperature is considered (Figure 3.12, middle), there is better agreement with experimental data, particularly for high production conditions – thus higher irradiance and therefore higher module temperatures. Similar improvement is observed when angular losses are considered (Figure 3.12, bottom). For November, this effect is less relevant, due to the closer to normal incidence.

Electricity production from the strings connected to Inverter 3 is lower than the other strings. The shadow casted by the trees located near the easternmost part of the façade (which can be seen in Figure 3.6) might be the cause for such differences. Notice that the LiDAR data (and therefore the DSM used for the assessment of obstructions to light) is from 2006, when the trees were much younger, and shorter.

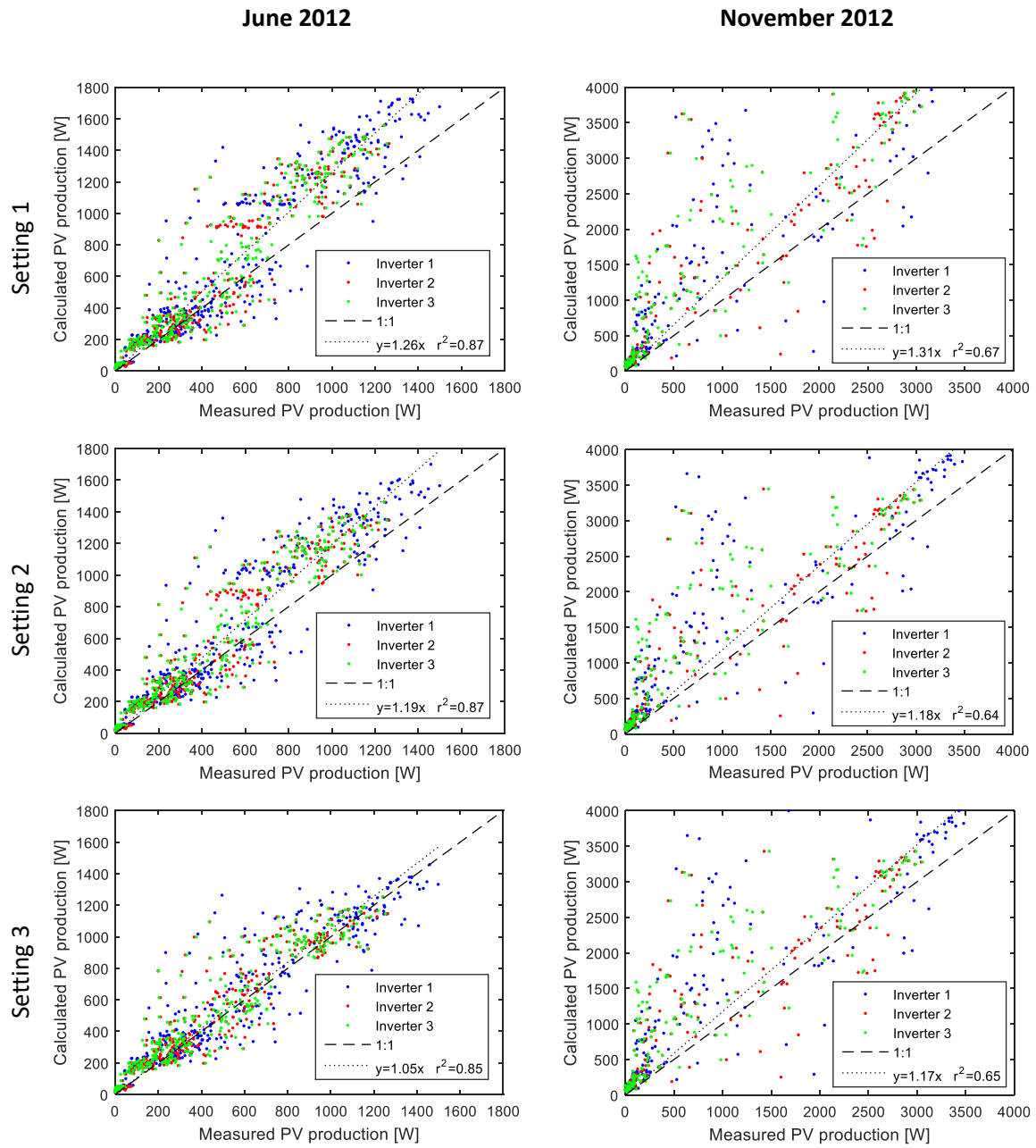

Figure 3.12 - Comparison between the calculated and measured PV production by inverter, for June (left) and November (right) of 2012: Setting 1 (top); Setting 2 (middle); and Setting 3 (bottom). (Freitas and Brito, 2017a)

The impact of considering the temperature and the angular losses on the model performance is shown in Figure 3.13, which represents boxplots of the hourly relative deviation for the different simulation settings. In the summer the model overestimates the production in the morning, around noon and early evening, especially for Inverter 3, whose strings are partially shadowed more often than the others. Furthermore, the earlier and later hours of the day, with low levels of solar radiation, are still challenging moments for the modelling of PV production. Considering temperature losses leads to slight improvements whilst the impact of angular losses almost zeroth most of the boxes and median lines. It should be noticed that the range of the vertical axis units is 4 times larger in November and therefore these effects are much less pronounced in the winter months.

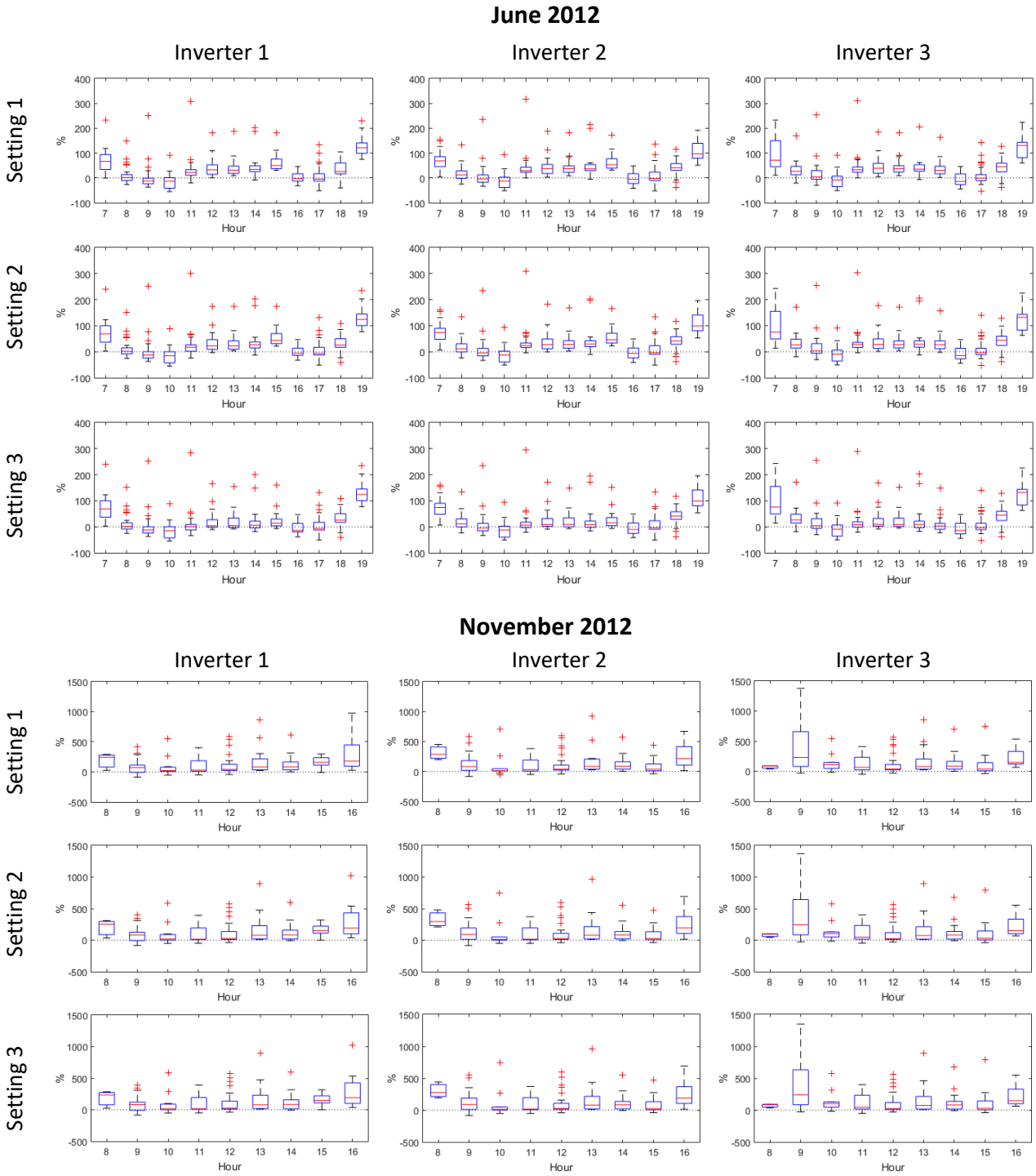

Figure 3.13 – Boxplot representation of the hourly relative deviation in June (top) and November (bottom) of 2012, for the 3 Inverters (columns) and through the 3 Methods (rows). (The tops and bottoms of each "box" are the 25th and 75th percentiles, the red line in the middle of each box is the median, the black lines extending above and below each box are the extreme values and the red crosses are the outliers.) (Freitas and Brito, 2017a)

Detailed analysis of model errors shows that highest deviations correspond to diffuse fractions between 30% and 80% (semi-cloudy skies) and lowest deviations correspond to overcast hours. This is due to the fact that background diffuse radiation is being modelled as isotropic: overcast conditions

are typically isotropic, whilst semi-cloudy and clear skies feature anisotropy, which the model did not properly describe. The high distribution of sky divisions in the zenith seems to portray the circumsolar contribution in clear sky conditions well in June, as the sun is almost overhead at noon, with smaller deviations being observed for diffuse fractions around 20% (Freitas and Brito, 2017a).
The nMBE, nMAE and nRMSE are shown in Table 3.1. Considering temperature losses leads to an average reduction in the nMBE, for the 3 Inverters, of around less 5% in June and 11% in November. A similar improvement is observed for systematic errors, since nMAE decreases 5% and 10% and nRMSE decreases 6% and 15%, respectively. Consideration of angular losses leads to almost no changes in November (the errors differ only in 1%) but significant improvement in June, with further decrease in all errors: 10%, 12% and 11% absolute improvement.

Table 3.1 – Normalized Mean Bias Error (nMBE), normalized Mean Absolute Error (nMAE) and normalized Root Mean Squared Error (nRMSE) by Inverter, for June and November of 2012, for Settings 1, 2 and 3. (Freitas and Brito, 2017a)

		nMBE [%]			nMAE [%]			nRMSE [%]		
		Inv 1	Inv2	Inv3	Inv 1	Inv2	Inv3	Inv 1	Inv2	Inv3
1	jun/12	25%	30%	29%	33%	36%	34%	45%	49%	48%
	nov/12	55%	42%	65%	64%	52%	70%	92%	74%	97%
2	jun/12	20%	24%	24%	28%	31%	30%	39%	42%	41%
	nov/12	43%	32%	52%	53%	43%	58%	77%	61%	82%
3	jun/12	7%	12%	12%	20%	20%	21%	29%	30%	30%
	nov/12	42%	31%	51%	52%	42%	58%	76%	61%	81%

Combined electricity production measured for the three inverters reached about 515 kWh in June and 1055 kWh in November, whereas the estimated production was respectively 568 kWh and 1489 kWh - 10% to 30% overestimation.
Full model (i.e. setting 3 including both temperature and angular losses) performance features the highest errors for Inverter 3, particularly in the winter. Inverter 1 features the lowest errors in June and Inverter 2 the lowest errors in November. Overestimation of inverter 3 yields is attributed to poorly modelled partial shading in the morning, due to the model low spatial resolution ($1m^2$, much coarser than the solar cell size) and overgrown trees. Errors for inverters 1 and 2 may also be attributed to shading events, associated to a building to the west and by another group of trees located southwest of the façade, casting shadows all over the façade in the late afternoon (Rodrigues, 2008).
Overall, PV production estimations produced using the SOL model fairly agree with the experimental data, featuring nMBE ranging from around 7% to 51%, nMAE from 20% to 58% and nRMSE from 29% to 81% - higher values observed for the winter month. Part of these errors are attributed to limitations of the solar radiation to PV generation conversion model, which is not included in the SOL model and was developed for this particular set of tests.
The DSM $1x1m^2$ resolution, which is much larger than the dimensions of a solar cell, hinders the model ability to fine scale rendering of shadows, underestimating partially shadowing electric losses. The impact of anisotropic diffuse radiation is clearly observed in the model assessment, with poorer results for partially cloudy sky conditions.
As the model underestimated the irradiation in the approximate position of the sensor, it would be expected that the estimated PV production would have behaved similarly. However, the smaller size of the sensor compared to the DSM resolution, and the poorly modelled partial shading in the façade, prevented better accuracy. This suggests that the horizontal irradiation (input to SOL) ought to be measured on-site, without casted shadows.

Another challenge relates to low light conditions, which may also justify the overestimation in the low power regimes. A more detailed PV cell model, including the bypass diodes, would be needed to accurately simulate the behaviour of the PV strings under such partial shading conditions (Stamenic et al., 2004). However, this was disregarded during the validation procedure given the resolution of the DSM, that is 10 times lower than the solar cell dimensions. Otherwise, the propagation of errors would have increased, as well as the computation complexity.

3.2.2 Application of SOL

The solar potential of four dissimilar urban areas (Figure 3.14), three in Lisbon, Portugal, and one in Geneva, Switzerland, was computed using SOL for typical meteorological data series of each city. Area A, built around 1950-60, is located in the centre of Lisbon and features both low and irregular buildings and 10 story residential blocks. Area B, also in Lisbon, is a parish originally developed in the early 20th century, with narrower roads and tall trees. Typical buildings are 3 to 5 stories high with inner quadrangles. Area C, corresponding to the campus of the Faculty of Science (FCUL), does not represent a typical urban arrangement, given its spread out academic buildings. Area D, in Geneva, is mostly composed of residential 6 story buildings geometrically distributed. All DSMs considered have a spatial resolution of 1m^2, but their coverage differed slightly: 500x500 m^2 for areas A and B, 400x380 m^2 for area C and e 300x300 m^2 for area D.

Figure 3.14 – Bird's eye view and street view of the 4 studied areas: A (38.748630, -9.136996), B (38.738929, -9.144399) and C (38.756064, -9.156481) in Lisbon, Portugal; and D (46.229499, 6.079182) in Geneva, Switzerland, retrieved from Google Maps.

Figure 3.15 shows the cumulative yearly solar irradiation in the 4 studied areas. In general, the potential is higher in rooftops and ground than in the vertical surfaces. Vertical façades achieve about 50% and 60% of the rooftops irradiation levels, in Lisbon and Geneva, respectively. These results highlight the increasing interest of façades for higher latitudes. Also, considering the available area, one can conclude that the effective use of façades for solar applications may double or treble the total solar potential of an urban neighbourhood.

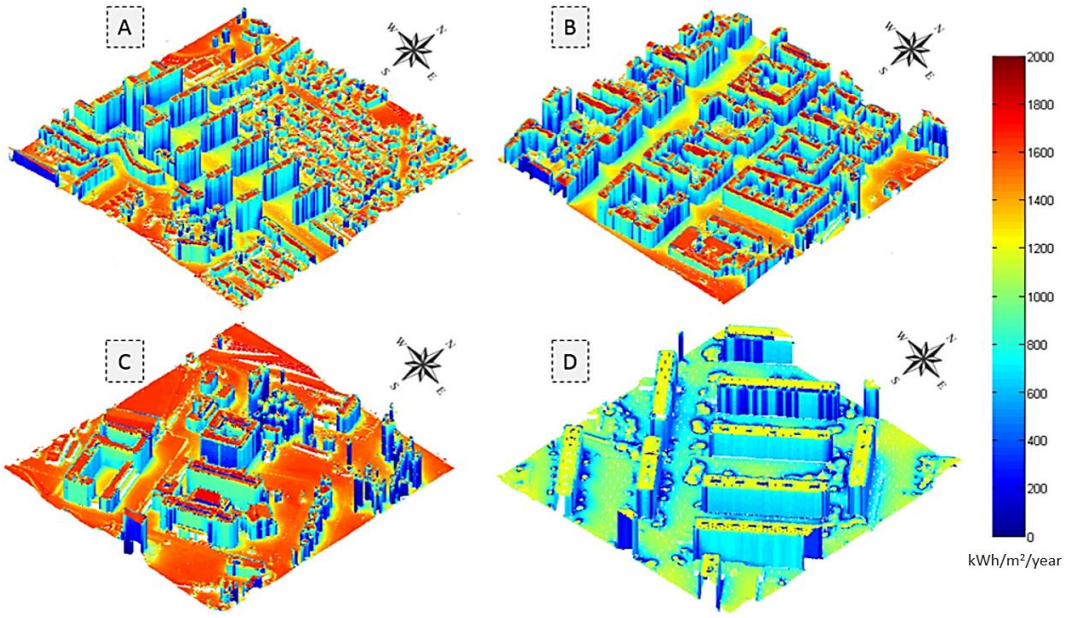

Figure 3.15- Yearly solar irradiation in the areas A, B, C and D. The false colour scale highlights the places with lower (blue) and higher (red) solar potential. The vertical dimensions are different in the 4 maps: tallest buildings reach around 60m in area A, 50m in area B, 40m in area C and 30m in area D (Freitas et al., 2016b).

Further analysis requires the selection of building surfaces. Using ArcGIS (ESRI), points belonging to buildings were extracted from the geographic database based on the spatial relationship between those points in the DSM and the layer containing the vector footprints. Only residential buildings were selected, since the footprints layer was incomplete.

Figure 3.16 presents irradiation histograms for different classes of surfaces in buildings: rooftops and façades with different orientations. The more frequent levels of solar irradiation on the rooftops in Lisbon are significantly higher than in Geneva (1700kWh/m^2/year versus 1200kWh/m^2/year), as expected given its lower latitude and milder climate. For the façades, it is curious to note that there is a peak of irradiation on the 300 and 650kWh/m^2/year in areas A, B and C, but an 800kWh/m^2/year peak is also notable in area C, due to larger spacing between buildings and consequent fewer shading events (Figure 3.15, C).

North-facing façades feature very low potential, with an irradiation level mode of 300kWh/m^2/year, which might indicate similar levels of isotropic diffuse irradiation in Lisbon and Geneva. In Lisbon, a few façade points facing north reach 650kWh/m^2/year. This relatively high irradiation level is observed in summer when the azimuth at sunrise/sunset is closer to the northeast /northwest at Lisbon's latitude (38.7N), and not at Geneva's latitude (46.2N).

The solar potential in façades is related to the spatial arrangement of buildings (T. A. de L. Martins et al., 2016). In area A, high-rise buildings have their larger façades oriented to the east and west (Figure 3.15, A) but most of the predominant smaller buildings feature south-facing façades. Their overall contribution is equivalent (Figure 3.16, A – orange line versus yellow and green lines). The same result is observed for area D, but in this case the more common façade orientations are southeast and

northwest (Figure 3.15, D). South facing façades in area B seem to be prone to shading events due to the intricated building arrangements, and its relative relevance to the solar potential is significantly reduced. Its indented topography leads to a higher façade area, thus higher total façade irradiation, but higher mutual shading, and therefore lower average irradiation density.

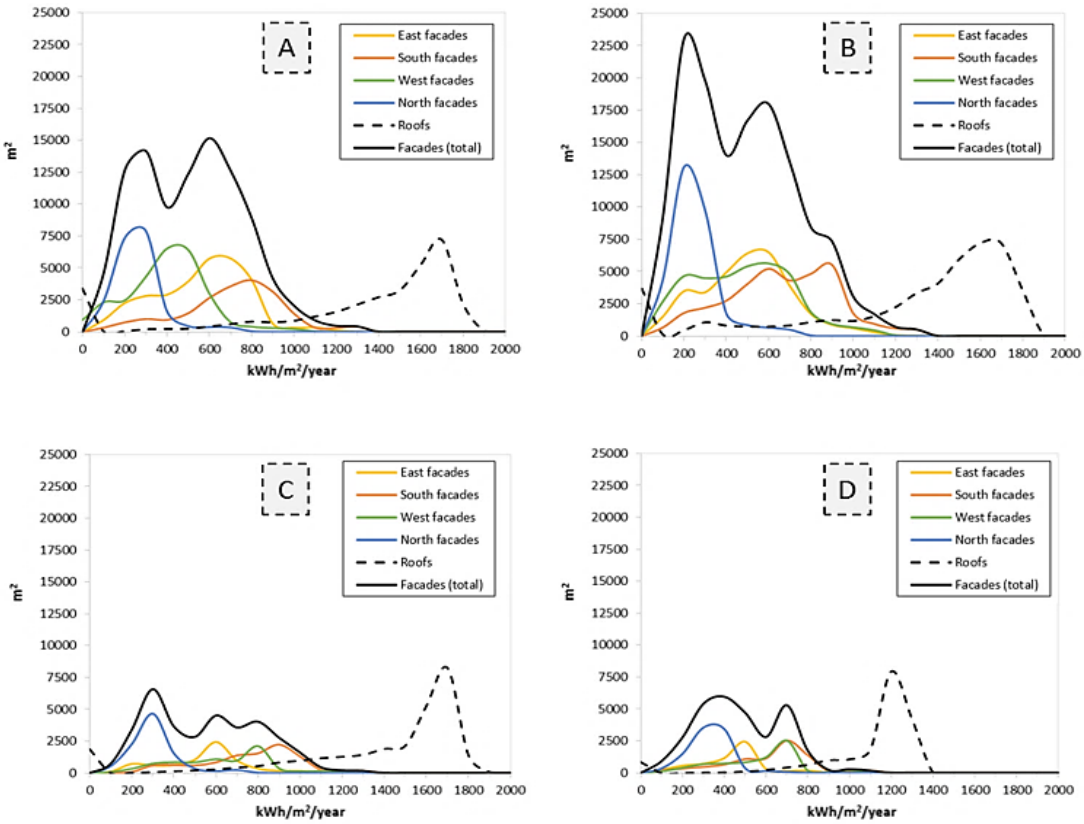

Figure 3.16- Annual solar potential histogram. Dashed lines refer to roofs and solid lines to façades with different colours according to South, East, West and North orientation (i.e. points with azimuth inside the intervals [45°, 135°[, [135°, 225°[, [225°, 315°[e [315°, 45°[where 0° denotes North) (Freitas et al., 2016b).

The annual PV potential in the 4 areas is presented in Table 3.2. The fraction of ground covered by buildings is similar across all case studies, although only residential buildings are considered in areas A and B. Area C features, in average, the lowest buildings, while D is characterized by a greater homogeneity of heights as its average building height is the closest to the maximum height. Area A is the one that encompasses more diversity.

Table 3.2 – Contribution from rooftops and façades to the solar potential of the studied areas. Shaded values correspond to points with irradiation > 900kWh/m^2/year.

	DSM area [m^2]	Building area [%]	Average building height [m]	Maximum Building height [m]	Total PV [%]		Total PV [kWh/year/m$^2_{\text{building footprint}}$]	
					Rooftop	Façade	Rooftop	Façade
Area A (Lisbon)	500x500	13	18	67	47	53	149	166
					91	9	141	14
Area B (Lisbon)	500x500	19	20	51	49	51	145	150
					90	10	135	16
Area C (Lisboa)	400x380	18	14	44	68	32	157	75
					94	6	150	10
Area D (Geneva)	300x300	20	18	34	60	40	125	84
					97	3	113	3

The contribution of façades to the overall PV potential in areas A and B is as relevant as that of rooftops: the larger available area compensates the lower irradiation levels. Due to the less favourable geometry and lower built area, the PV potential of façades in areas C and D are only about a 1/3 of the total solar potential.
If a profitable PV system could be deployed in places with irradiation levels above 900kWh/m^2/year (shaded values in Table 3.2), the contribution from rooftops would be overwhelming as only 3% to 10% of the PV production per m^2 of footprint would originate from façades.

Some conceptual simplifications and limitations are worth discussing. First, for simplicity, partial shading is disregarded as this correction is not expected to be very relevant, since the spatial resolution (1 point per square meter) is of the order of magnitude of the considered PV module area. If higher resolution DSM were used the effect of partial shading on the solar yields could be more accurately evaluated. Nevertheless, this impact can be minimized through techniques reviewed in (Bidram et al., 2012) or through re-arrangement of the module interconnections (further explored in Chapter 5).
The inclination and orientation of the solar PV panels were considered to be those of the building surfaces: simulated PV modules on façades were vertical with the orientation of the façade, while PV modules on the roof followed the rooftop pitch. This option might underestimate the solar potential, in the sense that PV modules could be integrated on shadings structures or simply be mounted on other building features with an optimum tilt. Although it depends on the local architecture, (Verso et al., 2015) suggests that the option for optimum tilt on flat roofs could represent a 12% increase in the solar potential of an urban area.
As for the façades, the validation results for the SOL model (sub-section 3.2.1), reported an overestimation in the order of 51% for partially shaded group of vertically installed PV string, thus other mechanisms might balance out the factors prompting underestimation in the highly exposed cases. These will be addressed with further detail in Chapters 4 (alternative façade architectures for irradiation maximization) and 5 (optimization of interconnections of partially shaded PV strings).
It ought to be emphasized that the study of neighbourhood PV potential required an approach that is more suitable for the large-scale analysis of an urban region, which, thus, involves simplifications regarding local weather conditions (such as wind speed, reflected radiation, detailed partial shading, etc.) that may differ significantly among specific applications. These variables may strongly impact the solar electricity yields of particular building façades or rooftops, especially those hosting back ventilated PV systems.
One last remark concerns the urban layout and streets arrangements, which directly relates to the solar potential of a city. Urban compactness aspects such as the spacing between buildings, streets width and orientation should thoroughly be planned to maximize solar exposure in building façades. The study conducted in (Mohajeri et al., 2016), which exhaustively addresses several neighbourhoods in Geneva, provides very clear indications on the impacts of urban compactness in the solar potential of façades. It notes that there is a tendency for an increase in annual solar irradiation from the city core to the suburbs (Area D belongs to the latter). Moreover, the PV potential for façades is low in all neighbourhoods with high plot ratio, volume-area ratio, building density and site-coverage, having the latter the highest effect: façade PV potential decreases from 20% in low compact areas to 3% in high site-coverage areas. These parameters can be optimized as done in (A.L. Martins et al., 2014)(Vermeulen et al., 2015) in a trade-off between electricity production and visual and thermal impacts.

3.2.3 Application of DIVA

The digital model of the buildings and surroundings used in SOL is based on LiDAR data, however, as reviewed in section 2.1, vector data of building footprints, when existing, allow for straightforward creation of city models. Rooftops and façade details can then be sketched to produce a full 3D and more realistic model. Since SOL was not originally scripted to work with this type of data, the CAD/plugin tool DIVA (version 4 for Grasshopper) was employed to assess the accuracy of irradiation simulations using the distinct methodologies. Georeferenced vector-based building footprints and 1m^2 resampled elevation data from an airborne LiDAR assessment were used, from which two distinct building blocks were extracted. Block 1 and 2 are located in Lisbon (and will be further described and their solar potential analysed later in this thesis).

The workflow within DIVA consists on assigning the geometries of interest, usually represented in Rhinoceros 3D viewport, to a specific geometry component in Grasshopper. For instance, in Figure 3.17 a preview of a "Mesh" component containing several groups of rooftop LiDAR meshes is shown (orange). Through a drag/drop process, the remaining components can be added from DIVA toolbar to the Grasshopper canvas and connected to one another as per the analysis goal. In this case, the rooftops are connected to a "Scene Object" component to acquire material attributes, which then connects to a "Grid" component that creates the sensor points for irradiation simulation. This last step is carried on by the "Radiation Map" component. Project location, quality of the raytracing simulation and daily hour range are some of the mandatory input settings, but it is also possible to define how many of the processes will run in parallel.

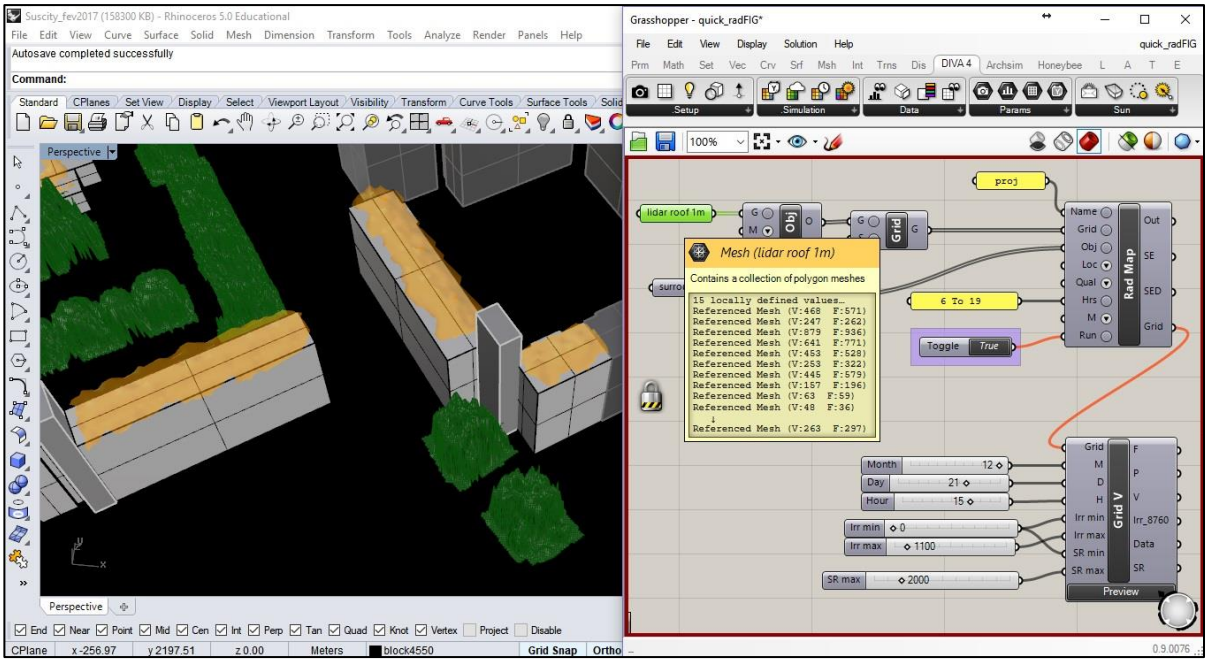

Figure 3.17 – Rooftop meshes over the building geometries in Rhinoceros 3D viewport (left) and a detail on DIVA-for-Grasshopper Radiation Map components (right).

i) Footprint method

The building footprints in vector based format (Figure 3.18, top) and their corresponding height information, stored in shapefile type, were input to Rhinoceros 3D/Grasshopper environment using the plug-in Merkat GIS (Lowe, 2015). Then, through list manipulation and selection operators the footprints of all the buildings were extruded to their respective heights forming flat 3D volumes, i.e. flat vertical façades and horizontal rooftops. The buildings of interest and the shadow casting

elements, such as surrounding buildings and trees, were separated and input into different functions of the irradiation analysis component in DIVA.

ii) LiDAR method

The DSM derived from the airborne LiDAR data (Figure 3.18, middle), stored in ascii table form, was imported into Rhinoceros 3D as a point cloud and underwent a Delaunay triangulation process. The resulting mesh contained the rooftop surfaces alone, due to the way airborne LiDAR acquires data, and it was carefully inspected to separate the surfaces of interest from obstructions, such as other buildings and trees.

iii) Sketch method

This method builds upon the *footprint method* (i), but aims to further detail the rooftop representation (Figure 3.18, bottom) by manually sketching its features according to Google Earth views of the buildings. Trees were included as shadow casting spherical volumes.

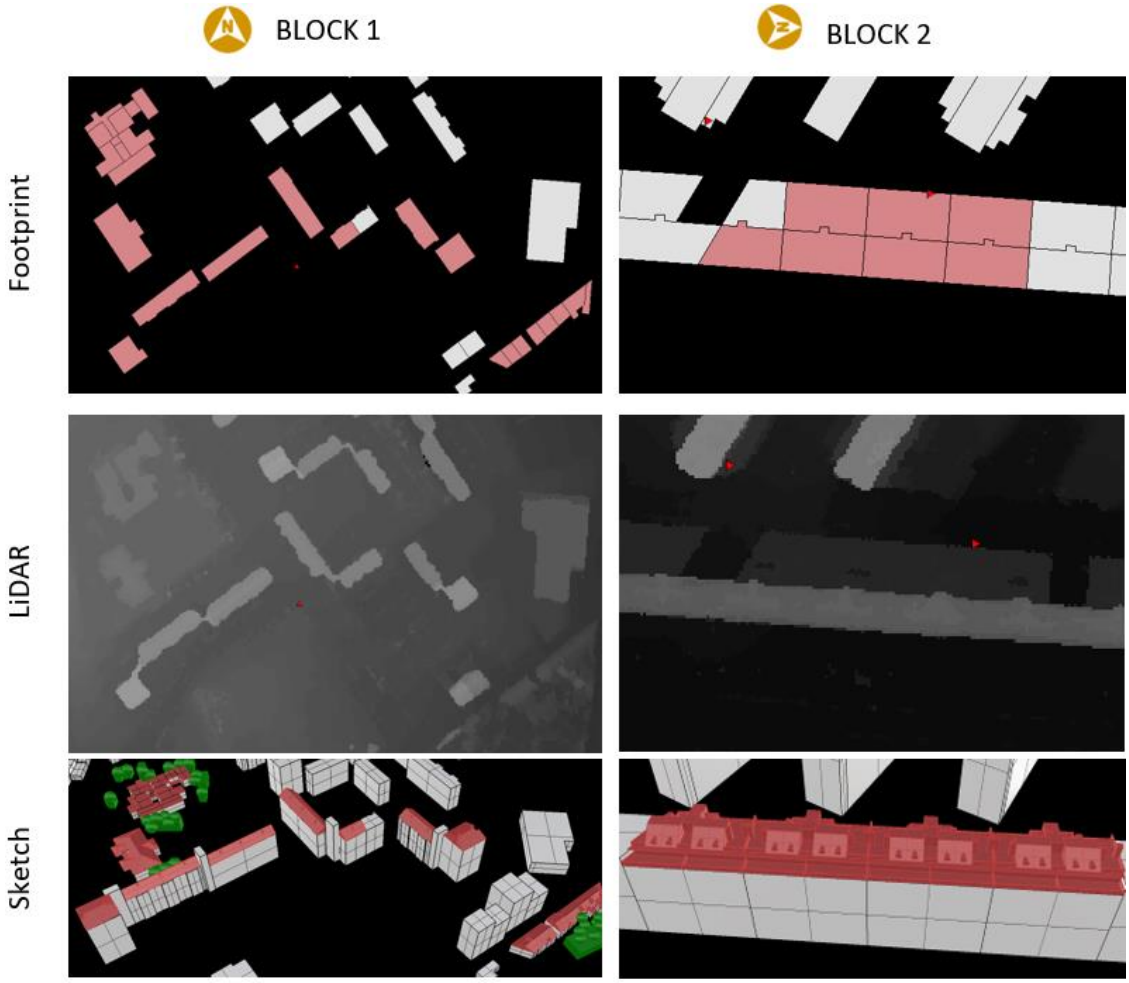

Figure 3.18 - Input features for estimating the irradiation using the footprint method (top), the *LiDAR method* (middle) and the *sketch method* (bottom), for Blocks 1 and 2. Note that only the buildings with red rooftops are part of the studied blocks.

In Figure 3.19, the irradiation levels in the buildings of interest are represented. Rooftop surfaces have greater irradiation potential, in particular when tilted facing southeast (coloured in yellow). However, most of the south/southeast facing building façades feature irradiation levels above 900kWh/m^2/year, which might still represent areas of high interest for PV installation (as will be discussed in Chapter 6).

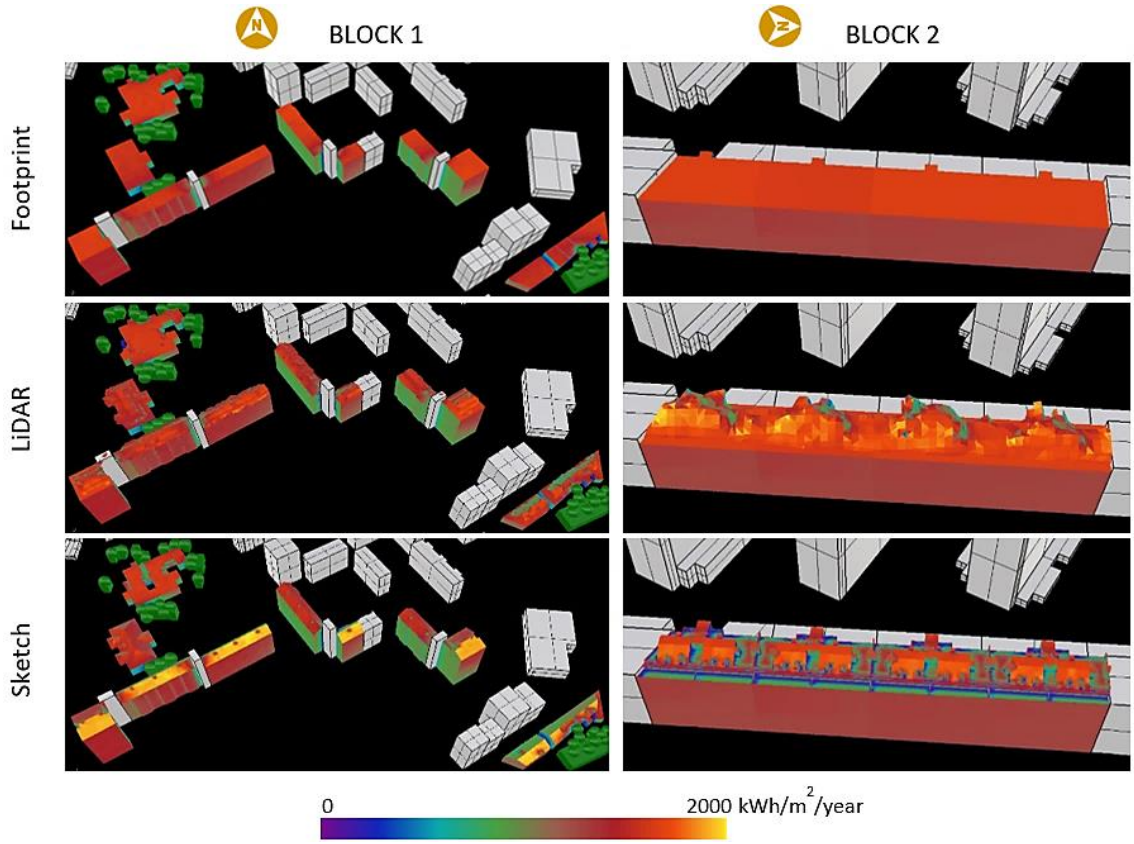

Figure 3.19 - Annual solar irradiation for Blocks 1 and 2 using the footprint method (top), the LiDAR method (middle) and the sketch method (bottom).

Most rooftops are coloured in red and orange in the *Footprint method* as they are all flat and horizontal, while the *LiDAR method* shows some levels of green (in the current image perspectives) over the approximated shapes of the rooftop features. The most realistic approach is given by the *Sketch method*, where the different potential throughout the gable rooftops of Block 1 and the complex shapes of Block 2 are visible.

To evaluate the differences between methods, relatively to the reference method (i.e. the *Sketch method*), they were aggregated in hourly bins and plotted in the form of boxplots for Block 1 and 2 (Figure 3.20). The *Footprint method*, in the case of Block 1, overestimates the irradiation potential in about 25% of the time, particularly from 9h on, when the gable rooftops with different orientations unevenly receive radiation. The underestimation occurs in the early morning and late afternoon, with many outliers going up to more than 50%. As for the *LiDAR method*, there is no overestimation but a clear underestimation of around 20% throughout the day. For Block 2, due to the flat horizontal rooftop representation, the *Footprint method* underestimates the irradiation in the morning (mostly below 50% but up to 100%) and overestimates in the afternoon (up to 50%), whereas the *LiDAR method* seems very close to the sketch method until 14h, when it starts overestimating slightly, up to 50%, but seldom reaching 100%. It should be highlighted that early and late hours of the day, even when considering façades, feature very low irradiances and therefore this apparently high relative deviations are not very significant in absolute (kWh) terms.

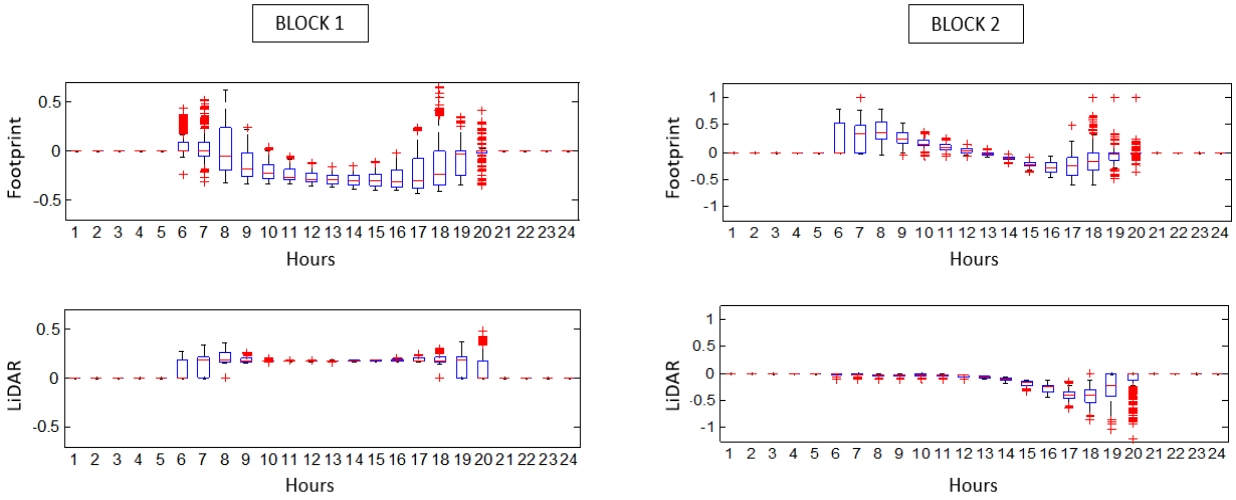

Figure 3.20 - Hourly difference relatively to the *Sketch method* between solar irradiation on rooftops estimated using the *Footprint method* and the *LiDAR method*, for Block 1 and 2. Negative values mean overestimation. (The tops and bottoms of each "box" are the 25th and 75th percentiles, the red line in the middle of each box is the median, the black lines extending above and below each box are the extreme values and the red crosses are the outliers.)

All three methods have advantages and disadvantages: the footprint method is the less labour-intensive but less accurate, whereas the sketch method is more realistic but produced thousands of surfaces that significantly slowed down the computational processes. As for the LiDAR method, it featured a good compromise between accuracy of modelled irradiation and computational requirements. Nevertheless, new LiDAR surveys are costly and demanding, whilst footprints are more common and easier to modify.

Lastly, it is worth mentioning that the comparison did not concern façades, given the lack of architectonic detail on the representation of these surfaces. The spatial resolution of the DSM promptly compromised such detailed analysis at the rooftop level, since it does not capture the presence of artefacts, roof overhangs, small chimneys, dormers, or antennas, and thus it was unlikely that further details could be achieved for façades. The large number of buildings, of course, did not allow for a more accurate modelling of façade elements in a timely manner.

3.3 Outdoor PV glare potential

The assessment of the solar potential of façades described in the previous section showed that, due to the large available area, vertical façades offer a very significant opportunity for large scale deployment of photovoltaics in the urban landscape. However, results also hinted to one serious obstacle to its implementation: at current prices, profitable PV systems are generally limited to locations with irradiation levels above 900kWh/m^2/year, which are easy to find on rooftops but much less available on vertical surfaces. This issue will be discussed in more detail later in Chapter 6. This section explores another issue that is often discussed as a relevant obstacle to the deployment of PV façades: the impact of glazed PV façades on outdoor visual comfort. This effect is popularly known as PV glare.

3.3.1 Application of DIVA and LadyBug

The case-study building[4] for the PV glare assessment is a commercial high-rise building located in the centre of Lisbon, in a predominantly residential area in a mixed-use neighbourhood delimited by a traffic road to the north and west (Figure 3.21, left). It is not known if the building was designed prior to the construction of its closest surrounding buildings and road, or if the planning of its façade materials took into consideration possible reflection impacts on the outdoor environment. The latter would not be surprising, since there is little regulation regarding such phenomena and no universally accepted criteria that defines acceptable limits of reflected visible light (Danks et al., 2016).

Figure 3.21 – Case-study building, located in Lisbon, with high reflective glass façades: bird's eye view (left) and reflection detail (right). Retrieved from Google Earth at 38.7445618, -9.159805.

Besides aesthetics, the rationale for the use of high reflective glazing in buildings is usually the limitation of excessive solar gains. However, reflection glare can be hazardous to passers-by on the streets below, or vehicle drivers. If reflections on windows and frames may be associated to blinking glare that distracts, the full glazing skin of this building has the potential to provoke continuous glare, causing visual fatigue and even disability. This effect is more pronounced in north-south oriented streets with glass covered buildings (Shih and Huang, 2001).

Similarly to glazing materials, conventional PV modules also reflect radiation, in particular when the angle of incidence of the solar rays exceeds 70°, as discussed in section 3.2.1. According to the experimental tests reported in (Juutilainen et al., 2016), a raw solar cell has a relatively high angular response (i.e. low reflectance) that remains around 85% even at 85°. Its reflectance increases when encapsulant materials are added. Therefore, the main source of reflection in a commercially available module is the front cover materials, especially the front glass.

To estimate the glare potential in the case-study building if, instead of high reflective glass, it was covered with conventional PV modules, a computational approach must be employed. Calculations involving solar radiation, physical properties of building and environment materials and a retinal function to emulate the human eye are required. For instance, (Ho et al., 2015) developed Solar Glare Hazard Analysis Tool (SGHAT) to evaluate glare probability at a site and calculate the retinal irradiance and subtended angle of the glare source to predict potential ocular hazards ranging from temporary after-image to retinal burn. However, the tool is not publicly available and it is not clear if it extends to building façades.

Due to its extensively documented capabilities to deal with radiation phenomena, the plugin DIVA (version 4) for Rhinoceros 3D/Grasshopper was used instead. A footprint-derived digital model of the building and its surroundings was available (Figure 3.22). Local trees and urban equipment were not

[4] This case study is one of three case studies of PV glare assessment currently being developed in collaboration with the MSc student Ines Martinho, under the author's supervision.

included in the simulation. To minimize computing time, only the equinox and solstice days were analysed: the 20th of March, the 20th of June, the 22nd of September and the 21st of December.

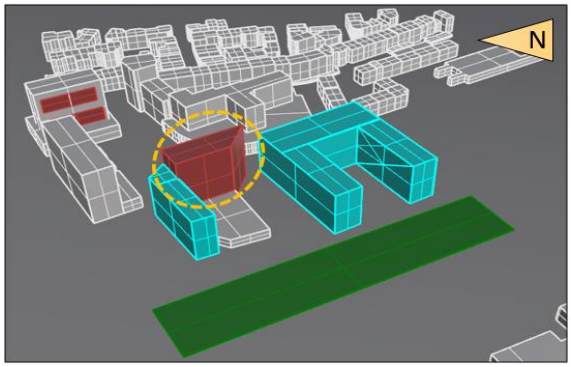

Figure 3.22 – Digital surface model of the target building (circled) and its surroundings (green represents grass, blue the nearby buildings with blue façades and red are mirror surfaces).

Firstly, a forward raytracing analysis of the urban context was carried out, which will help understanding how the solar rays bounce off building surfaces and where concentration will likely happen, allowing the identification of the most impacted locations. The plugin LadyBug "Sunpath" and "Bounce from surface" components were used for this purpose. The former displays, among other options, a solar path diagram over the digital urban model including the position of the sun for the time of the day and year (Figure 3.23, top). The resulting solar vectors can be used as input to the "Bounce from surface" component to simulate multi-reflections and identify those reaching the ground and/or other building façades (Figure 3.23, bottom).

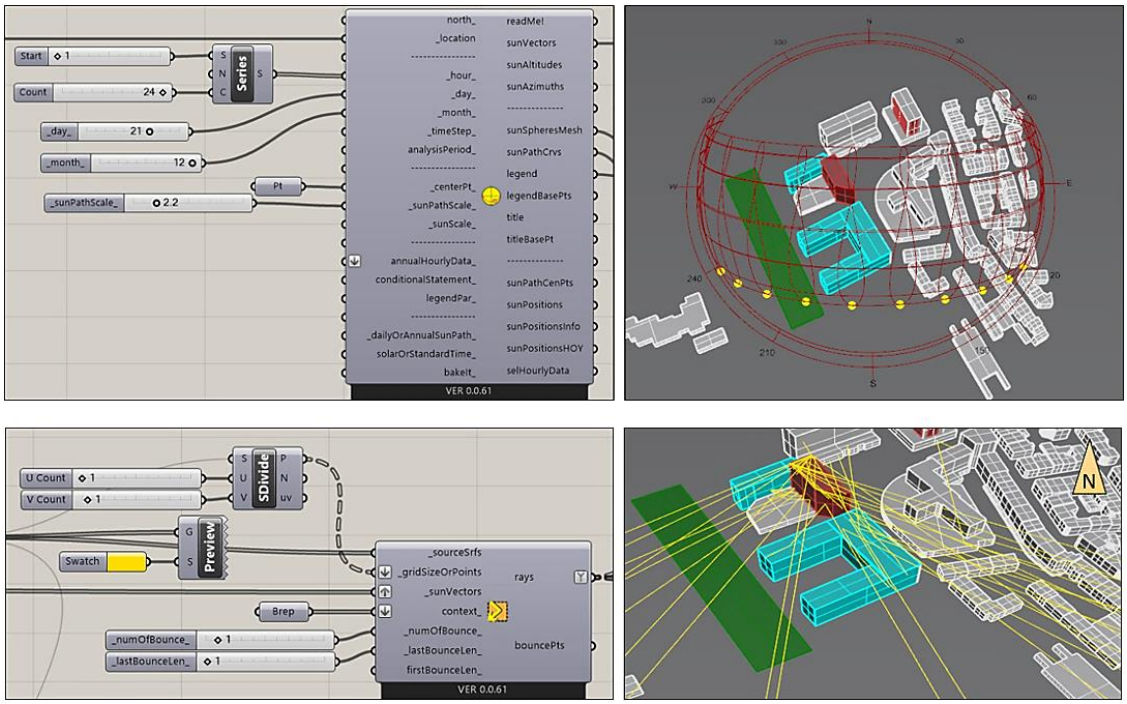

Figure 3.23 – Example of the LadyBug component "Sunpath" with solar path diagram and hourly sun positions for December (top) and component "Bounce from surface" with respective sun rays (bottom).

The combined analysis for the four days reveals the areas that are probably more affected by reflection glare, identified in Figure 3.24 (left) using blue dots. Glare analysis using DIVA requires the placement of perspective cameras. Three locations were chosen according to the likelihood of reflection glare

mapping (Figure 3.24, right): one in the square (1), another close to the road (2) and a third on the street to the left of the building (3). The last position represents the perspective shown in Figure 3.21 (right).

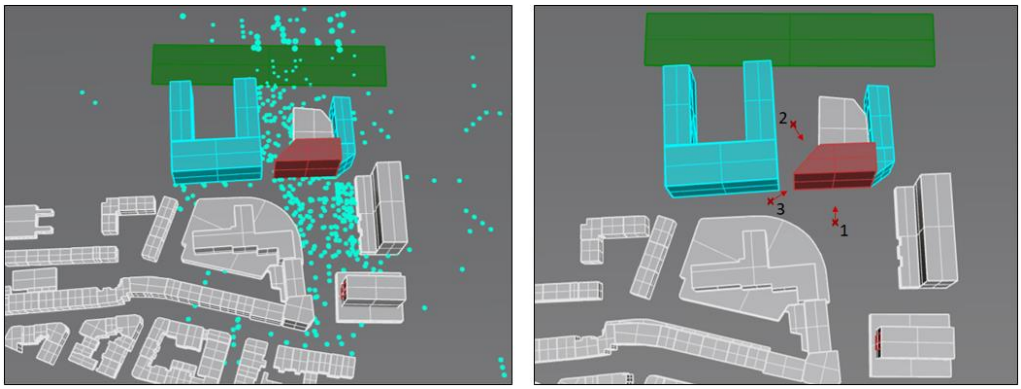

Figure 3.24 – Cumulative density of reflected rays that intersect the ground in the four typical days (left) and camera positions (right).

The "Glare analysis" component in DIVA also requires the definition of the sky for luminance simulation and the material properties of the surfaces. The first was set to "Perez from weather file", which consists on adapting the sky model of Perez to the typical meteorological data of the site. For the material properties, described in Table 3.3, the lighting materials database (Jakubiec and Balakrishnan, 2015) and default Radiance material functions were used. To emulate the real context, the surfaces of the closest buildings (shown in blue) were assigned glass material. Other buildings' surfaces were assigned white colour (specified as white street paint), a few mirror areas, oak leaves were used for nearby grass and bushes and ground was assigned asphalt. Simulations explored different materials including high reflective mirror, PV modules, glass and new/old white street paint. It must be noted that, although there is a full characterization of two PV modules in the lighting materials database, the PV material used was in fact a specular plastic to emulate the front cover of the module, since the more realistic material definition does not yet work in DIVA for Grasshopper.

Table 3.3 – Relevant visual properties of the different material functions used.

	R_{total} [%]	R_{red} [%]	R_{green} [%]	R_{blue} [%]	Specularity [%]	Transmittance [%]
Mirror	72	72	72	72	-	-
PV	3.87	3.6	3.83	5.32	2.99	-
Low-e glass	71	71	71	71	-	65
New white street paint	64.02	66.06	64.18	50.89	0.55	-
Old white street paint	39.09	42.60	38.63	29.32	0	-
Oak leaf	5.61	4.01	6.6	1.88	0	-
Asphalt	4.17	4.29	4.14	4.01	0	-

False colour fish-eye projections of the camera perspectives were produced, one for each investigated time and material. Figure 3.26 (left) shows an example of a luminance image. The colours correspond to levels of luminance, truncated at 10000 cd/m^2: a reference level for unbearable glare (Yang et al., 2013). DIVA can calculate several glare metrics for each luminance image, however, those metrics refer to indoor glare, characterized by reflections from a working surface inside interior spaces, and do not hold for outdoor glare, which involves the presence of the sun and a wide spread environment. Thus, a different approach had to be followed to evaluate glare events in an outdoor urban context and understand which material causes less visual impact. The frequency of the different luminance

classes among the hourly images produced for the typical days was estimated through analysis of the pixel colours in each image using MatLab image processing routines. An image containing the discrete scale bands was first analysed to extract the RGB values for each colour band (Figure 3.25). Then, a mask was drawn on each image, excluding all but the building façades under analysis (Figure 3.26, right). The RGB values for each pixel, and their respective luminance class, were determined according to the RGB of the scale bands, depicted in Figure 3.25.

	R	G	B
Glare_1 (500 cd/m^2)	119	9	140
	120	9	140
	117	10	140
	119	10	139
	120	10	141
	119	9	142
	119	9	139
Glare_2 (1500 cd/m^2)	10	10	182
Glare 3 (2500 cd/m^2)	15	100	191
	16	99	191
	13	101	191
	14	99	190
	15	100	193
Glare 4 (3500 cd/m^2)	10	173	170
	12	172	170
	9	174	170
Glare 5 (4500 cd/m^2)	36	176	67
	34	175	79
	32	176	79
	35	177	67
	38	176	67
	36	177	65
	36	176	69
Glare 6 (5500 cd/m^2)	115	138	82
	114	139	82
	117	138	82
	115	139	81
	115	138	84
Glare 7 (6500 cd/m^2)	154	96	82
	155	96	82
	153	97	82
	154	97	80
	153	97	82
Glare 8 (7500 cd/m^2)	163	57	59
	162	58	59
	165	56	59
	164	58	60
	163	57	57
Glare 9 (8500 cd/m^2)	174	22	35
	176	21	35
	173	23	35
	174	22	34
Glare 10 (9500 cd/m^2)	228	31	15
Glare 11 (>10000 cd/m^2)	255	150	23
	254	151	22
	255	146	31
	255	145	32
	255	150	25
	254	251	48
	255	251	48
	254	252	46
	254	251	50

Figure 3.25 – RGB values for the different shades in the false colour bands of glare images.

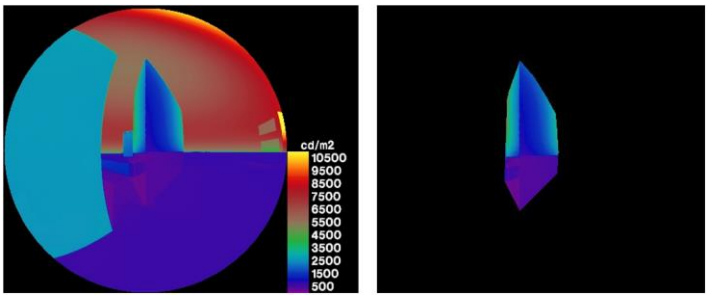

Figure 3.26 – Example of a false colour luminance image for Camera 3, for the 20th of June at 10h (left) and respective mask excluding all but the target building façades (right).

A luminance class exists in an image and is assigned frequency equal to 1 if there are, at least, ten pixels belonging to that class. Otherwise, the class is not identified as present on the image. The value ten was assumed after observing small artefacts in some of the images: a yellow dot (small aggregation of pixels) is sometimes visible in the façade, however it is uncertain if it represents a specular reflection of the sun. The maximum frequency value for a luminance class is, therefore, the total number of hours analysed multiplied by the number of cameras. In Figure 3.27, the cumulative frequency of luminance classes for the four typical days is represented for the different simulated surface materials.

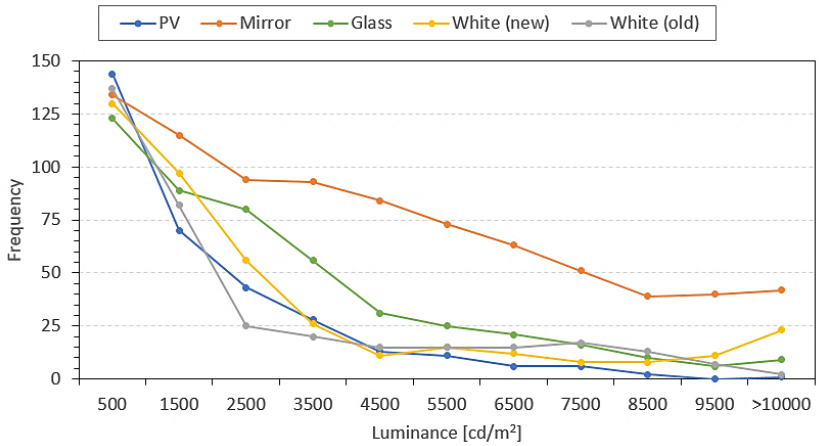

Figure 3.27 – Cumulative frequency of luminance classes per façade material.

The lower classes of luminance are, as expected, the most frequent since they correlate with lower radiation sources – more common in urban settings. Mirror and glass have similar frequencies in the acceptable glare range (0-3200 cd/m^2); these frequencies are very high compared to the other materials. In the discomfort glare range (5600-10000 cd/m^2), the frequency of glare events remains high for mirror but a significant decrease is observed for the glass façade. Both new and old white paints and PV materials' luminance frequencies stagnate above 4500 cd/m^2, except for new white paint that features a slight increase in 8500 cd/m^2 due to its higher reflectance and specularity. Intolerable glare (>10000 cd/m^2) is highest for mirror, followed by new white paint and glass. Old white paint and PV feature residual intolerable glare suggesting that the integration of PV modules on façades leads to lower glare issues than when using conventional office building materials such as glass or mirror.

Further insight can be obtained through careful inspection of some images from different moments of the day. Figure 3.28 shows examples of luminance images produced for the morning, midday and afternoon periods, in the summer solstice, autumn equinox and winter solstice, using PV and mirror materials. Camera 1 highlights the hazardous reflections caused by a full mirror façade coverage, especially in the morning and afternoon of summer and autumn (and spring). People walking down the square on a summer morning must bear the luminous intensity from the sun itself and from a

second 'sun' mirrored in the façade. In autumn, the sun is behind the building but the mirror façade reflects back radiation that bounces off from another mirror covered building façade on the other side of the square. From Camera 2, near the main traffic road, intolerable glare occurs mostly in autumn (spring) and winter during the morning and midday. A more intricate view is that of Camera 3, which records dramatic reflections onto the street passers-by and vehicles in the afternoon throughout the year, except in winter. On other occasions, the mirrored building seem to blend with the surroundings and sky, becoming almost indistinguishable in the false-colour images.

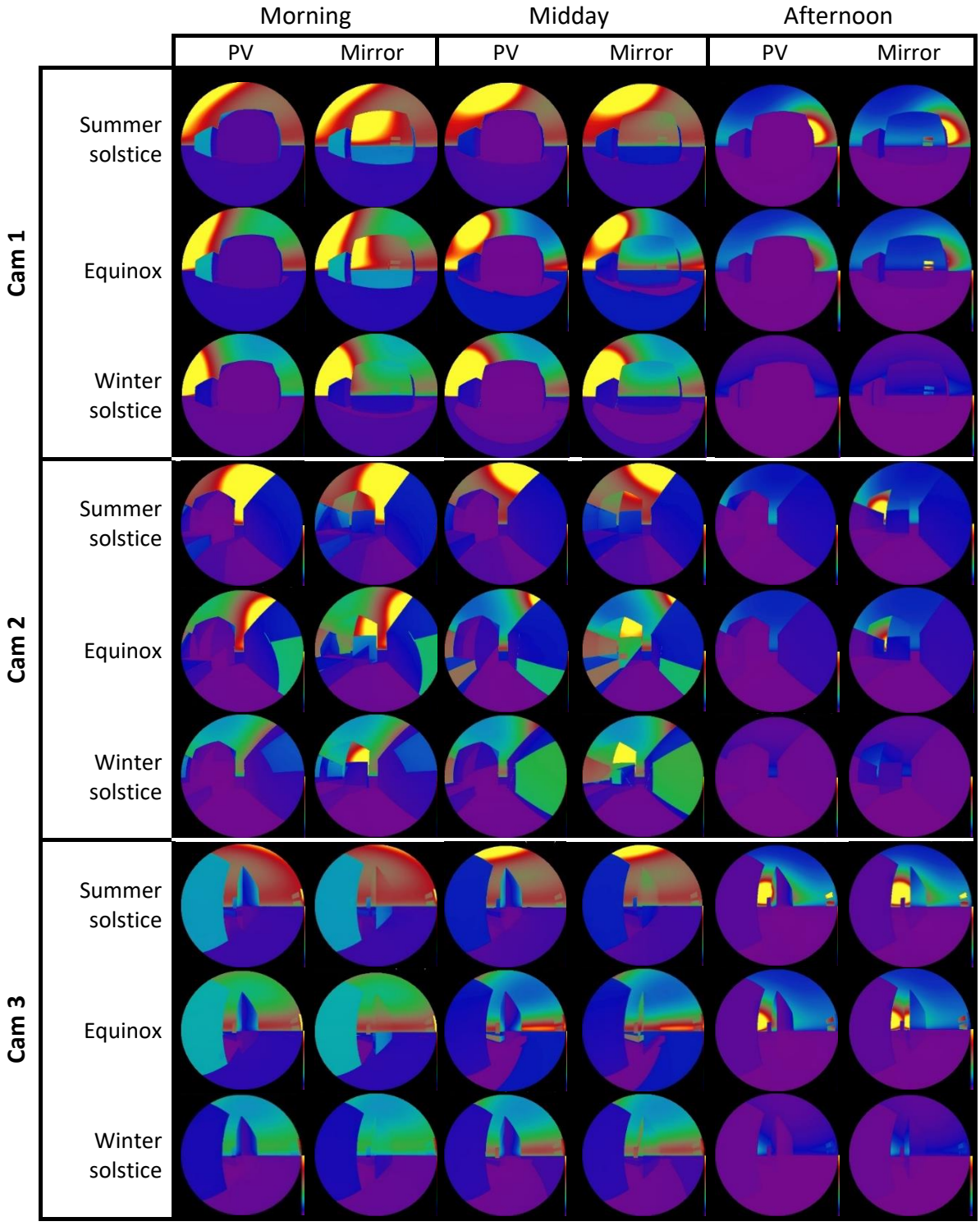

Figure 3.28 – PV and mirror luminance images for cameras 1, 2 and 3 in the summer and winter solstices and autumn equinox, for the morning, midday and afternoon periods.

Different results were obtained for the PV coverage scenario. The intolerable glare events can only be detected by Camera 3's perspective in the afternoon of summer and autumn (spring) days, when the angle of incidence of the sunrays in façade is high. In all other times and perspectives, the PV material is effectively reducing glare. This is not surprising since the purpose of a PV module is to convert incoming irradiation into electricity and therefore the higher the surface's reflectance the lower the photovoltaic conversion efficiency.

It must be noted that, apart from visual impacts of PV, large scale deployment of photovoltaics has been associated to heat island effect (Barron-Gafford et al., 2016). It is unclear if the same will occur under a massive deployment of PV in the cityscape. In (Tian et al., 2007), simulations for an urban location in China revealed that, although the building surfaces experienced important temperature and heat flux variations, the air temperature of urban canyons with integrated PV varied little compared to a non-PV scenario. In fact, the opposite was obtained: the increase in conversion efficiency lead to a reduction in the urban canyon air temperature. Another study concerning the large-scale PV deployment in Los Angeles region (Taha, 2013) corroborated the findings in the previous reference.

3.4 Conclusion

This chapter introduced the use of two solar radiation assessment tools suitable to evaluate the solar potential of PV façades: the SOL model, a customized 3D radiation model developed at the Faculty of Sciences of the University of Lisbon, and the DIVA/Ladybug plugins for Rhinoceros 3D.
The SOL model was validated against experimental data for a case study of a vertical wall in a flagship nZEB building in Lisbon, the Solar XXI building in Lumiar. Its SVF algorithm was also experimentally validated using the classical fisheye photographic method. Results suggested opportunities for improvement, in particular regarding angular losses and anisotropic diffuse radiation modelling. Nevertheless, the model was shown to be sufficiently accurate to be useful for the assessment of PV potential. Its application to different case study areas in Lisbon and Geneva has highlighted the relevance of PV façades, effectively doubling the solar potential in two of the areas analysed, and increasing the solar potential in about +50% in the two other case studied areas.
The application of the DIVA/Ladybug plugin method was used to confirm that $1m^2$ LiDAR-derived digital surface models allow for fairly accurate irradiation estimates in building rooftops and to assess the possible effect of PV glare, sometimes perceived as a possible obstacle to large scale deployment of PV in the urban landscape. An extreme case study was explored in detail showing that PV façades can actually act as efficient glare mitigating surfaces.
The model results also suggested that the deployment of solar façades may be hindered by the lower irradiation levels, which lead to less favourable economics. Hence, strategies and technologies for maximizing PV façade yield ought to be explored. This is the topic of the next chapter.

4. MAXIMIZING THE PV POTENTIAL OF FAÇADES

The solar potential of a city can be realized through energy technologies that adapt to its forms. Photovoltaics is the most promising candidate to tackle the challenge of electricity supply in urban agglomerates, especially due to its modular and multifunctional nature. Building integrated photovoltaics (BIPV) can be perceived either as construction material that are PV enabled or as PV modules that serve as construction elements. The BIPV market is expanding as new solar cell technologies with improved performance, colour and morphological properties emerge in the PV market, providing architects and designers with a wide spectrum of possibilities to create nZEB. New buildings may go beyond the conventional forms to optimize solar radiation collection; façades may act as both conveyers of a greener image and maximisers of solar harvesting.
In this Chapter, PV technologies for integration in façades are reviewed. Then, different façade layouts, including louvers, geometric forms and balconies, are studied and optimized for annual solar irradiation. [5]

4.1 Introduction

The 2020 horizon goals (European Commission, 2014) and the high electricity consumption in densely populated cities, along with the continuous decrease of PV system costs, turned the urban environment into a playfield for building applied/integrated photovoltaics (BAPV/BIPV). The acronym BIPV technically refers to systems and concepts in which the photovoltaic element can also act as a building component, meeting all the building envelope requirements such as mechanical resistance and thermal insulation, whereas BAPV requires additional mounting systems (Scognamiglio and Røstvik, 2013)(Bonomo et al., 2017). The latter conventionally employs flat PV modules, but flexible PV has been used for integration to more complex shapes. Moreover, new PV technologies offer more sizes, degrees of flexibility, shapes and appearance, making PV particularly suitable for replacing or being used together with materials that are common in architecture, such as glass or metal, in opaque and in semi-transparent surfaces (Verberne et al., 2014).
Most BIPV refers to conventional roof-mounted PV modules, which account for 80% of the BIPV market (Shukla et al., 2017), but façade integrated PV is also becoming attractive. In one hand, as explored in Chapter 3, façade area may double the solar potential of a neighbourhood. Thus, buildings forms must adapt to maximize solar exposure. On the other hand, façades are the "face" of the buildings, the part of the building with higher visual impact. The deployment of façade PV must meet aesthetical requirements. Hence, a façade PV is both an engineering and a design challenge. Fortunately, the aesthetics and optimized performance of such systems can be thoughtfully tested through state-of-the-art software, namely CAD/plugin-based tools that model and simulate building integrated energy systems as discussed in Chapter 2.
Liveability, thermal and visual comfort to the spaces inside of buildings determine that façades cannot be fully vertical, opaque and flat: structures such as windows, louvers, sunshades and balconies are examples of elements that constitute a façade and contribute to the outdoors/indoors synergy (Roberts and Guariento, 2009). Contemporary construction also often features non-flat façades, sometimes with very complex shapes, and a vast range of materials and colours. In the perspective of

[5] Chapter includes work published on:
- Freitas, S., Brito, M.C., "Maximizing the Solar Photovoltaic Yield in Different Building Façade Layouts". 31st EUPVSEC, Set 2015, Hamburg, Germany. DOI:10.4229/EUPVSEC20152015-6AV.5.6
- Freitas, S., Brito, M.C., "Bifacial PV integrated on building balconies". 32nd EUPVSEC, Jun 2016, Munich, Germany. DOI:10.4229/EUPVSEC20162016-6DO.8.1

fostering BIPV in cities, these non-vertical (but vertical façade integrated) structures would interact with solar radiation differently throughout the day, prompting peak electricity production at different hours. If proper BIPV elements are selected to this end, great amount of façade area, which would otherwise remain untapped, will gain a new complementary functionality.
(Polo Lopez et al., 2014) emphasized the complementary relationship that other building construction technologies should have with BIPV façade systems to make them appealing to architects and engineers, who prefer more standardized products. On the other hand, BIPV represents a key driver for contemporary innovation (Bonomo et al., 2017). The construction industry has also been pro-standardization, thus the development of market for BIPV solutions for façades with unconventional layouts relies on the development of a solution that keeps the trade-off between bulk production and design flexibility (Hagemann, 2011). Nonetheless, and in particular concerning cityscapes, the opportunity for the growth of BIPV is almost limitless: the BIPV systems surveyed in (Bonomo et al., 2017) confirm that BIPV façade applications are a cost-effective substitute for conventional façade solutions, especially if considered in the earlier stages of building design and construction. However, the demand is relatively low and economies-of-scale are yet to be fully realized.

4.2 Solar on façades

Several building elements can integrate PV, but when the focus is on the façade there is a wider range of opportunities: there are cold façades, warm façades, glazing and accessories applications. Figure 4.1 shows examples of façade features and how PV modules can be deployed. They may be integrated into unitised curtain wall systems, in the vision area or in the spandrel area of the façade, and single or double-glazed units can be replaced by clear or opaque, single- or double-glazed PV modules (Roberts and Guariento, 2009).

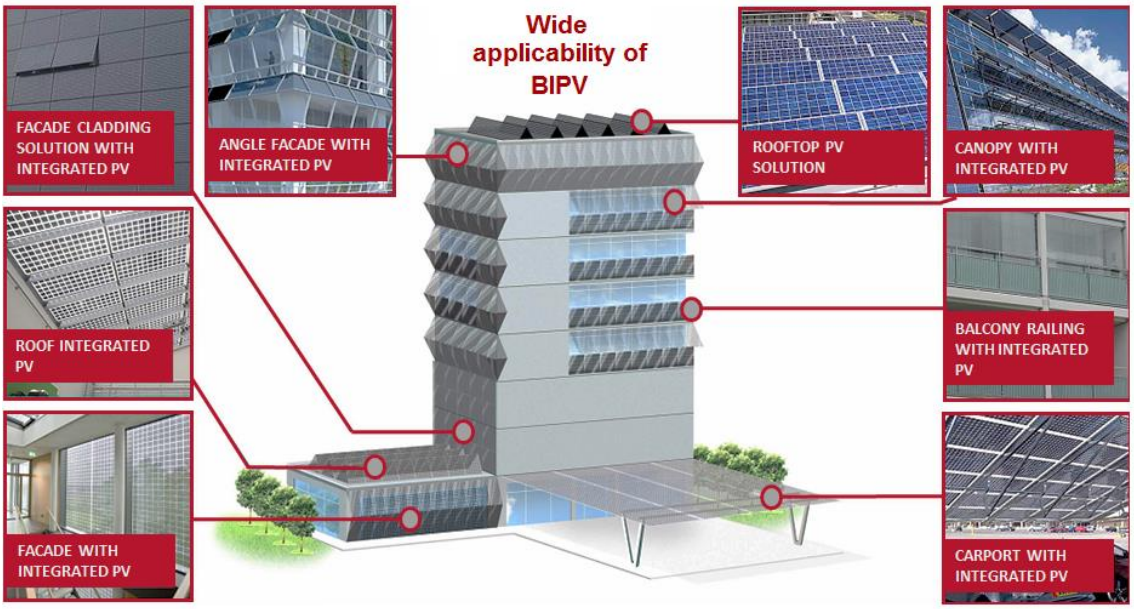

Figure 4.1 – Examples of distributed in-house electricity generation with a synthesis of PV and conventional construction materials. (ViaSolis, 2017).

i) Cold façade

Cold façades are typically load-bearing sub-frames, with an air gap and a cladding panel. They are “cold” because, during hot weather, the heat from the sun is dissipated through the naturally ventilated air cavity, bringing a cooling effect for the wall and for the PV modules (Shahrestani et al.,

2017). The integration of PV modules in this case can be that of a conventional cladding element or a rainscreen cladding.
The latter (Figure 4.2) features an outer skin of rear-ventilated cladding to the building, but has a form of double-wall construction. The outer layer is used to keep out the rain and has no connection to the warm areas of the building, while the inner layer provides thermal insulation, prevents air leakage and carries wind loading. PV rainscreen cladding typically employs opaque units, thus it represents an economic alternative in opaque façades, since mature existing PV technology can be used. The ventilated cavity also provides space and camouflage for electric wirings passages.

Figure 4.2 –Back ventilated glass PV rainscreen system, Dresden, Germany (Bendheim, 2010).

ii) Warm façade

When an exterior wall is attached to the building structure and does not support the loads of the building it is called a curtain wall (Figure 4.3). It ought to resist water and air infiltration and wind forces acting on the building. They are also referred to as warm façades since the thermal-insulation layer is applied directly to the surface of the building, generally embodying a layer of glass supported by aluminium or steel frames that provide daylighting and aesthetics. The integration of PV is done by replacing conventional glass with an active glazed pane including PV. Cable routes are concealed by the load-bearing frames.

Figure 4.3 – PV curtain wall in Greenstone Government of Canada Building (Manasc Isaac, 2005).

Solar gains, indoor thermal and visual comfort become more difficult to control when using highly glazed curtain walls, thus additional infills such as louvres, operable windows or vents may need to be included to avoid those issues. Compared to a rainscreen, the lack of rear ventilation of the PV modules might also cause a reduction in electricity production (Koehl et al., 2016). A double-skin façade (Figure 4.4) can be a solution to this, although it is more complex and expensive.

Figure 4.4 – Double skin PV façade with 0.8m of air gap in the Norwegian University of Science and Technology, Trondheim (Horisun, 2000).

In a double-skin façade, two building skins are separated by a ventilated cavity, which improves building performance by adapting itself to ambient conditions and balancing out seasonal climate fluctuations. The thermal buffer between the inner façade and the outer skin can be used passively or actively to regulate heat, cold, light and wind impacts on the indoor spaces. The width of this space can be as small as the width of a window or sill or as large as the width of a catwalk, walkway or hallway. Photovoltaics are integrated in the outer glazing façade, functioning also as solar shading devices that can improve electrical and thermal performance (Gaillard et al., 2014)(Elarga et al., 2016).

iii) Glazing

Windows are installed or integrated within the load-bearing exterior walls of the building, either as unitary glazing elements or combined to form continuous bands. These are essential to provide natural light and, when movable, ventilation to the interior spaces, as well as regulate indoor thermal comfort and psychological wellbeing of building occupants.

Figure 4.5 – Solar PV window tests at FLEXLAB, Solaria BIPV (Solaria, 2016).

PV windows can be achieved though the encapsulation of solar cell material within glazed panes (Figure 4.5), hold by aluminium, steel or wood frames. Depending on the solar cell technology, different degrees of transparency and cover for electric wiring passage can be attained.

iv) Accessories

The design of buildings usually contemplates additional functional elements such as balconies, parapets, outdoor partitions, window shutters and shading systems. The architectural drive to improve comfort of occupants with respect to daylighting and views to the outside led to large glazed façades in office and commercial buildings. Shading systems are essential to control the indoor microclimate and avoid excessive solar gains. Shadings can be external, interposed or internal; fixed, manually or

with electrical tracking; vertical, horizontal or oriented; lamellar, micro-lamellar, sail, grid; curtain or blind; mobile screen or panels; solar film, selective or prismatic glass.

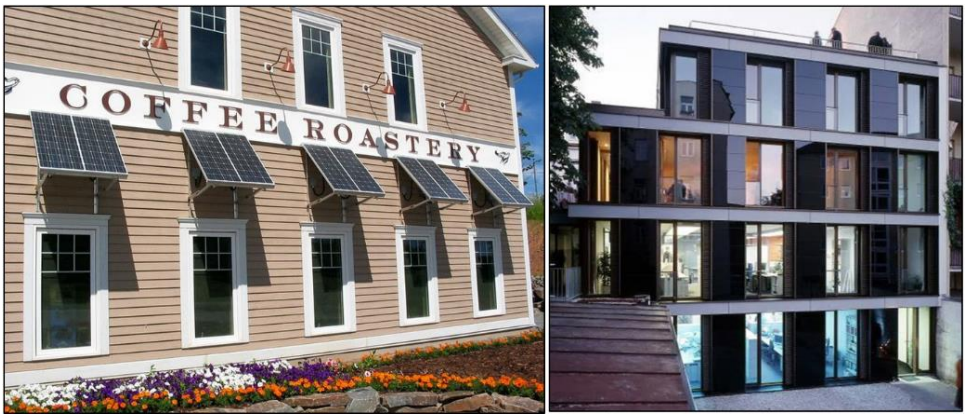

Figure 4.6 – Solar sunshades at a museum in Canada (Taste of Nova Scotia, 2015) (left) and sliding window shutters with frameless PV modules in a German house (Manz AG, 2017) (right).

The shadow function is easily combined with electricity production through the lamination of solar cell material into the shading structure. Different types of façade shadings include: i) external louvres that can be mounted close or at a distance to the envelope, however the resistance to wind loading and durability might be low and the access for cleaning and maintenance might not be easy; ii) sunshades, which are suitable surfaces for PV modules, given their tilt and ventilation, but the self-shadowing onto each other under certain sun angles reduces output-power performance; and iii) sunscreens, sunshades closer to vertical and moderating transmission. If tilted to the adequate inclination and properly oriented, they can provide protection from direct sunlight and significant PV output.

4.3 PV technologies for façades

The examples in Figure 4.2 to Figure 4.6 show use of conventional PV technologies in façade elements, crystalline silicon (c-Si) modules recognizable by their dark blue colour. PV on flat and opaque surfaces is still the most common, since it relies on mature technology that can easily be applied on existing building structures. However, the BIPV market offers plenty of other solutions for applications that require different degrees of flexibility and colour, unconventional shapes or transparency. This may be achieved with unconventional module assemblies with c-Si solar cells or other materials, such as amorphous silicon (a-Si) and other thin-films (Lee and Ebong, 2017) or organic polymers (Ameri et al., 2013). Furthermore, the electricity generation can be combined with other functionalities, such as pre-heating of air and water.

i) Shapes

The arrangement of conventional c-Si solar cells makes it possible to construct flat modules with simple geometrical shapes, thus a degree of standardization is possible. This solution is particularly interesting for irregular surfaces, where filling all the available space might be an uneasy task.

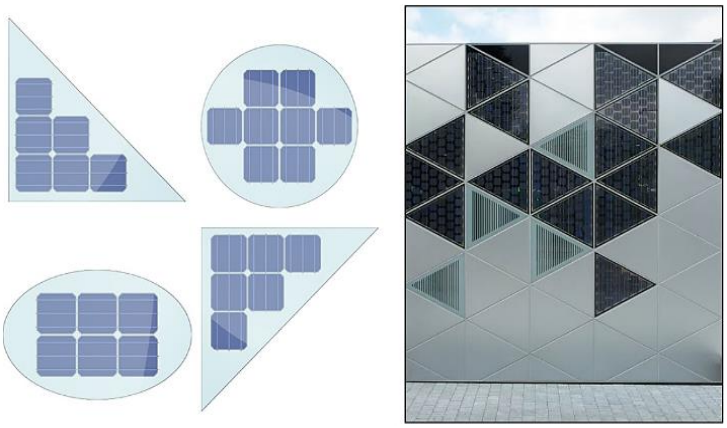

Figure 4.7 – Triangular c-Si modules installed in one façade of the International Centre for Design, in Saint-Etienne (Vincent Fillon, 2009).

ii) Flexibility

Some irregular and curved surfaces are also 3D complex. In this case, PV modules that can bend are the most appropriate option regarding aesthetics and an efficient use of all the available area. Thin film materials such as a-Si and Copper Indium Gallium Selenide (CIGS), are usually used to fabricate these modules, which also have other advantages such as their lightweight, wind and crack resistance and lower output reduction due to partial shading. Bendable perovskites solar cells are being developed, promising combining the benefits of high efficiency and ease of processing over large areas (Di Giacomo et al., 2016).

Figure 4.8 – Thin film PV products integrated on building façades: a-Si modules (EcoFloLife, 2017) (left) and CIGS (Global Solar Inc., 2017) (right).

iii) PV-air/water-heating

It is possible to direct outdoor air pre-heated by the hot back surface of PV modules, coupled with an unglazed transpired collector, into a double-skin façade air cavity. This pre-heating of air helps reducing air conditioning electricity loads in the warming season and cools down the PV modules. Other schemes to accomplish pre-heating of outdoor air though façade integrated PV systems are reviewed in (Lai and Hokoi, 2015).

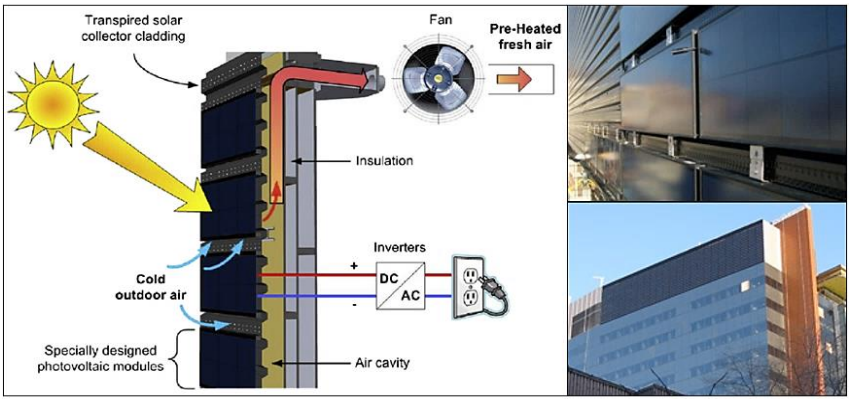

Figure 4.9 – Air-based PV-thermal system in a building façade in Montreal (Athienitis et al., 2011).

A hybrid between electricity production and pre-heating of water can also be achieved by circulating water in back surface of the PV modules. This solution might help reducing PV modules temperature, while pre-heating water and cooling down the walls. However, the combined efficiency of these systems is lower that the individual efficiency of a PV or solar thermal system alone.

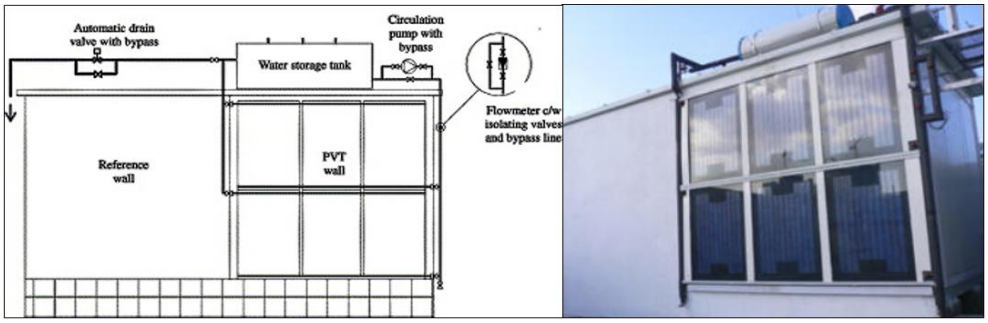

Figure 4.10 – Façade integrated PV-thermal prototype in Hong Kong for water pre-heating (Chow et al., 2007).

iv) Bifacial

Solar cells designed to harvest from both the front and the back sides are known as bifacial cells. The front surface is as the industry-standard in screen printed solar cells while the back surface has a 'finger' grid, instead of a reflective aluminium contact, to allow sunlight through the rear. Typically modules are made on high quality silicon solar cells and have transparent encapsulating, such as glass, on both sides. This module technology is especially suitable for areas with high availability of diffuse radiation, which bounces off the ground and surrounding elements. When vertically installed, bifacial modules have the potential to peak their electricity production twice during the day. This effect is more pronounced if east-west-facing, halving the number of conventional modules needed for an equivalent installation.

Figure 4.11 - Bifacial wall at Green Dot Animo School (left) and a façade bifacial prototype with white reflector sheet (Hezel, 2003) (right).

v) Colour

Standard dark blue PV modules are difficult to hide if the aesthetics require them to. Generally, the use of coloured glass (Figure 4.12, top left) or different anti-reflection coating thickness (Figure 4.12, top right) allows the camouflage of PV systems. The front glass of BIPV modules can also be printed (Figure 4.12, bottom left) using digital techniques, increasing the possibilities of design. These modules performance can drop more than 10% in comparison to non-printed modules, due to cells shadowing (Frontini et al., 2016) and changes in reflection and transmission (Eder et al., 2017). Another alternative is the use of a scattering filter to reflect visible light, letting only infrared light into the cell, the white PV module (Figure 4.12, bottom right). Relatively higher output and lower module temperatures can be achieved in comparison to c-Si dark panels (Söderström et al., 2017).

Figure 4.12 – Red glass-glass PV modules in the balustrade of Villa Circuitus, in Sweden (Wesslund and Kreutzer, 2015) (top, left); green PV sunscreens, in London (LOF Solar Corporation, 2014) (top, right); green screen printing on front glass of façade integrated c-Si modules, in Oslo (Issol, 2015) (bottom, left); vertical white PV modules (Solaxess, 2017) (bottom, right).

Another procedure for merging the PV modules with construction materials has been presented in (Slooff and et al., 2017): coloured graphics are added at the inside of the module through the interconnection of the cells via a back contact conducting foil. The appearance of the modules is easily changed. The power loss is proportional to the percentage of coverage (Figure 4.13, left). Opaque and low glare coloured modules (Figure 4.13, right) have been fabricated using a complex nano-scale multilayer deposition by plasma process. The coloured appearance results from the reflection of a narrow spectral band in the visible part of the solar spectrum, whilst the remaining solar radiation is transmitted to the solar panel to be converted into energy. The drop in efficiency is between 10-14%, depending on the module colour (John Fitzgerald Weaver, 2017).

Figure 4.13 – Disguised PV modules for façade application (Slooff and et al., 2017) (left) and coloured PV façades in a school in Copenhagen (John Fitzgerald Weaver, 2017) (right).

The use of other PV technologies also enables the change of the PV module colour. Dye-sensitized solar cells (DSSC), organic photovoltaics (OPV) (Figure 4.14), and perovskite solar cells (Di Giacomo et al., 2016) have a flexible lightweight structure and are adaptable to almost any surface. The fact that they absorb light in a bulk, instead of as a discrete interface like standard PV, permits good low and diffuse light performance, angular independence and an efficiency that rises with temperature, although the cell degrades faster with higher temperatures.

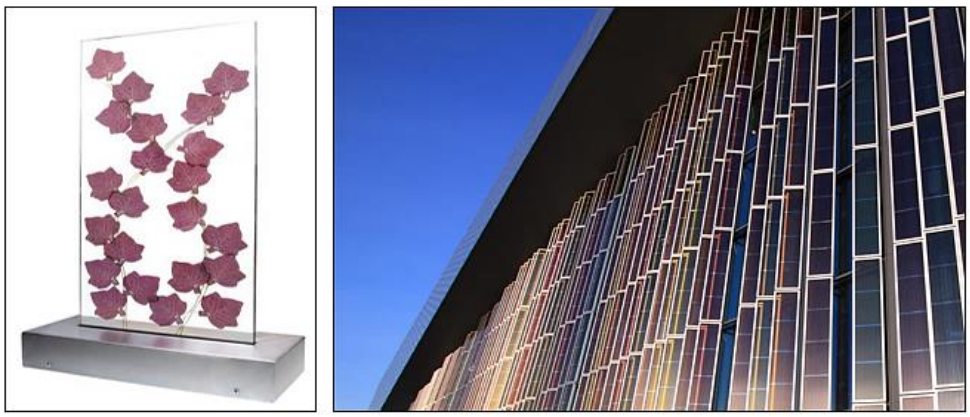

Figure 4.14 –Glass with OPV design for vertical applications (OPVIUS, 2017) (left) and tracking DSSC sunshades in the façade of Swiss-Tech Convention Centre in Lausanne (Solaronix, 2014) (right).

OPV, in particular, uses sustainable carbon-based organic materials, thus being a kind of plastic. It is even possible to manipulate the electrode and the polymer to produce decorative elements (Lee et al., 2015) (Figure 4.14, left). Power conversion efficiency of DSSC and OPV is, however, still lower than 10% (Berny et al., 2016) and it depends on the thickness and dye colour: red is more efficient, given its higher absorbance in the wavelengths where spectral solar radiation peaks (Kang et al., 2013). Furthermore, both feature short operational lifetimes.

vi) Transparency

The level of visible transmittance characterizes transparent or semi-transparent or translucent products for façades, which can provide lighting and visual penetration. Rather than having reflective, tinted or fritted windows to reduce solar transmission, semi-transparent photovoltaic windows may be used to reduce solar heat gains while generating electricity. Two different strategies can be employed: modules with Si-based cells arranged and spaced in a way that lets light to pass between the opaque cells; or see-through modules with thin films (Figure 4.15). Some technologies may alter the visual perception of the occupants of buildings, due to colour and/or shadow pattern effects.

Figure 4.15 – Example of semi-transparent PV canopy (left) and a solar OPV window made from a mixture of carbon, hydrogen, oxygen and nitrogen (Solar Window Technologies, 2017) (right).

Photovoltachromic cells (PVCC) that rely on electrochromic materials, liquid crystals and electrophoretic/suspended-particle devices are paving the way to curtain-free smart windows (Kwon et al., 2015). These switch between the transparent and opaque states (Figure 4.16), by changing their visible and thermal transmittance characteristics, to obtain a desired level of lighting or heating from solar energy in response to external triggers.

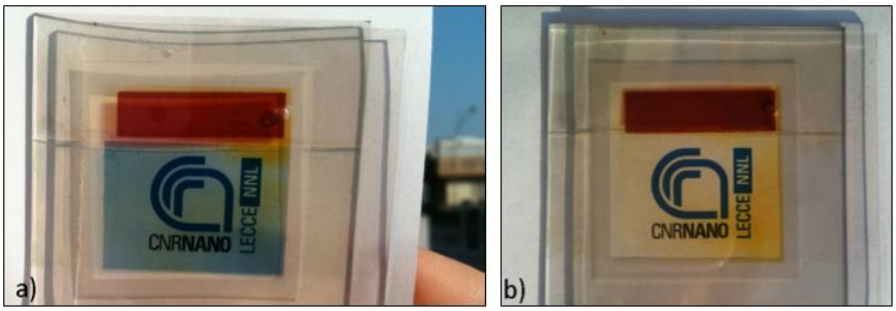

Figure 4.16 – Prototype of a PVCC in: a) opaque state, under 1 sun; and b) bleached state, under <1 sun (Favoino et al., 2016).

Totally transparent PV is also achievable by using devices that let visible light to pass through while absorbing in the infrared and ultraviolet, which is the case of the OPV developed in (Lunt and Bulovic, 2011), or redirect infrared light toward solar cells integrated in the edges of windows, such as the luminescent solar concentrator introduced in (Zhao and Lunt, 2013) and the PowerWindows product from (Physee, 2017) (Figure 4.17, left). The efficiency of these modules is still very low. Nevertheless, if one wants to maintain traditional non-PV glass windows, louvers with integrated PV cells can also be used to regulate incoming sunlight while producing electricity (Koo et al., 2017)(SolarGaps Inc., 2017) (Figure 4.17, right).

Figure 4.17 – Transparent luminescent solar concentrator with PV cells attached to the edges (Physee, 2017) (left) and external PV louvers for Windows (SolarGaps Inc., 2017) (right).

vii) Concentration

Concentrating solar PV, which means that an external element refracts the sunlight onto a solar cell, can also be applied to building façades. The idea of deploying a total internal reflection prism in building walls goes back 40 years (Mills and Giutronich, 1978) and, since then, research has explored intricate arrangements using reflective and curved surfaces and lenses to couple light concentration with PV in façades.

In (Chemisana and Rosell, 2011) and (Valckenborg and et al., 2016), two different approaches for reflective concentration using planar elements are presented: the first is installed vertically (Figure 4.18, top) and can control incoming sunlight with its solar tracking, while the second is horizontal, known as the ZigZag Solar commercial product (Figure 4.18, bottom), suited to the spandrel areas of the façade and making different use of direct sunlight throughout the day.

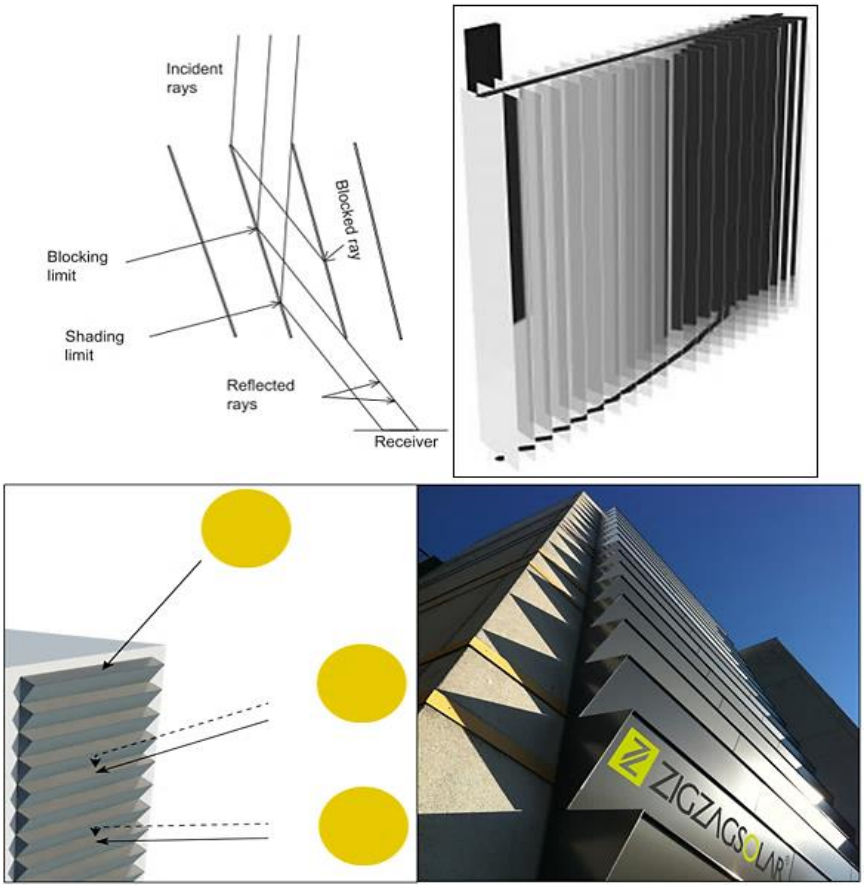

Figure 4.18 – Vertical (Chemisana and Rosell, 2011) (top) and horizontal (Valckenborg and et al., 2016) (bottom) reflective solar concentrators.

Vertical low concentration through reflection can also be achieved using compound parabolic elements (Figure 4.19). (Mallick and Eames, 2007) reported an electric power increase of almost 2 times when compared to cells without the concentrator, although the electrical conversion efficiency was only 10.5%. Results of the same order were produced by the prototype reported in (Brogren et al., 2003).

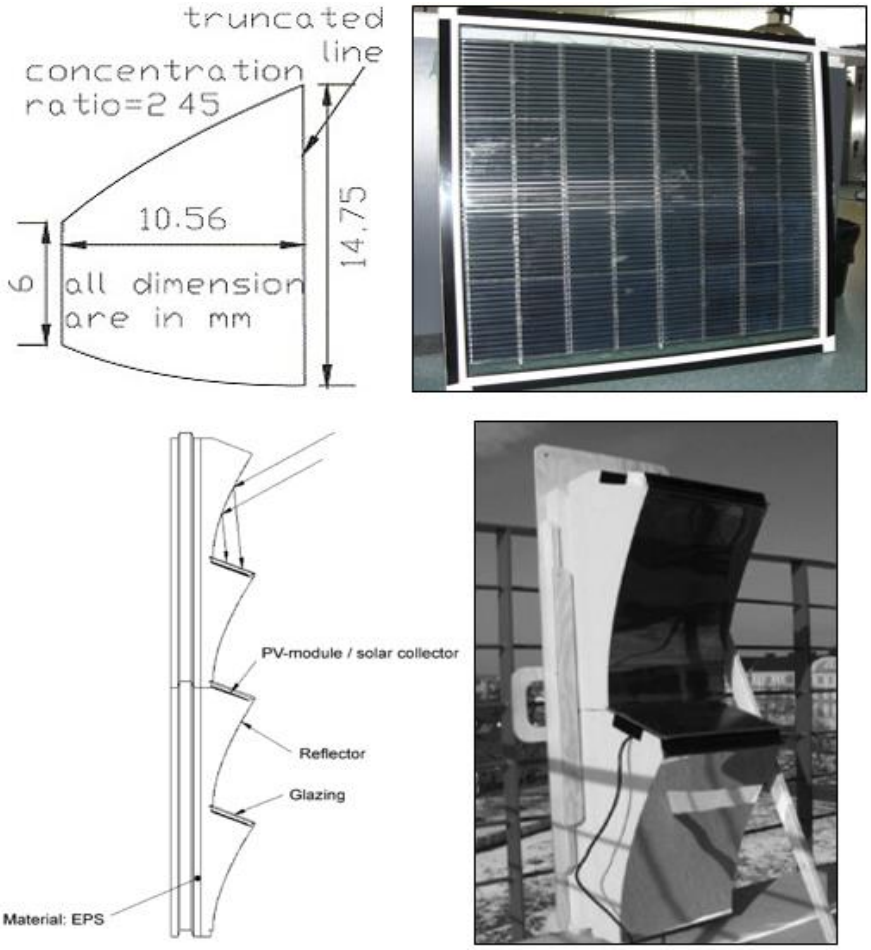

Figure 4.19 – Examples of stationary 2D parabolic concentrators for wall integration: (Mallick and Eames, 2007) (top) and (Brogren et al., 2003) (bottom).

Rather than using only 2 dimensions for concentrating mostly the direct radiation, a dielectric material can be employed to explore total internal reflection phenomena (Figure 4.20). Such systems usually have a wider acceptance angle, enabling sunlight capture throughout the day from both direct and diffuse radiations, which makes them best suited for inclined building surfaces.

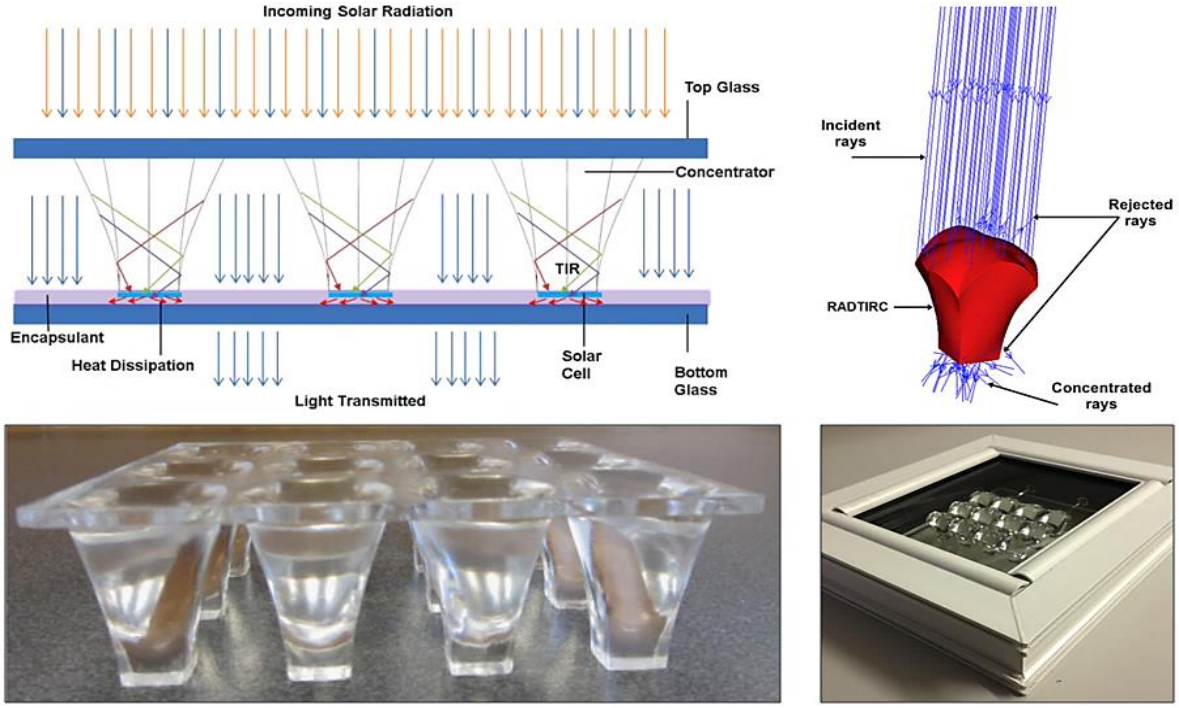

Figure 4.20 – Total internal reflection 3D solar concentrators (Baig et al., 2015) (left) and (Abu-Bakar et al., 2016) (right).

The prototype in Figure 4.20, right, originated the BIPV product for glazed surfaces called Solar Squared (Nelson, 2017). The system was outperformed by a standard flat PV panel with the same area as the concentrator face, due to optical losses as the incidence angle varied, and to output reduction due to the increase in cell temperature. The increase in production goes up to 4 times when sunrays are within the half-acceptance angle range of the concentrator. Another advantage of these systems is their semi-transparency that provides daylighting to interior spaces, however the visual perception of occupants ought to be evaluated.

Higher concentration systems (Figure 4.21 and Figure 4.22), on the other hand, typically feature a low acceptance angle, therefore requiring sun-tracking to properly capture direct radiation. Great reduction in cell area is also achieved, with alleged higher cost-efficiency. These systems are characterized by theoretical geometrical concentration ratios in the order of the hundreds, in practice reduced to two thirds (Bunthof et al., 2016).

Different approaches in terms of shapes and integration can be taken. Single lens application such as the one in (Bunthof et al., 2016) demonstrated a 24% conversion efficiency from a dual-axis tracking planar Fresnel lens module (Figure 4.21, top) using high efficiency triple-junction PV cells, whereas in (Caula, 2012) a concentrating sphere lens is presented (Figure 4.21, bottom). The latter aims to improve energy efficiency by 35% by incorporating a fully rotational natural optical tracking device that is adequate for functioning on inclined surfaces and curtain walls. It can also make use of diffused daylight, and even moonlight, for site context applications.

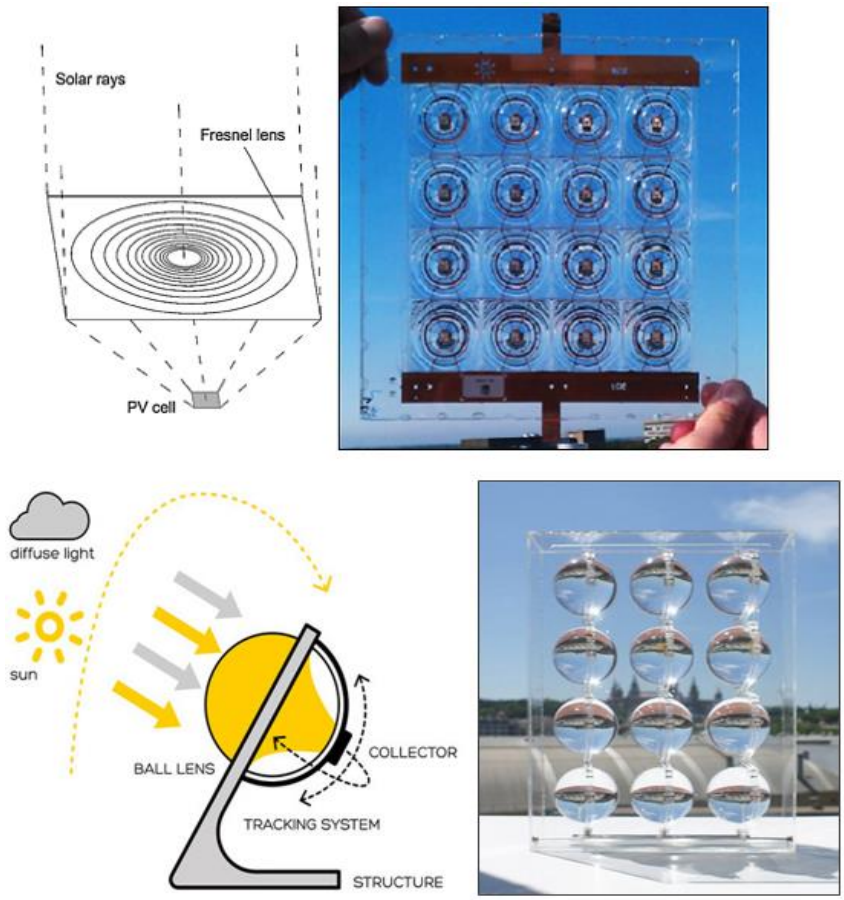

Figure 4.21 - Flat CPV module with Fresnel lenses for façade integration (Bunthof et al., 2016) (top) and concentrating spherical glass lens with dual axis tracking and triple junction PV cells (Caula, 2012) (bottom).

A secondary concentrator is generally added to homogenise the light passing through the primary optics onto the receiver and to include a tolerance to light rays off the focal area of the primary lens, in case of misalignment. In this case, the planar property is lost but other functionalities may arise, such as unitary sun tracking and the re-use of thermal energy trapped inside the glass for heating and cooling of spaces. In Figure 4.22, two examples of prototypes that make use of the heat generated inside the system are illustrated, although they do not include a secondary optics.

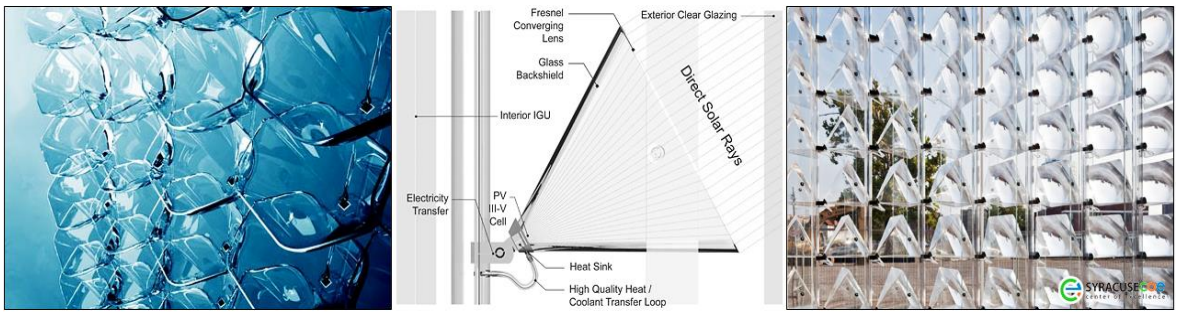

Figure 4.22 - Integrated Concentrating Solar Façade prototypes for building-integrated PV (CASE, 2016).

Concentrating glass solar PV units are mounted on a tracking mechanism that responds to the position of the sun to maximize light gain through kinetic receptors. In the first system, glass pyramid shapes (Figure 4.22, left) magnify the light and increase the natural lighting inside a building. The design is also meant to capture thermal energy trapped inside the glass pyramids for use in the building's

heating and cooling systems. The same principle (Figure 4.22, middle) is applied in the second system with a Fresnel lens (Figure 4.22, bottom). In (Zhu et al., 2018), a similar system was tested, concluding that a secondary optics would double the maximum allowable deviation of the concentrator at the exchange of -2% in the overall optical efficiency.

The most thrilling developments have, nonetheless, happened at the level of the low concentration accomplished through luminescent solar concentrators (LSC). The search for a PV technology that matches colour and semi-transparency has rediscovered the seminal work of the mid 70's (Weber and Lambe, 1976). An LSC typically consists of a polymer layer containing luminescent particles, such as organic dyes or inorganic quantum dots that absorb solar radiation. The absorbed light is emitted afterwards, but a fraction of it will remain trapped inside the material, due to total internal reflection, and will travel until it reaches one of the side edges. If PV cells are connected to the sides of the device, the incoming light will be converted into electricity (Figure 4.23, left). Unlike geometrical concentrator, LSC makes more efficient use of both direct and diffuse sunlight without the need for sun tracking (Slooff and et al., 2016). This technology is, therefore, especially adequate to building integration purposes, even when surfaces are curved. In (Inman et al., 2011) it was found that quantum dot hollow cylindrical LSC have higher absorption of incident radiation and lower self-absorption than filled cylindrical and planar geometries with similar geometric factors, resulting in optical efficiencies that can go up to 7%, depending on quantum dot concentration. Nonetheless, significant degradation was observed in 6-month-old cylindrical prototypes. On the other hand, ray-tracing simulations discussed in (Vishwanathan et al., 2015) achieve efficiencies for organic dye bent LSC prototypes of about 4%, which varied with the type of illumination, prototype size and dye concentration. The major challenge for commercial deployment of dye LSC technology is its photo-stability under UV light, despite stability tests for over 2 years have shown that good candidates exist for use in commercial type LSC (Sark et al., 2008).

Figure 4.23 – Underlying principle behind LSC (left); LSC installed in vertical noise barriers (Slooff and et al., 2016) (middle); and cylindrical LSC with near-infrared quantum dots (Inman et al., 2011) (right).

Concentrating PV technologies for glazed surfaces can also attain full transparency while passively regulating incoming light and heat. In (Connelly et al., 2016), a reflective concentrating PV smart window for buildings is described: a thermotropic layer with integrated PV cells automatically responds to climatic conditions by varying the balance of solar energy reflected to the PV for electricity generation and transmitted through the system into the building.

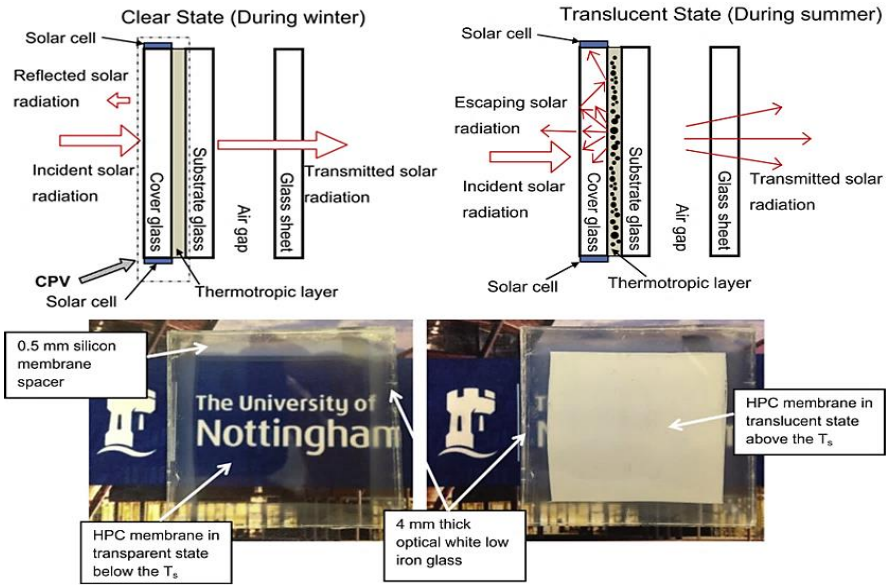

Figure 4.24 – Transition from fully transparent to translucent state of the reflective concentrating PV smart window prototype (Connelly et al., 2016).

This prototype switches from transparent to a translucent state (Figure 4.24) at 42°C, whilst its transmittance decreases from 90% to 20%. It is a technology that holds great potential for application in next generation of smart windows.

Holographic planar concentrators (HPC) are a concept of low concentration PV suitable for vertical façades. They consist on the arrangement of PV rows with a layer of holograms, patterns created in the material that diffract light. This layer directs light into a glass sheet where it continues to reflect internally until it reaches a PV stripe. The concentration goes up to 3 in the product described in (Rodríguez San Segundo and et al, 2016). A specific range of frequencies can also be selected and focused onto solar cells with higher spectral response at these frequencies, thus maximizing electricity conversion. In the same sense, heat-generating frequencies can be directed away from the PV cells, avoiding additional cooling requirements. Different holograms can be designed to focus light with different angle of incidence thus avoiding the need for sun tracking.

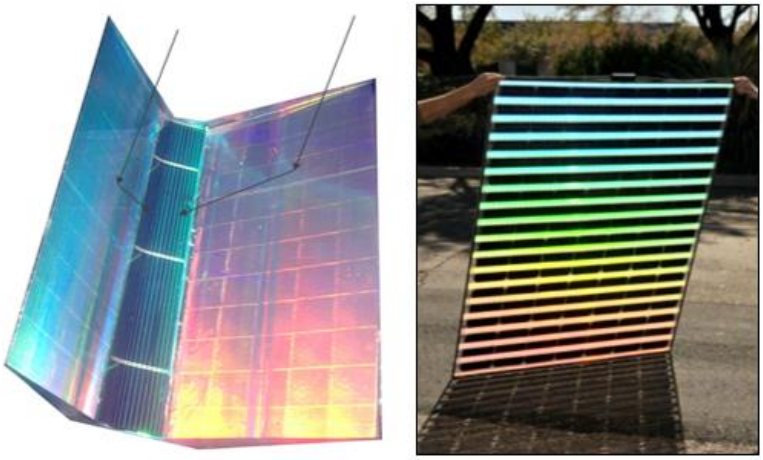

Figure 4.25 - Trackless holographic concentrating PV modules for buildings and urban furniture (Rodríguez San Segundo and et al, 2016) and the Holographic Planar Concentrator by Prism Solar Technologies, Inc.

It is worth noting that concentrating PV technologies, may not be a profitable option for implementation on vertical building surfaces. In the study presented in (Freitas and Brito, 2017b), it

was estimated that solar façades will generate relatively more electricity at higher latitude sites with high fraction of diffuse radiation. Thus, concentrating technologies that work generally based on the direct component of solar radiation, such as façade integrated concentrating PV, might have a very limited potential.

viii) Other

Many non-PV energy products can be harmoniously integrated on façade walls and accessories. In Figure 4.26, an example of façade and balcony applied solar thermal collectors with single-axis tracking (Sunaitec, 2014) is shown, and in Figure 4.27, the appearance of an innovative concrete-based product, called DysCrete, that produces electricity from solar radiation.

Figure 4.26 – Solar thermal collectors integrated in façade elements (Sunaitec, 2014).

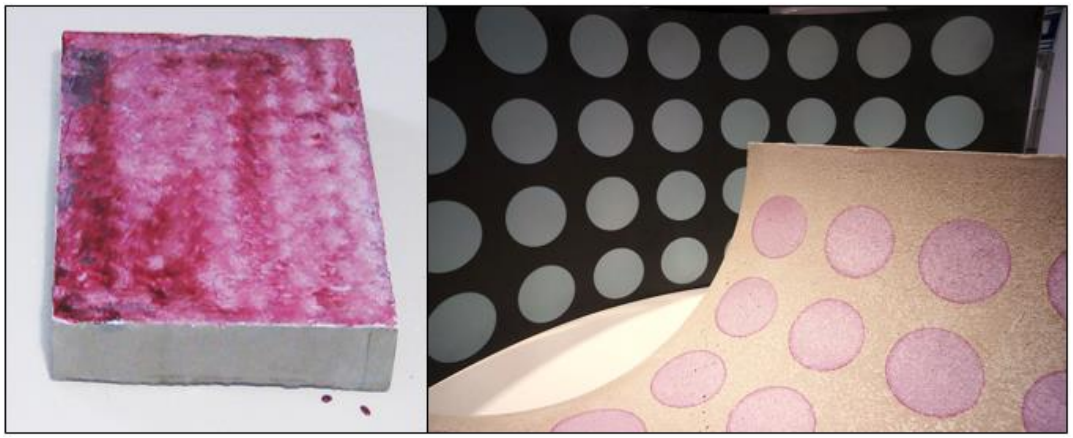

Figure 4.27 – Electricity generating dye-sensitized concrete prototypes with colour and bending properties (Building Art Invention, 2017).

DysCrete is based on the same underlying principles of DSSC and OPV, using organic dyes to absorb light and produce electricity through electrochemical reactions. A simple structure of functional layers combine to form a redox reaction coating that generates energy through an electrochemical process when exposed to light. The layer system can be tuned to specific wavebands of light, by adjusting the dye and electrolyte components (Building Art Invention, 2017). Two major advantages of dye-sensitized concrete is its relatively low production cost, since the spray-coating method can be performed in situ, and its response to diffuse light, which make it suited for manufacturing prefabricated concrete elements for building construction and new types of building façades.

Table 4.1 summarizes the relevant characteristics of the reviewed PV technologies, their suitable façade application and rough module/prototype average efficiency.

Table 4.1 – Summary of reviewed PV technologies for building façade applications.

Module	Main features	Façade application	Average efficiency [%]
c-Si	Dark blue, coloured/printed front glass, selective filter for white or tuned anti-reflection coating for colour; flat; simple shapes; lifetime around 25 years	Cold façade, warm façade, spandrel, accessories	17
a-Si	Dark blue or coloured/printed front glass; thin film; bendable; complex shapes	Cold façade, warm façade, spandrel, glazing, accessories, canopy	8
CIGS	Dark blue or black; bendable; thin film; complex shapes	Cold façade, warm façade, spandrel, accessories	13
Bifacial c-Si	Dark blue; semi-transparent; flat; simple shapes; both sides active	Warm façade, glazing, accessories, canopy	19
Dye, organic	Translucent red to green colour spectra; thin film; complex shapes; degradation under UV light	Spandrel, glazing, accessories, canopy	6
Photovoltachromic	Translucent blue to yellow	Glazing	4*
Reflective concentrator	Reflective, 2D compound parabolic or 3D total internal reflection elements with c-Si cells; semi-transparent; simple shapes	Spandrel, glazing	10
Lens concentrator	Fresnel lens with dual-axis tracking or rotational spheres with triple-junction cells; semi-transparent; re-use of thermal energy	Glazing, accessories	<35
Luminescent concentrator	Translucent large colour spectra or transparent to opaque; quantum dot, dye polymer or thermotropic layer with c-Si cells; translucent; flat, bendable or cylindrical; simple shapes; dye degradation under UV light	Glazing, accessories	4
Holographic concentrator	Diffracting material and internal reflection with c-Si cells	Spandrel, accessories	18

*cell

4.4 Solar radiation yield optimization

The fast development in PV technologies for building integration enables new questions such as which façade designs maximize the electricity generation in BIPV installations, in different locations in the world, and contribute to zero energy buildings (Scognamiglio and Røstvik, 2013). Although these questions call for the assessment of the energy performance of a façade integrated PV system in a holistic way, considering its thermal, daylighting and aesthetical functionalities - how it contributes to the passive design of a building. In this Section only the electricity generation functionality is addressed. Unconventional façade forms are studied and their PV potential estimated: first, the layout of walls and shadings is varied and its dimensions optimised for solar irradiation and PV yields; and, then, the same is done to balconies.

4.4.1 Wall and shading forms

To identify the most suitable façade designs for PV generation, six different layouts were modelled, motivated by existing architectonical deployment of PV in unusual features. In Figure 4.28, the integration of c-Si modules in horizontal louvers is visible in 1 and 3, whereas a vertical louver installation appears in 2 and 4. Pictures number 1 and 2 concern rotated louvers, and folded louvers in 2 and 4. The remainder, although non-PV, represent design possibilities for more complex integration of PV cells.

The layouts explored (Figure 4.29) consisted on horizontal (1) and vertical (2) rotated louvers, horizontal (3) and vertical (4) folded louvers and wall geometrical figures such as ellipsoids (5) and hexagonal pyramids (6). A seventh layout consisting on a flat vertical PV façade was also modelled for comparison with the more complex ones. The PV elements are integrated on an archetype of a representative apartment flat with 10x10x3m^3.

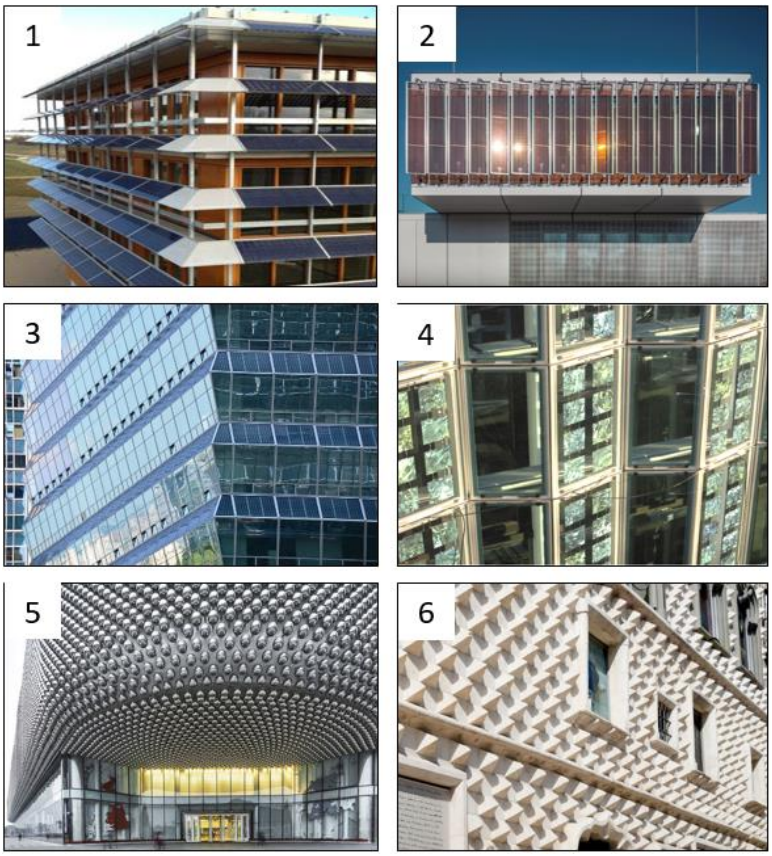

Figure 4.28 – Examples of functional and unconventional façade elements in: Belgium (IBA Technics, 2015) (1), Germany (Stylepark, 2016) (2), Korea (American Institute of Architects, 2015) (3), France (Vergne, 2011) (4), China (Frearson, 2013) (5) and Portugal (CML, 2017) (6). Geometries in pictures 5 and 6 are non-PV.

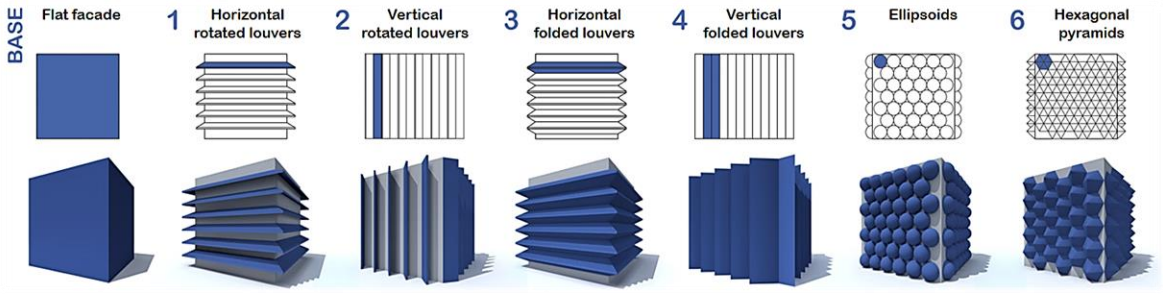

Figure 4.29 - Studied façade layouts: flat walls (base), horizontal and vertical rotated/folded louvers (2-4), wall ellipsoids (5) and wall pyramids (6). PV surfaces are coloured in blue.

No surrounding elements such as other buildings or trees were considered as shadow casters. Two locations with dissimilar weather conditions were analysed: Lisbon, a mid-latitude sunny city (38N), and Oslo (59N), an extreme latitude place with low solar resource. Only the east-, south- and west-facing façades were studied.

The CAD software Rhinoceros 3D and its integrated graphical algorithm editor Grasshopper were, again, employed for the parametric modelling of the façade layouts, as well as the plugin DIVA (version 3) (Jakubiec and Reinhart, 2011). Annual solar irradiation on the surfaces of interest was calculated (Figure 4.30) with a 0.1m^2 spatial resolution point grid, with a cumulative sky approach to reduce execution time.

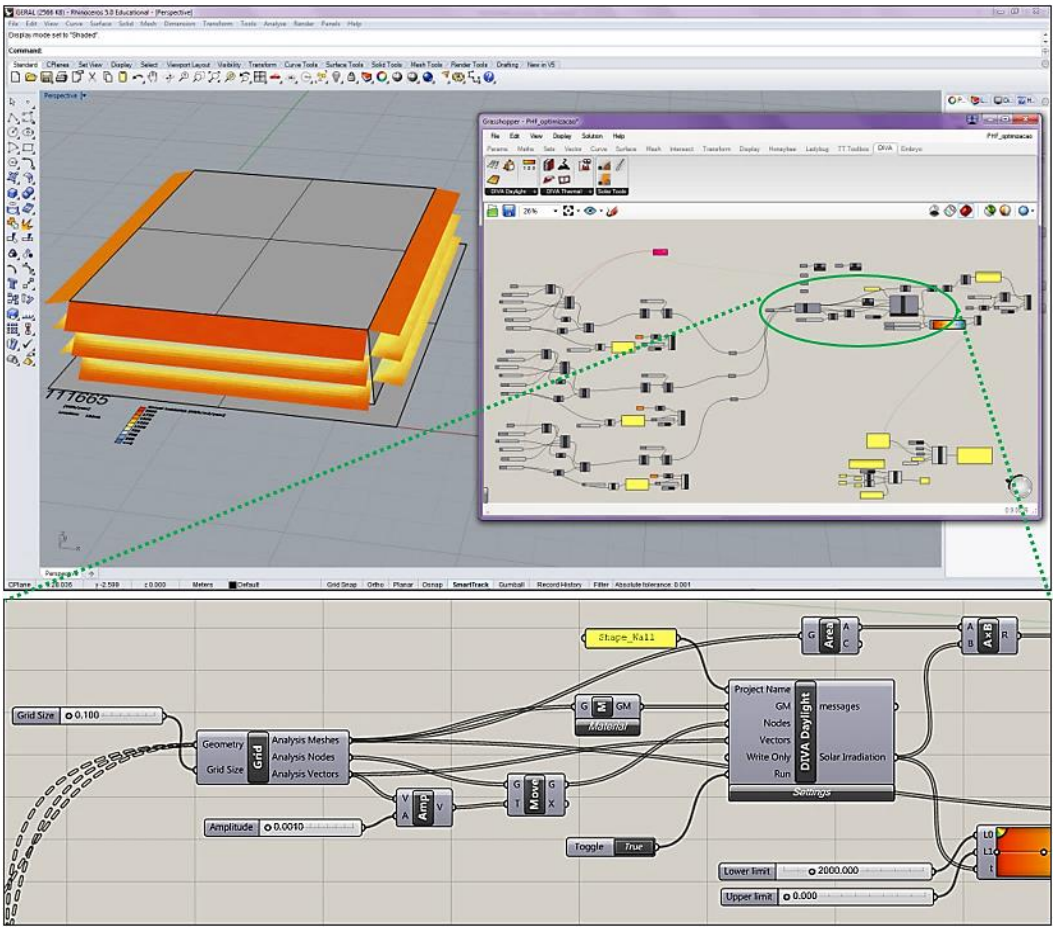

Figure 4.30 - Overall workflow view of the modelling tools (top) and a detail on the DIVA 3.0 solar irradiation components used (bottom).

The length of both horizontal and vertical rotated louvers was fixed at 1m and the rotational angle could vary from 0° (horizontal) to 90° (vertical). The maximum offset length of 1m was also set for the folded louvers, but the horizontal shearing angle could change, between -45° and 45°, as well as the number of elements. As for the other forms, a sub-group of elementary geometries was modelled, which would then populate the vertical façade according to its dimensions. In this case, both horizontal and vertical shearing angles could vary from -90° to 90° and the offset length between 0.1m and 1m. The changing parameters sliders were input to Galapagos (David Rutten, 2017), a Grasshopper component (Figure 4.31) for single-objective optimization.

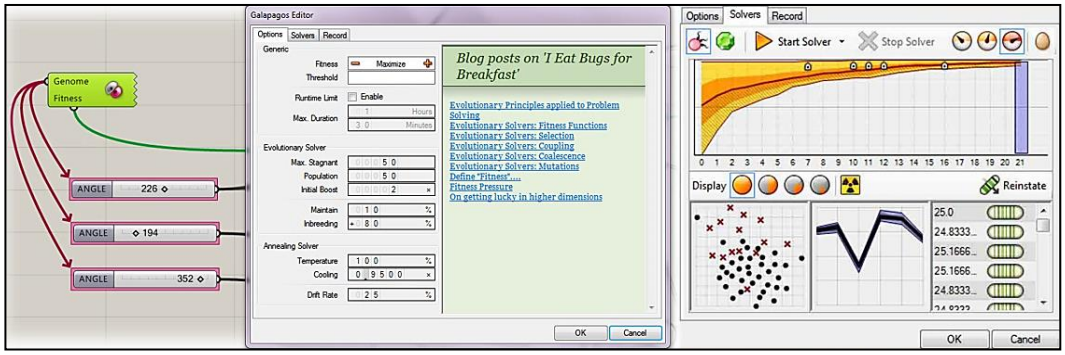

Figure 4.31 – Overview of the evolutionary optimization through the component Galapagos. In the leftmost side, the component is connected to the sliders that define the tilt angle of horizontal rotated louvers.

The evolutionary solver in Galapagos was used for the optimization. It starts by launching a number of random parameter combinations, which interact amongst themselves throughout several iterations until a parameter set (i.e. one possible optimal solution) is reached that maximizes, or minimizes, an objective[6]. The input parameters depend on the façade layout and can be the tilt angle, the number of elements, the offset length and the shearing angles, whilst the objective is always the maximization of yearly solar irradiation.
The optimization of rotated louvers in one façade involved only 1 parameter (3 for all façades), while the layouts with more complex features involved up to 4 parameters (12 for all façades). In the first case, 10 seconds were needed for the simulation of a single layout solution, which means that the whole optimization process (i.e. computation of all possible solutions throughout the iterations) took about 4 hours (using a machine with an Intel Core i7-3630QM CPU @ 2.40GHz). The latter took twice that time. For simplicity, given the high computation time during the optimization process, the PV generated electricity yields were estimated through multiplication of an average solar cell efficiency of 15% by the total annual solar irradiation of each façade layout. A performance ratio of 80% was also included to account for temperature losses due to building integration.
An overview of annual solar irradiation optimization for the six layouts is presented in Figure 4.32 to Figure 4.35. Left columns correspond to Lisbon and right columns to Oslo.

i) Flat wall

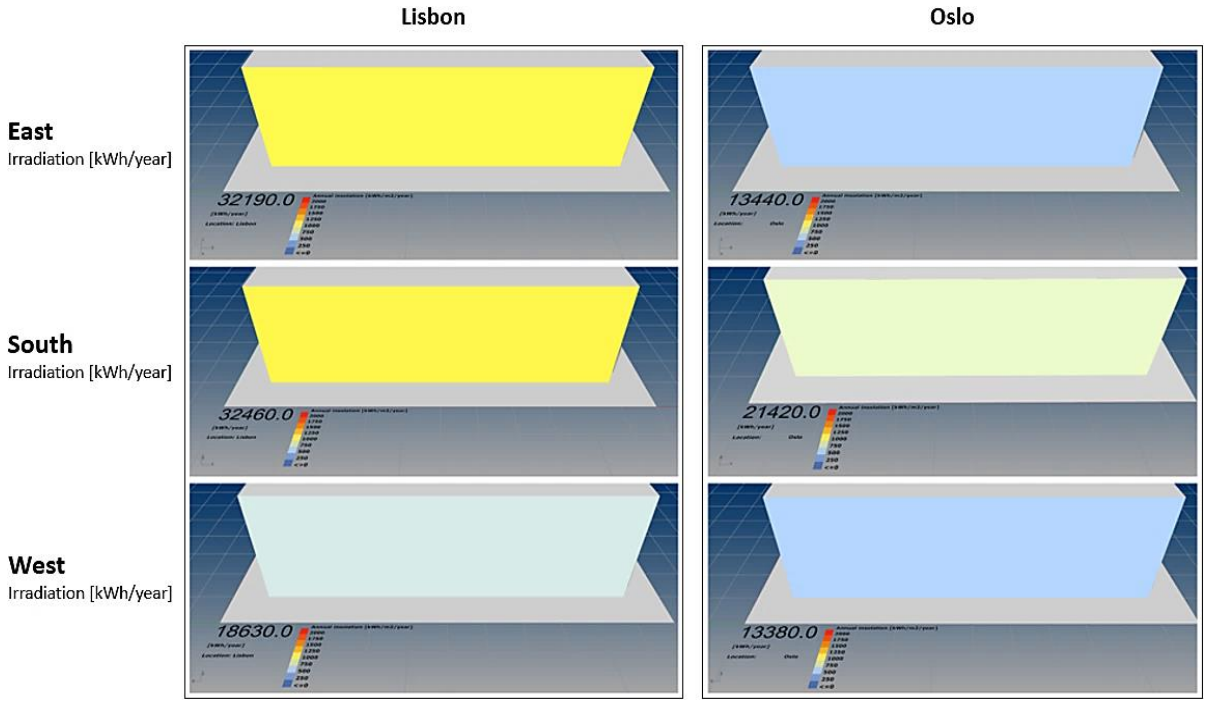

Figure 4.32 – Annual irradiation for the east- (top), south- (middle) and west-facing (bottom) vertical façades in Lisbon (left column) and Oslo (right column). The value in the lower left corner of each image corresponds to the total annual solar irradiation [kWh/year].

It can be inferred that there might be a predominance in aerosols and/or semi-cloudy or overcast conditions in the afternoon in Lisbon, given the similar irradiation in the façades facing east and south and lower levels in the one facing west.
Although the sun path is closer to the horizon in Oslo, thus favouring vertical surfaces, the annual number of sunlight hours is reduced. Consequently, the irradiation levels in Oslo are very low: the east-

[6] For a full discussion on evolutionary algorithms cf. sections 5.1 and 5.2, in Chapter 5.

facing façade reaches up to 42% of Lisbon's, the south-goes up to 66% and the west-facing up to 72%. Nevertheless, the optimization of façade structures might help enhancing the collection of solar radiation.

ii) Rotated louvers

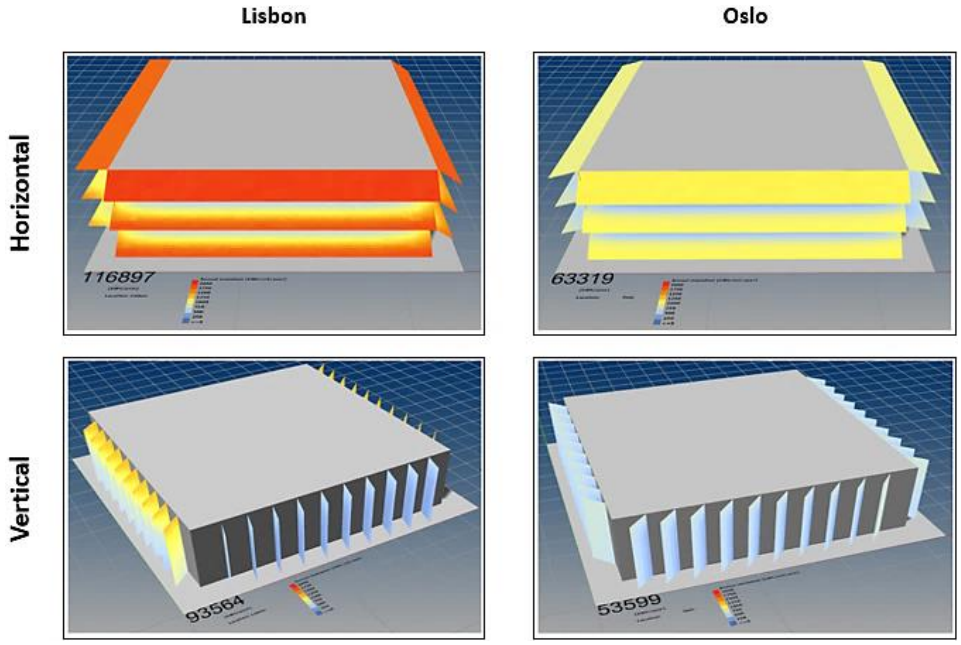

Figure 4.33 - Optimal E+S+W rotated louvers, for Lisbon (left column) and Oslo (right column).

The angles for horizontal rotated louvers are, respectively for Lisbon and Oslo, -33° and -8° on the east, -37° and -46° on the south and 0° and -14° on the west. In Lisbon, the optimum tilt of south facing louvers is identical to the latitude, even with mutual shadowing. As for the vertical louvers, with PV on both sides, the orientations are -43° and 45° on the east, 16° and 45° on the south and -41° and 45° on the west (positive/negative angle means to the right/left from the normal plane and ascending/descending). For Lisbon, the east façade louvers are tilted so that the morning high radiation is gathered, whilst south facing benefit both morning and afternoon and the west façade ones try to get more irradiation around noon, given the lower irradiation levels to the west. For Oslo, optimized louvers seem to be oriented towards solar radiation levels at around noon.

iii) Folded louvers

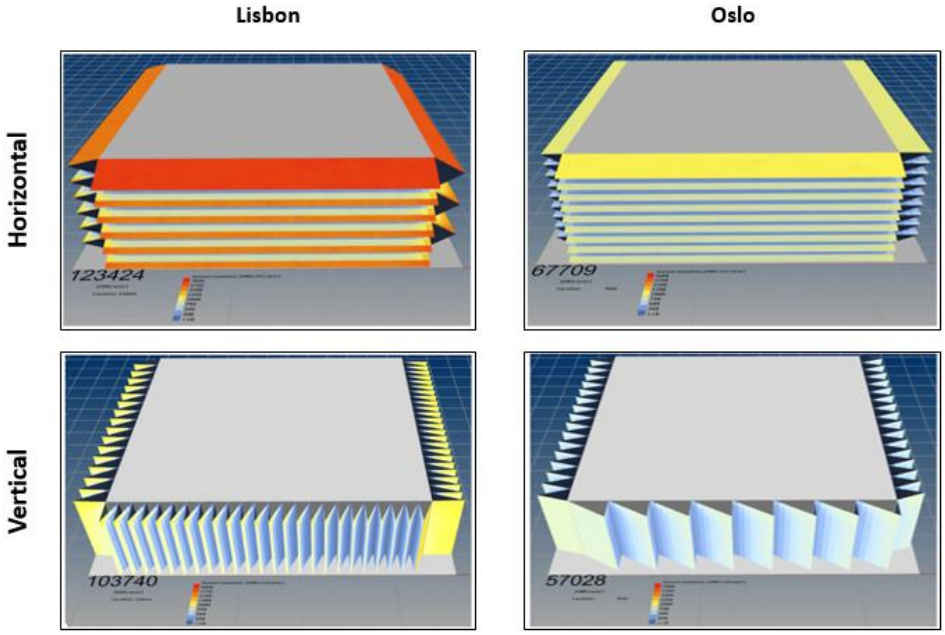

Figure 4.34 – Optimal E+S+W folded louvers, for Lisbon (left column) and Oslo (right column).

The optimization of horizontal and vertical folded louvers involved 3 parameters: the offset length, the number of elements and the shearing angle (in the x- and z-axis). Figure 4.34 shows the optimized results for horizontal and vertical layout. In this case, the louvers seem to adjust so that the faces that are closer to the façade edges gather most of the direct solar radiation coming from the south. Isotropic diffuse radiation might also contribute to the homogeneous levels of solar irradiation over the vertical folded louvers in Oslo.

Table 4.2 – Optimized parameters for E+S+W horizontal and vertical folded louvers in Lisbon and Oslo. Positive/negative angle means to the right/left from the normal plane and ascending/descending.

		Lisbon			**Oslo**		
		East	South	West	East	South	West
Horizontal	Length	1m	1m	1m	1m	0.9m	0.6m
	ZZ angle	-1°	72°	-7°	68°	70°	-72°
	Elements	3	6	6	9	9	9
Vertical	Length	1m	1m	1m	0.9m	0.8m	1m
	XX angle	57°	-57°	57°	-10°	86°	2°
	Elements	24	24	16	16	8	16

iv) Wall geometries

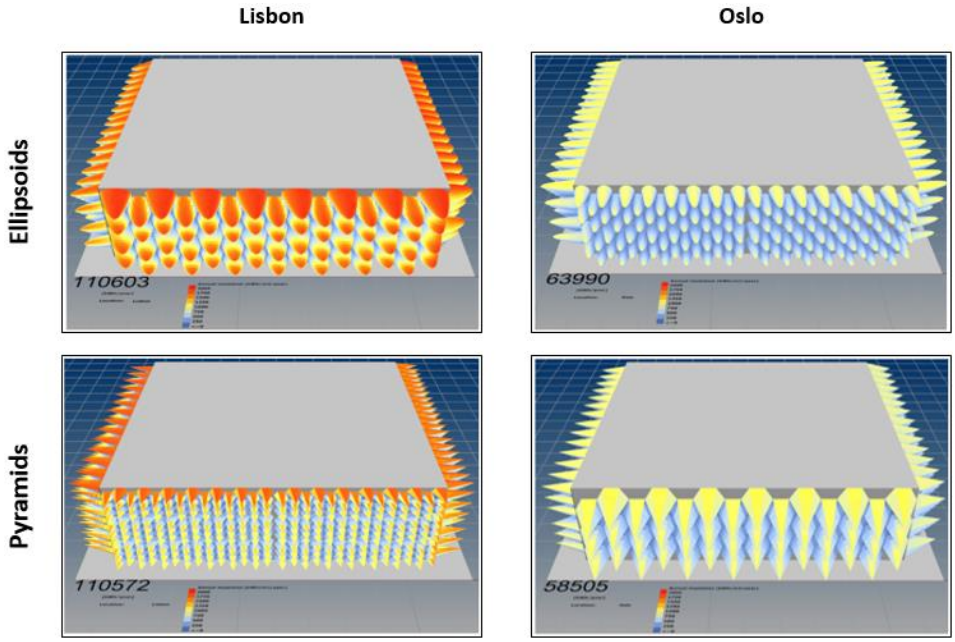

Figure 4.35 - Optimal E+S+W wall ellipsoids and hexagonal pyramids, for Lisbon (left column) and Oslo (right column).

As for the folded louvers, the ellipsoids and pyramids were optimized by varying their offset length, x- and z-axis shearing angles and number of elements Figure 4.35). The base radius of the geometries adapted to fit the façade dimensions according to the number of elements.
It is interesting to note that larger geometries were preferred over smaller ones, which might be due to larger solar irradiation on the top row elements. For Lisbon the total irradiation is similar for both ellipsoid and pyramid layouts, although the south-facing façade has smaller features. The opposite is observed for Oslo. The optimized geometries to the east and west, as observed in previous layouts, appear to stretch out of the façade to expose the maximum of surface area to the solar radiation around noon and diffuse radiation throughout the day.

Table 4.3 - Optimized parameters for E+S+W wall ellipsoids and hexagonal pyramids in Lisbon and Oslo. Positive/negative angle means to the right/left from the normal plane and ascending/descending.

		Lisbon			**Oslo**		
		East	South	West	East	South	West
Ellipsoids	Length	0.8m	1m	0.9m	1m	1m	1m
	XX angle	-11°	73°	36°	-64°	-15°	-29°
	ZZ angle	25°	51°	14°	13°	16°	47°
	Elements	64	64	128	128	128	128
Pyramids	Length	1m	0.8m	1m	1m	1m	1m
	XX angle	52°	-13°	-73°	-65°	-5°	-38°
	ZZ angle	-17°	-27°	-26°	-18°	0°	-6°
	Elements	252	252	252	84	42	168

Regarding the electricity generation from the different façade layouts, it can be observed that all optimized layouts perform better than the base scenario (Figure 4.36, top). Horizontal folded louvers (3) achieve about 50% (40%) higher yields for Lisbon (Oslo), followed by horizontal rotated louvers (1), ellipsoids (5), pyramids (6), vertical folded louvers (4) and vertical rotated louvers (2).

It can be said that the relative results are independent from location, since the increase/decrease across the six layouts is similar for both locations, ± 10%.

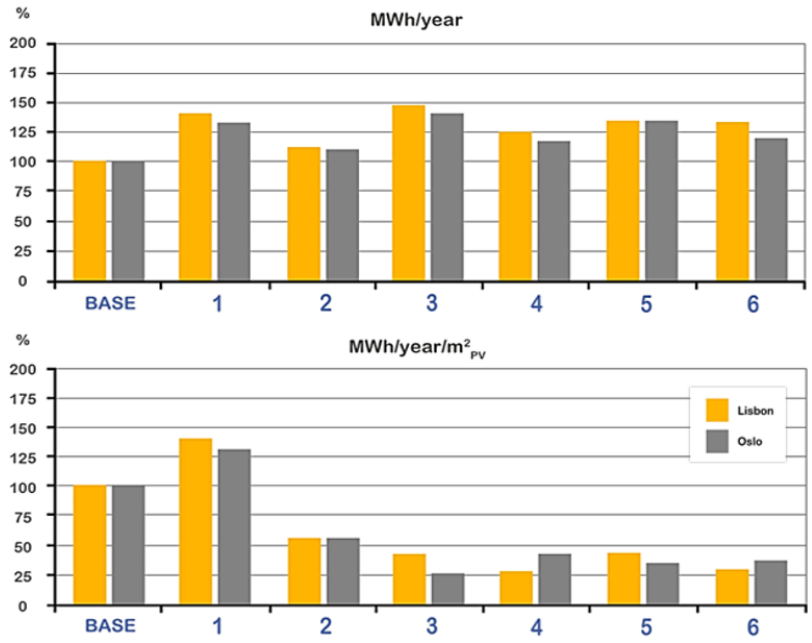

Figure 4.36 – Estimated annual electricity production from the different façades for Lisbon (yellow) and Oslo (grey): layout total (top) and density per PV occupied area (bottom). (100% means 10.0 MWh/year and 0.11 MWh/year/m^2_{PV}, for Lisbon, and 5.8 MWh/year and 0.06 MWh/year/m^2_{PV}, for Oslo) (Freitas and Brito, 2015).

However, the amount of solar cell area required to fill all the surfaces points to high investment costs of vertical louvers and wall geometries (Figure 4.36, bottom). PV integrated on horizontal rotated louvers, thus, achieves higher electricity yields while making use of the same area as a flat vertical façade integration.

The positive results from the layout with horizontal rotated louvers lead to further analysis for Lisbon. Southeast and southwest façade orientations were introduced and louver tilts optimized (Figure 4.37). The optimized layout, with southeast louvers tilted -42° and southwest -22°, gathers 12% more radiation than the configuration with horizontal louvers and achieves 70% of the performance of its optimal E+S+W equivalent while using 33% less PV area.

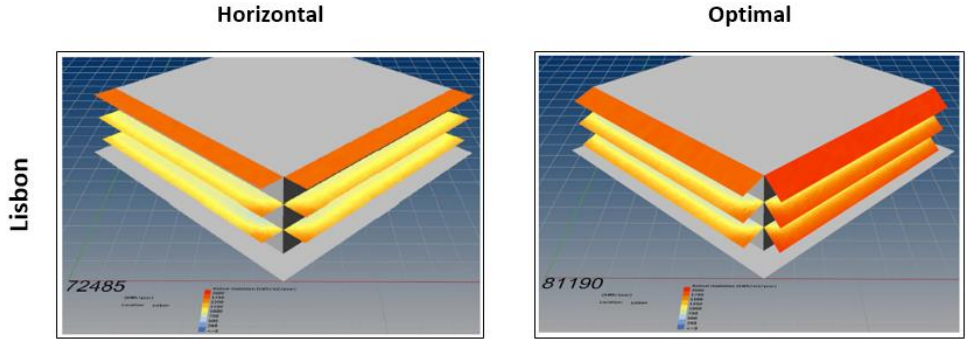

Figure 4.37 – Horizontal (left) and optimal (right) SE+SW rotated louvers, for Lisbon (Freitas and Brito, 2015).

Moreover, knowing that partial shading has a significant impact on the performance of BIPV systems (Catani et al., 2008), due to the non-linear response of PV modules under non-homogeneous solar irradiation, the changes in louver tilts under partial shading were investigated. At the time there was

no Grasshopper component for detailed PV cell simulation, hence an external routine was written in MatLab to estimate the output reductions also accounting for the angle of incidence response, according to Eq. (3.3).

This new analysis included the option for a semi-transparent PV for glazing surfaces, in between the louvers, with a conversion efficiency of around 8% (Pandey et al., 2016). The meteorological dataseries used are those of DIVA, which are used to calculate the hourly irradiance on arbitrary orientation and tilt according to Eq. (2.2) but disregarding the reflected component. For simplicity, a conservative approach was followed: i) the PV output from louvers is null when there is mutual shadow on the louvers (i.e. solar zenith is higher than the angle between sunscreen edge and the wall); ii) PV production from glazing is unaffected by shadows and high incidence angles (DSSC and OPV perform well under diffuse light); iii) diffuse radiation is isotropic; and iv) the upper louver is not PV enabled, as it might be part of the roof. Figure 4.38 illustrates the results.

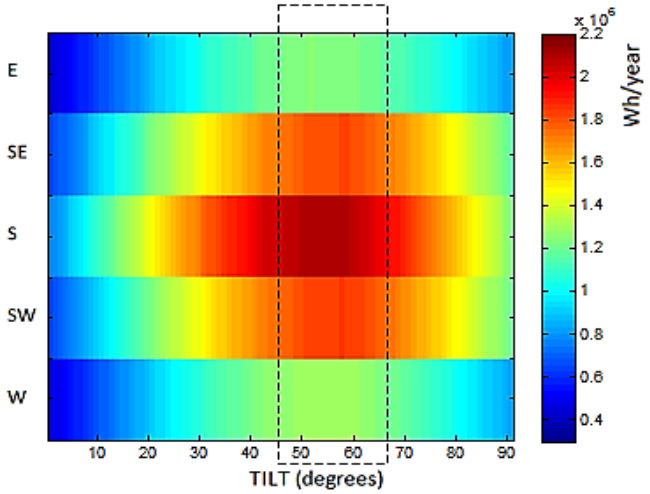

Figure 4.38 – Yearly irradiation for optimal louver tilt under conservative partial shading, for east-, southeast-, south-, southwest- and west-facing façades (Freitas and Brito, 2015).

The concern for partial shading produces significant impacts, with the most beneficial louver tilts changing from the range 0° - 42° to 50° - 60°. Assuming that PV output from louvers is null when there is mutual shading is too conservative and, thus, one would expect lower tilts in these conditions. However, it seems that isotropic diffuse radiation plays an important role in these configurations, as the systems seem to favour yield from semi-transparent PV integrated on the glazed rather than the production from conventional louver applied PV.

Other methodological limitations ought to be discussed. In one hand, losses due to temperature effects were simplistically included in the total PV yield estimates through an 80% performance ratio. Nevertheless, the objective functions in this study referred to total irradiation yields, instead of PV yields, thus one can expect the accuracy of the Radiance-based tool results to be high. On the other hand, when partial shading conditions were simulated outside DIVA, this accuracy was lost to a certain extent since multiple reflections could not be taken into account. Moreover, losses due to angle of incidence work differently as the PV module technology changes, which was not incorporated.

Façade layouts including other forms could have been modelled, such as in two more recent studies. In (Hachem and Elsayed, 2016), horizontal, vertical and dual saw-tooth, rectangular, truncated rectangular, triangular, truncated triangular, hexagonal and truncated hexagonal pyramid layouts are evaluated for a south-facing façade. An optimization is also conducted to increase the surface area for potential integration of PV without significantly compromising the heating and cooling loads of the building. In the same sense, (Stamatakis et al., 2016) optimized and evaluated thirteen PV shading devices deployed in a southern façade in a multi-criteria, both quantitatively and qualitatively: energy

optimization (heating–cooling–lighting loads) and user comfort (outdoor view–glare–aesthetic aspects). Curiously, the horizontal rotated louvers equivalent in this study was among the less suitable solutions, whilst brise solei (sunshades usually consisting of horizontal or vertical strips of wood, concrete, etc.) was the most proper. The reference to these studies helps underlining that the integration of PV into the building must be thoughtfully planned and address all the roles PV might play in the building functions, which, in short, exist to serve its occupants.

4.4.2 Balcony dimensions

Building façades are a mix of wall and window surfaces: elements that remain inside the building footprint. In this sense, a balcony represents not just a way of extending the floor area of an apartment but also of creating additional quality space, improving liveability. The opportunities for integration of solar PV cells on these accessories are immense, given their exposure to sunlight, variety of construction materials and design possibilities (Figure 4.39). The front surface of a balcony railing is not the sole interesting part. The reflectance properties of the surface materials that constitute and surround a balcony make them potential candidates for concentrating solar radiation on the rear surface as well and, therefore, increase overall electricity production from balcony integrated PV: whilst the front surface harvests plain direct radiation, the cells on the back surface make use of diffuse radiation, originated from the many reflective bounces of the sunrays hitting the nearby surfaces.

Figure 4.39 – Examples of balcony integration of PV in Finland (Solpros, 2003) (top left), Germany (Donahue, 2017) (top right), Austria (LOF Solar Corporation, 2010) (bottom left) and France (SADEV, 2015) (bottom right).

One particular configuration worth exploring is using bifacial PV. These modules feature front and rear efficiencies of 16% and 14% (Primsolar, 2016), respectively, and an 80% and 70% performance ratio to

approximate the observations reported in (Soria and Gerritsen, 2013)(Lindsay et al., 2015)(Reise and Schmid, 2015)(Comparotto et al., 2015). For simplicity, the detailed model of PV cells or the impacts of non-homogeneous irradiation were not included.

A balcony can be recessed, if its dimensions do not exceed the building footprint limits and its open space goes inwards, or precast, if the railing and the floor comes outwards the façade. Both configurations might work with PV, therefore the parametric modelling, using Rhinoceros 3D (McNeel, 2016) and Grasshopper (Davidson, 2017), and optimization was conducted considering 3 features: width, depth and offset. The depth and offset of the balcony could change between 0.1m and 2m, and the width from 1m to 7m in the course of the optimization process. A fixed balcony door height was set to 2.5m and the railing to 1m (Figure 4.40). The construction materials were also varied between white or generic walls and glazing or mirror for the door. These and the PV surface materials are described in Table 3.3.

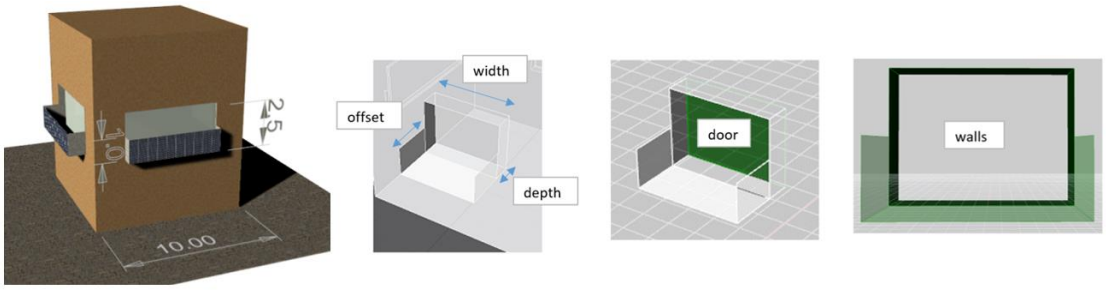

Figure 4.40 – Render view of archetype with PV modules on the balcony railings (left) and detail of the elements considered in the parametric modelling (right) (Freitas and Brito, 2016).

Solar radiation data series for three locations with dissimilar climate conditions were considered: Oslo (Norway, 59.95°N 10.75°E), Lisbon (Portugal, 38.71°N 9.14°W) and Abu Dhabi (United Arab Emirates, 24.47°N 54.37°E). As in the previous Sub-section, the plug-in DIVA (version 4.0) (SolemmaLLC, 2016) was used to compute yearly solar irradiation on both front and back surfaces of the balcony railings. A 0.1m^2 point grid resolution and cumulative sky approach were employed to reduce computation time, since the optimization procedures of intricate designs is time consuming. The component Galapagos was used for the optimization of balcony dimensions aiming for the maximization of PV generation density per module area (kWh/year/m^2).

For each location, two optimization routines were executed: first for east, south, west and north and then for south-east, -west, northeast, -west façade orientations. Only 2 ambient bounces were allowed for the Radiance simulations, but the optimal configuration was simulated a second time with 5 so that more meaningful estimates could be produced.

Table 4.4 shows the materials assigned to the different surfaces on the optimal balcony configurations.

Table 4.4 - Materials assigned to the optimized balcony designs (Freitas and Brito, 2016).

	ABU DHABI		LISBON		OSLO	
	Walls	Door	Walls	Door	Walls	Door
East	white	mirror	white	mirror	white	mirror
Southeast	white	mirror	white	mirror	generic	mirror
South	white	mirror	white	mirror	white	mirror
Southwest	generic	glazing	generic	glazing	generic	mirror
West	white	mirror	white	glazing	generic	mirror
Northwest	generic	mirror	generic	glazing	white	glazing
North	white	mirror	white	mirror	white	mirror
Northeast	white	glazing	white	glazing	generic	glazing

An example with a detailed overview of the solar irradiation over the optimal balcony railings is presented in Figure 4.41 for Lisbon. The depth, width and offset dimensions obtained for optimal configurations in the three locations are summarized in Figure 4.42.

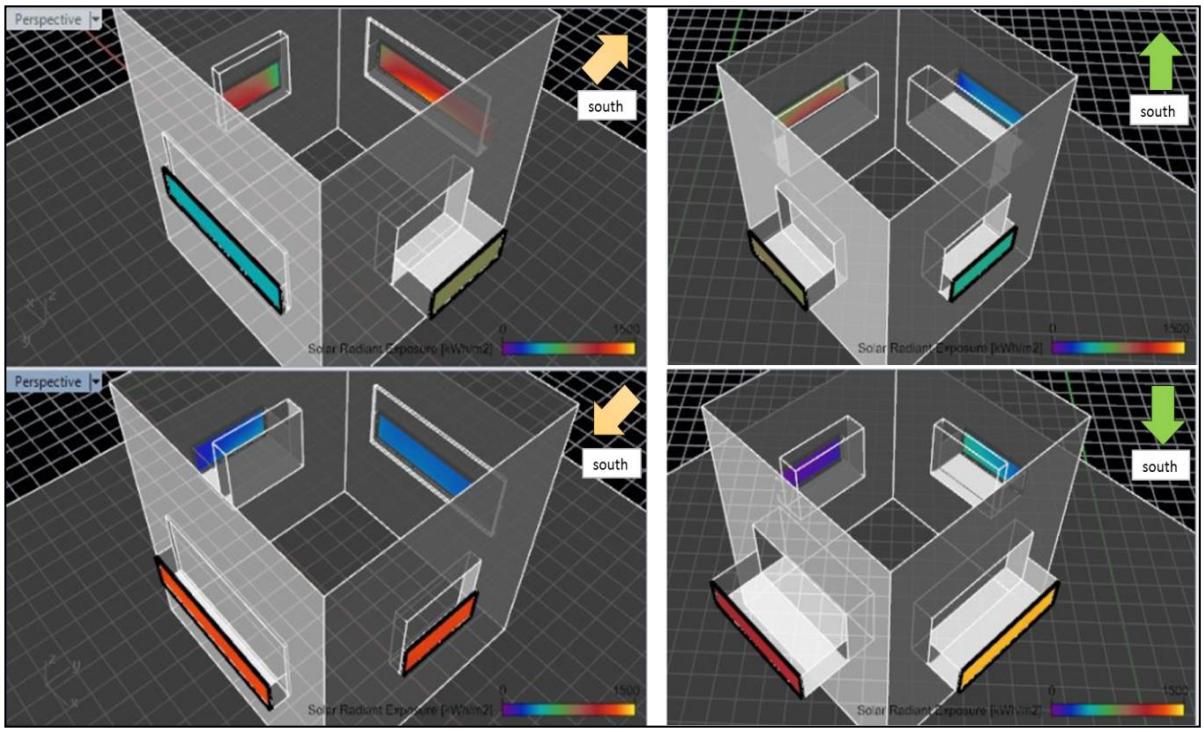

Figure 4.41 - Lisbon: annual solar irradiation in the front and back railing surfaces for the E+S+W+N (left) and NE+SE+SW+NW (right) configurations (Freitas and Brito, 2016).

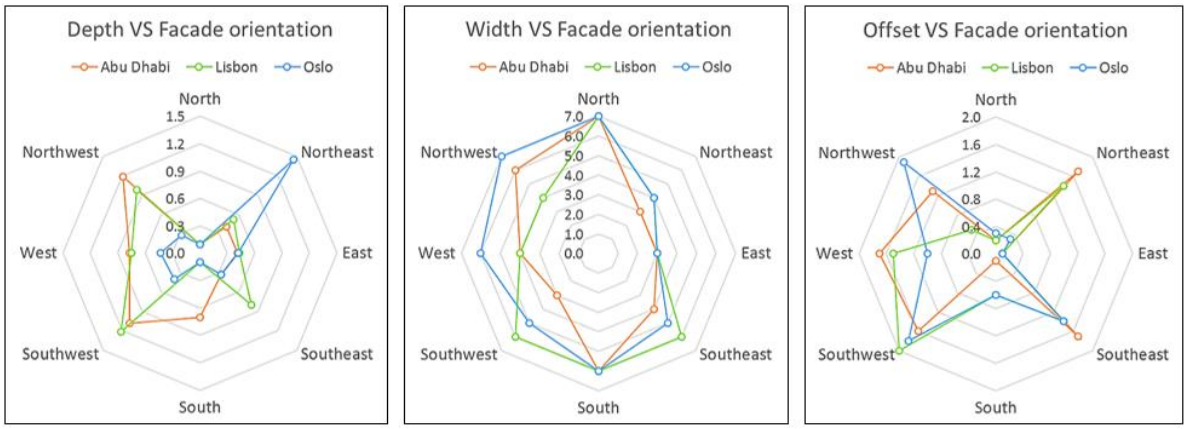

Figure 4.42 - Balcony depths, widths and offsets [m] obtained in the optimization process (Freitas and Brito, 2016).

There is a preference for deeper balconies on the South-West facing façades in Abu Dhabi and Lisbon, while for Oslo they should be less deep, except for those facing the Northeast. As for the width, all locations feature large widths in the North-West-South orientations, with Oslo featuring the widest ones. The offsets also show a clear leaning to small values for the South, East and North orientations, but higher values for the remainder.

Regarding the surface materials, as expected, high reflective materials such as white walls and mirrors are more predominant. However, the Southwest, Northwest and Northeast were attributed slightly less reflective materials. This would require more careful inspection, since there is no trivial way to

find if the interaction of light with surfaces really caused this preference, or if it relates to methodological limitations, such as the fact that neither a ray-tracing with 2 ambient bounces or an annual cumulative sky approach are ideal for studies of light interaction with intricate designs.
Comparing the PV generation density results for the optimized configurations in the three locations (Figure 4.43), it can be inferred that the most interesting façades for the integration of bifacial PV are all but those facing North in Abu Dhabi and facing West and North in Lisbon. In Oslo only the South-facing façades are attractive.

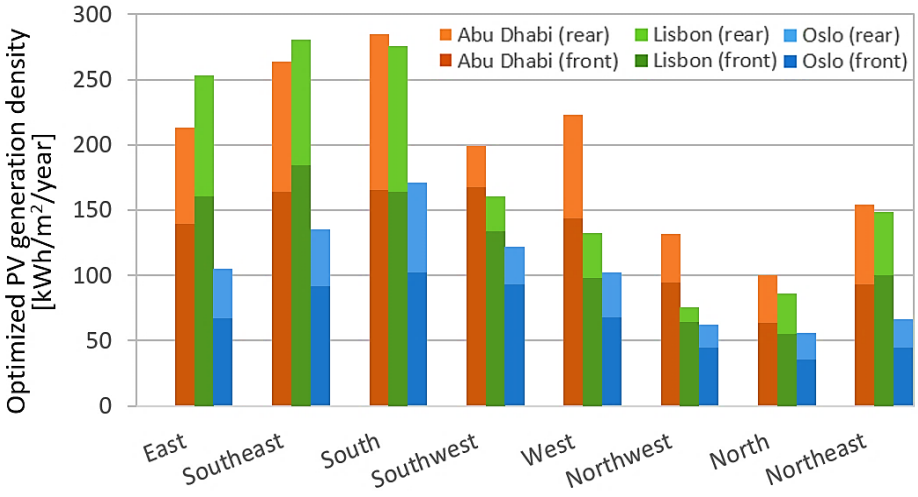

Figure 4.43 - Estimated front and rear PV generation density [kWh/m2/year] for each orientation and location with optimized balcony dimensions and materials (Freitas and Brito, 2016).

Although the increment in total incident radiation is, in general, very high even in orientations that would, at first, be discarded, it can be noted that some still do not encourage the application of bifacial PV panels since the contribution of the rear surface to the annual electricity produced is almost residual. This is the case of most north facing balconies that feature small offsets but large widths, where non-bifacial PV should be deployed instead.
In Abu Dhabi, a low-mid latitude city, the overall electricity production from balconies might achieve levels of up to 1MWh/year, given the high solar resource, but a complementary evaluation on the effects of high ambient temperatures on the PV yields under such conditions should be conducted. On the other hand, and as expected, Oslo's balcony configurations feature very low levels of PV generation, with wide north-facing balconies attempting to harvest most of the diffuse radiation. However, only the south-facing balcony reaches interesting electricity generation levels – almost the same as a balcony on a northeast-facing façade in Abu Dhabi. Concerning Lisbon's optimal solutions, the conclusions are similar to Abu Dhabi's, with a tendency for small east- and west-facing balconies and wide ones in the south and north façades.
To better understand the importance of the door, floor and wall materials as reflecting surfaces, from where the sun rays might bounce off and into the rear PV surface, poor reflecting materials were assigned to those elements on each of the optimized designs and recomputed the solar irradiation (Figure 4.44). As expected, the orientations that feature higher increments due to the use of bifacial PV modules are more sensitive to the use of materials with lower reflectivity. Three important effects can be pointed out: i) orientations such as East-South are highly direct sunlit, so a small change in reflectivity of surrounding materials causes significant changes; ii) orientations that feature low levels of direct irradiation mainly rely on the reflected diffuse irradiation, so poor reflective surfaces will also have a strong impact; and iii) light interacts differently when physical properties of surfaces vary, thus probably there are better geometries for this new set of balcony materials. The value of the optimization is highlighted, given that it leads to an average increment of around 20% (from 4% and

up to almost 30%) in comparison with a low reflective scenario, with the greater impact being observed in eastern/southern façade orientations.

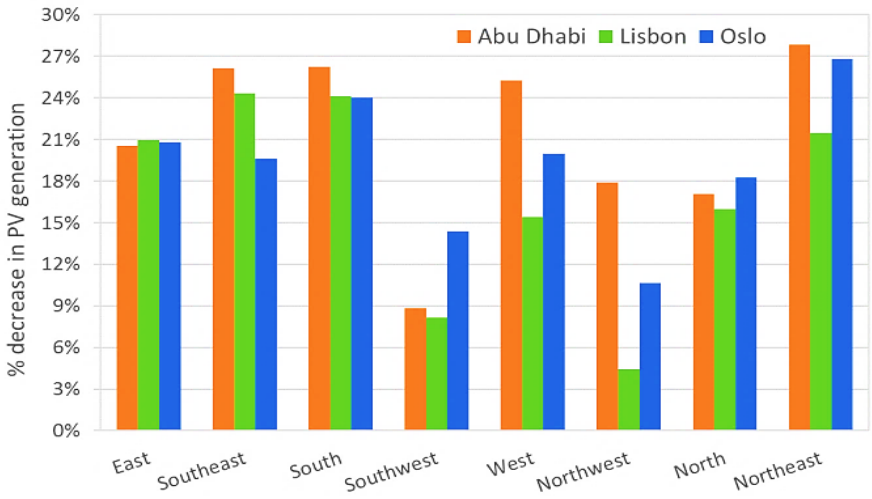

Figure 4.44 - Decrease in PV generation from the optimized dimensions and materials to the scenario with poor reflective materials.

Partial shading on the rear surface also causes a decrease in output, although it is slight given its lower irradiation and lower conversion efficiency. The presence of a person in the balcony is one example of a source of shading, which causes the radiation to interact differently with the surface materials and, thus, decrease the PV production of bifacial modules integrated in the railing. This impact was evaluated by including a human-like figure in the centre of the balcony floor (Figure 4.45), with a "dark blue jeans" material assigned to it (Vrhel, 2015). The radiation simulations were re-run, but, for simplicity, only for the optimized south facing balcony in Lisbon.

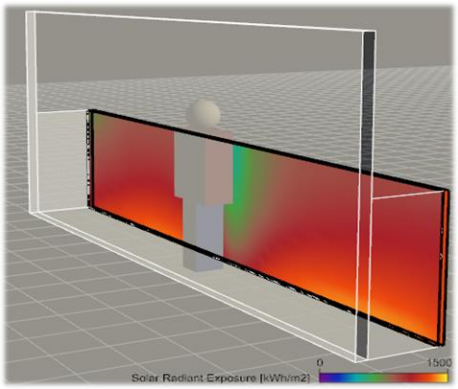

Figure 4.45 - Detail of the simulation with partial-shadow cast by a person standing in a south facing balcony, in Lisbon (Freitas and Brito, 2016).

Although Figure 4.45 depicts the cumulative annual irradiation in the rear surface of the bifacial module (and it would be more realistic to assume permanent furniture and not a person in the balcony), the significant impact that this new element adds to the inter-reflections between the balcony surfaces is clear. The estimated PV generation decreases about 5%.

Comparing the estimated bifacial PV yields with hypothetical monofacial yields in a flat PV wall (i.e. monofacial PV area equal to the balcony door area), the bifacial generation would only differ in average -15% from the monofacial scenario, ranging from +8% to -32% in Abu Dhabi, +7% to -49% in Lisbon and +6% to -39% in Oslo, in the whole set of orientations. Still, further analysis would provide

more insight into the impacts of partial-shading, that are expected to happen due to the nature of a space such as a balcony.

The optimization of the façades and balconies are missing: i) an objective function that concerns the investment costs; and ii) a more detailed PV module (including bypass diode) model that properly portrays their behaviour under partial shading. The former could be incorporated in a multi-optimization algorithm, considering different solar cell costs, while the second is more challenging given its computational requirements. The individual modelling of PV modules and cells is itself time consuming, thus calculating solar irradiation over each individual cell in an hourly time step might become infeasible for intricate façade layouts. Nevertheless, given Grasshopper scripting components (for Python, Visual Basic and C#, at least), it would be possible to do such analysis inside one single software. Otherwise, solar radiation results would have to be exported to an external numerical software, such as MatLab, where the electrical simulation would take place. The results would then influence the input for parametric modelling in the next iterations, and so on until the optimum is reached (Hofer et al., 2016). Dedicated tool suites can also be developed to thoroughly study BIPV (Eisenlohr et al., 2017).

4.5 Conclusion

The design opportunities for solar façades that arise from new BIPV technologies are considerably beyond what conventional modules have offered since the Mataro library PV installation, in 1995. Alongside this, architects have become more aware of the need for PV integration into their projects and the subsequent innovation it represents. On the other hand, the often anticipated economy of scale of BIPV is yet to be realized, due to its incompatibility with most standardized processes at the core of construction materials industries.

In the long future, it is likely that PV will become an intrinsic part of buildings, so that occupants will not notice it and the electricity production functionality will be as trivial as water supply pipe systems or electricity wiring. PV systems might as well take part in kinetic architecture and bring “life” to animated building skins.

However, in the meantime, there are opportunities for applications such as bifacial PV on balconies, flexible and colourful customized modules on shadings and spandrel areas on façades in different locations in the world. The optimal configurations must adapt towards optimized harvesting of both direct and diffuse solar radiation whilst keeping thermal comfort and the visual perception of occupants at satisfying levels.

Partial shading is particularly damaging for the performance for BIPV on façades and requires particular attention. These effects may be limited by the use of micro-inverters at the module level. At the string level, it leads to further optimization challenges to photovoltaic systems. This is the scope of the next chapter.

5. OPTIMIZATION OF PV INTERCONNECTIONS

Cityscapes are particularly diverse in terms of morphology. Buildings are the most predominant elements, but there are also trees and urban equipment interacting with solar radiation. These features can become shadow casters on BIPV systems, if they obstruct the path of the sun rays. Façade integrated PV, thus, has a greater probability of suffering output reductions due to partial shading. Such impact might be reduced if the placement of modules evades less sunlit areas but as shadow patterns are constantly morphing, it may not be straightforward to identify those places not contributing to overall yields during hours of greater solarshine. A holistic approach must be followed to tackle this particular challenge.

In this Chapter, an artificial intelligence technique is developed and tested for different building surfaces. The heuristic consists on a multi-objective genetic algorithm aiming at maximizing the PV production of a system and minimizing its costs through adequate placement and interconnections between PV modules. The solutions obtained are compared with conventional configurations and with micro inverter scenarios. [7]

5.1 Introduction

The project of a PV system is relatively straightforward for systems deployed in non-obstructed areas, which is the case for most non-urban PV plants. The process becomes more challenging when surfaces with intricate shadowing events are involved. In these circumstances, the incident solar radiation is non-uniformly distributed as continually varying shadow patterns. Since interconnection between PV modules is done in series (PV strings), a slight shadow cast on one of the cells is enough to significantly impact the production of the whole module and, consequently, the string. Due to changing sun-paths throughout the day and the year, achieving the most adequate string arrangement becomes a very complex problem of systems optimization.

Continuous and complex optimization problems, which cannot be fully represented and solved through well-defined mathematical formulations, can be solved through evolutionary strategies. When a problem has neither a unique and trivial solution or the search space is excessively large, or even if the problem has more than a single objective, Evolutionary Algorithms (Bäck et al., 1993) or Genetic Algorithms (GA) (Goldberg, 1989) are numerical modelling approaches that can be employed. The underlying principle of these algorithms is based on Darwin's principle of "survival of the fittest": populations of individuals are created and subjected to selection, recombination and mutation operators (or only mutation in the case of evolutionary algorithms), and the fittest individuals are passed on to the next generation.

A few studies regarding the optimization of PV systems using evolutionary strategies can be found in literature. For instance, (Kornelakis and Koutroulis, 2009) present a sizing optimization scheme for grid connected PV using a GA to maximize the total net profit of the systems. The study does not include losses associated to temperature or inverter-to-array sizing ratio, though, and the proposed technique is only suitable for pitched or flat rooftops where mounting frames can be used to adjust tilt angle. (Sulaiman et al., 2012) introduces evolutionary programming to optimize the installation area with the prerequisite of maximising the technical or economic performance. The algorithm is based on pre-

[7] Chapter includes work published on:
- Freitas, S., Serra, F., Brito, M.C. "PV layout optimization: string tiling using a multi-objective genetic algorithm". Solar Energy, Volume 118, Aug 2015, 562–574. DOI:10.1016/j.solener.2015.06.018
- Freitas, S., Serra, F., Brito, M.C., "Multi-objective genetic algorithm for the optimization of a PV system arrangement". ISES Solar World Congress, Nov 2015, Daegu, South Korea. DOI:10.18086/swc.2015.05.16

defined sets of inverters and PV modules that would optimize, technically or economically, the performance of a fixed system. Despite overcoming the limitations of previous approaches, the optimal sizing points to a unique very long PV string, not actually feasible in practice. Gómez-Lorente et al (Gómez-Lorente et al., 2012) study the optimization of sun tracking PV plants in terms of reducing associated electrical losses. Different evolutionary algorithms were compared, with random mutation featuring the fastest convergence and identical accuracy. Another GA was explored in (Shirzadi et al., 2014) to minimize the mismatch losses in PV arrays. In this purely theoretical study, the module parameters were statistically obtained from the technical specifications of a real PV module and the radiation set to be uniformly distributed, without shading effects. Nevertheless, the approach can be applied to a real system for arranging PV modules with known measured parameters.

The alternative approach to partial shading loss minimization would be the use of AC modules with micro inverters as an alternative to conventional string based systems (Kurokawa et al., 1997). Micro inverters provide system immunity to output power drop when a module is partially shaded, therefore avoiding mismatch losses. However, their installed power cost is higher and maintenance can be costly and hard to perform in urban environments, such as in vertical mounted systems, given that the micro inverters are usually attached to the back side of the module.

To overcome the limitations in the reviewed literature, and to provide an intelligent approach to optimized both technical and economic potentials of building deployed conventional PV systems, a multi-objective genetic algorithm (MOGA) was created. The tool and its tests will be described in the next Sections. This proposed approach aims to lessen partial shading impacts whilst avoiding movable parts or dynamic changes to the system. It is worth noting that smart and sophisticated, but far more complex and expensive, ways of avoiding partial shading impacts in real time have emerged. These techniques concern the electronical level of the modules and enable the PV strings to reconfigure their interconnections under whichever irradiance conditions. In (La Manna et al., 2014), dynamic string reconfiguration using switches is reviewed, concluding that it could be possible to design a reconfigurable interconnection device supporting different interconnection topologies, but costs would be increased due to the many switches involved and their limited lifetime.

5.2 Multi-Objective Genetic Algorithm

The technical and economic optimization of a PV system requires a multi-objective approach aiming simultaneously at the maximization of the energy yield (denoted E_{syst}) and minimization of the system costs (denoted C_{syst}). This approach produces non-dominated solutions, establishing several Pareto fronts or isocurves (Fonseca, 1995), i.e. groups of solutions optimizing both objectives and that are compared among each other based on their objective values (in this case, E_{syst} and C_{syst}). The solutions that belong to the outermost Pareto front dominate all the others, and so on. When comparing solutions in a specific Pareto front, it is impossible to find one solution that improves one condition without worsening the other. In the present study, an increase in PV production will lead to an increase in the system costs, and vice-versa. Hence, from a set of optimal Pareto solutions, one will be able to choose the strings' layout that better suits the project goals, in terms of the trade-off between yield and cost.

A non-dominated sorting genetic algorithm was scripted in MatLab environment. The algorithm mechanism and the operations involved in its execution are shown in Figure 5.1.

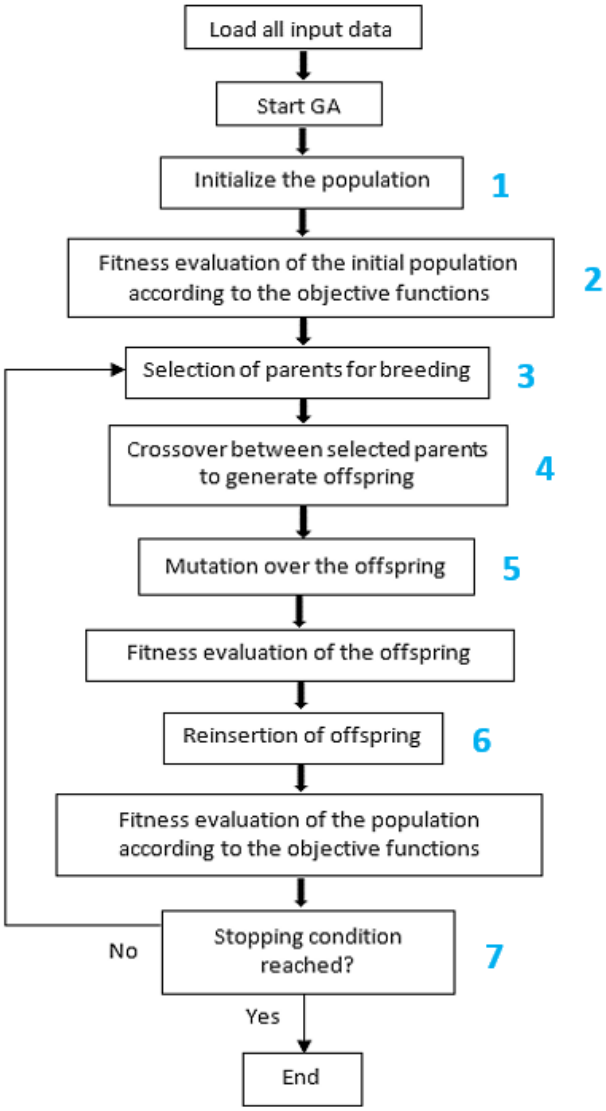

Figure 5.1 – Main scheme of the genetic algorithm (Freitas et al., 2015a).

All input data sets associated to the solar radiation data required for the energy yields and system costs calculations were previously stored in MatLab *.mat* matrices so that they can be loaded only once, when the code starts running. This eases the handling of large data sets and lowers the computational time.

The genetic algorithm per se starts afterwards. The first step concerns the creation of an initial population with an even number of candidate solutions. Each one can be addressed as an "individual" or "chromosome" and its information, i.e. its genes, is encoded in vector form.

5.2.1 Encoding

The encoding has to simultaneously describe the position of each module in the available positions of the rooftops or façades and inform on how it is connected to other modules. This was achieved through integer-valued encoding. The encoding strategy of a hypothetical arrangement is presented in Figure 5.2.

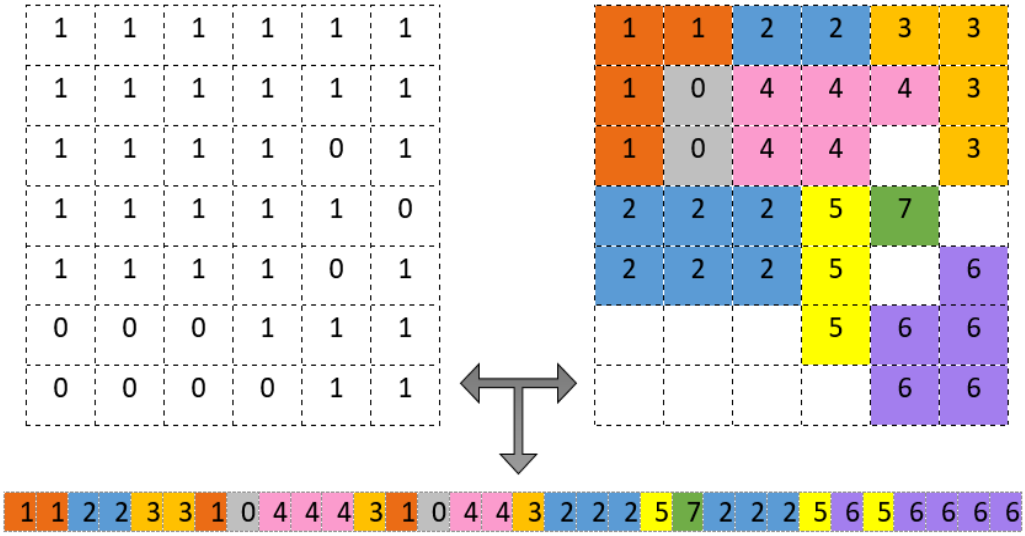

Figure 5.2 – Example of a chromosome and its encoding strategy. The different colours highlight different PV strings (Freitas et al., 2015a).

The binary matrix on the left-hand side of Figure 5.2 stores the available and unavailable positions for placing modules with ones and zeroes, respectively, and, given the spatial resolution of 1m^2, it provides height and width information. The coloured matrix on the right informs on the PV string layout, i.e. each colour/number identifies all modules belonging to different strings. In a row wise procedure, a module can be saved to a vector as an integer number corresponding to the "colour" of the string it belongs to. This vector only contains the information regarding the available positions (the 1s in the binary matrix), but when a zero is saved (e.g. 8th and 14th positions in the hypothetical chromosome) means that no module is assigned to that position, despite it is available. The decoding of the information is straightforward by checking back the available positions in the binary matrix.

The initial population of chromosomes is generated randomly on an attempt to cover the search space as widely as possible: a set of uniformly distributed pseudorandom positive integers, including zeroes, is generated to occupy all the genes, corresponding to a random distribution of modules per layout. The first generation of individuals is constrained to a maximum number of PV strings, limiting the variety of integers that can be generated throughout the generations (which could jeopardise convergence).

5.2.2 Fitness and objective functions

Having generated a set of chromosomes, a fitness value is calculated for each. Fitness values are constant and defined linearly or non-linearly according to the population size. In single objective optimization problems, the fitness is assigned based only on the chromosome ranking, but in multi-objective problems it is done according to a Pareto ranking. Several fronts are defined and all individuals in the same front share the same rank (Fonseca, 1995). In this case, the fitness values are assigned to all individuals according to their rank and, then, the averaged fitness value is given to all the individuals in the same front.

One of the objective functions consists on the maximization of the annual photovoltaic yield and the other objective function encompasses the minimization of the total system cost. However, while PV production and module costs may be directly computed from the positions of the modules and the strings they form, calculation of the costs include considering wiring and inverters requiring a different approach.

i) Annual PV yield

Knowing the solar irradiation distribution all over a surface for all n_t sun-hours of a typical meteorological year, hourly and annual accumulated PV electrical production can be estimated for all the modules in that surface. Similarly to the workflow in Sub-section 3.2.1, the ambient temperature data associated to the typical meteorological year in Lisbon is used to estimate hourly module operating temperature. The indexes in Eq. (3.2) underwent slight adaptations to the problem at hands:

$$T_{m,h} = T_{a,h} + \frac{T_{NOCT} - 20°C}{800\ Wm^{-2}} G_{tilted,h}\ , \tag{5.1}$$

where T_a is the ambient temperature [°C], $NOCT$ is a Nominal Operating Cell Temperature [°C], $G_{tilted,h}$ is the global irradiation on the tilted plane [Wh/m^2], the index m identifies a module in the layout and h is the time index [h]. Table 5.1 summarises the electrical parameters of a typical 1m^2 PV module (to match spatial resolution of the irradiance data) used in the optimization process.

Table 5.1 – Typical pc-Si module parameters.

PV module parameter	Value
V_{oc} [V]	32.6
I_{sc} [A]	5.51
V_{mp} [V]	23.5
I_{mp} [A]	4.95
V_{s_max} [V]	1000
T_{NOCT} [°C]	47
η_{ref} [%]	13
γ [%/°C]	-0.44
β [V/°C]	-0.0033
a_r	0.159

As PV modules are connected in series in a string and subjected to losses due to angle of incidence ($AL_{\alpha,h}$), the hourly expected energy yield of each PV string ($E_{s,h}$) can be estimated also adapting the indexes of Eq. (3.1) and (3.3) respectively to:

$$AL_{\alpha,h} = \frac{1 - e^{-\frac{\cos\theta_h}{a_r}}}{1 - e^{-\frac{1}{a_r}}}\ , \tag{5.2}$$

$$PV_{S,h} = min\left(P_{ref}\frac{Dir_{tilted,m,h}AL_{\alpha,t} + Dif_{tilted,m,h}}{G_{ref}}\left[1 + \gamma\left(T_{m,h} - T_{ref}\right)\right]\right) n_{m,S} A \eta_{i,s} PR\ , \tag{5.3}$$

where the index S identifies a PV string, the index p identifies the positions of the modules connected to string S, $n_{m,S}$ is the total number of modules belonging in string S, A = 1 is the individual module area, $\eta_{i,S}$ = 0.95 denotes an average efficiency of the inverter i connected to string s and PR = 80%. The $min()$ function, a conservative approach, reflects the fact that the current in a string is determined by its lowest producing module.

The PV production function of a layout with n_S strings can be defined by a summation of the hourly PV yield of all strings throughout the year:

$$E_{syst} = \sum_{S=1}^{n_S}\sum_{h=1}^{n_h} PV_{s,h}\ . \tag{5.4}$$

ii) Total system costs

The system costs of a PV layout comprise three components: the cost of the modules plus the copper wiring required to connect the modules in series and the inverters needed for the DC to AC output conversion. Neither maintenance or operating costs nor discount rates were taken into account. The system costs function defined by:

$$C_{syst} = C_m \sum_{s=1}^{n_s} n_{m,s} + \sum_{s=1}^{n_s} L_s C_s + \sum_{i=1}^{n_i} C_i \,, \tag{5.5}$$

where C_m = 150€/m^2 is the (fixed) cost of the PV module, L_s and C_s are the length and wire costs for string s, respectively, and C_i is the cost of each selected inverter. Thus, the first summation refers to the module cost, the second summation to the wiring cost and the third to the inverter costs.

The typical constraint of 3% for the maximum voltage drop allowed on a PV string was implemented. Taking the copper resistivity value as $2.112 \times 10^{-8}\Omega\mathrm{m}$, the adequate conductor section can be selected for each string by knowing the threshold current intensity that different sections can bear. Copper wire characteristics rated at 90°C (NFPA, 2014) were considered and respective average cable copper wire costs assumed according to their American Wire Gauge.

Apart from the conductor section, wiring costs are also dependent on the total length required to connect PV strings. Considering the linking node as the centre of a module, a mixed-integer linear optimization procedure was included to find the shortest linking path between modules in the same PV string. This is based on the determination of all possible link combinations between all nodes. Since the circuit must be closed, the obtained length must be multiplied by 2 in the case of linear strings (for instance, string 5 in Figure 5.2). Nonetheless, the wiring length that goes from the modules to the respective inverters is neglected and, thus, a single module string does not have wiring costs.

While cycling through the variety of PV strings in an individual, two equality constraints must be assured: the number of copper wire segments (links) is equal to the number of modules (nodes) and each node only has two links attached to it. Solutions with intersections or sub-circuits inside the same PV string undergo re-optimization until there is only one valid path linking all modules. The method presented in (MathWorks, 2014) was adapted to meet the objectives set.

In order to distribute the PV strings to a set of inverters, two main constraints must be applied to prevent unfeasible solutions: $N_{m,S}$ the maximum number of modules connected in a string, Eq. (5.6), and $N_{s,i}$ the maximum number of strings connected to a certain inverter i, Eq. (5.7).

$$N_{m,S} \leq \frac{min\left(V_{s_{max}}, V_{DC\ max,i}\right)}{V_{oc}[1 + \beta(-10 - 25)]}, \tag{5.6}$$

$$N_{s,i} \leq \frac{I_{DC\ max,i}}{1.25 I_{sc}}. \tag{5.7}$$

For each layout another linear optimization procedure is executed to select the inverters according to three inequality constraints. The first one relates to the maximum input DC voltage that each inverter can handle $V_{DC\ max}$, i.e. the maximum number of modules in a string linked to the inverter i must be lower than $N_{m,i}$, Eq. (5.6), and the second relates to the maximum input DC current allowed to the inverter $I_{DC\ max}$, which is controlled by the maximum defined by $N_{s,i}$, Eq. (5.7). Lastly the total power of the strings linked to the inverter must, of course, be lower than $P_{DC\ max}$. These properties of 13 inverter models are presented in Table 5.2, including the maximum values allowed for the DC input current $I_{DC\ max}$, the DC input voltage $V_{DC\ max}$, and the DC input power $P_{DC\ max}$, as well as prices. It

must be noted that assuming that the O&M costs are independent of the layout connection of the strings is an optimistic approach regarding the micro-inverter solution.

Table 5.2 - List of properties of 12 inverters and 1 micro-inverter. Prices retrieved between December 2014 and August 2015 from (Wholesale Solar, 2015)(CCL Componentes, 2014)(Energy Matters, 2014)(MG Solar, 2014).

Model	P_{nom} [kW]	$Avg\ Price$ [€]	$V_{DC\ max}$ [V]	$I_{DC\ max}$ [A]	$P_{DC\ max}$ [kW]
SMA micro	0.24	150	45	8.5	0.24
Fronius 1.5-1	1.5	893	420	13.3	1.5
Fronius 2.0-1	2	916	420	17.8	2
Fronius 2.5-1	2.5	938	420	16.6	2.5
Fronius 3.0-1	3	960	550	19.8	3
IG 20	1.8	832	500	14.3	2.70
IG 30	2.5	1220	500	19.0	3.60
IG 40	3.5	1568	500	29.4	5.5
Plus 60-V1	6	1474	600	27.5	6.32
Plus 70-V2	6.5	1579	600	30.0	6.88
Plus 80-V3	7	1678	600	32.0	7.36
Plus 100-V3	8	1693	600	37.1	8.43
Plus 120-V3	10	1885	600	46.2	10.59

The lower bound to this linear optimization is set to 0 while the upper bound is the number of available positions in the available surface area, so that the possibility of a layout where all strings are individual modules with the same inverter model can be covered. In case there is no convergence to a feasible inverter distribution, the inverter cost is set to infinity and thus the individual will be assigned the lowest fitness value.

Summarizing, the multi-objective optimization problem can be defined as:

i) maximize the system annual energy yield (E_{syst}) and minimize the system costs (C_{syst});

ii) aim at the PV layout with minimum cost for the energy produced in 25 years $\left(\frac{C_{syst}}{E_{syst}\times 25}\right)$, i.e. find $min\ f\left(E_{syst}, C_{syst}\right)$ in the 1st pareto front.

Subjected to the following constraints (case-study dependent):

- initial population $0 \leq s \leq 6$ (rooftop) or 4 (façade)
- $0 \leq G_{p,t} \leq 1000$ [Wh/m2]
- $0 \leq \theta_t \leq 90$ [°]
- $0 \leq T_{a,t} \leq 36$ [°C]
- $0 \leq n_{m,s} \leq 18$ (rooftop) or 32 (façade)
- $0 \leq E_{s,t}$ [Wh]
- $0 \leq C_m \leq n_{m,s} \times 150$ [€]
- $0 \leq L_s \leq min\ distance\left(n_{m,s}\right)$ [m]
- $0 \leq C_s \leq 26.486$ [€/m]
- $0 \leq C_i \leq 1885$ [€]

5.2.3 Selection

After all the population has been ranked according to the fitness values of its individuals, they are probabilistically selected for recombination, i.e. breeding. The selection of parents is done through a roulette wheel algorithm. This method is also known as stochastic sampling with replacement, which means that the selection probability of each individual is attributed according to its fitness value, therefore, the fittest have higher probability of being chosen for recombination in random trials. A selective pressure of 2 was used to enhance the probability of selection of the fittest individual comparing to the average probability of selection of the population.

5.2.4 Crossover

To ease the computation time while keeping high variety of genetic information, the recombination is done after decoding the selected chromosomes from integer to binary values, as only parts of the individuals are exchanged between them. The probability of crossover was set to 100%, meaning that all selected parents will produce offspring. Multi-point crossover is employed, i.e. two crossover positions in the chromosome are selected uniformly at random and the variables are exchanged between the individuals between these points, producing two offspring.

5.2.5 Mutation

Resulting offspring has a chance of suffering mutation. The mutation algorithm is also binary-based and consists on uniformly altering the chromosomes at random by flipping variable values, i.e. a 0 becomes a 1 and vice-versa. The rate of mutation is 3%, since the binary crossover already introduces high variety to the offspring.

5.2.6 Reinsertion

Before inserting the offspring into the present population, the chromosomes are once again encoded from binary to integer values. Their fitness values are calculated and the offspring is ranked afterwards. Two reinsertion algorithms are implemented: whereas one states that only a percentage of the fittest offspring are inserted into the population by replacing the least fit parents, the other does the same but reinserts random offspring. The number of individuals is kept constant throughout the generations by eliminating the same number of parents as the number of inserted offspring.

5.2.7 Stopping condition

One from two conditions can stop the algorithm run. One concerns the maximum number of generations (Table 5.3) and the other relates to the objective functions: as the population is ranked in Pareto fronts, a stopping condition can be set by finding, in each generation, the individual that holds the minimum estimated levelized cost of electricity production [€/kWh] (in 25 years). Comparing this value from one generation to the other, if a lower €/kWh is found in the previous generation the value is stored. The generational loop stops whenever the fourth minimum cost of energy €/kWh that prevails during, at least, 100 generations, is found. Yet, as it might be convenient to monitor the several variables evolved in the course of the optimization process, in case this ratio remains unchanged for too many generations the algorithm can be stopped manually.

Table 5.3 – Parameter specifications for the GA used in the rooftop and façade case-studies.

Parameters	Rooftops	Façades
Population size	100	50
Max generations	250	400
Crossover type	Binary	Binary
Crossover points	2	2
Crossover probability	100%	100%
Mutation probability	3%	2%
Selection type	Roulette wheel	Roulette wheel
Selective pressure	2	2
Reinsertion type	Random	Elitism
Reinsertion percentage	30%	10%

The parameters in Table 5.3 are more severe for façade studies, since the genes were larger than in the rooftop case, in an attempt to make the population converge faster.

5.3 Case-studies

The developed MOGA relies on irradiation data to investigate the module sittings and string interconnections maximizing yearly electricity generation and minimizing investment costs. Two case studies were addressed to test the algorithm against conventional and micro-inverter arrangements.

i) Comparison with conventional arrangements

A dummy synthetic rooftop and ready results from the SOL model (Redweik et al., 2013) concerning the study of Lisbon areas B and C from sub-section 3.2.2, were used to estimate hourly electricity production from the surfaces of interest.

Concerning the synthetic DSM, it was built assuming the average elevation for the city of Lisbon, from which a 4x8m^2 rooftop case-study (here on designated as “rooftop 1”), the circled one in Figure 5.3, underwent irradiation calculations. The tilted roofs are facing south.

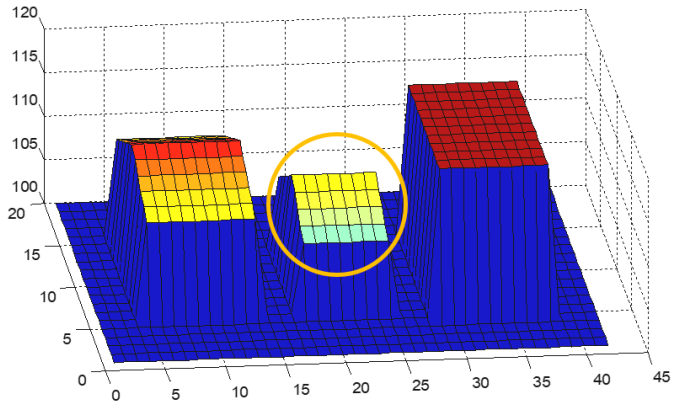

Figure 5.3 - Rooftop 1 (yellow circle) and surroundings coloured according to the height. The ground height of 100m corresponds to the average of the city of Lisbon (Freitas et al., 2015a).

The adjacent buildings were created to cast very well defined and predictable shadow patterns: in the morning the building to the right is responsible for casting a shadow on the middle rooftop while the left one obstructs most of the sunlight in the later hours of the day (Figure 5.4). The original rooftop model has a defined area of 4x8m^2 but the edges of the roof were excluded for realism.

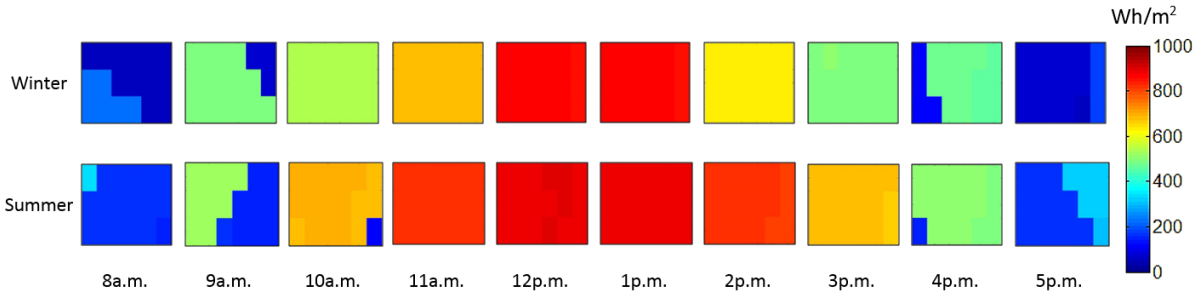

Figure 5.4 - Orthogonal view of the hourly irradiation [Wh/m^2] in rooftop 1, for a winter (top row) and a summer (bottom row) day. (Freitas et al., 2015a).

The other case study, denoted "façade 1", refers to the façade marked with the yellow sector in Figure 5.5. Hourly irradiation was calculated using the SOL model (the building is located in area C described in sub-section 3.2.2). The wall is facing south-southeast and has an area of around 7x6m^2. Due to the existence of stairs, windows and other structures, not all positions are suitable for the placement of PV modules. Thus, when extracting the irradiation values of this façade, a first constraint on the area availability is imposed. In Figure 5.6, hourly irradiation levels in the façade are presented for a summer and a winter day. The unavailable areas for PV modules are coloured in white.

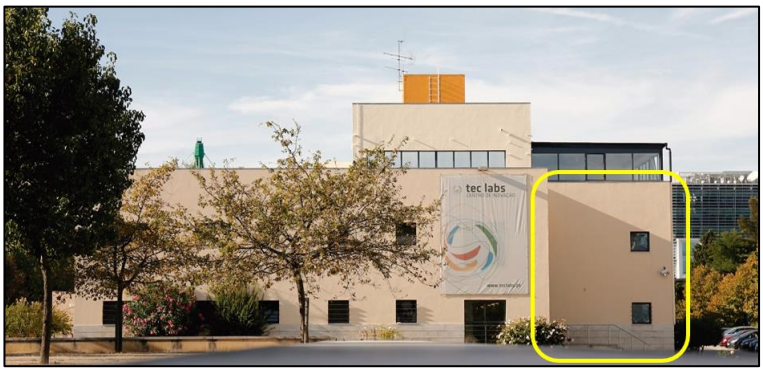

Figure 5.5 – Photograph of an afternoon shadow cast on façade 1 (portion signed in yellow).

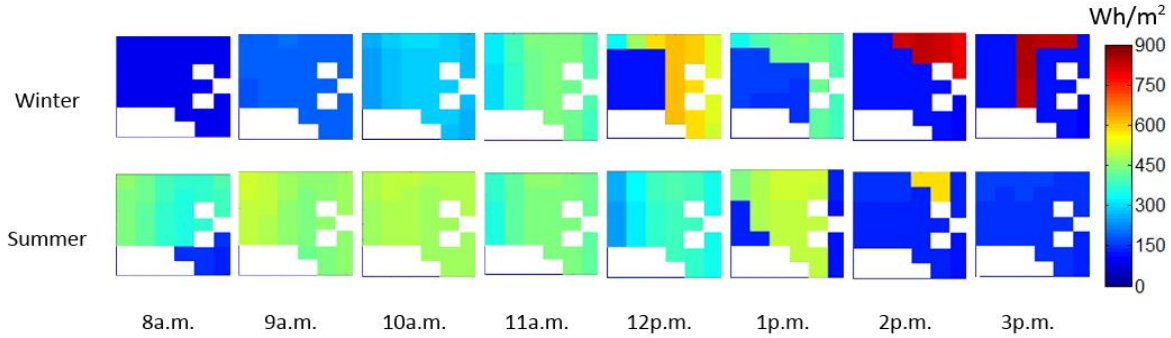

Figure 5.6 – Orthogonal view of the hourly irradiation [Wh/m^2] in façade 1, for a winter (top row) and a summer (bottom row) day. White denotes excluded positions (Freitas et al., 2015a).

Higher levels of irradiation are visible in the upper row, reaching global irradiation values around 900Wh/m^2 in the afternoon in winter. Different shadow patterns are also evident, since the incidence angles of the sunlight change during the day and the year. Irradiation patterns near the right edge of the building, in particularly at 3pm in the winter day is probably an artefact of the simulation. This irradiation data was used as is, without any corrections, to further test the robustness of the MOGA.

ii) Comparison with micro-inverter arrangements

The other case studies comprise a rooftop and a façade in area B, described in Sub-section 3.2.2. These will be denoted as “rooftop 2” and “façade 2”. The first is a 3x6m^2 south-facing portion of a rooftop, marked in Figure 5.7, left. The second is also marked in yellow and it is a 7x5m^2 portion of a façade facing west.

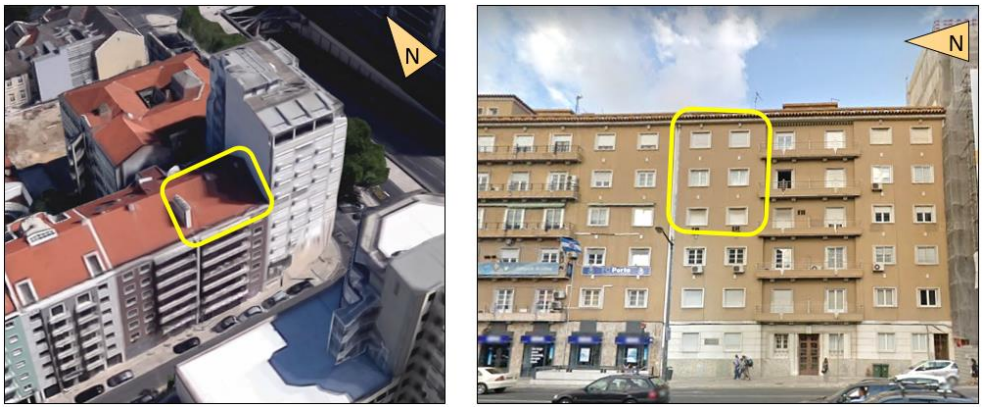

Figure 5.7 - Bird’s eye perspective to rooftop 2 (left) and street view of façade 2 (right), retrieved from Google Earth at approximately 38.7398959, -9.1463554.

5.4 Results

The optimal results for the 4 case-studies will be described in this Section. Rooftop 1 and façade 1 will be compared with conventional sitting scenarios, whereas rooftop 2 and façade 2 will be compared against micro-inverter solutions.

5.4.1 Comparison with conventional arrangement

The layouts shown in Figure 5.8 represent conventional interconnections, the first is a line wise and the other a column wise placement PV strings.

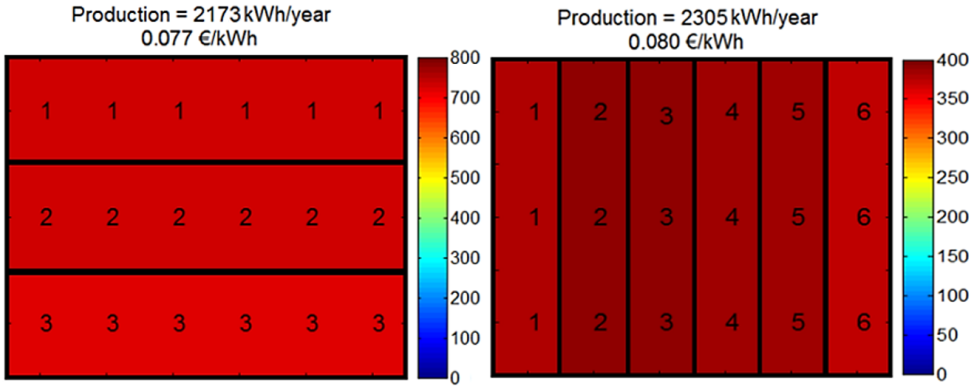

Figure 5.8 – Yearly total PV production per string of a typical line wise (left) and a column wise (right) distribution of PV strings, for rooftop 1. Note the different colour scale values in the two graphs (Freitas et al., 2015a).

The conventional arrangements in rooftop 1 feature high PV production, with similar annual yields from all the strings. The system costs are slightly higher in the second layout due to the chosen inverters, although a column wise placement allows slightly higher production.

One possible optimal solution for this case-study, with similar electricity yields but 20% lower cost of energy, was reached within 70 generations (Figure 5.9, left), with the MOGA set to random reinsertion at a rate of 30%, a population of 100 individuals and a maximum of 6 PV strings per layout in the initial population.

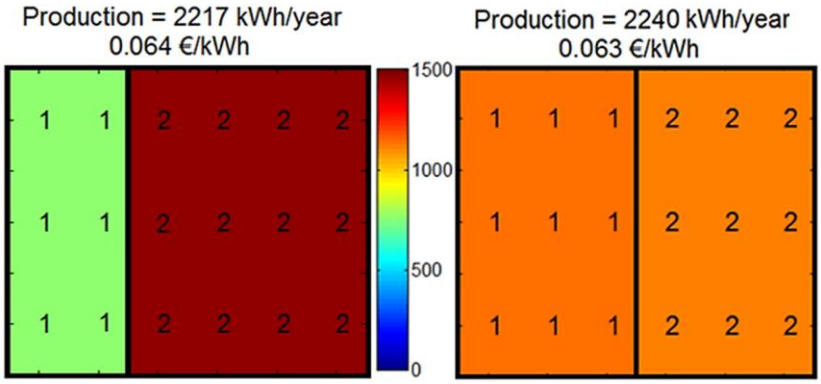

Figure 5.9 – Rooftop 1 layout with lowest cost of electricity achieved in the 70th (left) and 250th (right) generations (Freitas et al., 2015a).

Reviewed literature recommended a higher number of generations (above 200, at least), thus, despite having found a possible optimal solution in the 70th generation, the optimization process continued until there were no longer significant changes in the best solution (Figure 5.9, right).
Figure 5.10 presents an overview of the evolution of the layouts across the generations. As expected, the cost variables tend to become lower as the electricity production variables increase (blue lines). Initially, the population is largely dispersed and the best solution (red lines) jumps arbitrarily along the generations. From the 70th to the 250th generation, the best solutions somehow steadied, although a slight disturbance around the 130th generation is visible (possibly the evasion of a local minimum). The execution of the algorithm was manually stopped in this case, given the convergence in the Cost of Energy chart (Figure 5.10 ,top) after the 150th generation. In fact, from the 70th to the last generation there were no significant improvements, making the achieved solution a possible absolute minimum.

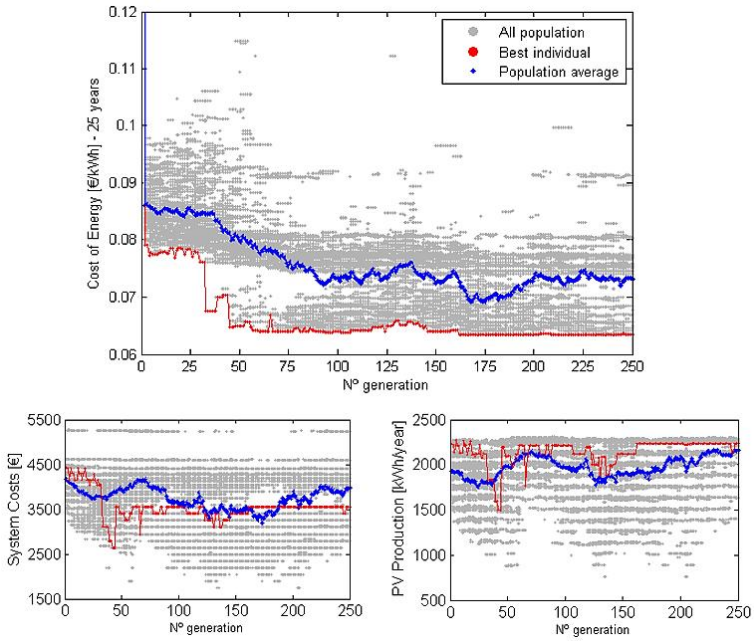

Figure 5.10 – Charts with the overview of the relevant Cost and Energy variables during the optimization process, for rooftop 1 (Freitas et al., 2015a).

The Pareto curve analysis (each one was assigned a number according to the dominance order, in Figure 5.11) for the initial and last generation shows the widening of the search space and a successful optimization process. Each of these solutions is itself an optimum according to the multi-objective function criteria. The final selection of the layout configuration to implement in the system project can be based on these results plus other conditions such as a minimum cost of electricity (€/kWh), a minimum PV production level, a maximum cost level, etc.

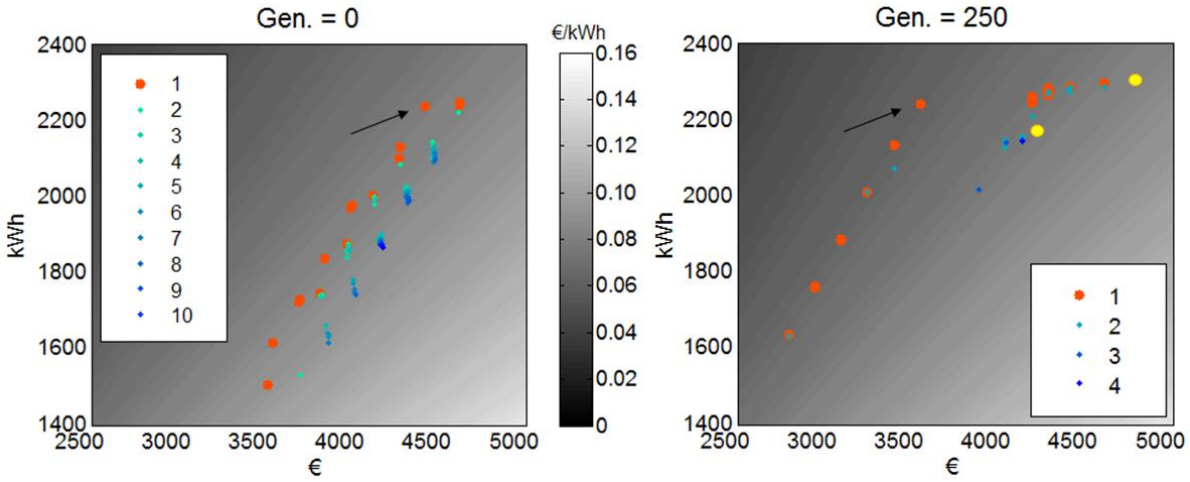

Figure 5.11 - Comparison between the Pareto fronts from the initial (left) and 250th (right) generations, for rooftop 1. The arrow points the individual with minimum cost of energy [€/kWh] (i.e. 0.063€/kWh and 2240kWh/year) and the yellow circles mark the location of the conventional solutions presented in Figure 5.8 (i.e. 0.077€/kWh and 2173kWh/year; 0.080€/kWh and 2305kWh/year). Background shading marks different levels of €/kWh (Freitas et al., 2015a).

As for façade 1, the conventional layout of columnar strings (Figure 5.12) resulted in limited energy production and high cost of energy.

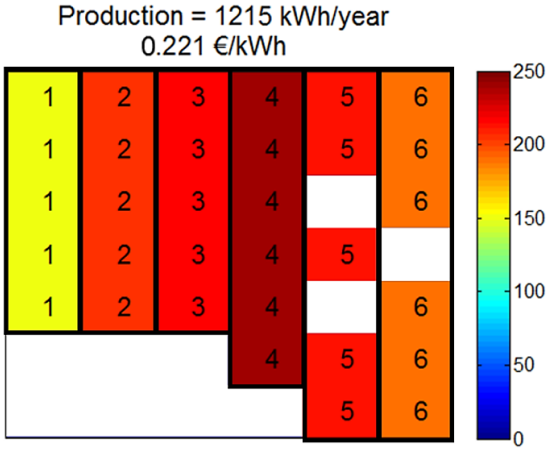

Figure 5.12 – Yearly total PV production per string of a typical column wise distribution of PV strings, for façade 1. White areas mean unavailable positions for module deployment (Freitas et al., 2015a).

Optimized configuration achieves 6% lower cost of electricity with a 6 PV strings system (Figure 5.13). From initial to last generation, the energy yield became about 25% higher with similar system costs reducing significantly the ratio of €/kWh. Among the three solutions presented, the GA provides the best answer to the trade-off between yields and costs.

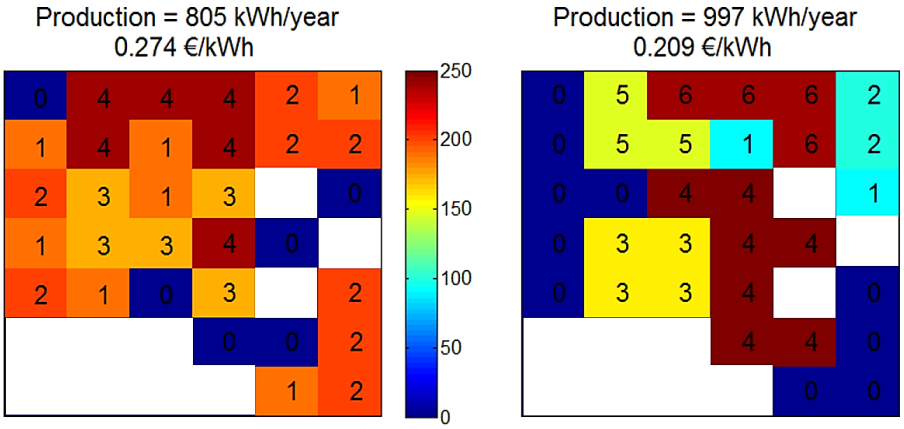

Figure 5.13 - Façade 1 layout with lowest cost of electricity achieved in the initial (left) and 400th (right) generations. Zeros (darkest blue) denote areas without deployment of modules and white means unavailable positions (Freitas et al., 2015a).

At the initial stage of the simulation, there were several dispersed Pareto fronts which became more defined throughout the generations, with only two fronts remaining in the last generation (Figure 5.14).

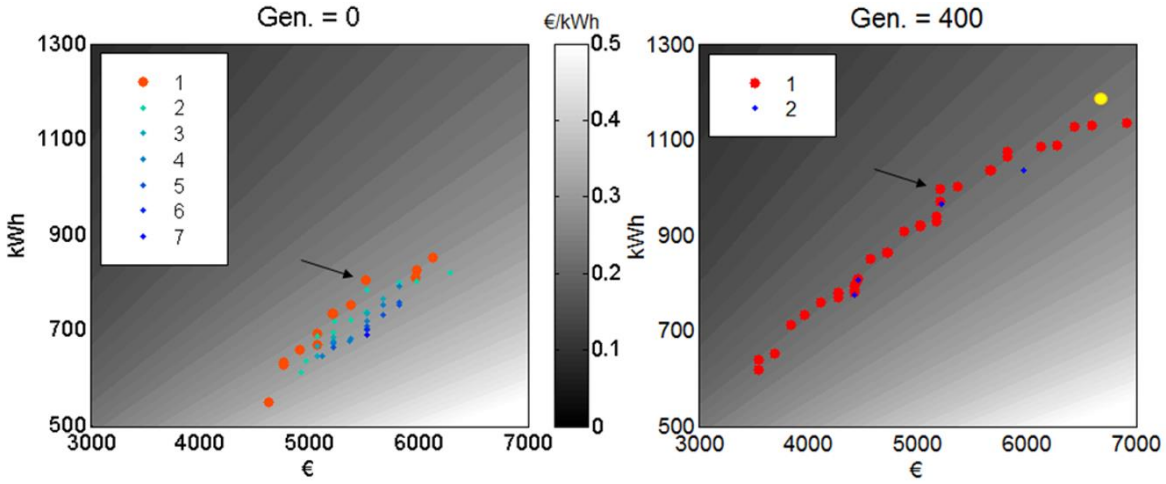

Figure 5.14 – Comparison between the Pareto fronts from the initial (left) and 400th (right) generations, for façade 1. The arrow points the individual with minimum cost of energy [€/kWh] in (i.e. 0.209€/kWh and 997kWh/year) and the yellow circle marks the location of the conventional solution presented in Figure 5.12 (i.e. 0.221€/kWh and 1215kWh/year). Background shading marks different levels of €/kWh (Freitas et al., 2015a).

The upper side of the last generation Pareto curve (Figure 5.14, right) comprehends façade layouts where strings are more disperse, featuring higher energy yields due to higher number of PV strings but at higher costs because of an increased number of inverters. On the other hand, the lower and middle parts of the Pareto are characterized by layouts containing less strings and more zeroes in the positions that are less sunlit. Of course, the final decision for the project will depend on the weight specified to the different objective values. In the case of a façade, aesthetical concerns might also influence the decision.

An overview of the results for the relevant parameters can be grasped from Figure 5.15. It can be noted that the optimization cycle ended in the 400th generation, since only 3 relative minima were found. Similarly to rooftop 1, a plateau seemed to be reached by half the simulation.

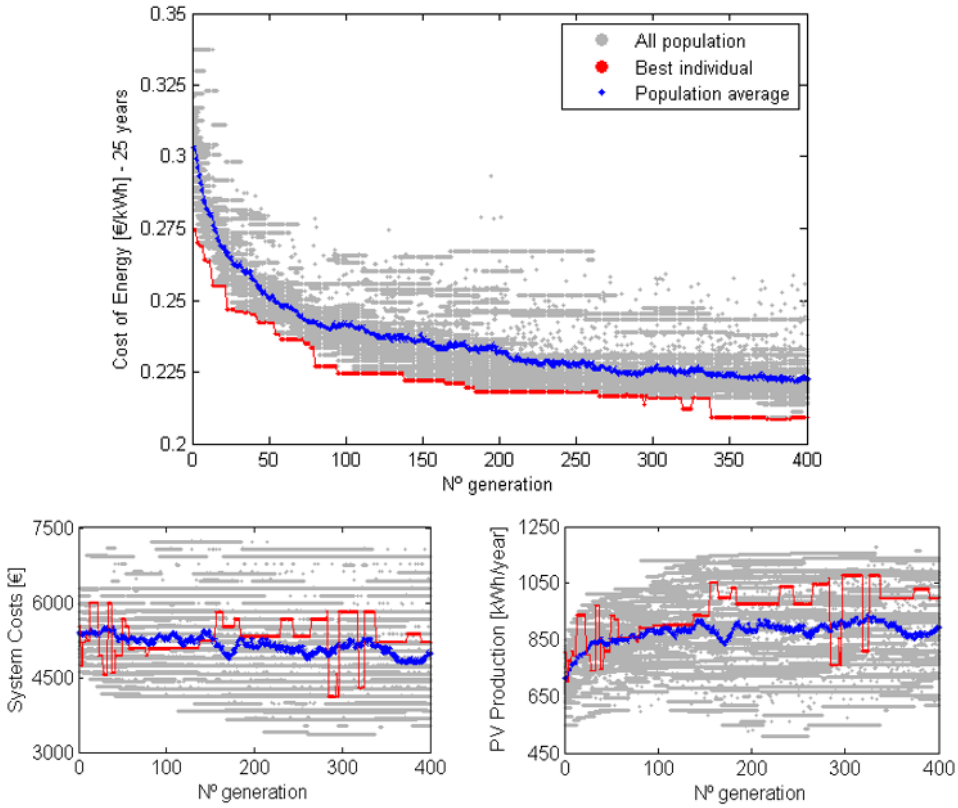

Figure 5.15 - Charts with the overview of the relevant Cost and Energy variables during the optimization process, for façade 1 (Freitas et al., 2015a).

5.4.2 Comparison with micro-inverter arrangement

In Figure 5.16, the optimal layout for the highly obstructed south-facing rooftop under study (rooftop 2) featured a cost of energy of around 0.22€/kWh, with 5 strings clustered in the most sunlit areas and two positions without modules, whilst individual modules with micro-inverters achieved 0.29€/kWh.

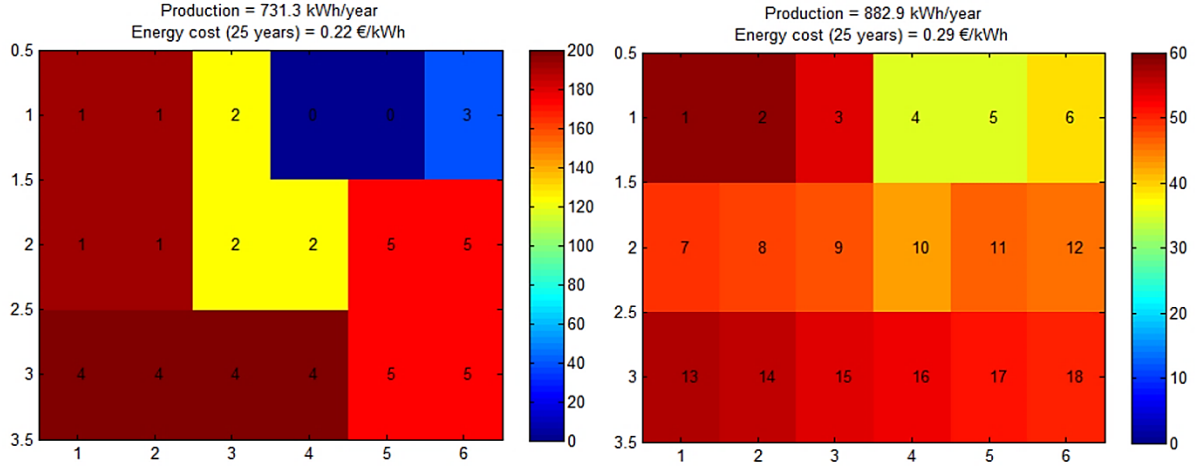

Figure 5.16 - Yearly total PV production per string of the optimized distribution of strings (left) and the micro-inverter scenario (right), for the rooftop 2. Zeros (darkest blue) denote areas without deployment of modules. Note the different colour scale values in the two graphs (Freitas et al., 2015b).

Higher electricity yielding solutions, with higher costs, are in the right side of the Pareto front, whilst more affordable configurations, with lower electricity production, can be found in the left side (Figure 5.17). The layout with micro-inverters is located on the rightmost tip of the Pareto front (green triangle), achieving the highest yields but requiring a considerable investment, far from the best ratio €/kWh.

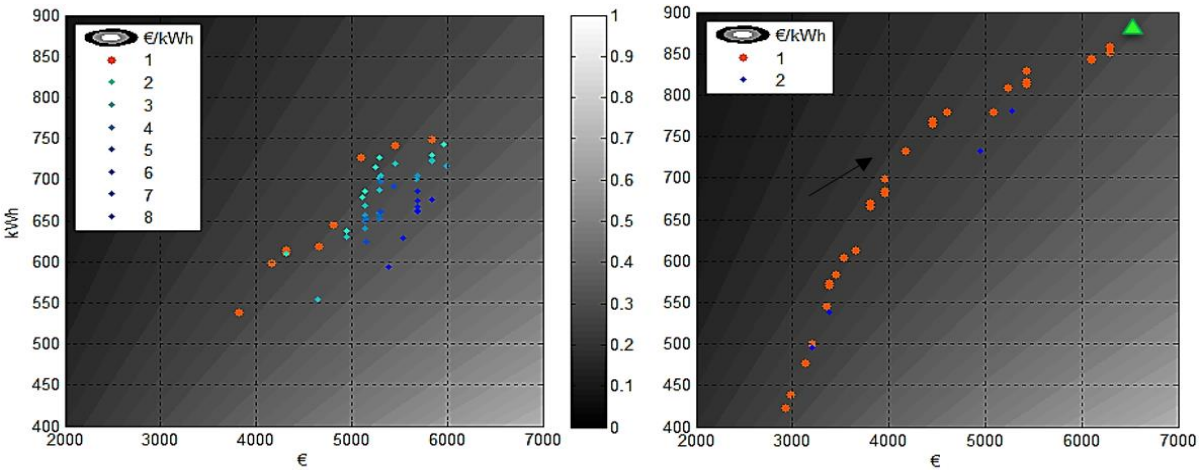

Figure 5.17 - Comparison between the Pareto fronts from the initial (left) and 400th (right) generations, for façade 2. The arrow points the individual with minimum cost of energy [€/kWh] (i.e. 0.22 €/kW h and 731 kW h/year) and the green triangle marks the location of the micro-inverter scenario (Freitas et al., 2015b).

Façade 2 optimal layout (Figure 5.18, left) reveals that a west-facing partially obstructed façade can match PV production of a micro-inverter rooftop PV arrangement in non-optimal conditions (0.30 vs 0.29 €/kWh). The Pareto fronts of the initial population and the last generation (Figure 5.19) also corroborate the observations done to rooftop 2. Optimal interconnections and module placement for rooftop 2 and façade 2 feature cost of energy 23% and 24% lower than the equivalent micro-inverter solution.

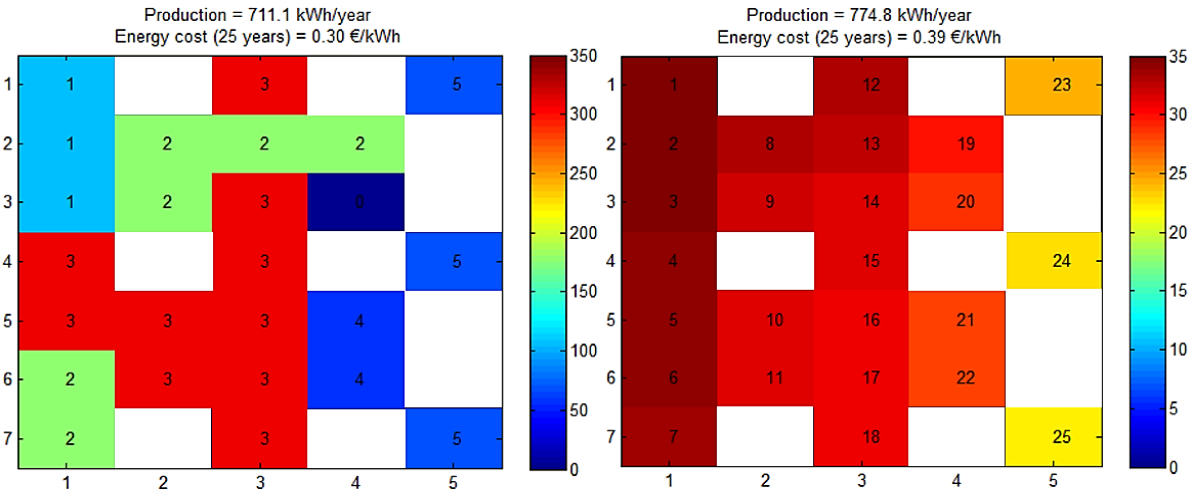

Figure 5.18 - Yearly total PV production per string of the optimized distribution of strings (left) and the micro-inverter scenario (right), for the façade 2. Zeros (darkest blue) denote areas without deployment of modules and white means unavailable positions. Note the different colour scale values in the two graphs (Freitas et al., 2015b).

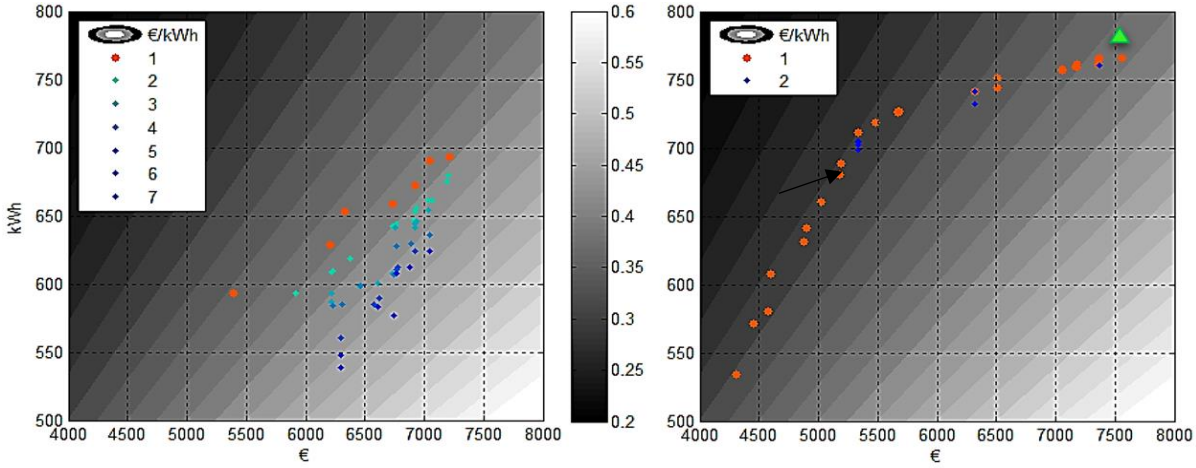

Figure 5.19 - Comparison between the Pareto fronts from the initial (left) and 400th (right) generations. The arrow points the individual with minimum cost of energy [€/kWh] (i.e. 0.30 €/kW h and 711 kW h/year) and the green triangle marks the location of the micro-inverter scenario (Freitas et al., 2015b).

Table 5.4 summarizes costs and yields of a conventional columnwise arrangement and optimized layouts for the 4 case-studies. The micro-inverter scenario is equivalent to a raw output from the SOL model, i.e. the PV yield of a system and its costs correspond to the aggregation of the individual yield and cost of each m^2 in the rooftop or façade.

Table 5.4 – Yields and Costs obtained for the 4 case-studies in conventional columnwise, micro-inverter and optimized arrangements.

	Conventional		Micro-inverter		Optimized	
	Yield [kWh]	Cost [€]	Yield [kWh]	Cost [€]	Yield [kWh]	Cost [€]
Rooftop 1	2305	4610	2649	6147	2240	3528
Rooftop 2	726	4606	883	6402	731	4022
Façade 1	1215	6713	1493	8550	997	5209
Façade 2	754	5490	775	7500	711	5333

Although the addressed case-studies are worst case scenarios, for their particular challenging shading conditions, it is clear that considering partial shading in PV systems is essential for the assessment of the PV potential in a neighbourhood or city, especially when regarding building façades.

5.5 Discussion

The developed multi-objective genetic algorithm (MOGA) helped finding solutions that keep the trade-off between PV system costs and electricity yield in different façade and rooftop case-studies. For the synthetic partially obstructed rooftop (rooftop 1) the optimum solution costs 0.063€/kWh, below the column wise configurations. The same was observed for the southeast-facing façade (façade 1) reaching 0.209€/kWh, 5% cheaper than the typical arrangement. This façade is characterised by low afternoon insolation and relatively complex shadow phenomena, which, still, did not prevent the MOGA from finding optimal solutions.

Regarding rooftop 2, a partially obstructed building rooftop facing south extracted from a DSM, a more profitable string arrangement was found that overcomes a micro-inverter scenario in 23%. A result of the same order was obtained for façade 2, a west-facing façade also derived from the same DSM. Nevertheless, the optimum arrangement calculated for rooftop 1 (0.063€/kWh) is more profitable than rooftop 2's (0.22€/kWh), despite the same location and orientation. The surroundings of the two rooftops systems are different and thus the shadows prompt dissimilar irradiation profiles, leading to a cheaper optimized string arrangement and inverter set for rooftop 1. The same happens between façade 1 and façade 2, but, in this case, the west-facing façade was expected to produce less electricity than the southeast-facing one and, thus, be less profitable. Overall, the rooftop optimum layouts are more clustered and elegant than the façades', probably due to the less complex shading patterns.
It must be kept in mind that the obtained solutions are solely possible optima, rather than absolute optima. Hence, given the complexity of the problem at hands and the lengthy chromosomes used to encode it (18 to 32 genes), it cannot be guaranteed that the search space was entirely covered. For shorter chromosomes (e.g. bellow 11, which corresponds to the MatLab function *perms* threshold), and if the computation of objective functions is not time consuming, it is possible to construct and evaluate all possible combinations using the number of genes within a reasonable time frame.
Depending on the initial conditions set to the genetic algorithm and the number of available positions, the execution time can vary. Also, when secondary functionalities, such as the recording of all solutions and Pareto graphics are disabled, the execution time becomes considerably lower. For instance, in the study of façade 1 with an initial population with 4 strings per layout, binary crossover and mutation, population with 50 individuals and a total of 400 generations, about 3 computation hours were needed, whereas an initial population of 100 individuals with enabled recording of all intermediate data was 1/3 more time-consuming. The fact that crossover and mutation are binary-based simplifies the operations, as only bits are manipulated, and achieves a compromise between the reliability of results and computation time. Parallel computing could also minimize execution time.
Although the diversity of layouts and subsequent convergence is unpredictable when the MOGA first starts, it could be confirmed that for smaller data grids the best solutions tend to be reached faster than for larger grids and that the whole population tends to scatter more if the initial forced number of strings is higher. Due to binary operations and subsequent higher integer variety, it becomes more difficult to form longer strings, therefore the tendency is to cluster short strings in more sunlit areas and single module strings, or no modules at all, in positions that are less exposed to sunlight.
The unconventional string interconnections obtained for the façades might trigger questions related to aesthetics and to the wiring. Concerning cabling routes, it was verified that these do not impact significantly on the system costs, therefore, the interconnections can somehow extend without compromising the arrangement performance (as long as the connections follow the order established by the algorithm). This would be particularly important when cabling crosses window positions, which is the case of strings number 1 and 4 in façade 1 (Figure 5.13, right) and strings 2 and 5 in façade 2 (Figure 5.18, left).

5.6 Conclusions

Genetic algorithms are non-trivial but reliable methods to find solutions for complex problems. Arriving at the best solution for a partially obstructed building integrated PV system that maximizes electricity generation while minimizing installation costs is one example. Although the basics of genetic algorithms remain the same throughout different problems, the encoding is usually situation specific. In the mentioned example, the chromosomes should describe both a module's position and relationship towards its neighbours so that the impact of partial shading was captured.

Different surface tilts and orientations can cause unpredictable shadow casting and the availability of positions in rooftops and façades can prompt the most intricate optimal string interconnections. This represents the true value of a heuristic such as a genetic algorithm to the problem of optimizing string layouts: conventional or intuitive solutions may not reach close to what can be obtained by emulating the evolution of species in nature. In fact, conventional arrangements were shown to be up to 18% more costly than a genetic algorithm optimized layout. The use of micro-inverters optimizes energy yields but at the upper bound of cost, as high as 24% more costly than an optimized PV configuration. Results discussed in this chapter again showed that PV façades energy yield and cost is clearly less favourable than PV on roofs. The next chapter explores one of the important benefits of deploying solar on façades: the value of off peak production.

6. OFF PEAK VALUE FROM PV FAÇADES

The PV potential in the built environment is not confined to individual buildings. The aggregation of the total rooftop and façade PV potential in a neighbourhood or a city might be able to satisfy a relevant fraction of its combined electricity consumption, even at off-peak production hours. The contribution of the different building surfaces to the electricity supply will vary seasonally and according to the urban layout, therefore, a cost-effective investment will feature a different share of rooftop and façade. This Chapter assesses the role of façades and other vertical features for the photovoltaic potential of two representative neighbourhoods in Lisbon, considering the estimated local electricity consumption. Annual, monthly and hourly analysis are presented and the best rooftop/façade PV mix is proposed. [8]

6.1 Introduction

Solar power has relatively low energy densities, thus large areas are required to produce relevant amounts of electricity. Urban environments generally encompass high density of tall buildings hence the available rooftops area becomes scarce for energy supply from solar systems. Building façades offer an attractive and complementary option. If the whole available area in buildings was used for deploying PV panels, and neglecting shadings from the surroundings, the total annual electricity production of a neighbourhood would double that of the roof, as seen in Chapter 3. This ratio grows as buildings become taller. However, the overall cost of the generated solar electricity [€/kWh] in a building would also increase, since less than optimum inclination/orientation should be weighted by economic constraints. Nonetheless, the consistent reduction in the costs of PV, expected to persist in future years (Wirth, 2017), opens a window of opportunity for this type of applications.

Due to varying sun paths throughout the day and the year, which characterize different angles of incidence of the sun rays, vertical PV façades are expected to produce relatively more power in winter and less in summer, and more in the early and late hours of the day, when the sun is lower in the sky. Since a building has typically four, or at least two, exposed façades with differing orientations, the solar façades of a building will peak power production at different hours. This can lead to a spreading of the peak of power production throughout the day and, thus, realizing a closer match to the electricity load demand, which can then result in significant savings in electricity storage and/or fossil fuel based backup power (Hummon et al., 2013). The importance of adjusting tilt and azimuth of PV installations as a means to widen the electricity generation over a larger period of time is also discussed in (Mohajeri et al., 2016), which highlights that higher tilts are the most favourable option for south-facing surfaces.

The generally lower solar irradiation levels on building façades have prompted exploration of different concepts and technological solutions for increasing radiation harvesting and electricity production on vertical surfaces, as demonstrated in Chapter 4. Since BIPV can replace other construction materials, its net cost is already lucrative in some applications (Verberne et al., 2014).

There is little literature quantifying the value of off-peak production from PV façades at the neighbourhood or city scale. One reason might be the lack of interest on such non-optimal surfaces, since PV used to be unaffordable. Another might be the inexistence of suitable software tools for simulation or real case studies with monitored data for examination. An example of the first is the work developed in (Hachem et al., 2011), which concluded that the rotation to the west may increase

[8] Chapter includes work published on:

- Brito, M. C., Freitas, S., Guimarães, S., Catita, C., Redweik, P. "The importance of façades for the solar potential of a city". Renewable Energy, Volume 111, Oct 2017, 85–94. DOI: 10.1016/j.renene.2017.03.085

façade irradiation and roof BIPV electricity generation for a summer design day. However, this study used only five small building archetypes. As for the second, in (Frontini et al., 2014) the retrofit of a building by façade PV deployment is described. It is observed that although façades are affected by partial shadows throughout the day, they contributed to the self-consumption of the building by increasing the number of hours with electricity production without compromising production at mid-day. (Sánchez and Izard, 2015) also used measurements from BIPV prototypes to highlight the contribution of façades and to state that a feasible matching demand can be achieved by a smart combination of different orientations.

In the next sections, the potential for off-peak production from solar façades was analysed in two neighbourhoods: Areas A and B from Sub-section 3.2.2. Hourly solar irradiation on all points on the ground, roof and façades of the respective LiDAR-based DSM (including the terrain, buildings and trees) of both areas were computed using the SOL model.

6.2 Electricity demand

For this study, the electricity demand in both areas was estimated using a top-down approach, where there is no concern for the stochastic behaviour of electricity demand at the individual level. It consisted on inferring the population distribution and multiplying it by the average electricity demand. Since the electricity consumption is distributed in the neighbourhood and not constrained to the building itself, the importance resides on the aggregated electricity demand per capita, which encompasses electricity consumption beyond the domestic individual end-users. A bottom-up approach based on the extrapolation of energy consumption of building archetypes could be used to refine the understanding of the details associated with the energy consumption (Swan and Ugursal, 2009). This method would, however, require information such as statistical data on household occupancy, appliances availability and use, among others (Torriti, 2014), that was unavailable for the present assessment.

To estimate the population distribution, the census population at block group level (INE, 2011) can be disaggregated by building using the 'residential volume' as a proxy variable. The procedure starts by using the LXI (LXI, 2012), an web-based GIS platform, to characterize each building as 'residential' or 'non-residential'. Furthermore, dwellings may be distinguished according to houses or apartment type of building. An additional restrictive criterion is implemented: only buildings with at least one floor above ground, which means an average height above 2.5m, are considered suitable for habitation. The number of residents per building is calculated through the method proposed in (Ural et al., 2011). Each building receives a proportional share of the resident population based on the ratio between its volume and the total resident volume in the block group, which is afterwards weighted by the height of the building.

The electricity demand of each building was then calculated by multiplying the estimated number of inhabitants by the per capita electricity consumption. For that purpose, hourly load diagrams for a full year (REN, 2011), normalized by the number of inhabitants in the country, were considered.

It is important to stress here the concept of non-baseload demand, against which the PV generation potential will be compared. It is defined as the minimum level of demand on an electrical grid over 24 hours and can be determined by subtracting from the hourly demand load the minimum load of the previous 24 hours. This minimum is expected to occur during the night period, when electricity demand tends to be lower.

The number of residents per building and their electricity demand are shown in Figure 6.1. Area A has the highest population density (a total of 3313 residents) and, thus, higher electricity demand, which is mainly concentrated in the central high-rise buildings. Conversely, Area B (with 3742 residents) is

more compact and uniform. The overall electricity demand was estimated at 63 GWh/year for Area A and 72 GWh/year for Area B.

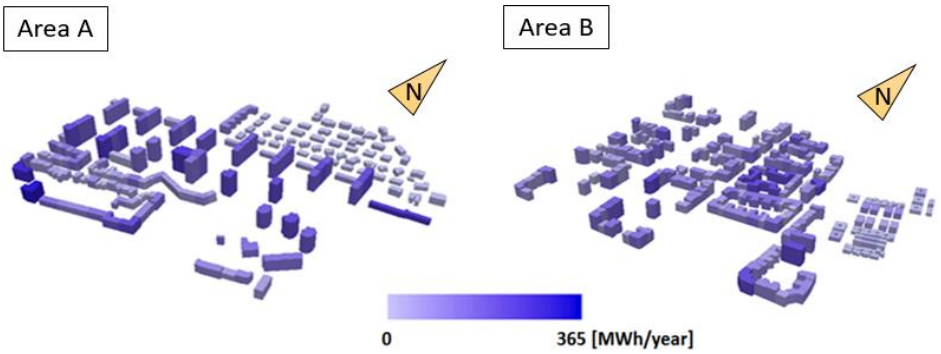

Figure 6.1 - Annual electricity demand per building, for Area A (left) and Area B (right) (Brito et al., 2017).

6.3 Annual energy production

Solar irradiation results from Chapter 3, computed for all ground and rooftop raster points and for all vertical surface hyperpoints, were used for hourly PV power estimation. It was seen that roofs and ground were clearly superior to vertical façades (Figure 3.15), which have significantly lower levels of irradiation, both in Area A, with high rise and generally unobstructed buildings and in Area B, with a compact arrangement of 4-story buildings. South-facing façades feature higher annual yields than east- or west-facing ones, which was evident on the central neighbourhoods in Area B. On the other hand, there is a certain degree of mutual shading in the lower floors, especially observable in the high-rise façades in Area A and in narrower streets of Area B, which prompts varying solar potential all over the same façade. Rooftops feature relevant levels of irradiation from 1000 to 1800kWh/m^2/year, depending, of course, on their orientation and inclination (Figure 3.16). Conversely, the incoming solar radiation is only in the 100 – 1000kWh/m^2/year range for façades, which are much more influenced by orientation, shading from neighbouring buildings and trees.

The PV potential was estimated following the same approach as in Sub-section 3.2.1. The accumulated monthly PV potential is depicted in Figure 6.2 according to 4 different classes: irradiation above 900, between 700-900, between 500-700 and below 500kWh/m^2/year. For comparison reasons, the estimated local non-baseload (solid blue line) and full load (dashed) electricity demand is also shown. Focus will be given to the non-baseload demand, assuming that other renewable energy sources, such as non-urban biomass, large hydro or wind (if associated to storage) would satisfy baseload demand.

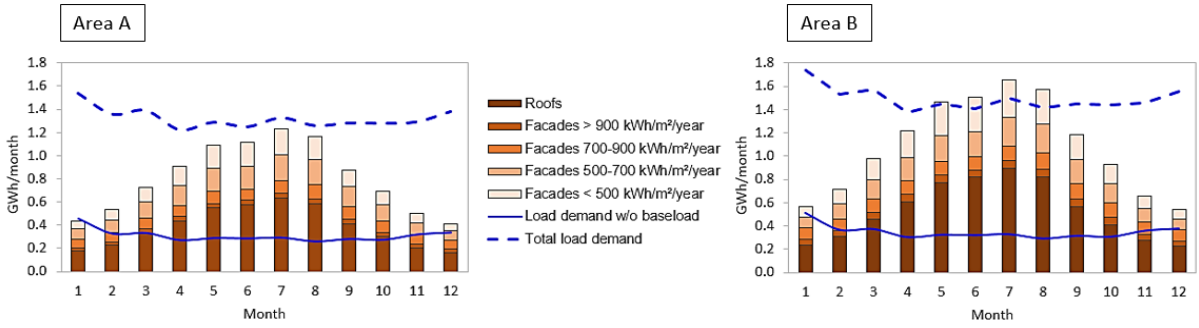

Figure 6.2 - Monthly PV potential (roofs: dark brown column; façades: lighter brown columns according to 4 different classes: above 900kWh/m^2/year, between 700 and 900, between 500 and 700, and below 500kWh/m^2/year) and electricity demand (blue solid line: non-baseload monthly electricity demand; blue dashed line: monthly total electricity demand) for Area A (left) and Area B (right) (Brito et al., 2017).

In annual terms, the roof PV potential in both areas exceeds the local non-baseload demand and can contribute to 26 % (Area A) and 36 % (Area B) of the total electricity demand, but the total PV potential increases 54 % and 73 % for Area 1 and 2, respectively, if the potential of PV façades is added to that of the roofs. However, the PV potential in Area B is more favourable than in Area A, for all months of the year.

It can be observed that, for the summer months, the total rooftop PV potential surpasses the non-baseload demand in both areas. Furthermore, if both façades and roofs are taken into account, the PV potential of buildings becomes in the order of magnitude of the total load demand being reached during the summer in Area B. These results highlight the relevant role that façade integrated PV systems can play in the electricity system in urban environments.

For the winter months, the load demand increases slightly due to more artificial lighting and heating demand during shorter and colder days and solar irradiation decreases significantly. It is not, therefore, surprising that the roof PV potential itself is unable to supply the non-baseload electricity demand during 5 months in Area A and 4 months in Area B. Yet, this non-baseload demand would be satisfied if the total PV potential of façades was realised (Table 6.1).

Clearly, the non-baseload electricity demand has potential to be satisfied by solar electricity, particularly during the summer months. However, complementary non-solar fuels would be required for the baseload production, which accounts for about ¾ of the total load demand.

Furthermore, given that, in 2015, in the district of Lisbon, 23% of the electricity demand was associated to residential loads (PORDATA, 2013), it can be inferred that the electricity generation from building deployed PV systems would be able to satisfy the monthly residential electricity demand of the city. This highlights the importance of PV on roofs and façades towards the propagation of nZEB in the urban environment.

Furthermore, the fact that two neighbourhoods with the same area and comparable resident populations feature relevant differences in the solar potential of roofs and façades, with Area B presenting a significant higher potential, despite average lower irradiation density due to the larger façade area, highlights the role of architecture and urban planning for the design of modern cities that can take the full potential of the solar resource to meet its local electricity needs.

Table 6.1 - Annual energy demand and solar electricity production for the different system classes represented in Figure 6.2.

	Area A	Area B		
Total load demand [GWh/year]	17.9	15.9	including baseload	
	4.2	3.7	not including baseload	
Energy production [GWh/year]	4.6	6.4	Roofs	≤ 1800 kWh/m^2/year
	1.7	2.4	Façade	≤ 500 kWh/m^2/year
	1.9	2.1		500 – 700 kWh/m^2/year
	1.1	1.4		700 – 900 kWh/m^2/year
	0.4	0.7		≥ 900 kWh/m^2/year
	9.7	13	Roofs and façades	

6.4 Payback time analysis

Different classes of financial payback of investment can be drawn from the classification of façades according to yearly solar irradiation in Figure 6.2. In this sense, darker brown (above 900kWh/m^2/year) are profitable PV investments even in current market conditions, where one may assume an average

building applied PV system cost of 300€/m^2 (Verberne et al., 2014) and a grid selling price of 0.156€/kWh (ERSE, 2016a). Lighter browns (below 500kWh/m^2/year) might only be interesting as an investment when PV costs drop significantly. The financial payback time is estimated through:

$$Payback\ [years] = \frac{300\ [€/m^2]}{System\ class\ [kWh/m^2/year] \times \eta_{ref} \times PR\ \times 0.1555[€/kWh]} \quad (6.1)$$

where η_{ref}=15% is the typical efficiency of a 1m^2 module, PR=80% is the performance ratio and $System\ class$ can be found in Table 6.1.
Table 6.2 stresses the financial payback time estimated for high generating rooftops and the different façade classes. It can be highlighted that the combined payback of deploying PV on all rooftops and high performing façades, those with irradiation above 700kWh/m^2/year, would be 19.5 and 18.7 years for Areas A and B, respectively.

Table 6.2 - Financial payback time of investment for an average rooftop system and the threshold of the different façade classes.

System class		Payback time [years]
Rooftop	1800 kWh/m^2/year	8.9
Façade	900 kWh/m^2/year	17.9
	700 kWh/m^2/year	23.0
	500 kWh/m^2/year	32.2

Moreover, Table 6.3 presents the optimum mix of rooftop and façade PV systems for different levels of combined payback times. These results were obtained by ordering the points on roofs and façades according to their payback time (lower paybacks first). The global payback is the weighted average of the paybacks, where the weights are the fraction of the area with that particular payback.
For both areas, only rooftops PV allows for payback times below 10 years, whilst a 50/50 mix would lead to payback times of 15 years, with a slightly higher share of façades in Area B. Such long payback times confirm that, with current costs, and disregarding purposes other than electricity generation, façade PV might only be attractive in very particular conditions. Still, significant reductions in PV costs are expected in the medium term (IEA, 2014). With halved costs achieved by 2030, mass deployment of solar façades in the urban environment will certainly be triggered.

Table 6.3 – Mix of roof and façade PV systems for different combined payback time periods.

Combined payback time [years]	Area A		Area B	
	Roofs	Façades	Roofs	Façades
10	100%	---	100%	---
12	78%	22%	78%	22%
15	50%	50%	48%	52%

With these numbers in mind and referring to Figure 6.2, one concludes that Area B's non-baseload electricity demand could be covered for 10 months of the year by cost-effective investments on rooftop and façade PV systems. As for Area A, where most façades are east- and west-facing and generating less than 500kWh/m^2/year, the contribution of profitable PV deployment on façades would only be marginal, reducing the deficit from 5 to 4 months.

The estimated payback times obviously depend on the average efficiency of the modules. If PV efficiencies above 20% had been assumed, as it is expected by 2030 (IEA, 2014), payback times for rooftops would have been reduced to just over 6 years and best locations in façades would have reached about 13 years. This would translate into around 38% of PV on façades, on both areas, for a combined payback time below 10 years.

6.5 Hourly photovoltaic supply

The impact non-optimally inclined and oriented solar façades and, therefore, the value of their off-peak PV production can be grasped from Figure 6.3 and Figure 6.4. The first compares the solar irradiation distribution over Area A and B at midday in a winter day (top row) and at 9am in a summer day (bottom row). The latter shows the hourly balance between local electricity demand and the photovoltaic potential in roofs and façades, for the same days.
The winter day, as expected, features relatively low overall solar irradiation, with south-facing façades reaching higher irradiation than roofs (or ground) at midday. On the other hand, the solar potential on façades facing east and west is reduced at that time. However, for the early hours of a summer day, it can be verified that the winter peak is largely surpassed, even at this early time of the day: high-rise façades reach about the same irradiation levels as horizontal rooftops. It is also evident that roofs (and ground) still have much higher solar irradiation density than façades, regardless of their orientations.

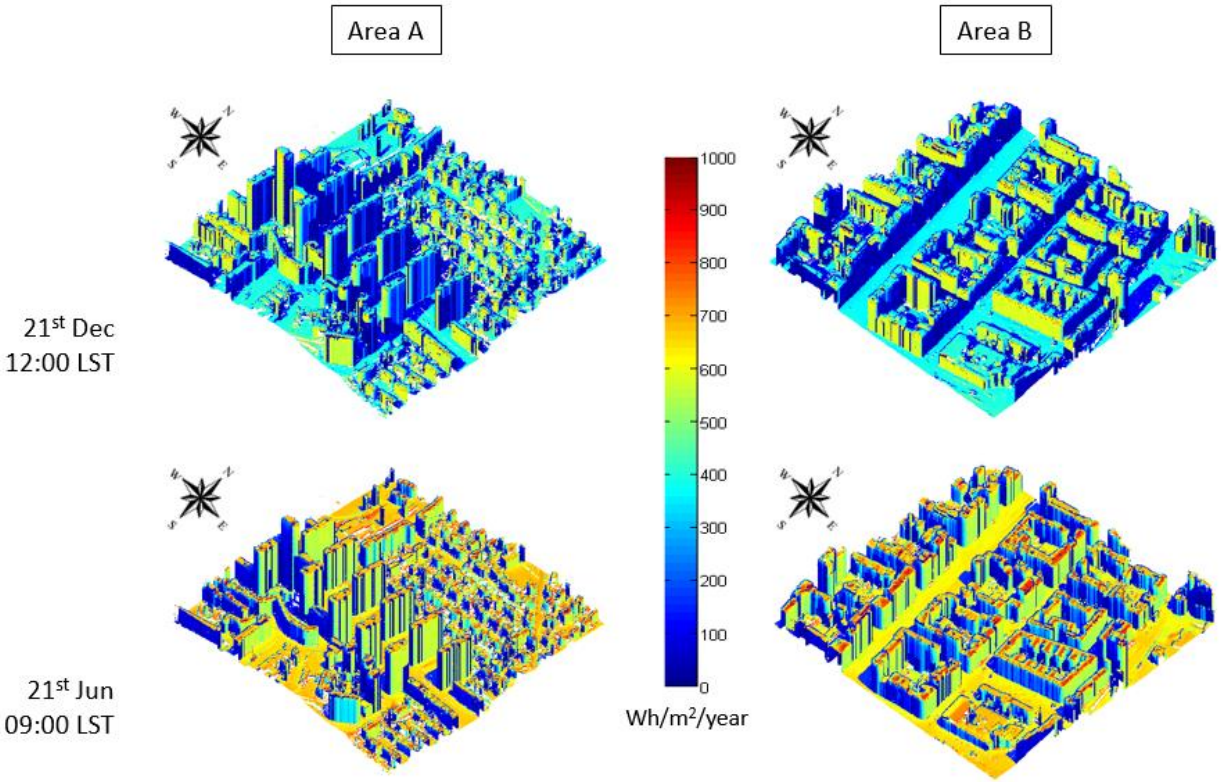

Figure 6.3 - Solar radiation for Area A (left) and Area B (right) at 12:00 LST on December 21st (top) and 09:00 LST on June 21st (bottom) (Brito et al., 2017).

Regarding the hourly PV supply potential (Figure 6.4), results confirm that, for the winter day, the overall PV generation is insufficient to cover the local daily electricity demand for both areas, due to lower levels of solar irradiation and relatively short days (note the different hour range from the winter to the summer day). However, if beyond rooftops façades are also included, the combined peak PV

power can achieve electricity demand around noon. The added value of off-peak PV supply is, in this case, not significant since reduced sunrise and sunset azimuths do not beneficiate solar exposure of non-south façades during winter days. In fact, façade peak production happens at the same time of rooftops', which is not coincident with the morning or the evening increased demand (typically associated to artificial lighting).

Concerning the summer day, the total rooftop potential peak power itself exceeds demand at midday, whilst the façade-only potential peak power exceeds morning demand in both areas. The complementarity between PV production from rooftop and façade systems is, therefore, emphasised during summer, with a more pronounced effect in Area B.

It must be stressed that, during the summer, the morning and afternoon peak production of east- and west-facing façades, respectively around 9h and 16h, exceeds that of south-facing façades around solar noon. The latter do not have a great share in the solar electricity production diagram, since the solar height (in Lisbon) favours solar roof and not vertical surfaces at midday.

The total electricity demand during daylight hours could be several times satisfied by local photovoltaic production, doubled for Area A and more than tripled in Area B, if full rooftop and façade PV potential was exploited. Given that the dynamics between peak production and rooftop and/or façade orientation leads to a global complementarity between the diversity of building surfaces in a neighbourhood, even if regulatory or technical restrictions to the use of PV systems would significantly limit the technical potential of building surfaces, the supply for total local demand during daylight hours would still be assured in the summer months.

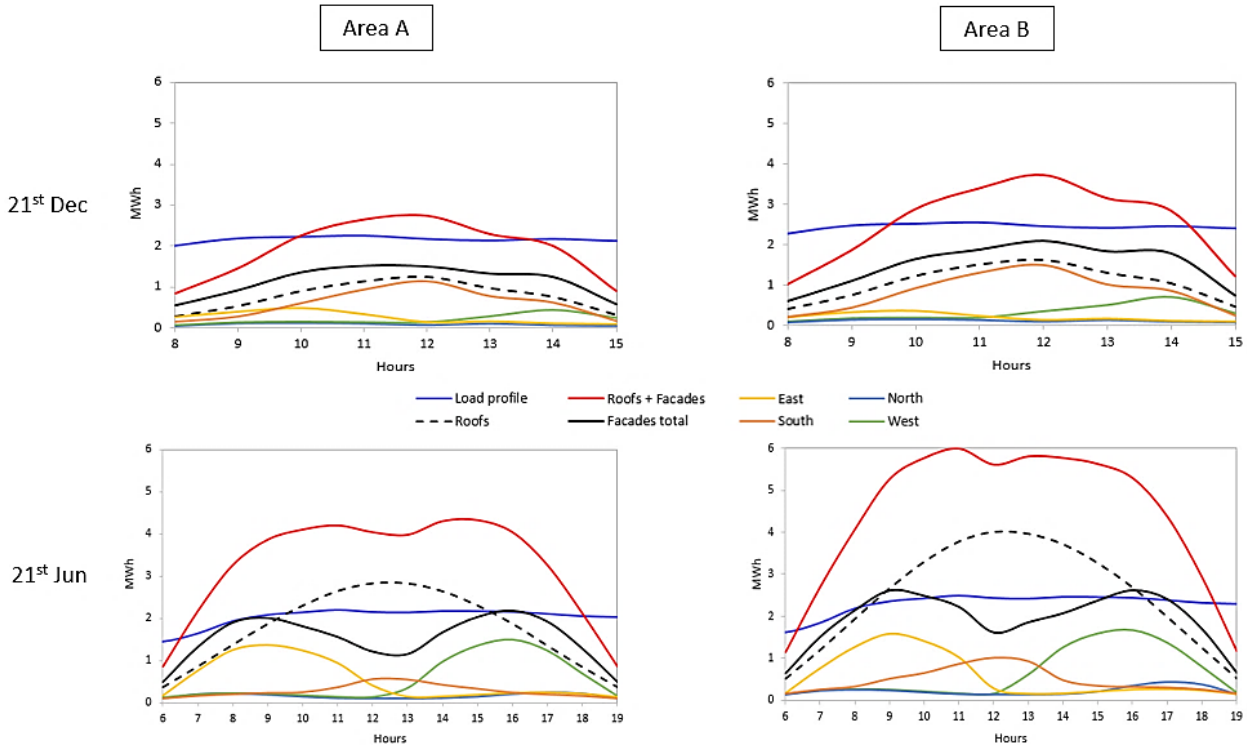

Figure 6.4 - Hourly electricity demand (dark blue line) and photovoltaic potential of roofs (black dashed line), all façades (black solid line), south façades (orange), east façades (yellow), west façades (green), north façades (light blue) and roofs and façades (red), for Area A (left) and Area B (right) for a winter day (top) and a summer day (bottom) (Brito et al., 2017).

If commonly available PV modules successfully reach an increased efficiency of 20% by 2025 (IEA, 2014), assuming that the available area on roofs and façades remains unchanged, it would represent an increase of about 30% on the estimated electricity production (at all times of the day and year,

since the efficiency is a multiplicative factor in the present model). The impact would be significant on the presented results, but one must not disregard the role of other PV technologies, such as less efficient semi-transparent ones, which could be used in glazed surfaces. Since these might occupy 25% of the façade area, the overall PV potential growth is slightly reduced. However, aspects such as the underestimation of façade irradiation by the SOL model and the non-optimized string interconnections might balance out.

One last remark on the benefits of higher PV efficiency is that it would help solar roofs to address the electricity demand on their own: PV installed on rooftops and on the best performing façades (those featuring irradiation > 900kWh/m^2/year) would undoubtedly satisfy non-baseload consumption throughout the year, in Lisbon. The contribution of such PV systems to the adjustment of electricity generation to the load diagram would be enhanced, therefore, the development of cost-competitive higher efficiency PV modules is paramount for prompting large-scale PV deployment in cityscapes.

6.6 Conclusions

Rooftops alone cannot tackle current electricity demand, therefore building façades have a role in sustainable, fully decarbonized urban landscapes. Façades receive lower levels of solar radiation than roofs, irrespective of their inclinations, but their significantly higher area can enhance the total urban PV potential, which, in annual terms, can satisfy up to 50-75% of the total electricity demand in a Mediterranean mid-latitude contemporary neighbourhood. The highest producing solar façades are the south-facing ones, which can reach irradiation levels of more than 1 MWh/m^2/year.

During the winter, with increased heating and artificial lighting demand, and lower irradiation available, both rooftop and façade PV are essential to cover the non-baseload demand, since façades can potentially double the solar electricity generation, due to their more favourable inclination. This effect is mostly evident around midday because relatively shorter days prevent east- and west- facing façades from being as sunlit as they are in the summer. Façades are paramount to achieve full solar supply in that time of the day. As for the summer, façades contribute for a relevant spread of the peak PV production throughout the day, especially in the morning and afternoon when the demand can only be satisfied with the help of PV façades. Furthermore, the total individual rooftop and façade potential can exceed the non-baseload demand, but if aggregated it surpasses the total local electricity demand (in the studied areas).

At current market conditions, non-baseload demand could be satisfied by profitable PV investments on both façades and rooftops for up to 10 months of the year. A conservative economic analysis shows that payback times inferior than 10 years can only be achieved if 100% of the PV deployment is on roofs, whereas a 50/50 share between façades and rooftops would lead to payback times of about 15 years. However, the efficiency of the modules plays an important role: if commercially available modules became 20% efficient, paybacks of 10 years would be reached with a 38% share of façade deployment.

7. IMPACT ON THE GRID INFRASTRUCTURE

A massive deployment of PV in the built environment might shift the typical peak of production from midday towards morning or afternoon. This effect becomes noticeable when the variety of rooftop orientations in a city is regarded, but it can be amplified when façades are added to the PV potential. A better demand-supply match can be achieved through differently oriented façade PV systems, however, at a large-scale, it might overwhelm the distribution grid assets due to excessive electricity generation. Power transformers capacities might not be sufficiently large to accommodate the PV surplus in future solar cities.
In this Chapter, the hourly power balance at the transformers in a suburb in Lisbon, and their spare capacity, is evaluated considering full integration of PV into building façades and rooftops. An empirical solar factor to account for future high PV penetration in the sizing of transformers in urban areas is proposed. [9]

7.1 Introduction

Emerging popularity of urban PV installations often leads to concerns regarding its impacts on the grid at different times of the day. Therefore, it becomes important to estimate possible outcomes of large-scale PV deployment: voltage rise and fluctuations, power fluctuations and reverse flow, power factor changes, frequency regulation and harmonics, unintentional islanding, fault currents and grounding issues, etc (Karimi et al., 2016). These effects are exhaustively discussed in (Passey et al., 2011), where mitigation approaches and barriers are proposed. One of the core challenges lies in urban distribution transformers, the gateways for electricity exchange between the grid and buildings. Their power capacity must be sufficient not just to supply building load demand but also to accommodate the surplus PV generated electricity (i.e. which was not self-consumed).
A distribution power transformer (PT) is expected to have an operational lifespan of about 30 years (Harden, 2011)(Manito et al., 2016). The standard sizing practice contemplates the installation of oversized equipment to ensure a lower load level on the transformer until an upgrade to its capacity is required to allow for future demand growth. This translates into Eq. (7.1).

$$P_{PT} = C_{diversity} \times \sum_{c}^{N} P_{contract} \times F_{safety} + P_{over}\ , \tag{7.1}$$

where P_{PT} stands for the transformer power capacity, $P_{contract}$ is customer c's contracted power, N is the expected number of customers, F_{safety} is a safety margin of 1.5 to account for the power factor and for future load growth, P_{over} is the oversized power capacity defined by the standard size of the transformer that is available for commissioning and $C_{diversity}$ is a diversity (or simultaneity) coefficient which is usually defined by:

$$C_{diversity} = 0.2 + \frac{0.8}{\sqrt{N}}\text{, for residential customers,} \tag{7.2}$$

[9] Chapter includes work published on:
- Freitas, S., Santos, T., Brito, M.C., "Sizing of urban distribution transformers in a neighbourhood with PV generation and energy storage", Poster presentation/paper at the 33rd EUPVSEC, Sep 2017, Amsterdam, The Netherlands, doi: 10.4229/EUPVSEC20172017-6BV.3.95
- Freitas, S., Santos, T., Brito, M. C. "Impact of large scale PV deployment in the sizing of urban distribution transformers". Renewable Energy, Volume 119, Apr 2018, 767-776. DOI: 10.1016/j.renene.2017.10.096

$$C_{diversity} = 0.5 + \frac{0.5}{\sqrt{N}}, \text{ for commercial customers.} \quad (7.3)$$

PTs in a distribution grid usually disregard future PV production potential (Joshi, 2008)(Passey et al., 2011). However, since building deployed PV systems are becoming more common in urban environments, present and future local distribution grid ought to consider high PV penetration (Braun et al., 2012).

The impacts on the grid of large-scale PV deployment and the maximum PV penetration levels to avoid power quality control issues is a controversial topic in the literature, as reviewed in (Eltawil and Zhao, 2010). (Santos-Martin et al., 2016) provides a literature review of studies addressing the power quality of distribution networks, along with the simulation of the potential impact of distributed rooftop PV generation on a low-voltage network in New Zealand, using GIS tools. It was found that the hosting limit for PV on urban networks is around 45%, although in most cases the overvoltage would not be much higher than the statutory limit. In (Vera et al., 2014), network details from the city of Corrientes, Argentina, are used to simulate the optimum conditions for the connection of PV systems to the urban grid. Time-resolved distribution of voltages in each node of the power network, distribution of currents in power lines, the energy supplied to the users, etc., shown that both penetration levels of PV in the power grid and interconnection points must be evaluated to avoid detriment in the quality of energy supply service. An analogous study carried out in (McPhail et al., 2016) for the low-voltage grid in the region of Queensland, Australia, concluded that the range of maximum rooftop PV hosting capacity per customer is between 1.6 - 5 kVA. For an urban distribution grid at Maribor, Slovenia, power quality assessment showed that low power output due to grid connected PV systems could compromise voltage quality, violating harmonic distortion requirements (Seme et al., 2017).

Nonetheless, the potential of distributed generation might represent a means of supplementing grid capacity and consequent postponement of substantial investment on expansions or upgrades of the distribution systems, such as acquiring new power transformers (Piccolo and Siano, 2009). However, as high PV penetration affects the operations of distribution networks that PV systems are connected to, grid reinforcements are still required and ought to be done in a cost-effective manner. In (Chun-Lien Su and Hsiang-Ming Chuang, 2014), an heuristic optimization method is proposed to maximize reliability of power supply and quality while minimizing line losses and investment cost. The combination of control variables, such as line switch and feeder reconfiguration, line upgrading, construction of a feeder and/or a transformer substation, encompass the optimal long-term investment strategy and network arrangements in the planning period. Manito et al (Manito et al., 2016) focused on how grid connected PV would affect utility transformers' lifespan. The authors confirmed that the maximum PV penetration level depends on the load curve and the irradiation levels on site, with high irradiation sites showing a smaller hosting capability due to transformer overload, but feature a potential for 60% reduction in losses at the transformer. Load profiles of commercial buildings might prevent excessive aging of the transformers, whereas residential load profiles are innocuous. It was also highlighted that the deferral of equipment replacement may occur, although proper tuning between generation and demand is crucial, otherwise large-scale PV penetration might be harmful to the grid's assets. Although infrastructure costs traditionally include the cost of transformer, cables, etc., and operation costs refer to the cost incurred due to losses in the network, thanks to new possibilities such as demand-side management and distributed generation, the investments are no longer limited to electrical equipment alone, as demonstrated in (Ramaswamy et al., 2016). In this study, simulations considering a typical medium-voltage network in Wallonia,

Belgium, shown that a significant impact on the total cost of the network by using load and generation flexibility will be realized when the grid infrastructure is mainly sized by the peak.

Among the studies reviewed, none provides a method for the distribution grid operators to account for high PV penetration in the long-term sizing of transformers for a new built area, neither to evaluate if the current assets will be able to accommodate future large-scale deployment (expected to happen between 2025 and 2030). The power gap (P_{GAP}) of the power transformers ought to be estimated under such scenario to assess if there is enough spare capacity for accommodating all urban solar potential or if transformers will require upgrade in the medium term. Since part of the energy demand in building will be supplied by PV (self-consumption), P_{GAP} may be defined as:

$$P_{GAP}(t) = P_{PT} - [PV(t) - P_{demand}(t)]\,, \tag{7.4}$$

where PV is the generated PV electricity and P_{demand} is the local power demand. A positive gap means that PV can be accommodated as is (without any upgrades to the grid), whilst a negative gap indicates that the local grid would require upgrade prior to the deployment and connection of all that PV to the grid. Recalling the factors F_{safety} and P_{over} from Eq. (7.1), the transformers' capacity is by default highly oversized, hence no power losses were considered in the following power balance estimations. Since suburb level PV deployment is considered, no special focus is given to the network details or voltage issues in this Section, otherwise the systems' potential should be classified according to the best performing system classes (defined in the previous Chapter, sub-section 6.3) to comply with the safety limits proposed in the reviewed literature.

7.2 Case-study

This study considers the area of Alvalade, also in Lisbon (Figure 7.1). It contains parts of Area A from the previous Section (orange dashing) and features twice the number of buildings (about 550). The available data set includes the power capacity of all transformers in the area, as well as georeferenced vector footprints with information on building heights and respective number of floors.

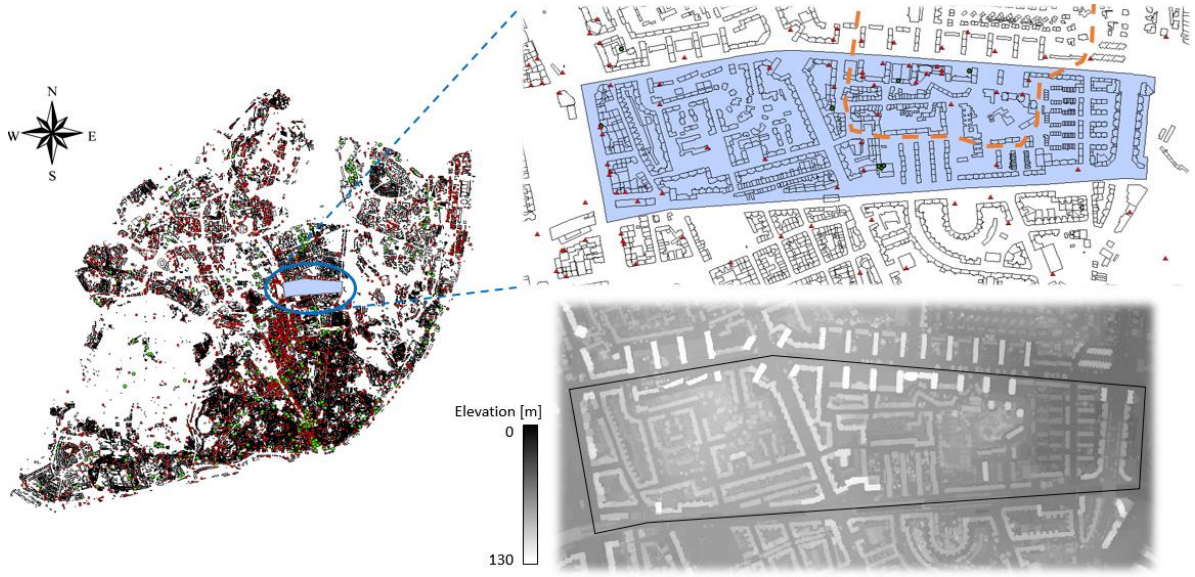

Figure 7.1 - Delimitation of Alvalade within Lisbon (blue area), part of Area A (orange dashed line), location of the transformers (red dots) and respective DSM of the area (Freitas et al., 2017a).

In the absence of information on the local grid network describing the interconnections between buildings and transformers, it was assumed that each transformer has its own influence zone, delimited by Thiessen polygons (i.e. polygons whose boundaries define the area that is closest to each point relative to all other points) using the location of the transformers (red dots in Figure 7.2, top). Then, the building polygons whose centroids (i.e. the arithmetic mean position of all the points in each polygon) fall inside an influence zone are assigned to the respective transformer. Using the centroids of the building polygons assures a one to one connection and, therefore, each point belongs to a single influence zone.

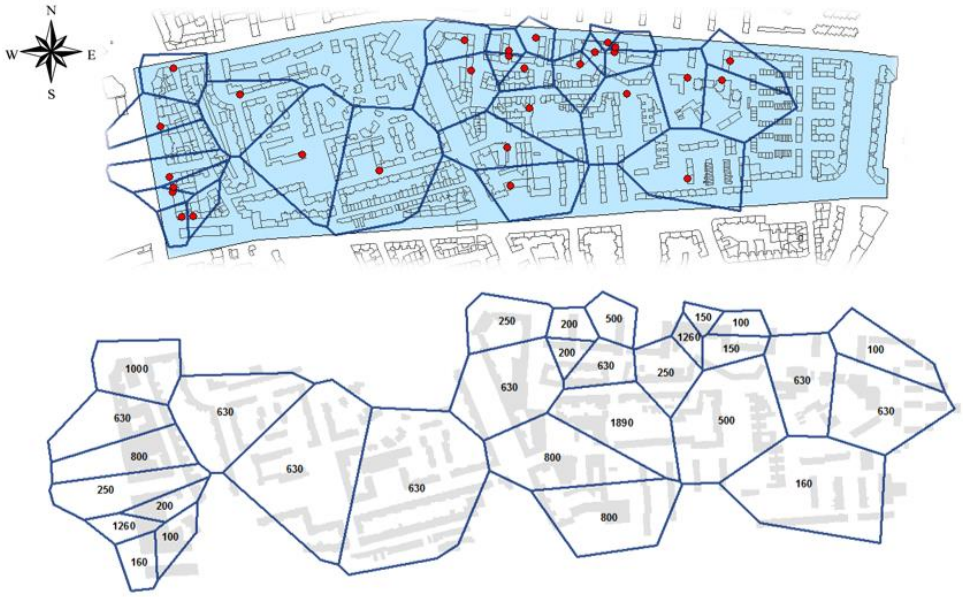

Figure 7.2 - Thiessen polygons depicting the influence zones of all transformers (top) and transformer power capacities [kVA] (bottom) (Freitas et al., 2017a).

The influence zones approach might hold a methodological limitation, since a cost-effective electricity grid topology should follow the streets arrangement and building delimitations (Buhl et al., 2006). The distribution of nominal transformer power capacity (Figure 7.2, bottom) also supports this observation, in the sense that some small influence zones feature very high capacities and vice-versa.

7.2.1 Solar PV potential

Two distinct approaches were used to assess the solar potential: i) the *Peak power method*, which is straightforward and considers the available area and the PV module peak power; and ii) the *Irradiance method*, which estimates hourly solar radiation considering mutual shading and typical meteorological conditions, requiring very high computation time. First a rooftop PV only scenario is analysed and, then, a rooftop plus façades scenario to incorporate the value of off peak façade electricity generation (Brito et al., 2017).

i) Peak power method

This method assumes that at each hour the maximum PV generation equals the maximum installed peak power, i.e. it disregards the fluctuation of irradiance during the day, shading effects, the tilt and orientation of building surfaces, and different contributions from the direct and diffuse components of solar radiation. The hourly PV generation calculated through this method is constant for every hour

of the year, depending solely on the available area on rooftops and façades. It is, of course, expected to overestimate the PV potential, but represents a maximum threshold.
Assuming typical 1m^2 c-Si panels with P_{ref} =160W/m^2 peak power, the PV production potential for each influence zone z, at time t, can be estimated using:

$$PV_{1,z}(t) = P_{ref} \times PR \times A_{build}\ , \tag{7.5}$$

where PR is a performance ratio (80%) and A_{build} is the total available area on all roof and façade surfaces [m^2] within the respective transformer influence zone z.
There were footprint segments shared by two buildings that required special attention, otherwise the installed peak power on façades would have been grossly overestimated.

ii) Irradiance method

Time-resolved PV potential generation is paramount for the identification of the moment of peak production. This particular occasion will define if the overall transformer spare capacity is sufficient for accommodating all potential PV electricity generation in an urban suburb. Since the peak of production depends on azimuth and slope of the building surfaces, different transformers will feature peak electricity injection at different times of the day. The existence of large façade areas ought to further shift peak production.
The *Irradiance method* relies on two different software tools to produce hourly time step solar irradiance results for rooftops and façades for the detection of the instants of highest injection of PV generated electricity into the grid.

Rooftops

The SolarAnalyst (Fu and Rich, 1999) extension for ArcGIS, reviewed in Section 2.3, and one of the most commonly used GIS software, was employed for the calculation of hourly solar irradiance on rooftops. A 1m^2 resolution LiDAR-derived DSM of the area and the diffusion portion and transmissivity assessed for each month were used. The approach reported in (Gomes, 2011) was followed to compute solar irradiance in tilted rooftops using the building footprints.

Façades

Since the SolarAnalyst extension is not yet capable of handling full-3D solar irradiance simulations, another tool had to be used to estimate the vertical PV potential. The 3D building model generated in ArcScene (Figure 7.3) was imported into Rhinoceros3D (McNeel, 2016). Hourly solar irradiance was computed for the vertical surfaces employing the Grasshopper plugin LadyBug, also reviewed in Section 2.4. This step was performed inside a main loop that cycled through the total of 550 buildings and a nested one for the hourly irradiance calculations. Thanks to these loops the software did not crash due to the huge amount of building geometries.

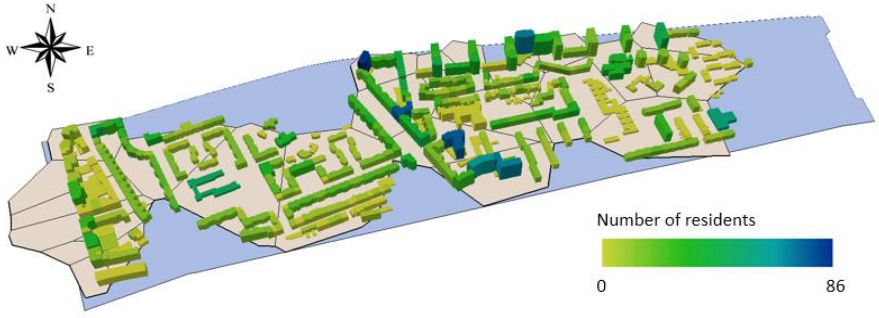

Figure 7.3 - 3D model of the buildings inside the transformer influence zones and the number of residents per building (Freitas et al., 2017a).

Four reference days were considered in the hourly simulations: the 21st days of March, June, September and December. The irradiance results were input into Eq. (7.6) to estimate the PV potential, again assuming standard 1m^2 panels with 15% efficiency.

$$PV_{2,z}(t) = G_{tilted,z}(t) \times \eta_r \times PR\,, \tag{7.6}$$

where $PV_{2,z}$ means the PV generation potential [kW] obtained through the Irradiance method for a transformer influence zone z, at hour t, G_{tilted} is the total hourly solar irradiance in the plane of the building surfaces [kW] and η_r is the reference PV module efficiency (15%).

7.2.2 Power demand

Real metered data from Alvalade was not available, therefore time-resolved power demand by building ($P_{demand,b}$) had to be estimated. Reference consumption profiles for low voltage clients in class C (contracted power below 13.8kVA) for 2017 (ERSE, 2016b) were used. These profiles are estimated and published by the national transportation grid operator every year for billing purposes, and are applied to customers who do not own a net metering device. Knowing that average yearly electricity consumption in the city of Lisbon is around 1.3 MWh/year/person (Brito et al., 2012), the profiles were adjusted to Alvalade (Figure 7.4).

$$P_{demand,b}(t) = N_{p,b} \times P_{demand,ref}(t)\,, \tag{7.7}$$

where $P_{demand,b}(t)$ is the electricity consumption [kW] in building b at hour t, $N_{p,b}$ is the number of residents in building b and $P_{demand,ref}(t)$ is the value of the reference electricity demand at hour t [kW]. The power demand by influence zone z is, thus, the summation of all $P_{demand,b}$ where $b \in z$.

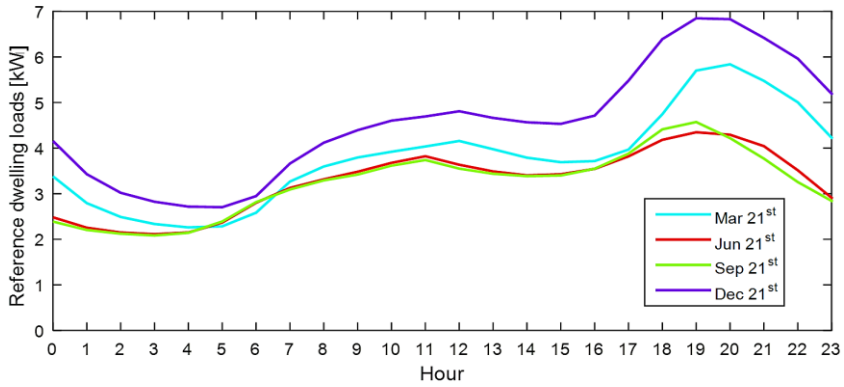

Figure 7.4 - Seasonal reference electricity loads for single dwellings (Freitas et al., 2017a).

It can be observed that the reference demand profiles are typical of residential buildings: baseline consumption mostly during late-night time, with swift increase in the early morning (6/7h), a slight peak around noon and a more pronounced ramp in the early evening (16/17h). Although some of the buildings in Alvalade are of mixed use (i.e. comprehend both residential and office or commercial sections with quite dissimilar demand profiles (Jardini et al., 2000)), the overall aggregation of loads is expected to produce a profile that is closer to a residential profile. It can be observed that the consumption is higher in December (purple line), due to increased artificial lighting and heating needs. The profiles for June and September are similar, possibly due to the tendency for summer weather to extend into autumn months in recent years.

7.3 Results

In the next sub-sections, results produced by the Peak power method and the Irradiance method are compared. The overwhelming impacts of large-scale PV façade deployment are discussed and a solar factor is proposed as a means to lessen long-term grid failures.

7.3.1 Transformer spare power

According to the *Irradiance method*, which produced hourly irradiance results, the whole transformers grid will suffer the highest PV electricity injection at 12h of June 21st in the rooftop only scenario (Figure 7.5, top left) and at 10h of September 21st in the rooftop plus façades scenario (Figure 7.5, top right). The period of electricity production is widened and the peak shifted towards the morning period with the inclusion of façades, except in December when this peak is shifted towards midday. Analogously to the findings in the previous Section, the PV potential here estimated is more than doubled when façades are included and greatly surpasses the electricity consumption during daylight hours. Without façades, the PV production can only satisfy demand for a few hours in summer.

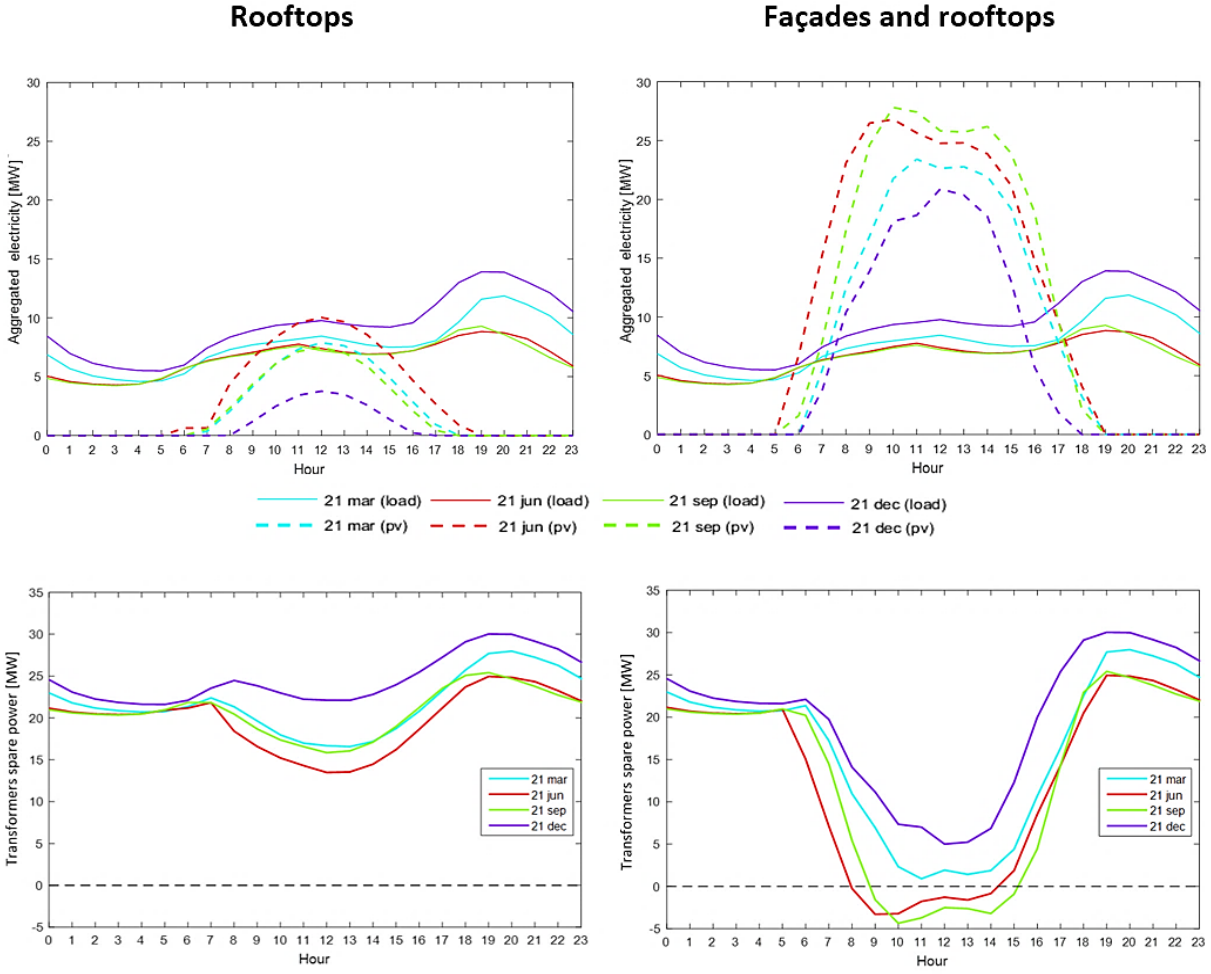

Figure 7.5 - Aggregated hourly electricity load and PV production (top) and transformers spare power (bottom), for the 21st of March, June, September and December, in the rooftops only (left) and rooftops plus façades (right) scenarios (Freitas et al., 2017a).

Consequently, the aggregated transformers spare power is always positive in the rooftop only scenario, for the four reference days. Although particular transformers may be faulty, the grid is able

to accommodate the rooftop PV power at all times. However, the same does not hold when façades are considered, most significantly between 8h and 15h in June and September, when, due to the vertical inclination and larger area, and more favourable weather conditions, they produce more electricity.

i) Rooftops only

The peak of PV production determined by the *Irradiance method* for the rooftop only scenario reaches about 10MW (summer day, at 12h), which corresponds to 62% of the total transformer power capacity (16.1MW).

The power gap for individual transformers is represented in Figure 7.6 as determined by the *Peak power method* (A) and by the *Irradiance method* (B). Yellow to red colours indicate deficit in transformer capacity, whereas white corresponds to sufficient spare capacity for satisfying the zones' demand. The aggregated capacity gap is 68% and 86%, respectively, for plots A and B. This means that, apart from a few local failures, the grid is resilient and has overall enough reserve capacity to accommodate peak electricity generation from rooftop PV. In fact, only one transformer presents a significant issue, given that its capacity (160kVA) might be too low to accommodate a very high PV potential from all the buildings it is connected to. To solve this, instead of upgrading the failing transformer, the reserve capacity of neighbouring transformers could dilute the surplus PV production in the red zone. This suggests that the grid ought to be optimized, representing a more affordable solution.

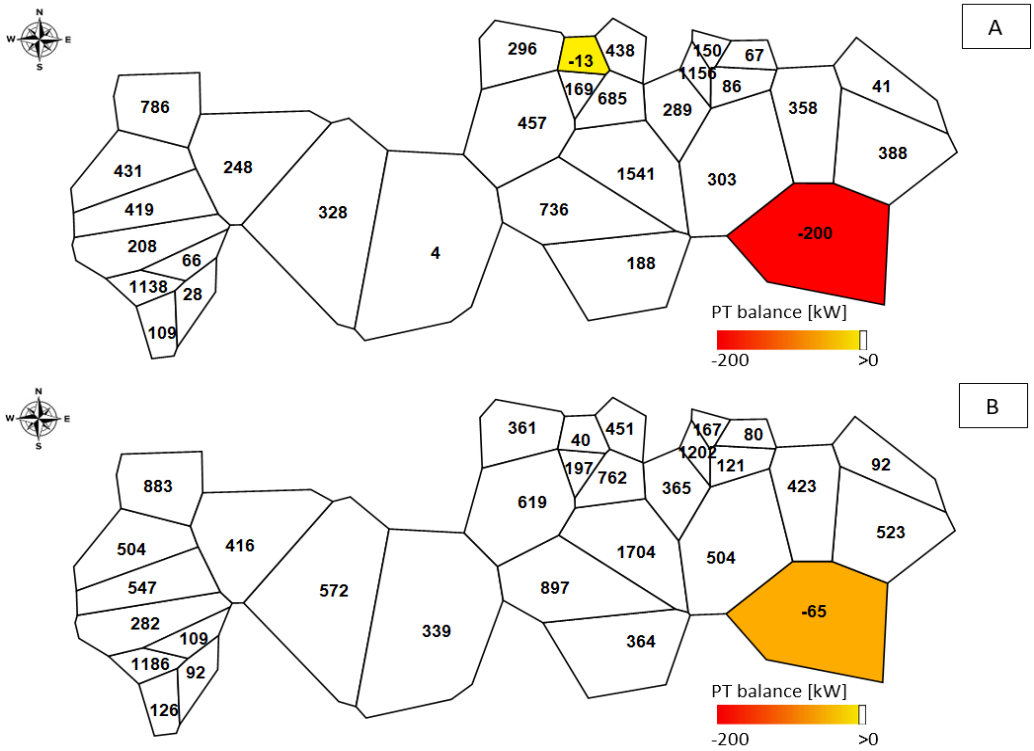

Figure 7.6 - P_{GAP} at each transformer influence zone considering rooftop PV generation using the *Peak power method* (A) and *Irradiance method* (B). Negative values/coloured zones indicate failure at the respective transformer (Freitas et al., 2017a).

Results of the two methods hold a quite linear relationship, featuring an overestimation of around 1% by the *Irradiance method* and a bias of 96kW, which is an important finding in terms of computational effort versus accuracy: the calculation of hourly solar irradiance on rooftops can, to a certain extent, be avoided and a straightforward estimate using reference PV peak power used instead. This is valid,

at least, for urban arrangements and architectures alike Alvalade's, where the PV potential on the variety of rooftop slopes and orientations seems to dilute into the potential of flat and horizontal surfaces, as proposed in (T. Santos et al., 2014). It can, therefore, be argued that the *Peak power method* considering the bias may be sufficiently accurate when only rooftop PV is targeted.

Figure 7.7 (A) highlights the differences between the spare capacity obtained through both methodologies, in terms of absolute difference and relatively to the nominal transformer capacity. Higher differences (red) seem to be related to a larger number of pitched rooftops, which are considered by the *Irradiance method* but not by the *Peak power method*. The fact that the *Peak power method* does not account for shading events may also justify the lower differences. Furthermore, larger influence zones tend to feature higher differences than smaller areas, given the uncertainty caused by a higher number of buildings.

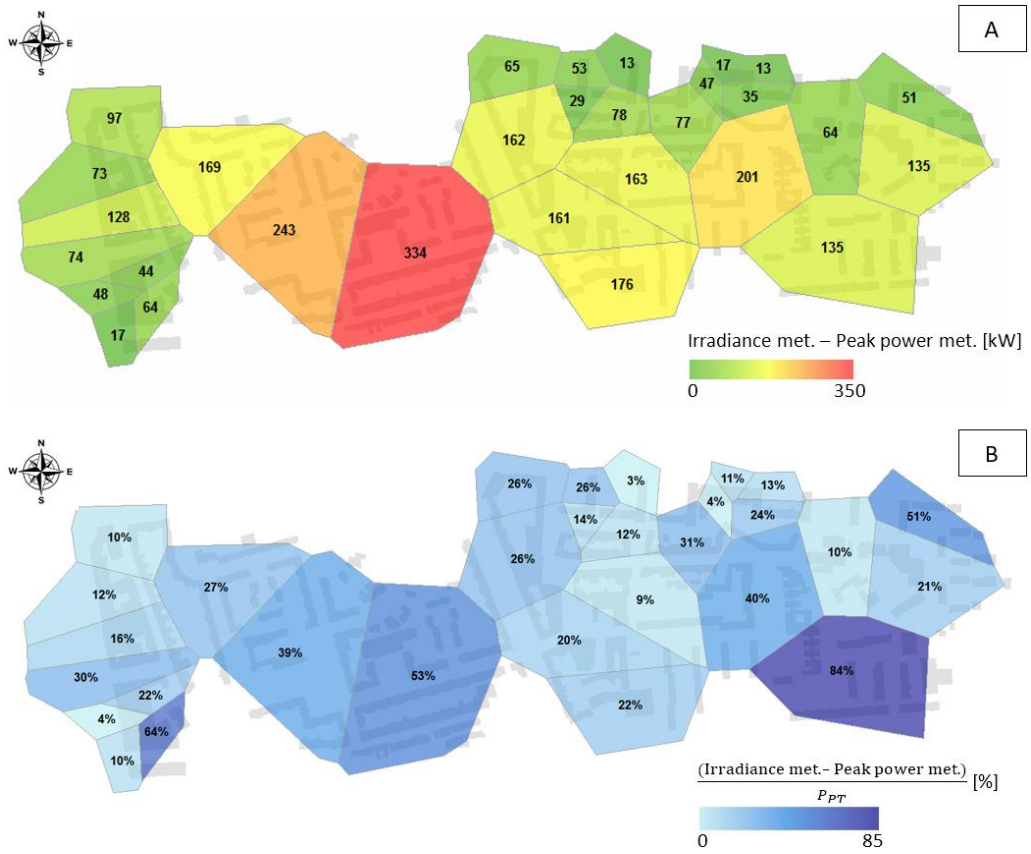

Figure 7.7 - Absolute difference between the *Peak power method* and the *Irradiance method* (A) and difference relative to the respective transformer capacity (B). The grey shadows in the background represent the building footprints (Freitas et al., 2017a).

Conversely, Figure 7.7 (B) shows how an upgrading process could be misled. For instance, considering the zone coloured with the darkest blue shade (southeast corner), the relative difference of 84% would translate into an upgrade of the same order of the nominal transformer capacity, whereas the calculated deficit is only of -65kW. On the other hand, an upgrade to the transformers in zones such as the light blue ones in the northwest corner, with around 10% relative difference, would not imply significant differences whatever the PV estimation method used.

ii) Façades and rooftops

When building façade PV potential is added to the rooftops', the transformer spare capacity estimates change dramatically. The maximum hourly PV potential determined by the *Irradiance method* now approaches 28MW, which is almost twice the whole transformer power capacity. As for the *Peak*

power method, the peak PV production reaches about 73 MW (5 times the grid capacity), overwhelming the aggregated transformer capacity. The electricity balance distribution on the 21st of September, at 10h, is represented in Figure 7.8.

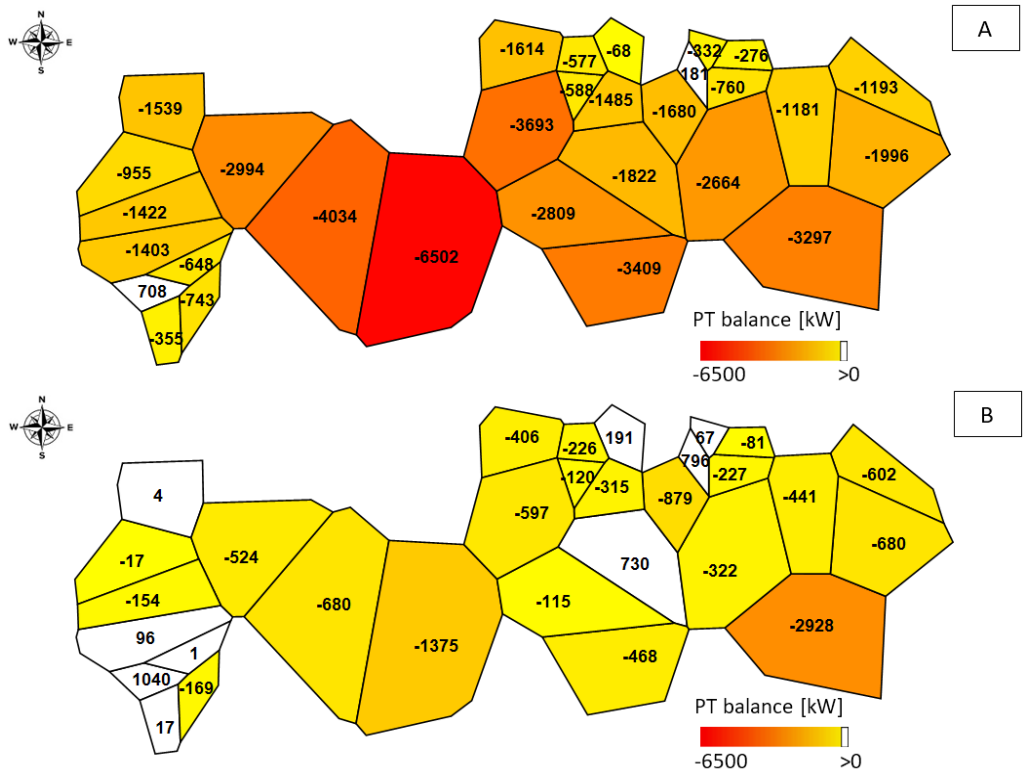

Figure 7.8 - P_{GAP} at each transformer influence zone considering rooftop and façade PV generation using the *Peak power method* (A) and the *Irradiance method* (B). Negative values indicate failure at the respective transformer (Freitas et al., 2017a).

The electricity balance is very negative almost everywhere when the Peak power method is employed. For the Irradiance method, which takes into account the lower irradiation on vertical walls and mutual shading, the transformers with the most significant failures when only the rooftops were considered are even more impacted after the inclusion of the electricity produced by PV façades. There are, however, zones featuring relatively fewer buildings with low energy consumption and/or smaller rooftops that could still accommodate surplus production from their neighbours (Figure 7.8, B).

In this case, the scattering of results between the two approaches is higher when façades are taken into account: a linear regression with a lower correlation (R^2 = 0.40) shows an average overestimation of 70% by the Peak Power method, with a more pronounced bias of 202 kWh, since the PV production of façades is highly overestimated by this approach. Therefore, the more computational intensive approach must be employed, given that proper analysis of irradiance limiting effects is critical to account for the contribution from solar façades. A similar distribution of absolute differences is obtained between the two methods after addition of façade potential (same colour pattern, but proportionally higher values in Figure 7.9, A).

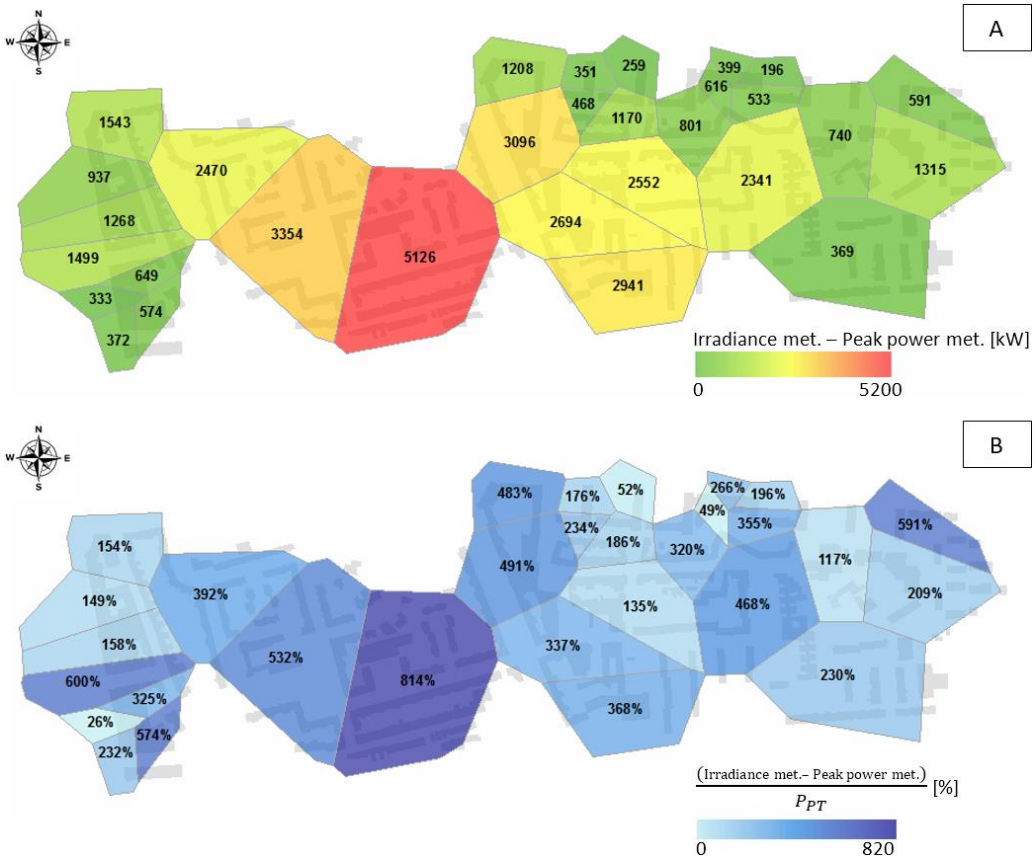

Figure 7.9 - Absolute difference between the *Irradiance method* and the *Peak power method* (A) and difference relative to the respective transformer capacity (B) considering building PV façades. The grey shadows in the background represent the building footprints (Freitas et al., 2017a).

In the worst case, if the simpler method was used, an upgrade to the most challenging transformer zone (dark blue shaded area) would surpass 8 times the transformer capacity. Moreover, after the individual transformer balance analysis, the *Irradiance method* points out that with the addition of façades the overall transformer grid has no spare capacity to accommodate such high electricity feed in, thus the upgrade of almost all the transformers would be mandatory, regardless of a few changes to some transformer interconnections.

7.3.2 Effect of storage

Considering the rooftops plus façades scenario as computed by the *Irradiance method*, and given that the aggregated PV generation exceeds the transformers capacity, an interesting strategy might be the inclusion of electricity storage as a means to increase the transformers availability to supply/receive what prosumers generate/consume. Li-ion technology batteries were assumed, with a roundtrip efficiency of 95% and a minimum state of charge of 20%, and capacities equal to 0, 0.25, 0.5, 1, 2 and 4 kWh/kW$_p$ were analysed.

The storage strategy was applied to the four reference days and followed four basic rules: 1) if the PV production exceeds the load demand, the surplus is used to charge up storage and the remaining production, if any, is sold to the grid; 2) the same as 1, but all the surplus is sold if the storage is already at maximum charge; 3) if the PV production is lower than the electricity demand, the deficit is drawn from the storage bank; and 4) same as 3, but if the storage hits minimum level, the remaining demand is purchased from the grid.

The hourly power gap at each PT (P_{GAP}), described in Eq. (7.8), becomes:

$$P_{GAP}(t) = P_{PT} + P_{demand}(t) + P_{storage}(t) - P_{PV}(t)\,, \tag{7.8}$$

where P_{PT} stands for the transformer nominal power capacity, P_{demand} is the local power demand, $P_{storage}$ is the total storage capacity and P_{PV} generated PV electricity.

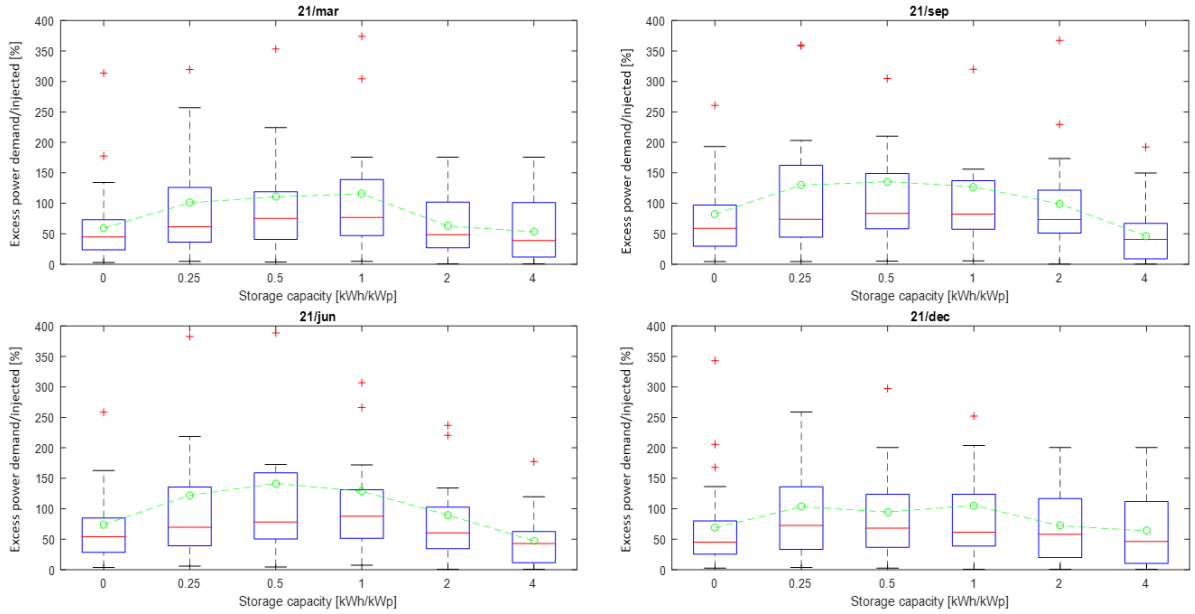

Figure 7.10 - Boxplots representing the distribution of the maximum excess power demand/injected, as a percentage of the transformers capacity, for different storage capacities in all hours of the typical days analysed. (The tops and bottoms of each "box" are the 25th and 75th percentiles, the red line in the middle of each box is the median, the green dots are the average, the black lines extending above and below each box are the extreme values and the red crosses are the outliers.) (Freitas et al., 2017b).

Figure 7.10 shows that a power capacity upgrade of 4 times would be required without storage (0kWh/kW$_p$). These impacts are further enhanced, for most influence zones, when the storage capacity exists but is relatively small (between 0.25 and 1kWh/kW$_p$). This occurs either because there is an instant when the batteries reach their maximum capacity and a high amount of electricity has to, suddenly, be fed into the grid, or the reverse, i.e. when batteries discharge completely and the demand must be satisfied by the grid. As for storage capacities above 2kWh/kW$_p$, a relief impact on the grid, in particular in the summer, seems to be produced.

7.3.3 Solar factor

The results discussed above highlight the importance of considering the potential deployment of PV in buildings when sizing local distribution grids. A forthright method for grid operators to do this, and valid for locations with similar urban arrangements and building architecture as Alvalade, can be achieved by introducing a new term (a solar factor F_{pv} that depends on the available surface area on rooftops and façades) to Eq. (7.9):

$$P_{PT} = abs\left(F_{pv} - C_{diversity} \times \sum_i^N P_{contract} \times F_{safety}\right) + P_{over}\,, \tag{7.9}$$

The solar factor may be determined empirically as (7.10).

$$F_{pv} = [0.38 \times (P_{ref} \times PR \times A_{build}) + 140] \times \frac{\overline{G_{horiz}}}{\overline{G_{horiz,Lx}}}$$

$$= (0.21 \times A_{foot} + 140) \times \frac{\overline{G_{horiz}}}{\overline{G_{horiz,Lx}}}, \quad (7.10)$$

where P_{ref} is the typical square metre PV panel peak power (0.16 kW/m^2), PR is the performance ratio (80%), A_{foot} is the total building footprints area in the location of interest, $\overline{G_{horiz}}$ is the average annual global irradiance on the horizontal plane [kWh/m^2/year] for the same location and $\overline{G_{horiz,Lx}}$ represents the same variable for Lisbon (1868 kWh/m^2/year (SolarGIS, 2017)).

This solar factor deals with variables of straightforward knowledge that characterize the urban solar access at a specific site, similarly to (Sarralde et al., 2015). The term 0.38 and the constant +140 are, respectively, the linear regression slope (R^2 = 0.75) and bias between the PV potential estimated by the *Irradiance method* and the *Peak Power method*, thus accounting for the site's latitude (i.e. the variable solar height during the year) and for the subsequent shading phenomena due to the urban layout and diversity of building heights and forms. Logically, the PV power per unit area and the performance ratio are independent of location. Moreover, the total building footprint area shows a strong correlation (regression coefficient of 4.3 with R^2 = 0.93) with the available surface on building surfaces, which is embedded in the final term 0.21, and the meteorological conditions of the site are introduced by the ratio between average irradiance and the reference irradiance for the specific location analysed in this study.

7.4 Conclusion

A scenario of high PV penetration, however, requires grid expansion. The sizing of urban power transformers for new built areas and the upgrade management of older electrified areas ought to consider future deployment of solar photovoltaics in buildings. If only rooftops are concerned, a simple and straightforward estimation method involving building footprints and PV module peak power represents a valid way of inferring future PV production, while saving time and computational resources. On the other hand, when façades are included, such approach is not appropriate due to lower irradiance and shading from other buildings, thus time-resolved irradiance calculations must be carried out.

Results show that large scale deployment of PV requires grid capacity expansion which ought to be considered in grid planning. An empirical recipe for transformer sizing including local PV deployable is proposed.

Results also show that the introduction of low capacity local storage, operating under PV self-consumption purposes, further enhances the need for grid capacity expansion. Large storage capacities, on the other hand, may be useful for low grid impact of massive PV production. The management strategy might be thought carefully along with proper deployment of PV systems, which should consider the demand profiles and the variety of surface tilts and orientations for achieving a better demand-supply match. This is the topic of the next chapter.

8. SOLAR COMMUNITY BIPV-LOAD-STORAGE

The benefits of combining electricity loads from several buildings and their respective solar PV potential enhances the match between demand and supply, smoothing peaks and reducing grid instability. With decreasing costs and rising popularity, urban community photovoltaic projects, within which the members share investments and revenues, have become more attractive.
This Chapter explores the role of façades on the combined effect of aggregating building demand, photovoltaic generation and storage on the self-consumption of PV and its impact on the grid. The main goal is to evaluate to what extent the building integration of PV alone avoids costs of extra storage while remaining profitable for users and innocuous for the grid. For this purpose, real aggregated electricity demand data from grid distribution transformers was employed; the amount of PV installed in each orientation in the façades and rooftops was optimized through a genetic algorithm aiming for the minimization of ramps and maximization of self-sufficiency; and two storage management strategies were employed, one for maximizing the prosumer profit and the other to reduce net load variance. [10]

8.1 Introduction

In 2015, almost 54% of the world's population was urban and its average electricity consumption exceeded 3.1 MWh/person/year (The World Bank, 2017). Cities have become hot spots for electricity demand, which has, to date, been mostly covered by fossil fuel combustion in utility scale power plants. This form of supply, however, directly contributes to global warming and should be replaced by another that could be commissioned locally, based on local resources and owned by the users. The commissioning of BIPV can bring buildings one step closer to the nZEB concept.
Since a perfect demand-supply match is difficult to accomplish, as verified in Chapters 6 and 7, the grid still serves as both a sink for surplus or a backup for insufficient PV generation. Although it depends on the particular legal framework (Comello and Reichelstein, 2017), from the point of view of the end-user this generally means a high valorisation of the self-consumed electricity and a penalty for the exported electricity. Therefore, an interesting PV system configuration is one that maximizes self-consumption (Luthander et al., 2015). But from the perspective of the grid operator, massive PV deployment could be a technical challenge associated with voltage and frequency regulation (Obi and Bass, 2016) and demand/feed-in ramping rates (Grueneich, 2015), i.e. the net load variance subsequent of changes in the power that is required from the grid to satisfy abrupt increase/decrease in load demand, or the rapid increase in prosumer exports to the grid. Hence, mutual excluding interests for prosumers and grid are apparent, which may eventually set a limit for maximum feed-in power from dwellings (Golden and Paulos, 2015). Nonetheless, this curtailment would entail a loss of production and, consequently, reduce prosumer revenue.
Although PV systems could – in principle – be commissioned according to a broader plan that ensures that the resulting solar electricity generation matches the demand profile of the PV host buildings, this entails a challenge because the behaviour of consumers cannot be trivially inferred. Real dwelling consumption profiles are intricate, featuring high variability and many spikes, which are hard to model in a consistent way (Gouveia and Seixas, 2016)(Grandjean et al., 2012). However, if several different profiles are aggregated, the resulting profile is a much smoother one, with a shape that has a greater

[10] Chapter based on author publications:
- Freitas, S., Reinhart, C., Brito, M. C. "Minimizing storage needs for large scale photovoltaics in the urban environment". Solar Energy, Volume 159, 1 Jan 2018, 375-389, DOI: 10.1016/j.solener.2017.11.011

probability of matching the shape of the PV generation profile. When complemented with storage technologies and suitable management strategies, the combined electricity system might be able to autonomously control ramps, or the net load variance, and enhance self-consumption and -sufficiency. Several studies have addressed the effect of the **aggregation of demand** profiles on self-consumption and -sufficiency rates of distributed solar PV systems, with and without community electricity storage. (Parra et al., 2015) used real demand data from a single home to a 100-home community to determine the optimum community electricity storage system in 2020 and in a zero-carbon year. Cost reductions about 37% and 66% were obtained for a single home. (Lopes et al., 2016) introduced the concept of a Cooperative Net Zero Energy Community, extending the discussion to the enhancement of load matching at the community level. Stochastic load profiles with time resolution of 1 min were employed to produce simulations that pointed out an increase in the self-sufficiency up to 21% and the self-consumption up to 15%. (Nyholm et al., 2016) used real data from 2000 households in Sweden in a model that minimizes the amount of electricity purchased from the grid. Different combinations of PV system sizes and battery capacities were considered, demonstrating that the latter can increase self-consumption in between 20% to 50%, but it strongly depends on the load profile of the dwellings.
It is equally interesting to evaluate the effect of the **aggregation of photovoltaic generation**. If, for instance, the community PV systems are mostly placed on south-facing rooftops, local high net load variance is expected at sunrise and sunset times. This effect could, thus, be mitigated by making use of the variety of orientations and inclinations (Hartner et al., 2015) provided by buildings, such as building façade area (Martínez-Rubio et al., 2016)(Martín-Chivelet and Montero-Gómez, 2017), which helps broadening the peak production throughout the day and providing electricity in the morning and late afternoon, as demonstrated in Chapter 6.
As for the effectiveness of battery storage systems implemented alongside PV, it has been widely documented in literature. Battery costs have been decreasing, although slower than PV's, and their reliability improved. Still, the majority of authors agree that electricity storage is still an unprofitable option for many users, except in very particular conditions or applications. (Weniger et al., 2014)(Naumann et al., 2015)(Merei et al., 2016)(Cucchiella et al., 2016)(Camilo et al., 2017)(Vieira et al., 2017) . On the other hand, the potential of **aggregation of electricity storage** has not yet been thoroughly explored. One example is the study presented in (J. M. Santos et al., 2014), which assesses the importance of distributed storage capacity at the residential level, side by side with the consumption and generation devices. It demonstrates that storage could be paramount for the grid management in high residential PV penetration scenarios, since it reduces the annual maximum power flow values (i.e. the peak power). However, the effect of storage is strongly influenced by its sizing and operating strategy, as discussed in (Parra et al., 2017). The performance, economic benefits and optimum battery capacities for community electricity storage systems were quantified as a function of the size of the community. The optimization algorithm featured demand load shifting strategies based on PV and load forecasts and showed that optimum storage capacity ought to ensure complete discharge during the peak period.

8.2 Case study

The project site is in east Lisbon, Portugal (Figure 8.1, top). The building blocks arrangement is relatively heterogeneous: on the right of the site boundary (by the Tagus river) there is a modern mix of high/medium rise residential buildings, offices, exhibition and recreational infrastructures, commercial buildings, green areas and garden paths; the centre and left side features older and relatively high-density blocks, mainly residential buildings with 2 to 3 stories. The growing predominance of pitched rooftops is apparent from the right to the left side of the project site.

The georeferenced shapefile dataset available for the site included, among other features, the building footprints, respective heights, the location of urban power distribution transformers and their interconnections to buildings. However, when crosschecking the location of the PTs and the electricity measurements provided, some of the PTs were missing from either the shapefiles or from the electricity registers, which shortened the list of usable Blocks/PTs pairs that could be used. Given the large dataset, and for simplicity, only two PTs were chosen. The criteria for this choice was based on the building rooftop features and façade orientations, as well as on the dissimilarity of the electricity demand profiles (but comparable annual aggregated electricity consumption).

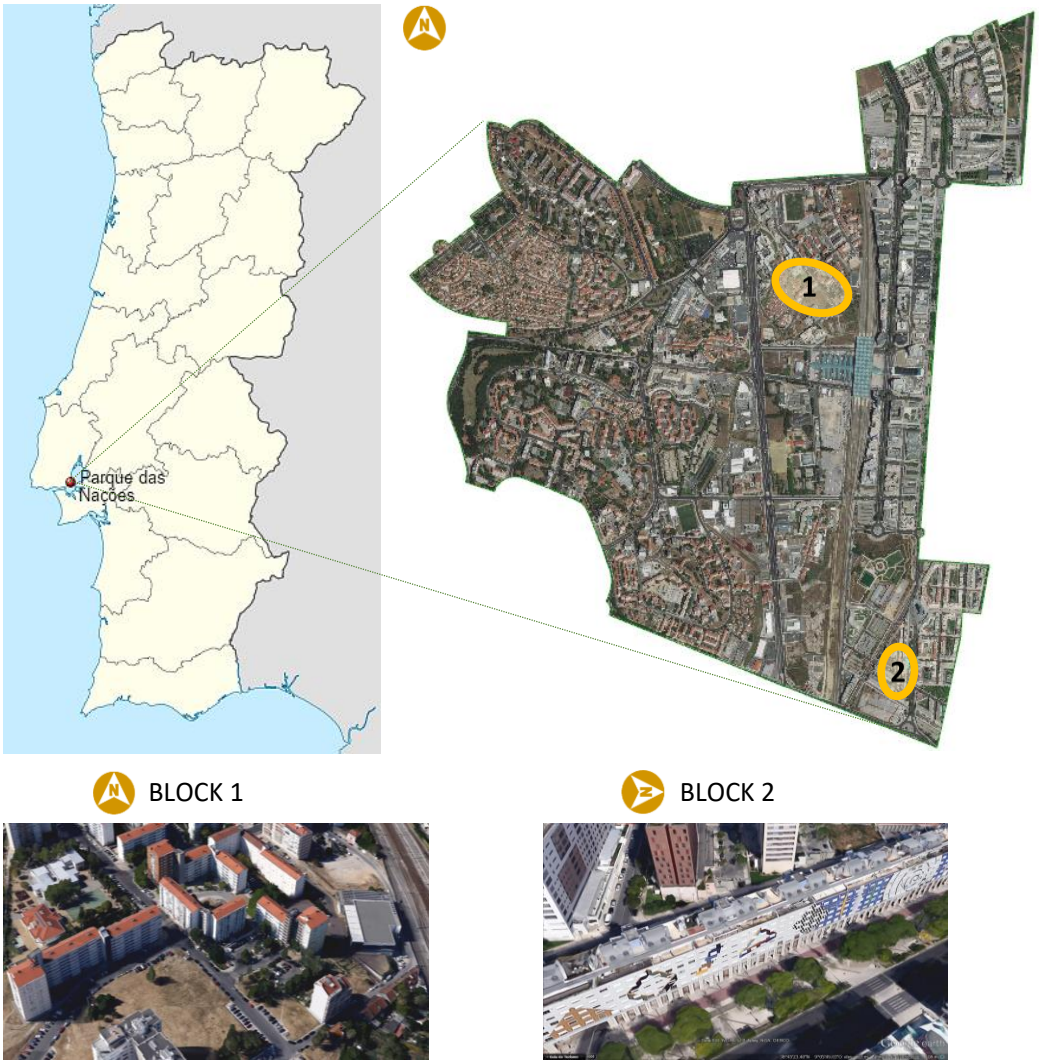

Figure 8.1 - Location of the project site (38°46'05" N, 9°05'38" W), urban context inside the project site boundary (top) and case-study Blocks 1 and 2 (bottom) (Freitas et al., 2018).

Figure 8.1 (bottom) shows the Google Earth view of the selected Blocks. The core of Block 1 is composed mostly of 8-10 stories residencies with gable rooftops and façades with diverse orientations. This Block also comprehends older and smaller dwellings surrounded by tall trees (lower right corner) and low-rise institutional buildings (upper left corner). Conversely, Block 2 is composed of 4 mixed use buildings: a residential fraction on the 6 upper floors and a commercial fraction on the 2 lower floors. Its rooftops are mainly tilted towards the east but are very complex in shape. There is a single façade facing east, with small trees in the front, and a west-facing façade that starts on the third floor, due to outward extension of the commercial buildings and large balconies.

8.3 Aggregated electricity demand

The available electricity demand data set refers to the year of 2015 and comprises time-resolved loads measured in the PTs connected to the case-study Blocks every 15 minutes, thus the consumption profile of each Block is an aggregation of the individual demands from all the different buildings. To avoid extensive computation time, these data series were resampled to an hourly time step. The hourly average electricity consumption for Block 1 and 2 is represented in Figure 8.2. These particular PTs have a nominal power capacity of 1260kVA and 630kVA, respectively for Block 1 and 2.

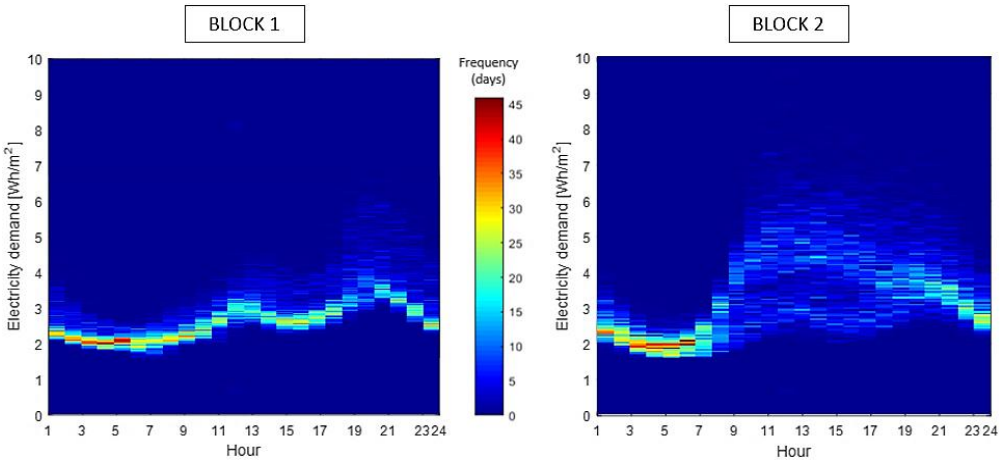

Figure 8.2 - Aggregated electricity consumption for Blocks 1 (left) and 2 (right): frequency of days with given demand normalized by total floor area (respectively 21242 m^2 and 17240 m^2) (Freitas et al., 2018).

Both Blocks 1 and 2 feature an average electricity consumption of about 58kW, with a quite distinct hourly demand: whereas Block 1 (mostly residential buildings) shows a load profile that resembles the shape of the national load profile, with clear morning/noon and early evening peaks, Block 2 (a mix of commercial buildings and dwellings) features a demand profile that bifurcates by 8h, when it either follows a similar behaviour that of Block 1; or ramps up in the early morning and remains relatively constant throughout the day, until 22h when the demand decreases. Block 1 demand profile seems less variable, with a load interval of around 80kW at 7h against Block 2's 130kW at 12h. Baseload demands are rather stable from 1h to 6h.

8.4 Aggregated PV generation

To estimate the hourly PV potential generation, hourly-resolved global irradiation in the plane of the surfaces of interest is mandatory. The irradiation computation, once again, relied on the plugin DIVA (Jakubiec and Reinhart, 2011), addressed in Sub-section 2.4.4. The *LiDAR method* addressed in sub-section 3.2.3 featured a good compromise between accuracy of modelled irradiation and computational requirements. It was, therefore, the method chosen for PV potential estimation.
Another important step was the determination of the surfaces' azimuth, so that they were aggregated from higher to lower level of irradiation by azimuth bins of 45° by 45°. In Figure 8.3 and Figure 8.4, the variability of irradiation levels by azimuth is displayed for both case-study Blocks.
For both Blocks it is confirmed that the area of façade is greater than rooftop area and that east to southwest orientations allow irradiation levels above 800kWh/m^2/year in the façade, which suggests their relevance to the PV potential of these buildings. The most predominant surface orientations in Block 1 are northeast, southeast, southwest and northwest, whereas for Block 2 they are mostly east-

and west-facing. The step-like representation of tilted roofs derived from LiDAR data and the existence of a school building with flat rooftops justifies the higher number of horizontal surfaces in Block 1.

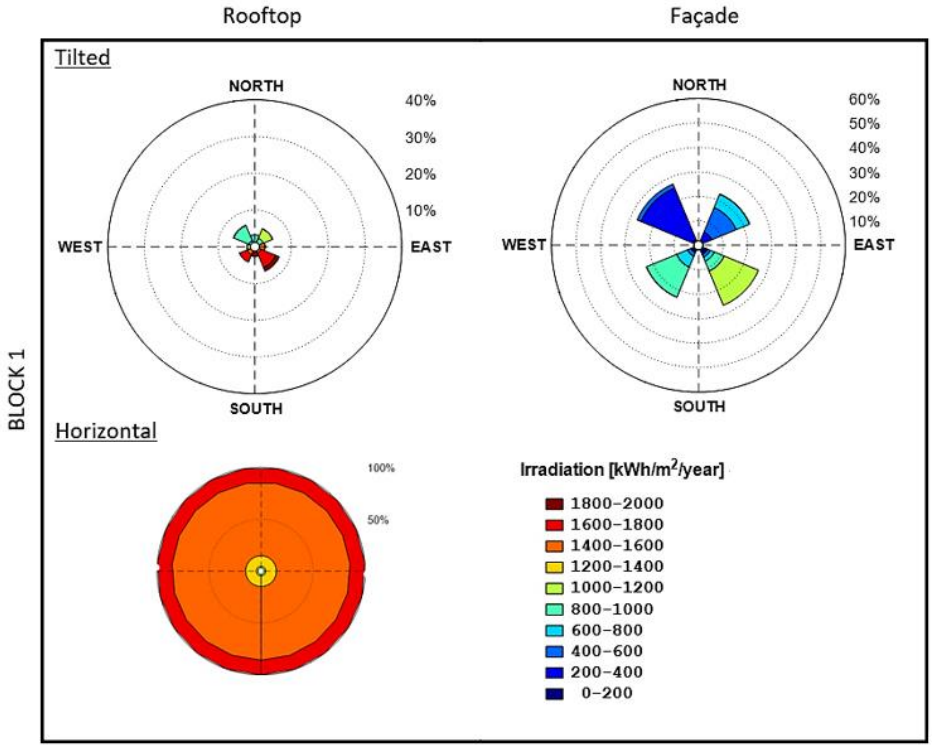

Figure 8.3 - Frequency of average surface irradiation levels in Block 1: tilted rooftop (total of 1875 surfaces), façade (total of 4114 surfaces) and horizontal rooftop (total of 3600 surfaces) (Freitas et al., 2018).

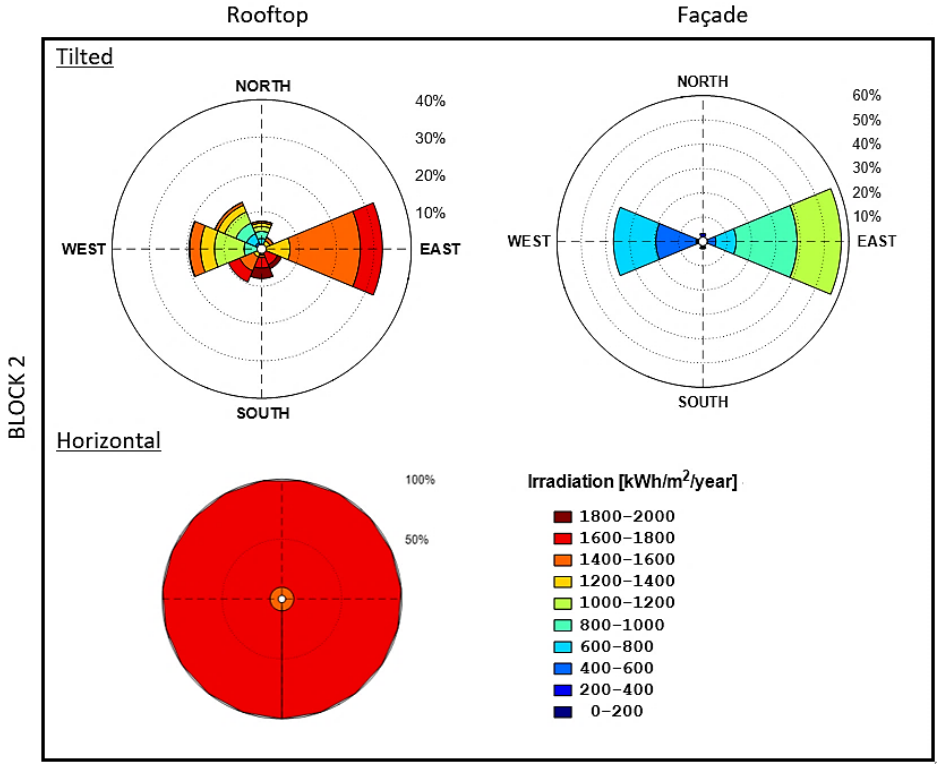

Figure 8.4 - Frequency of average surface irradiation levels in Block 2: tilted rooftop (total of 1832 surfaces), façade (total of 1161 surfaces) and horizontal rooftop (total of 10 surfaces) (Freitas et al., 2018).

After the production of hourly irradiation results, these were automatically operated within Grasshopper and saved to Excel spreadsheets using the TTtoolbox plug-in (The Core Studio Team, 2017), and imported afterwards as data matrixes to MatLab environment for further analysis. The manipulation of such large data sets would have been more demanding if done in Grasshopper alone. The hourly PV generated energy for Block b, $PV_b(h)$, was determined through the following expression:

$$PV_b(h) = \sum_{s=1}^{N_b} \left[G_{tilted,s}(h) \times \eta_r \left[1 - \Delta_\eta \left(T_a(h) + \frac{NOCT - 20}{800} \times G_{tilted,s}(h) - 25 \right) \right] \times A_s \times PR \right] \quad (8.1)$$

where s is the façade or rooftop surface index; N_b is the total number of surfaces in Block b; $G_{tilted,s}(h)$ is the hourly global irradiation on the tilted plane [kWh/m^2]; η_r=15% and refers to an average efficiency for several types of solar panels (Pandey et al., 2016); Δ_η=-0.5% and is the temperature coefficient for efficiency; $T_a(h)$ is the hourly ambient temperature obtained from Lisbon weather file; $NOCT$=48°C is the nominal operating cell temperature; A_s is the surface area [m^2]; and PR=80% [132][361][362] is the performance ratio to account for further energy losses, which may be caused by higher temperature due to building integration, angle of incidence losses (here disregarded, for simplicity), soiling, power electronics efficiency and inaccurately described partial shading from façade and rooftop elements.

With this procedure, it is possible to aggregate the PV potential either by the total or fractions of façades or rooftops or the block totals. An annual overview of the latter, for Block 1 and 2, is presented in Figure 8.5, where the load demand is also plotted for effects of comparison.

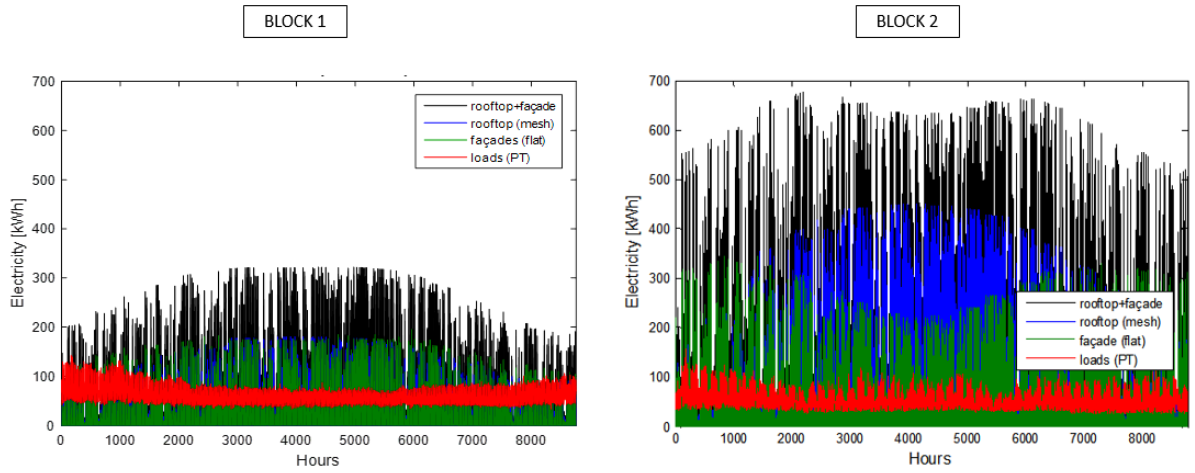

Figure 8.5 - Total hourly estimated electricity production from rooftops (blue), façades (green), rooftops and façades (black) and measured electricity demand (red), for Blocks 1 and 2, for one year.

The electricity demand in both Blocks (red) is greatly surpassed by its aggregated PV potential. Block 1 has relatively the same yields from rooftops (blue) and from façades (green), being higher in the summer. The combined yields from rooftops and façades (black) double and triple the average load demand, respectively, in the winter and summer. Block 2 features higher yields from façades in winter months, which switch roles with rooftops during the summer. The combined yields can be as high as 6 times the average load demand in this block.

It is interesting to note that, unlike the findings in Chapter 7, the two transformers addressed in this study seem to have enough spare power to accommodate the aggregated PV production even at peak times (note that some of the electricity produced during the peaks around the 2000th and 6000th hours of the year will be either self-consumed or stored).

8.5 Aggregated electricity storage

The electricity storage system comprehends elementary Li-ion batteries, currently the most promising battery technology with longer lifespan, higher energy densities and power than conventional lead acid, NiCd and NiMH batteries. In spite of cost and safety issues, the development of electric vehicles is expected to prompt their resolution (Diouf and Pode, 2015).
The storage method consists on several batteries aggregated as one big battery for each Block, with characteristics (Table 8.1) adapted from the commercially available Tesla Powerwall (Tesla Motors, 2017). The total storage capacities explored will be defined by factors of 0, 0.25, 0.5, 1 or 2 kWh of battery capacity (B_{bat}) per total kW of mounted PV peak power.

Table 8.1 – Elementary battery characteristics.

Parameter	Description	Value
C_{rate} [kW/kWh]	Charging rate relative to maximum battery capacity	0.5
C_{bat} [€/kWh]	Unitary cost of the battery	470
SOC_{min} [%]	Minimum state of charge relatively to the nominal battery capacity	20
SOC_{max} [%]	Maximum state of charge relatively to the nominal battery capacity	95
η_c [%]	Charge efficiency	95
η_d [%]	Discharge efficiency	95
η_{inv} [%]	Inverter efficiency	92
$lifetime$[years]	Battery lifespan	10

Losses due to charge/discharge and DC/AC conversion are included through the roundtrip efficiency of the inverter (Lingel et al., 2016).

8.6 Decision parameters

Since this study aims to understand how the placement of PV addresses the variation of the electricity demand and the role of storage from the point of view of both users and grid, a set of decision parameters were chosen to characterize the variety of solutions obtained: self-consumption rate (SC) to know how much PV generated electricity is effectively consumed by the loads (8.6.1); self-sufficiency rate (SS) to characterize the relevance of the self-consumed PV electricity (8.6.2); profit from the PV system (PPVS) to valorise the electricity produced by the PV system (8.6.3); and the net load variance, characterized by the root mean square deviation (RMSD), to quantify the impact in the electricity grid (8.6.4).

8.6.1 Self-consumption rate

This parameter translates into the percentage of the electricity generated by the PV system that was directly or stored and then consumed by the loads, and it is defined in Eq. (8.1).

$$SC = \frac{\sum PV - PV_{exp}}{\sum PV}, \tag{8.1}$$

where PV_{exp} refers to the PV produced electricity that was exported to the grid [kWh].

8.6.2 Self-sufficiency rate

If one wants to know the percentage of electricity demand that the self-consumed PV represents, the following expression can be used to determine the self-sufficiency rate:

$$SS = \frac{\sum PV - PV_{exp}}{\sum E_{dem}}, \tag{8.2}$$

where E_{dem} means the electricity demand [kWh].

8.6.3 Profit from PV systems

The value of the electricity by the community PV system is estimated under the Portuguese self-consumption law (ADENE, 2014), including investment, operation and maintenance costs. In one hand, it involves the self-consumed PV generated electricity that would otherwise be billed at around 0.155 €/kWh, single tariff for 2015 (ERSE, 2016a), and, on the other hand, the PV electricity that is injected into the grid, which is rewarded at 90% of the retail electricity market prices for 2015, i.e. around 0.055 €/kWh. PPVS is then defined as:

$$PPVS = \frac{-C_0 + \sum_{y=1}^{L} \frac{C_y\,(1+inf)^y}{(1+r)^y}}{\sum_{y=1}^{L} \frac{PV_y\,(1-dg)^y}{(1+r)^y}}, \tag{8.3}$$

where C_0 is the initial investment cost [€]; C_y is the return in year y; inf is the inflation rate (2%); r is the opportunity cost of capital (6.5%); L is the lifetime of the system (25 years); PV_y is the PV system electricity production in year y; and dg is the degradation rate for PV (0.25%/year).

$$C_0 = C_{pv,f} + C_{pv,r} + n_{bat} C_{bat}\,, \tag{8.4}$$

where $C_{pv,f}$ and $C_{pv,r}$, based on (Fath et al., 2015), are the cost [€] of the PV installation for the façade and rooftop, respectively, considering a decrease of costs due to construction material substitution; A_f and A_r, respectively, correspond to the areas of PV modules installed in the façade and rooftop [m^2]; P_{ref} is the PV peak power density (0.16 kW/m^2); n_{bat} is the number of batteries and B_{bat} is the storage capacity (0, 0.25, 0.5, 1 or 2 kWh/kW$_{pv}$) and

$$C_y = \left[\sum_1^{8760} PV_{exp}(h) e_s(h) + PV_{sc}(h) e_p\right] - C_{om} - C_{rep}\,, \tag{8.5}$$

where PV_{sc} entails the self-consumed PV generated electricity [kWh]; e_s is an hourly time series with the retail electricity market prices for 2015; e_p is the grid single tariff for 2015; C_{om} is the operation and maintenance costs (equal to 1% of C_0 a year) and C_{rep} is the replacement costs of the storage (equal to $n_{bat} C_{bat}$, but only applicable in years 10 and 20, and if $B_{bat} \neq 0$).

8.6.4 RMSD of the net load variance

The rate of electricity exchanges at the PT level (i.e. from the aggregated PV system, to the loads and from/to the grid) can be analysed in terms of hourly net load variance, colloquially known as ramps. Figure 8.6 illustrates the net load variance verified when consumption is done solely from the grid. The variance distribution is relatively symmetrical around 0kW, with most of it located between -10kW and 10kW, but reaching up to almost -30kW and 40kW.

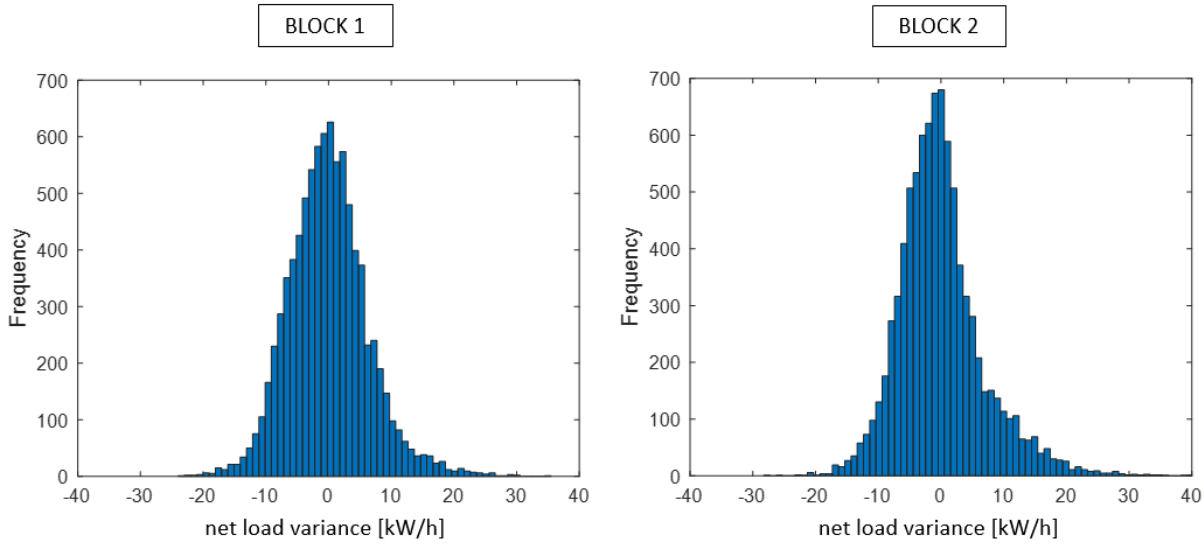

Figure 8.6 - Histogram of the hourly net load variance over the period of 1 year, for Blocks 1 and 2.

A parameter to describe how distant a net load variance series is from the ideal case (i.e. zero variance, electricity balance at the PT constant during the day) is crucial, thus the root mean squared deviation (RMSD), defined in Eqs. (8.6) and (8.7), was determined relatively to the ideal net load variance, which ought to be zero from the point of view of grid stability. Unlike the average of the series, the RMSD guarantees that the extreme values relatively more weighted.

$$RMSD_{NLV} = \sqrt{\frac{\sum_1^{8760}\left(0 - NLV(h)\right)^2}{8759}}, \tag{8.6}$$

$$NLV(h) = \left|PV_{exp}(h+1) - PV_{exp}(h)\right| - \left|E_{imp}(h+1) - E_{imp}(h)\right|, \tag{8.7}$$

where $NLV(h)$ is the hourly net load variance, E_{imp} is electricity purchased from the grid [kWh] and PV_{exp} is electricity sold to the grid. Since there is no simultaneous purchase and sell, $NLV(h)$ is defined to be positive if excess PV electricity is being sold to the grid or negative if demand is being satisfied by the grid.

8.7 Scenarios: PV optimization and storage strategies

Six scenarios were stablished to evaluate the impact of the location of PV panels, the storage capacity and its management in the grid stability and profitability for the solar community. The scenarios build up in complexity: scenario A-opt aims to maximize self-sufficiency and minimize $RMSD_{NLV}$ through an optimal placement of PV by orientation bins using a multi-objective genetic algorithm (8.7.1); scenario B-opt has analogous optimization objectives as A-opt but includes a storage strategy to maximize self-consumption (8.7.2 - i); and scenario C-opt builds up on B-opt but encompasses a storage strategy for the minimization of $RMSD_{NLV}$ instead (8.7.2 - ii). The three remainder are “business as usual” variations of these scenarios (denoted as A-, B- and C-bau) as a means for quantification of the improvements attained by the PV placement optimization. In these scenarios, the surfaces are simply extracted and aggregated from higher to lower irradiation levels until the PV peak power reaches the same value as in the corresponding optimized solution. The storage strategies do not change. Table 8.2 provides a summary of these scenarios.

Table 8.2 – Type of PV optimization and storage strategy in the considered scenarios ("bau" and "opt" stand for "business as usual" and "optimal" respectively).

Scenario	PV optimization	Storage strategy
A-bau	Higher irradiation places first	No storage
A-opt	Percentage of PV by orientation bins to maximize self-sufficiency and minimize $RMSD_{NLV}$	No storage
B-bau	Higher irradiation places first	Charge with PV surplus and discharge when PV deficits
B-opt	Percentage of PV by orientation bins to maximize self-sufficiency and minimize $RMSD_{NLV}$	Charge with PV surplus and discharge when PV deficits
C-bau	Higher irradiation places first	Minimize $RMSD_{NLV}$
C-opt	Percentage of PV by orientation bins to maximize self-sufficiency and minimize $RMSD_{NLV}$	Minimize $RMSD_{NLV}$

8.7.1 PV optimization

The placement optimization of PV panels over the building surfaces is the core routine for all scenarios and entails an adaptation of the multi-objective genetic algorithm described in Section 5.2. Of course, the encoding step, which needed proper adaptation to the specific problem in the present study, and the objective functions underwent reworks.

In the present case, the routine starts with the attribution of values to several parameters, loading the hourly irradiation and load demand data series and generating many random possible solutions (referred to as chromosomes or individuals) to the objective functions. The population size was set to 200, so that the search space would be enlarged, thus 200 first-generation solutions were created by distributing a semi-random number between 0 and 100 among the 17 free slots of 200 empty vectors. (Figure 8.7). Each free slot denominates an azimuth and the percentage refers to the quantity of surfaces facing that azimuth that will be selected, starting from the surfaces with higher irradiation.

	Façade								Rooftop								
	S	SW	W	NW	N	NE	E	SE	S	SW	W	NW	N	NE	E	SE	H
1	13	58	76	4	25	16	38	71	0	36	10	86	71	5	36	44	60
2	92	73	25	95	52	62	52	6	2	26	7	15	4	20	11	60	33
…					…								…				
200	30	62	0	21	54	8	23	3	53	62	35	4	26	53	0	25	36

Figure 8.7 - Example of the semi-random number generation in the encoding step of the optimization of the PV placement routine. (H stands for horizontal).

The fitness of all solutions was evaluated afterwards, in terms of the parameters $RMSD_{NLV}$ and self-sufficiency: the minimization of the first guarantees the goodness of the solutions from the point of view of the grid and the maximization of the second assures that the community will make the most of its PV installation. Similarly to the process in Chapter 5, the population of solutions was then grouped in pairs and underwent a 2-point crossover. The offspring had a 2% chance of mutation and only the 10% best replaced the 10% worst parents in the next generation. The resulting population was evaluated and Pareto fronts were constructed based on the population ranking.

At the end of each cycle, the stopping condition is checked, which in this case is a maximum number of generations of 200. The last generation is normalized according to the maximum $RMSD_{NLV}$ and self-sufficiency values. The normalized solution with slope equal to 1 is extracted from the Pareto front, assuming it is where the best compromise between $RMSD_{NLV}$ and Self-Sufficiency lies.

8.7.2 Storage strategies

A loop for the storage strategy was nested inside the PV optimization main routine. This loop runs individually for each one of the 200 solutions when their performance is being evaluated. Two different operation strategies were employed: i) strategy SC, for self-consumption maximization, and ii) strategy RMSD, for $RMSD_{NLV}$ minimization. The batteries were fully discharged at the beginning of the cycle and all the electricity exchanges with the grid were affected by the inverter efficiency. The storage capacities studied (B_{bat}) were 0, 0.25, 0.5, 1 and 2 kWh/kW_p.

i) Strategy SC

Given that the generated power is preferably used to satisfy the electricity demand while the surplus production is stored, this method maximizes self-consumption (Struth et al., 2013). Nevertheless, the batteries will likely be completely charged before the noon peak PV generation in clear sky days.
This strategy is specific of scenarios B-bau and B-opt and follows four core rules:

1) if the PV production exceeds the load demand, the surplus is used to charge up storage and the remaining production, if any, is sold to the grid;
2) Storage the same as 1, but all the surplus is sold if the storage is already at maximum charge;
3) if the electricity demand exceeds PV production, the deficit is drawn from the battery bank;
4) same as 3, but if the storage is entirely discharged, the remaining electricity demand is purchased from the grid.

ii) Strategy $RMSD_{NLV}$

The goal of this strategy is to minimize ramp $RMSD_{NLV}$ parameter, i.e. minimize the total amount of electricity exchanges with the grid by finding the best storage schedule. For simplicity, perfect forecast is assumed given the yearly load demand and PV generation historical data. A linear programming sub-routine based on (R. Martins et al., 2016) was written for this purpose.
Linear terms can be used to formulate this optimization problem, which is solved once for each day of the year. It translates into:

$$min \sum_{h=1}^{24} \left[E_{imp}(h) + PV_{exp}(h) + B_{exp}(h) \right], \tag{8.8}$$

where B_{exp} is the electricity exported from the batteries to the grid [kWh]. Note that this strategy allows the battery bank to sell electricity to the grid, since there might be times when it is useful to discharge the batteries for future charge when there is too much surplus, which might help reducing the net load variance.
As in any linear programming method, there are constraints that must be met:

$$\begin{cases} PV(h) = PV_{sc}(h) + PV_{bat}(h) + PV_{exp}(h) \\ E_{dem}(h) = PV_{sc}(h) + B_{sc}(h) + E_{imp}(h) \\ B_{soc,i}(h) = B_{soc,f}(h) + PV_{bat}(h) - B_{sc}(h) - B_{exp}(h) \\ B_{soc,f}(h-1) = B_{soc,i}(h), \end{cases} \tag{8.9}$$

where PV_{bat} entails the PV produced electricity that charges the storage bank [kWh]; B_{sc} is the load demand supplied by the batteries [kWh]; $B_{soc,i}$ and $B_{soc,f}$ are the energy state of charge of the batteries [kWh] respectively at the beginning and ending of hour h. In the first hour of the first day of the year, the storage is assumed fully discharged. After the equality constraints are defined as matrixes, the lower and upper bounds are defined. The lower bounds are 0 for all variables, except for

$B_{soc,i}(h)$ and $B_{soc,f}(h)$ that are defined by SOC_{min} and the PV peak power. The upper bounds for $PV_{sc}(h)$, $PV_{bat}(h)$ and $PV_{exp}(h)$ are equal to $PV(h)$; for $B_{sc}(h)$ and $E_{imp}(h)$ are equal to $E_{dem}(h)$; for $B_{soc,i}(h)$ and $B_{soc,f}(h)$ that are defined by SOC_{max} and the PV peak power; and for $B_{exp}(h)$ it is defined by the difference between SOC_{max} and SOC_{min} and the PV peak power. The *linprog* MatLab function is called to solve the optimization problem.

8.8 Results

This section presents and discusses the effect of optimizing the placement of PV by orientation bins of the available surfaces (8.8.1) and the impact of battery management and the general compatibility between the decision parameters is addressed (8.8.2).

8.8.1 PV placement optimization (scenarios A)

The convergence of solutions to a well-defined Pareto front (Figure 8.8) is paramount for the extraction of the optimal solution (as demonstrated in Chapter 5), which, in this case, is the PV configuration that maximizes self-sufficiency and minimizes the $RMSD_{NLV}$.

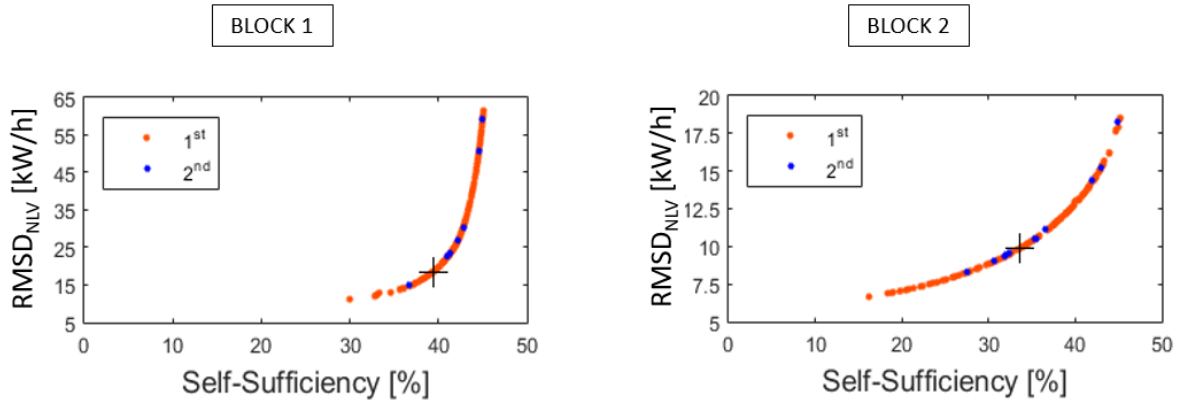

Figure 8.8 - Results from Scenario A-opt for Block 1 (left) and 2 (right): first (red) and second (blue) pareto fronts from the last generation. The cross marks the optimal solution. (Freitas et al., 2018)

The PV distribution solution that achieves the best compromise between the decision parameters is marked in the corresponding pareto front in Figure 8.8 and presented in detail in Figure 8.9.
A-opt results for Block 1 show maximum self-sufficiency rates of around 45%, which means that only 45% of the electricity demand is supplied by the community PV system, and minimum $RMSD_{NLV}$ of 10kW/h, meaning that the net load variance is relatively low comparing to the extreme values. However, the impossibility of achieving high self-sufficiency and simultaneously low $RMSD_{NLV}$ is apparent. The PV configuration that fulfils both criteria has a self-sufficiency of 39.4% and $RMSD_{NLV}$ of 18.6 kW/h. This solution features a façade installation area that is 6 times as large as the rooftop area, although façades have a non-optimal inclination and lower annual irradiation levels. Such preference is due to the lower amount of electricity produced when the demand is lower, but also because some orientations allow the spread of PV production throughout the day (Brito et al., 2017) (as explored in Chapter 6).

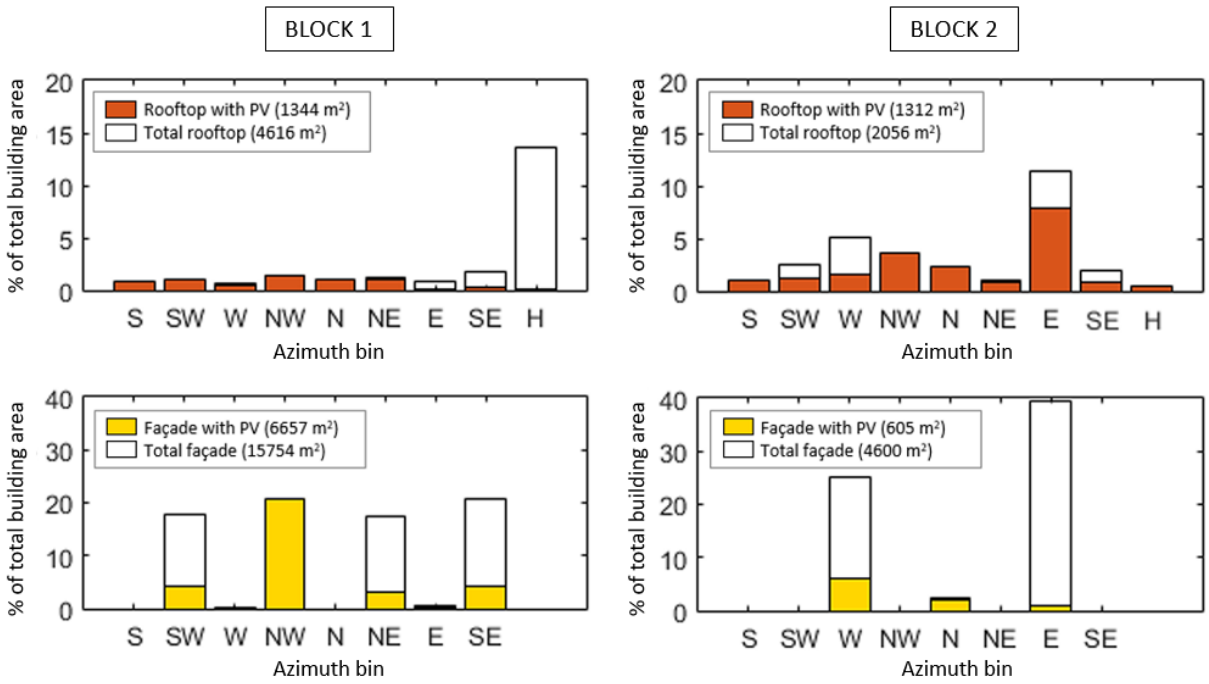

Figure 8.9 - Optimum distribution of PV area on rooftops and façades for Scenario A-opt (no batteries). yy-axis shows total area available (bordered bar) and used for PV (coloured bar) as a fraction of total building area, for each orientation. Results for Block 1 (left) and Block 2 (right), rooftops (up) and façades (bottom). H stands for horizontal rooftop surfaces. (Freitas et al., 2018)

The slots corresponding to north-west azimuths are fully occupied in both façades and rooftops, which would be counterintuitive if demand-supply adjustment was not considered. To avoid high net load variance and foster PV self-consumption, the optimal systems are biased towards such azimuths given an increased electricity consumption in the morning and in the late afternoon (Figure 8.2). This is particularly relevant in the summer due to larger sunrise and sunset azimuths, which allow the sunshine rays to reach north-facing surfaces.

Scenario A-opt results for Block 2 features a reduced range of $RMSD_{NLV}$ values, from around 7 to 19 kW/h, which is due to the smaller available area, in comparison with Block 1 that might feature high net load variance associated to PV produced electricity injection into the grid. Self-consumption covers a range from 15% to 45% and, again, the trade-off between self-sufficiency and $RMSD_{NLV}$ is clear. In this case, the optimal solution points to an occupation of more than 50% of the rooftop available area, whilst only 13% entails façade area. Block 2 features a large east-facing façade, but just a very small portion of it should host PV modules, so that major net load variance in the early morning can be evaded. Contrarily, the west-facing, and even north-facing, surfaces might contribute to a better adjustment of the supply to the demand in the late afternoon, when the consumption remains high but slightly constant for a few hours. Furthermore, the distribution of PV by rooftop surface azimuth also corroborates this, since the east-facing surfaces occupation is only about 10% - in the rooftop, the surfaces facing east are tilted but far from being vertical, which might adjust better to the morning peak demand.

Comparison of the best solutions of Scenario A-opt with Scenario A-bau (Figure 8.10) confirms the relevance of selecting the right percentage of occupancy by azimuth band in a building PV installation: in both Blocks, the “business as usual” approach would have fulfilled the well-performing rooftop surfaces first and the façades’ best afterwards. The north- and west-facing areas would have been neglected.

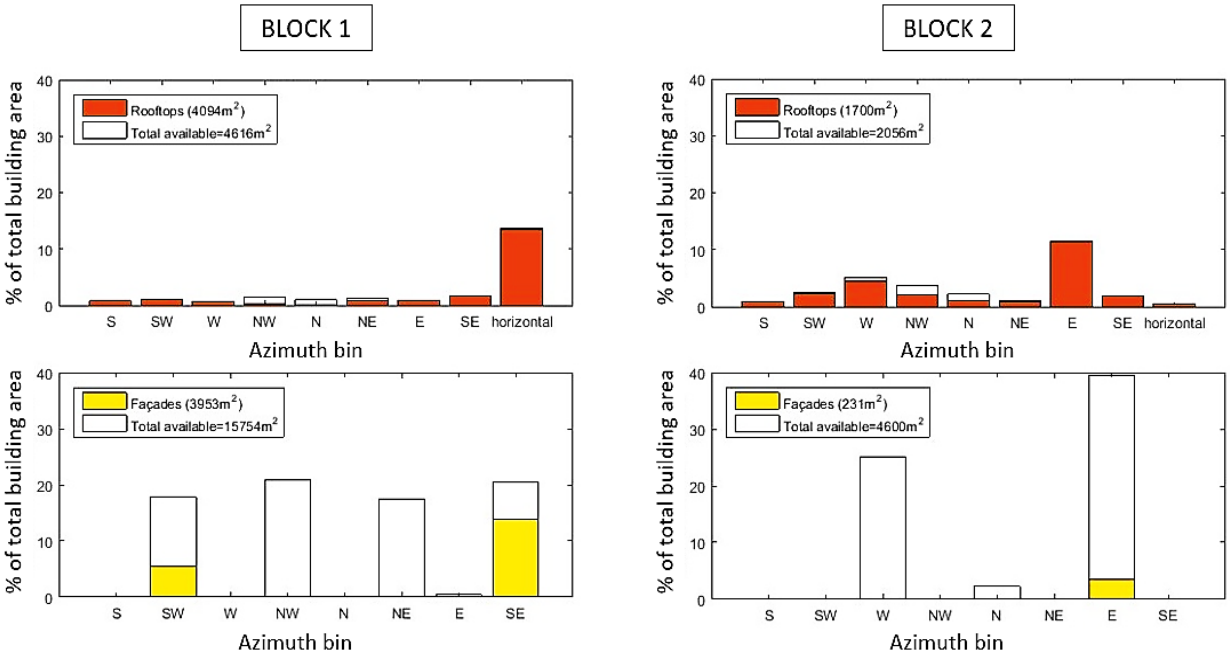

Figure 8.10 - Scenario A-bau for Block 1 (left) and Block 2 (right): percentage of occupancy by PV modules of the azimuth bins available in rooftop and façade surfaces.

To adequately grasp the importance of the optimization from Scenarios A-opt and A-bau, the remaining decision parameters must be known. Table 8.3 compares Scenarios A-opt and A-bau for both case-study blocks. A-bau features surplus production around noon (since PV is mounted in higher irradiance areas, i.e. mostly south-facing), while A-opt provides better demand-supply balance and, thus, much higher self-consumption. Self-sufficiency remains high, but it slightly decreased for the sake of reducing net load variance.

Table 8.3 – Annual PV generation and load demand [MWh/year], and decision parameter values for scenarios A-bau and A-opt for Block 1 and 2.

	Block 1		**Block 2**	
	A-bau	A-opt	A-bau	A-opt
E_{dem}	522		504	
PV	1039	329	272	186
$RMSD_{NLV}$	53.0	18.6	13.7	9.8
SS	45.0	39.4	41.4	33.6
SC	22.6	62.5	76.7	90.8
PPVS	0.10	0.15	0.16	0.18

Apart from $RMSD_{NLV}$ and self-sufficiency, the positive effects of adjusting the community electricity generation to its electricity consumption through inclination/orientation management of the PV modules are also noticeable in terms of self-consumed PV production (up to 90% in the Scenario A-opt for Block 2). Moreover, the PPVS obtained in Scenarios A-bau was always lower than in A-opt, stressing the high value of locally produced electricity (which avoided grid purchase). However, the self-sufficiency rates from A-opt solutions are 20% lower than A-bau's. This is not surprising since A-bau solutions would certainly belong to the right hand-side $RMSD_{NLV}$ tip in the Pareto fronts, thus holding more significant negative impact to the grid side than the user side.

8.8.2 PV placement optimization and storage strategy (scenarios B and C)

The numbers presented in the previous Sub-section might be increased using an appropriate storage strategy. It is expected that the optimal installed PV power changes as the storage capacity increases, which depends on the employed management approach. Through Figure 8.11 and Figure 8.12, the optimal percentage of façade and rooftop PV by azimuth bin can be compared, for all the storage capacities explored in Scenarios B-opt/B-bau and C-opt/C-bau (A-opt and A-bau are also represented as the null storage capacity case).

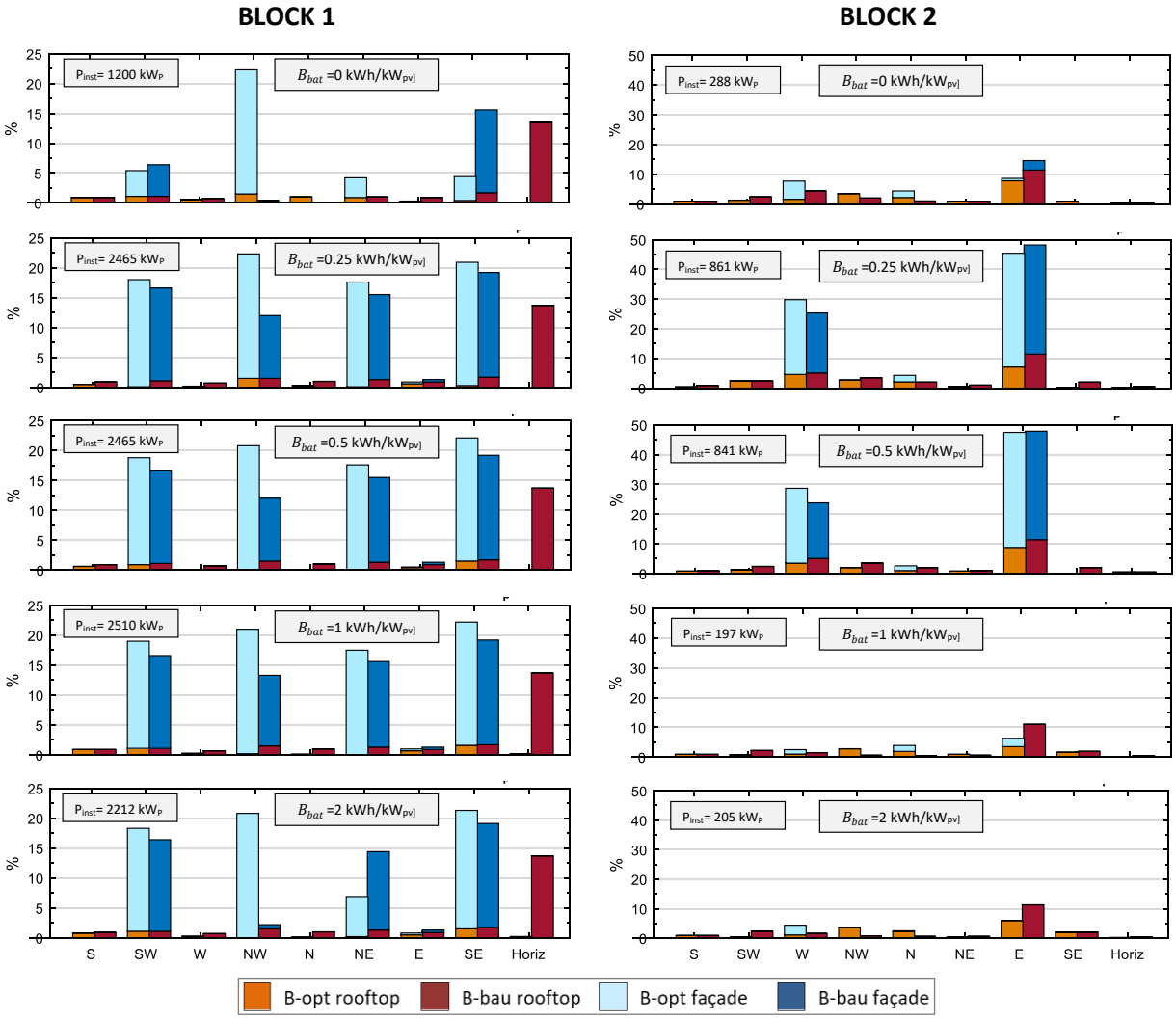

Figure 8.11 - Optimum distribution of PV area on rooftops and façades for Scenario B-opt (orange and light blue) and B-bau (red and dark blue), for Block 1 (left) and Block 2 (right), from lower (top) to higher storage capacity (bottom). yy-axis shows area used for PV as a fraction of total building area, for each orientation. The corresponding optimal PV peak power is given. Note that the percentages in the axis limits are different for the 2 blocks. (Freitas et al., 2018)

The optimal aggregated peak power for Block 1 under Scenarios B-opt/B-bau is twice as high as in Scenarios A-opt/A-bau, with increased share of façades (blue bars) in the SW, NW, NE and SE orientations. From B-opt to B-bau, almost all the rooftop surfaces are preferred over façade surfaces, since the irradiation levels are generally lower in the latter. It can be realised that for a block with a fair diversity of surface orientations and tilts (Block 1), the inclusion of storage capacity does not cause significant changes in the optimal installed peak power and PV layout (i.e. large systems increase self-

sufficiency, but the production from different façades peaks at different times of the day, which helps reducing net load variance). For large storage capacities, the SC strategy slightly pushes the systems towards lower installed peak powers, compromising self-sufficiency and $RMSD_{NLV}$, but increasing self-consumption. These findings suggest that an aggregated storage bank of 0.25kWh/kW_p that follows the strategy SC would, thus, be appropriate for this community. On the other hand, a larger storage cluster might be the best option for Block 2, as the recommended PV peak power is higher for small storage capacities (0.25 and 0.5kWh/kW_p). Given that the majority of building surfaces face east or west, the self-consumption will be high regardless of storage; therefore, one optimal solution consists on significantly reducing the deployed peak power to further decrease $RMSD_{NLV}$ (to avoid sudden net load variance due to a fully charged/discharged battery).

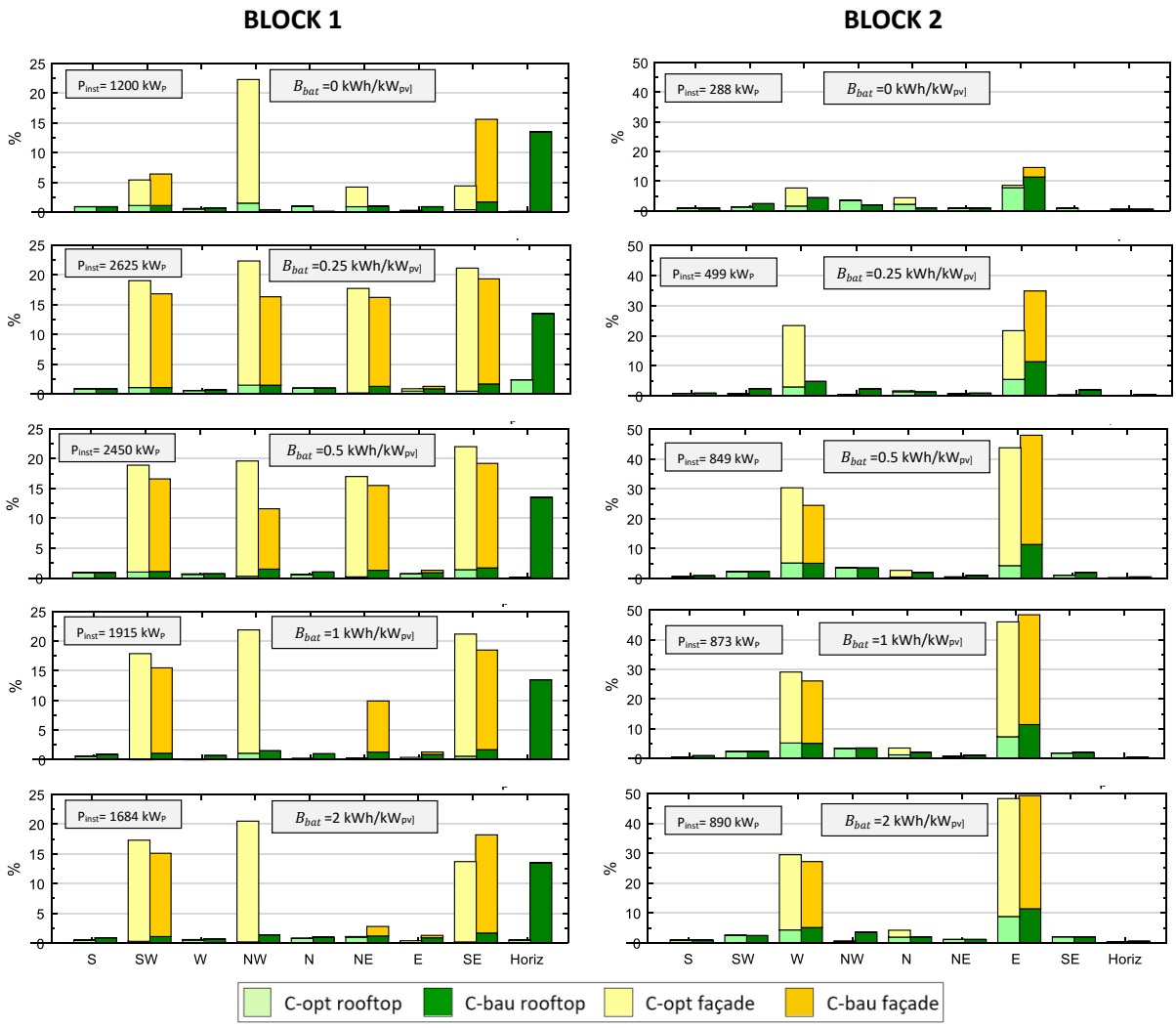

Figure 8.12 - Optimum distribution of PV area on rooftops and façades for Scenario C-opt (light green and light yellow) and C-bau (dark green and dark yellow), for Block 1 (left) and Block 2 (right), from lower (top) to higher storage capacity (bottom). yy-axis shows area used for PV as a fraction of total building area, for each orientation. The corresponding total PV peak power is given. Note that the percentages in the axis limits are different for the 2 blocks. (Freitas et al., 2018)

Although Block 1 features only slight changes in the distribution of PV for storage capacities equal to 0.25 and 0.5 kWh/kW_p under Scenarios B-opt, the converse is observed for Scenarios C-opt. Significant changes occur for storage capacities of 1 and 2 kWh/kW_p: the overall share of façades (yellow bars) is reduced, with no occurrence of façade surfaces facing NE, which might be thanks to the supply during

the night time/morning period assured by the large storage capacity. C-bau, however, retains only a small amount of PV on those places. The community PV capacity more than doubles from A-opt/A-bau to C-opt/C-bau, but keeps decreasing as storage increases. The contrary is observed for Block 2, where a significant increase in W and E façade surfaces can be noticed. The share of occupied azimuth bins remained practically unaltered from storage capacities 0.5 kWh/kW_p on: given that the RMSD strategy sought to minimize $RMSD_{NLV}$, it was not very effective since that goal had already been accomplished through a suitable placement of PV.

The overall quality of these aggregation solutions can be analysed considering the four decision parameters (compiled in Figure 8.13). The difference between scenarios B and C is the storage control strategy: the first can be understood as a 'selfish' strategy, which aims to maximize the benefit for the prosumers and the latter is a 'cooperative' strategy, to minimize impact on the grid. With a small battery, a selfish strategy can have a relevant impact on the community's self-consumption and self-sufficiency at the exchange for negative consequences to the grid: strong net load variance will occur when the battery is fully charged/discharged (which will happen frequently because the battery is small). On the other hand, a 'cooperative' strategy, thought to lessen net load variance, will prevent making full use of the (small) battery and, consequently, its effect on self-consumption will be much less significant. For large storage, both strategies lead to higher levels of self-consumption and (relatively) low net load variance.

Overall, the PV optimization method together with an adequate battery management (B-opt and C-opt, solid lines in Figure 8.13) can provide lower $RMSD_{NLV}$ than its equivalent scenario without PV optimization (B-bau and C-bau, dashed lines in Figure 8.13). This parameter also decreases from smaller to higher storage capacities. A storage management aiming to reduce $RMSD_{NLV}$ with perfect forecast (C-opt/C-bau) proves its effectiveness, whereas the maximization of self-consumption per se (B-opt/B-bau) might induce occasions when the batteries are at maximum/minimum level and cannot act - sudden high net load variance consequently takes place, as observed in (Luthander et al., 2015).

Self-sufficiency grows with battery capacity, more remarkably from 0 to 0.5 kWh/kW_p; this emphasizes the important role that aggregated storage has on improving what had already been achieved through the optimized aggregation and placement of PV. This parameter converges asymptotically to 100%, since the PV installation is fixed and optimized for an aggregated demand profile that varies throughout the day and year, and not to point-in-time situations. A slight change in a parcel of the system might produce benefits for an occasion but can be disadvantageous in another, even with storage it may be impossible to achieve perfect demand-supply match. Thus, the storage operation strategy and the characteristics of the consumption profile have a strong influence on what can be considered the absolute optimal configuration of PV and storage.

The trade-off between $RMSD_{NLV}$ and self-sufficiency is undoubtedly apparent: B-bau and C-bau, which prioritise high irradiation places, entail higher self-sufficiency than B-opt and C-opt, which seek for the best compromise between self-sufficiency and $RMSD_{NLV}$. This is more evident for Block 1 than for Block 2, where the PV configuration computed by C-opt or C-bau with storage equal or above 0.5 kWh/kW_p appear to be good solutions, with C-opt achieving a self-consumption rate slightly higher than C-bau. Regarding Block 1, the estimated self-consumption rates are very high for B-opt and C-opt, but halved for B-bau and C-bau, which underlines the importance of combining PV from diverse orientations and inclinations in optimal ways.

The PPVS parameter entails mostly negative values for both Blocks, only positive for small or null storage capacity. Such outcome is mainly due to the current impracticality of investing in high capacity storage, even as a community, as pointed out Section 8.1. Large shares of façade PV (in B-opt and C-opt), which is still less affordable than rooftop PV, might also contribute to higher investment. Moreover, weighted the advantages of deploying more façade PV and including larger batteries, the scale inclines towards the first, thus minimizing storage needs for urban solar communities.

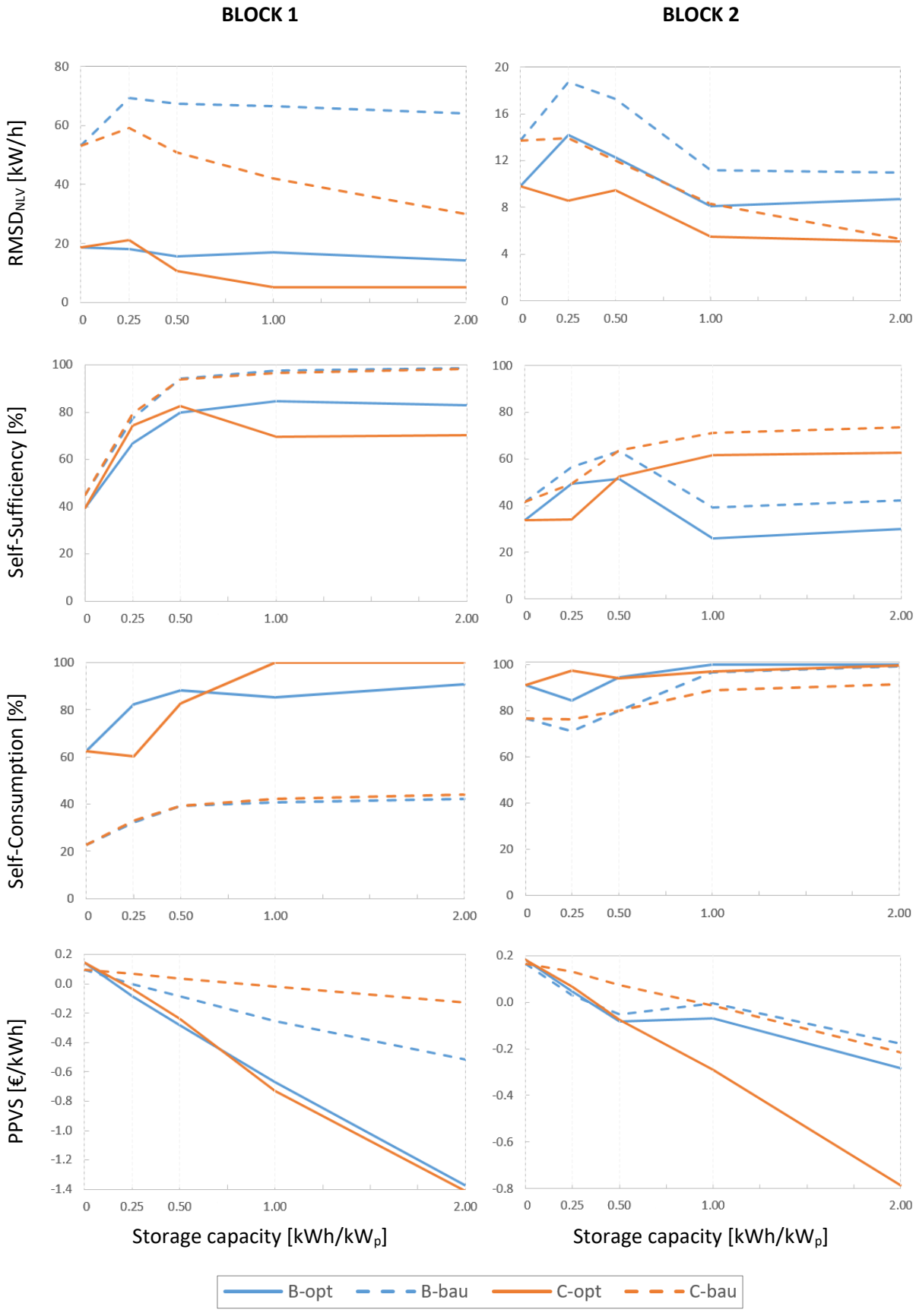

Figure 8.13 - Overall results for RMSD$_{NLV}$, SS, SC and PPVS as a function of storage capacity, for Scenarios B-opt (blue solid line), B-bau (blue dashed line), C-opt (orange solid line) and C-bau (orange dashed line). (Freitas et al., 2018)

8.9 Discussion

In this Section, a few methodological limitations of this study and further implications of its findings will be discussed.

First, it would be beneficial to extend the analysis to other PTs with dissimilar demand profiles and building blocks with different architectonic features. Ultimately, the study should encompass the broader cityscape level. In this sense, and given that the computation of time-resolved solar irradiation is labour-intensive, a possible strategy would be to, first, calculate a reference irradiation profile for all possible tilt and azimuth combinations and, then, assign those profiles to all the surfaces across the urban model, instead of computing each one at a time. However, a successful implementation of this approach would be compromised by the morphing of shadow patterns, a high resolution of tilt and azimuth angles and sub-hourly time step. Nevertheless, tiling strategies (Romero Rodríguez et al., 2017b) can be employed for massive urban models.
The demand-supply issues that distributed PV with storage faces were clearly identified, regardless of specific building morphologies and consumption profiles. Yet, the original time resolution of the demand profile (15min) was lowered to the hourly level. The higher the time step, the more demand and generation peaks and breaks are excluded (regardless of aggregation effects), making the net load variance analysis less accurate.
The use of a reference meteorological year also represents a limitation. Preferably, solar radiation measurements from a nearby station (of course, covering the same analysis period) would have given better insight into the relationship between electricity consumption and meteorological conditions. Assessing the influence of solar radiation variability on these results would also be interesting, since present and future variability might influence the optimal PV façade layout.
In the method for PV generation estimation, it was considered that the modules were deployed onto the surfaces as they are, i.e. without tilt or orientation changes (very common in horizontal and non-south-facing building surfaces), otherwise the complexity of this study would have increased greatly. However, this addition increases the cost of the system and often causes the systems to become less aesthetical appealing.

Regarding the economics of the systems, it must be noted that no economy of scale was considered for neither the aggregated PV nor the aggregated storage portions of the community investment. This could have significantly lowered the costs of the configurations that entailed large installed peak power. As for the storage, it is more difficult to infer at current market state. However, it is likely that the effect of the economy of scale will be pronounced in the medium-term, given decreasing battery prices (Liebreich, 2017), prompted especially by the urge for electrical mobility.
As for the aggregation per se, although it is suggested that the distribution PT grid defines the convenient size for a community project, there is no warranty that having the current PT capacities and interconnections is the optimal solution for massive PV penetration in the city of the future (as also observed in Chapter 7).

Nonetheless, it was demonstrated that aggregating demand, PV production and storage has advantages for the user and should therefore be encouraged. This fosters the creation of urban solar community projects, which consists on the cooperation between multiple members who can benefit from power and/or revenue from PV systems. In exchange, each individual gives his contribution to the communal project, for instance, in the form of an up-front purchase of an element for the PV system or monthly contributions on the electricity bill. The system owner, system host, installation

size, number of participants, individual country/state policy, etc., will vary as per the specificities of each project (Erin Takata, 2017).
It can be argued that, in first approximation, the costs for the electricity grid are mostly dictated by the maximum peak power. Hence, one concludes that local solar communities have the potential to assist the grid by lowering their local peak power. Table 8.4 summarizes the peak power obtained in the scenarios explored.

Table 8.4 – Maximum absolute peak power in the electricity grid [kW], for Block 1 and 2. Bold highlights the 3 lowest peak power achieved for each Block.

Grid peak power

$max[abs(supply - demand)]$

		Storage capacity				
		0 kWh/kW$_p$	0.25 kWh/kW$_p$	0.5 kWh/kW$_p$	1 kWh/kW$_p$	2 kWh/kW$_p$
Block 1	B-bau	476	539	539	540	533
	B-opt	142	142	142	160	142
	C-bau	476	587	580	543	710
	C-opt	142	223	**121**	**121**	**121**
Block 2	B-bau	126	133	133	126	126
	B-opt	126	126	126	126	126
	C-bau	126	119	135	**106**	245
	C-opt	126	119	**112**	**113**	115

Peak power features a broad range of values for scenarios involving Block 1. For Block 2, due to the prevalence of east-facing surfaces (Figure 8.4), the maximum peaks are all of similar magnitude. As expected, scenario C-opt with storage capacities above 0.5 kWh/kW$_p$ seems to allow lower costs with power supply for the grid.
Results reveal that conflicting interests between users and grid exist: higher returns to the solar community lead to increased burdens to the grid, whereas the smoothening of the demand profile leads to diminished returns for the PV owners. Nevertheless, traditional utilities have started making efforts towards understanding how the value from distributed generation and storage can be captured and fit into their business models (Trabish, 2017). Some key advantages of including those electricity systems relate to: reduced usage (or entirely removal) of expensive and polluting peaker plants, which usually sit idle for long periods of time; deferral of upgrades to utility assets or creation of new transmission and distribution lines; and lessened power outage events.
There are, at the same time, opportunities for the creation of new financial business models if the value of reduced peak loads is regarded, and benefit sharing between the grid and the local solar communities. As an example, a storage bank was recently connected to distribution circuits at Southern California Edison's Mira Loma substation (Cardwell, 2017) to help smoothing variations in the power flow from/to rooftop PV clients, hence avoiding curtailment of PV (i.e. loss of profitability for the community) and the need to supply when conventional power plants cannot meet the pronounced electricity demand in the early evening. In this example, however, the battery bank is centralized and owned by the grid, but new business models could explore different ownership aspects of the storage system, including distributed storage among the community and even third-party storage. These must bear in mind that the proper energy management of the solar community, and especially the control strategies for the batteries, has a critical impact on the overall system performance and the complementarity between solar community and grid (and/or, eventually, all other electricity consumers): a 'selfish' management algorithm could lead to a decrease of up to 35%

in self-sufficiency, while annual net load variance would grow up to 50%, with an average 20% higher peak power (Figure 8.13).
Building deployed PV systems only in locations with high solar exposure (typically those facing south), instead of making use of the diversity of surface tilts and orientations, will lead to adverse impacts on the grid. The latter contributes to flatten net load variance profile, since it prompts a wider period of PV electricity generation that matches the demand profile throughout the day. Therefore, façades that have been quantitatively considered as "less-than-optimum" places, now become advantageous to a greater purpose by providing quality electricity. Additionally, possible approaches to entice the installation of PV systems in façades might include the commonly adopted self-consumption metering solutions, which favour off-peak generation by valuing avoided consumption over excess generation, or 'time-of-use' feed-in tariffs, which realize higher returns early and/or later in the day.
Lastly, it must be emphasized that a massive growth in local solar communities will trigger a disruption in the electricity market, since prosumers wish to reduce the purchase of electricity from the grid while maximizing exchanges of power with other community members (through micro cooperative utilities). Given the potential for becoming notably present in the grid, the concept of citizen utilities will certainly convert into reality. As stressed in (Green and Newman, 2017), citizen utilities will need to be accommodated within the future distributed system paradigm, where the traditional grid will still have a role to play. This new energy market, managed by consumers, will introduce dramatic changes to generation, consumption and transaction of electricity.

8.10 Conclusion

The multitude of building surfaces with different tilts and orientations in the urban environment translates into a greater PV potential that, if well used, results in a better adjustment of local production to demand, in the context of self-demand PV systems with and without electricity storage. When the placement of the PV systems is optimized considering different generation profiles triggered by a diversity of surface tilts and orientations, the consumption from different buildings and the PV electricity production can be aggregated to improve the demand-supply match within a solar community, minimizing its storage needs.
The profitability of community PV systems might always be positive when no storage is considered (reaching almost 0.2 €/kWh in the studied cases), and decrease as storage capacity rises. However, the inclusion of electricity storage boosts both self-consumption and -sufficiency, which tend asymptotically to a very high value (even to 100%, in some scenarios). Net load variance has potential for reduction as storage capacity increases, although slight variations might be observable in the low storage regime.
From the point of view of a prosumer community, investments on PV may only be viable with null or very small added storage capacity. Conversely, the electricity grid prevents unmanageable net load variance while mitigating its consequent costs through higher storage capacities with proper management strategy. Hence, grid/local authorities ought to support the commissioning of grid, community or third-party owned storage capacity with adequate management standards to curtail or control net load variance. At the same time, new business models are required to share the added values between the interested parts.

9. CLOSURE

The sustainable development of present generations and their continuity into the future cannot be detached from renewable energy research and development. Technologies for converting solar radiation into electricity are especially relevant, since the sun is the most basic source of energy for planet Earth. A turning point was reached when PV became cheaper enough to be brought closer to electricity demand hot spots: buildings in the urban environment. Rooftop systems have been the most adopted solution, whilst façades are often disregarded. This thesis highlights the role of façades for the solar potential of cities and explores optimization alternatives and tools for its modelling.

The variety of cityscapes in the world prompts different solar potential, apart from the latitude bias, which must be assessed prior to the deployment of solar energy systems. Empirical solar radiation models have been developed and improved to estimate the solar radiation falling on surfaces with arbitrary orientation and tilt, coupled with long-term measurements from ground weather stations and/or satellite imagery. The intricacy of urban environments requires more sophisticated methods for the proper modelling of shadows. Diffuse radiation falling in a surface is challenging to compute given its anisotropy, thus buildings and context materials/coverage and the varying sky conditions must be accounted for. This is particularly relevant for building façades, since their vertical inclination gives them higher exposure to ground and surroundings reflected radiation and their sky view factors, smaller than rooftops', reduce background sky diffuse radiation according to the sky patches that are obstructed.

Improved computational power has driven the creation of sophisticated solar potential models relying on digital surface models that can portray building features with realism. Vector data with building footprints and LiDAR-derived elevation data are among the cost-efficient methods to create a 3D city model. Time-resolved irradiation in a full 3D environment including vertical surfaces can be estimated through state-of-the-art models, with emphasis on GIS, CAD/plugin and CityGML-based tools, although simplifications might be unavoidable when addressing high density environments. Results can easily be manipulated to produce significant content related to PV potential to aid in the process of urban planning and decision making towards sustainable cities.

Experimental validation is fundamental for urban solar potential models that include façades, as it helps identifying current limitations and where the accuracy of the algorithms fails. Pyranometers are not commonly installed in building façades to validate model simulations, however, it is possible to use generation data from PV systems. Irradiation simulations must be carried on over an updated surface model that includes trees, and then converted into electricity production before it is compared against reference façade and/or rooftop systems data. The spatial resolution dictates the complexity of the electricity conversion method, but the effects of temperature on the module efficiency, the effect of the angle of incidence on the radiation that effectively reaches the solar cells and partial shading in the PV strings are important loss mechanisms to consider at an hourly time frame and spatial resolution of $1m^2$.

Proper modelling of façade PV potential in places with dissimilar climatic conditions gives insight into where the contribution of vertical surfaces to the PV potential is more relevant and where its deployment should be encouraged. It is known that higher tilts favour PV production as latitude increases, as lower sun heights allow for the light to reach these surfaces close to the normal, but the fraction of diffuse irradiation might also enhance the relevance of façades in respect to the rooftops in mid-latitude locations. A building has mostly at least two façades facing opposite directions, hence higher diffuse radiation content traduces into more frequent overcast sky conditions that distribute the irradiation more evenly across the built environment.

Different PV technologies can be employed to make the most of a PV system regardless of climatic conditions. Whereas the mature technology of c-Si modules is an affordable and efficient solution, limited aesthetics have been their main drawback when building owners want concealed or disguised PV systems. Specific projects might result well with conventional flat and opaque modules, but façade products seek to achieve new colour possibilities for spandrel areas, higher degrees of transparency for glazing surfaces and flexibility for alternative architecture designs. Glass printing or anti-reflection coating tuning are techniques that allow for the customization of conventional façade PV systems. On the other hand, despite their lower quality, thin films are also an option to achieve translucent and colourful PV façade glazing or canopies. Vertically integrated bifacial modules represent a means to save space and to give an alternative look to façade elements such as balconies or railings. The raising popularity of, yet low efficient, luminescent solar concentrators has prompted the creation of commercial window products that make PV almost unnoticeable. Other types of concentrating alternatives are, however, inappropriate for façades as they are less responsive to higher diffuse content.

Building integrated PV can either be perceived as electricity generating devices that are an additional part of the building skin or the opposite, i.e. an intrinsic building element that has the added value of producing energy. This dual character of BIPV is what makes it particularly interesting for façade applications, given the variety of elements and the vast range of possibilities for PV integration. Other improvements of PV over conventional construction materials relate to the possibility of making use of the heat generated on the rear side of the modules to passively regulate indoor comfort and, in the case of semi-transparent and translucent technologies, regulate daylight levels in the interior spaces. Moreover, these complementary functionalities of BIPV can translate into financial payback.

Systems yields can be further maximized if early-stage façade designs contemplate the integration of PV. Horizontal tilted louvers can enhance the irradiation that reaches façade PV in about 30% in comparison to a flat vertical layout, whilst more complex forms increase yields at the cost of using much more PV material. Another alternative design encompasses the use of bifacial modules as balcony railings, where the back surface receives reflected radiation from within the balcony area. In this case, the rear surface of the module contributes with about 1/3 to the total production. These are examples of strategies to make good use of area that otherwise would remain idle.

Another important issue to take into account in façade PV systems is partial shading, which has a dramatic effect on the electricity production of PV strings, reducing yearly yields of the whole PV system in 6% to 24%. Micro-inverters represent a reliable but costly solution to the problem. Module sitting and string interconnections must be such that more sunlit areas get clustered and relatively short strings, whilst less lit places either get very short strings or individual modules or no modules at all. Optimal layouts keep the compromise between annual energy generation potential and investment costs.

Maximizing the electricity yields either through alternative façade layouts or by seeking the most adequate module technology have consequences on the outdoor spaces, such as visual discomfort or disability glare. Fully glazed mirror façades are relatively common architecture in dense modern cities, but there are no specific guidelines to regulate these issues. Highly reflective materials in building façades should be discouraged, despite the design goals, unless simulations prove its safety. Other way around might be to rethink the building layout to adopt PV technologies instead of conventional reflective materials. Although typical c-Si modules feature reflection losses for high incidence angles, these are not as dramatic as reported for mirror or glass. Nevertheless, PV glass technologies have emerged that seek to further reduce reflection losses.

The deployment of PV at a larger scale should primarily match the electricity consumption of neighbourhoods. Whereas typical south-facing rooftop PV generates surplus around midday, with the addition of solar façades it is possible to start producing earlier in the day, with east-facing façades,

and extended production to later, with west-facing façades. This helps widening the period of the day when local electricity demand can significantly be covered by solar, especially in the summer. Although the production of PV façades is higher in the winter, a lower number of sunlight hours reduces the contribution of solar to the supply chain.

The levels of irradiation over building surfaces translate into different classes of profitability for PV systems. Combination between façades and rooftops can be deployed as a function of the cost. In a city like Lisbon, a 50/50 mix would encompass a combined payback time of around 15 years, at current prices, whereas considering only the most exposed surfaces would lead to paybacks in the order of 19 years. Since the efficiency of the modules is expected to continue increasing with decreasing costs, a combined payback of around 10 years can be achieved through 40% of the PV deployment in façades. Further reduction of investment costs and increasing module efficiency will lead to high penetration of PV in the electricity grid. A scenario of full integration of PV into buildings in a suburb will, however, overwhelm grid assets such as distribution transformers with lower power capacities. The generation potential including façades must be taken into account when sizing transformers in new built areas or when upgrading the existing ones. New interconnections may also be planned, if neighbouring transformers have spare capacity to accommodate PV surplus, which is a cheaper solution than increasing transformer capacity in dense urban areas. More than faulty transformers, the whole local grid might become unmanageable if large amounts of PV are fed into the grid. Sudden net load variance, either due to abrupt breakdown in PV production in periods of high demand or increased PV supply when demand is lower, must be avoided since it causes grid management to compensate with fossil fuel peaking power plants.

The future of solar cities might reside in the creation of local solar communities, sharing the investment costs and revenues from PV and storage systems optimized to match the aggregated load profile. Community solar systems will be placed preferably in tilted rooftops and façades with orientations that will likely produce when consumption is more likely, i.e. they will make use of the variety of building surfaces and occupy only the places that match the requirements. Aggregated storage will work as a buffer to further maximize community's self-sufficiency, but also to avoid excess PV production being fed into the grid. The grid will continue playing its crucial balancing role, thus future electricity markets and business models need to consider the arising conflicting interests between prosumers and grid. Sharing the value of distributed generation and reduced peak due to the integration of PV in building façades will be one essential component of this integrated system.

10. REFERENCES

A.L. Martins, T., Adolphe, L., E.G. Bastos, L., 2014. From solar constraints to urban design opportunities: Optimization of built form typologies in a Brazilian tropical city. Energy and Buildings 76, 43–56.

Abu-Bakar, S.H., Muhammad-Sukki, F., Freier, D., Ramirez-Iniguez, R., Mallick, T.K., Munir, A.B., Mohd Yasin, S.H., Abubakar Mas'ud, A., Bani, N.A., 2016. Performance analysis of a solar window incorporating a novel rotationally asymmetrical concentrator. Energy 99, 181–192.

ADENE, 2014. Decreto-Lei n.º 153/2014 D.R. n.º 202/2014, Série I. Retrieved from: http://www.adene.pt/decreto-lei-no-152-2014-de-20-de-marco

Alias, A.-R., Pilouk, M., 2008. Spatial Data Modelling for 3D GIS. Springer, ISBN 3540741674.

Amado, M., Poggi, F., 2014. Solar Urban Planning: A Parametric Approach. Energy Procedia 48, 1539–1548.

Ameri, T., Khoram, P., Min, J., Brabec, C.J., 2013. Organic Ternary Solar Cells: A Review. Advanced Materials 25, 4245–4266.

American Institute of Architects, 2015. Design Excellence Awards. Retrieved from: https://www.aiachicago.org/dea_archive/2015/fki-tower-exterior-wall/

Angelis-Dimakis, A., Biberacher, M., Dominguez, J., Fiorese, G., Gadocha, S., Gnansounou, E., Guariso, G., Kartalidis, A., Panichelli, L., Pinedo, I., Robba, M., 2011. Methods and tools to evaluate the availability of renewable energy sources. Renewable and Sustainable Energy Reviews 15, 1182–1200.

Anthony, D., 2010. Where Will Solar Power Plants Be Built - Deserts or Rooftops? . Greentech Media. Retrieved from: https://www.greentechmedia.com/articles/read/where-will-solar-power-plants-be-built-deserts-or-rooftops#gs.DdF0njA

Anton, I., Tănase, D., 2016. Informed Geometries. Parametric Modelling and Energy Analysis in Early Stages of Design. Energy Procedia 85, 9–16.

Assouline, D., Mohajeri, N., Scartezzini, J.-L., 2017. Quantifying rooftop photovoltaic solar energy potential: A machine learning approach. Solar Energy 141, 278–296.

Athienitis, A.K., Bambara, J., O'Neill, B., Faille, J., 2011. A prototype photovoltaic/thermal system integrated with transpired collector. Solar Energy 85, 139–153.

Autodesk Inc, 2016. Dynamo BIM. Retrieved from: http://dynamobim.org/learn/

Autodesk Inc, 2017. Revit for Autodesk. Retrieved from: https://www.autodesk.com/education/free-software/revit

Azar, S., 2013. TownScope. Retrieved from: http://townscope.com/

Bäck, T., Rudolph, G., Schwefel, H.-P., 1993. Evolutionary programming and evolution strategies: Similarities and differences, in: Proceedings of the Second Annual Conference on Evolutionary Programming. pp. 76–78.

Baig, H., Sellami, N., Mallick, T.K., 2015. Performance modeling and testing of a Building Integrated Concentrating Photovoltaic (BICPV) system. Solar Energy Materials and Solar Cells 134, 29–44.

Barron-Gafford, G.A., Minor, R.L., Allen, N.A., Cronin, A.D., Brooks, A.E., Pavao-Zuckerman, M.A., 2016. The Photovoltaic Heat Island Effect: Larger solar power plants increase local temperatures. Scientific Reports 6, 35070.

Bendheim, 2010. Solarwatt GmbH. Retrieved from: https://bendheim.com/project/solarwatt-gmbh/

Berny, S., Blouin, N., Distler, A., Egelhaaf, H.-J., Krompiec, M., Lohr, A., Lozman, O.R., Morse, G.E., Nanson, L., Pron, A., Sauermann, T., Seidler, N., Tierney, S., Tiwana, P., Wagner, M., Wilson, H., 2016. Solar Trees: First Large-Scale Demonstration of Fully Solution Coated, Semitransparent, Flexible Organic Photovoltaic Modules. Advanced Science 3.

Bidram, A., Davoudi, A., Balog, R.S., 2012. Control and Circuit Techniques to Mitigate Partial Shading Effects in Photovoltaic Arrays. IEEE Journal of Photovoltaics 2, 532–546.

Biljecki, F., Ledoux, H., Stoter, J., 2017. Generating 3D city models without elevation data. Computers, Environment and Urban Systems 64, 1–18.

Biljecki, F., Ledoux, H., Stoter, J., Zhao, J., 2014. Formalisation of the level of detail in 3D city modelling. Computers, Environment and Urban Systems 48, 1–15.

BIMsolar, 2018. BIMsolar. Retrieved from: http://webdc-design.fr/bimsolar/en/bimsolar-4/

Bird, R.E., Hulstrom, R.L., 1981. Simplified clear sky model for direct and diffuse insolation on horizontal surfaces . National Renewable Energy Laboratory (NREL). Retrieved from: http://www.osti.gov/servlets/purl/6510849/

Bonomo, P., Zanetti, I., Frontini, F., van den Donker, M., Vossen, F., Folkerts, W., 2017. BIPV PRODUCTS OVERVIEW FOR SOLAR BUILDING SKIN, in: 33rd EUPVSEC. Amesterdam.

BP_Solar, 2006. 160-Watt Multicrystalline Photovoltaic Module. Retrieved from: https://www.solarpanelsaustralia.com.au/downloads/bpsolar_bp3160.pdf

Braun, M., Stetz, T., Bründlinger, R., Mayr, C., Ogimoto, K., Hatta, H., Kobayashi, H., Kroposki, B., Mather, B., Coddington, M., Lynn, K., Graditi, G., Woyte, A., MacGill, I., 2012. Is the distribution grid ready to accept large-scale photovoltaic deployment? State of the art, progress, and future prospects. Progress in Photovoltaics: Research and Applications 20, 681–697.

Bremer, M., Mayr, A., Wichmann, V., Schmidtner, K., Rutzinger, M., 2016. A new multi-scale 3D-GIS-approach for the assessment and dissemination of solar income of digital city models. Computers, Environment and Urban Systems 57, 144–154.

Brito, M.C., Freitas, S., Guimarães, S., Catita, C., Redweik, P., 2017. The importance of facades for the solar PV potential of a Mediterranean city using LiDAR data. Renewable Energy 111, 85–94.

Brito, M.C., Gomes, N., Santos, T., Tenedório, J.A., 2012. Photovoltaic potential in a Lisbon suburb using LiDAR data. Solar Energy 86, 283–288.

Brogren, M., Wennerberg, J., Kapper, R., Karlsson, B., 2003. Design of concentrating elements with CIS thin-film solar cells for façade integration. Solar Energy Materials and Solar Cells 75, 567–575.

Buhl, J., Gautrais, J., Reeves, N., Solé, R. V, Valverde, S., Kuntz, P., Theraulaz, G., 2006. Topological patterns in street networks of self-organized urban settlements. The European Physical Journal B 49, 513–522.

Building Art Invention, 2017. DysCrete. Retrieved from: http://www.baukunsterfinden.org/en/research/projects/dyscrete-energy-production-systems/

Bunthof, L.A.A., Kreuwel, F.P.M., Kaldenhoven, A., Kin, S., Corbeek, W.H.M., Bauhuis, G.J., Vlieg, E., Schermer, J.J., 2016. Impact of shading on a flat CPV system for façade integration. Solar Energy 140, 162–170.

Camilo, F.M., Castro, R., Almeida, M.E., Pires, V.F., 2017. Economic assessment of residential PV systems with self-consumption and storage in Portugal. Solar Energy 150, 353–362.

Cardwell, D., 2017. Tesla Gives the California Power Grid a Battery Boost - The New York Times . The New York Times. Retrieved from: https://www.nytimes.com/2017/01/30/business/energy-environment/battery-storage-tesla-california.html?_r=0

Carneiro, C., Morello, E., Desthieux, G., Golay, F., 2010. Urban environment quality indicators: application to solar radiation and morphological analysis on built area. Advances in Visualization, Imaging and Simulation 141–148.

CASE, 2016. High Efficiency Solar Energy Systems. Retrieved from: http://www.case.rpi.edu/page/project.php?pageid=1

Catani, A., Gómez, F., Pesch, R., Schumacher, J., Pietruschka, D., Eicker, U., 2008. Shading Losses of Building Integrated Photovoltaic Systems, in: 23rd European Photovoltaic Solar Energy Conference and Exhibition. Valencia, Spain.

Catita, C., Redweik, P., Pereira, J., Brito, M.C., 2014. Extending solar potential analysis in buildings to vertical facades. Computers & Geosciences 66, 1–12.

Caula, R., 2012. Spherical glass solar energy generator by rawlemon . Designboom. Retrieved from: https://www.designboom.com/technology/spherical-glass-solar-energy-generator-by-rawlemon/

CCL Componentes, 2014. Fronius Inverters. Retrieved from: http://www.cclcomponents.com/range.asp?ID=372

Chapman, L., Thornes, J.E., Bradley, A. V., 2002. Sky-view factor approximation using GPS receivers. International Journal of Climatology 22, 615–621.

Chemisana, D., Rosell, J.I., 2011. Design and optical performance of a nonimaging Fresnel transmissive concentrator for building integration applications. Energy Conversion and Management 52, 3241–3248.

Chimklai, P., Hagishima, A., Tanimoto, J., 2004. A computer system to support Albedo Calculation in urban areas. Building and Environment 39, 1213–1221.

Chow, T.T., He, W., Ji, J., 2007. An experimental study of façade-integrated photovoltaic/water-heating system. Applied Thermal Engineering 27, 37–45.

Chun-Lien Su, Hsiang-Ming Chuang, 2014. Distribution network reinforcement planning for high penetration level of distributed generation, in: 2014 IEEE International Energy Conference (ENERGYCON). IEEE, pp. 1170–1175.

CML, 2017. Casa dos Bicos ou de Brás de Albuquerque. Retrieved from: http://www.cm-lisboa.pt/en/equipments/equipment/info/casa-dos-bicos-ou-de-bras-de-albuquerque

Coccolo, C., Mauree, D., Kämpf, J., Scartezzini, J.L., 2016. Integration of outdoor human comfort in a building energy simulation database using CityGML energy ADE, in: Sustainable Built Environment (SBE) Regional Conference. Zurich, pp. 84–89.

Comello, S., Reichelstein, S., 2017. Cost competitiveness of residential solar PV: The impact of net metering restrictions. Renewable and Sustainable Energy Reviews 75, 46–57.

Compagnon, R., 2004. Solar and daylight availability in the urban fabric. Energy and Buildings 36, 321–328.

Comparotto, C., Noebels, M., Wefringhaus, E., Ferretti, N., Mancini, G., Berghold, J., Einhaus, R., Madon, F., 2015. Energy Yield Estimation of Monofacial and Bifacial Solar Modules. 31st European Photovoltaic Solar Energy Conference and Exhibition.

Connelly, K., Wu, Y., Chen, J., Lei, Y., 2016. Design and development of a reflective membrane for a novel Building Integrated Concentrating Photovoltaic (BICPV) “Smart Window” system. Applied Energy 182, 331–339.

Crawley, D.B., Lawrie, L.K., Winkelmann, F.C., Buhl, W.F., Huang, Y.J., Pedersen, C.O., Strand, R.K., Liesen, R.J., Fisher, D.E., Witte, M.J., Glazer, J., 2001. EnergyPlus: creating a new-generation building energy simulation program. Energy and Buildings 33, 319–331.

Cristóvão, A.R., 2016. Análise de obstruções à radiação solar em contexto urbano. MSc thesis, University of Lisbon.

Cucchiella, F., D’Adamo, I., Gastaldi, M., 2016. Photovoltaic energy systems with battery storage for residential areas: an economic analysis. Journal of Cleaner Production 131, 460–474.

Danks, R., Good, J., Sinclair, R., 2016. Assessing reflected sunlight from building facades: A literature review and proposed criteria. Building and Environment 103, 193–202.

David Rutten, 2017. Galapagos. Retrieved from: http://www.grasshopper3d.com/group/galapagos

Davidson, S., 2017. Grasshopper. Retrieved from: http://www.grasshopper3d.com/

Dean, J., Kandt, A., Burman, K., Lisell, L., Helm, C., 2009. Analysis of Web-Based Solar Photovoltaic Mapping Tools, in: ASME 2009 3rd International Conference on Energy Sustainability, Volume 1. ASME, pp. 85–96.

de Simón-Martín, M., Alonso-Tristán, C., Díez-Mediavilla, M., 2017. Diffuse solar irradiance estimation on building’s façades: Review, classification and benchmarking of 30 models under all sky conditions. Renewable and Sustainable Energy Reviews 77, 783–802.

Di Giacomo, F., Fakharuddin, A., Jose, R., Brown, T.M., 2016. Progress, challenges and perspectives in flexible perovskite solar cells. Energy Environ. Sci. 9, 3007–3035.

Diouf, B., Pode, R., 2015. Potential of lithium-ion batteries in renewable energy. Renewable Energy 76, 375–380.

Dogan, T., Reinhart, C., 2017. Shoeboxer: An algorithm for abstracted rapid multi-zone urban building energy model generation and simulation. Energy and Buildings 140, 140–153.

Donahue, T., 2017. Solar Panels On An Apartment Building. Retrieved from: https://www.gettyimages.pt/detail/foto/solar-panels-on-an-apartment-building-fotografia-de-

stock/110055267
Dubayah, R., 1992. Estimating net solar radiation using Landsat Thematic Mapper and digital elevation data. Water Resources Research 28, 2469–2484.
Dubayah, R., Rich, P.M., 1995. Topographic solar radiation models for GIS. International journal of geographical information systems 9, 405–419.
Duffie, J.A., Beckman, W.A., 2013. Solar Engineering of Thermal Processes, Solar Engineering of Thermal Processes: Fourth Edition. John Wiley & Sons, Inc., ISBN 9781118671603, Hoboken, NJ.
E.ON Solar, 2017. Google Sunroof zeigt Ihr Solarpotenzial!. Retrieved from: https://www.eon-solar.de/
EcoFloLife, 2017. Technology. Retrieved from: https://www.ecoflolife.com/technology/
Ecotect, 2010. Autodesk ECOTECT Analysis. Retrieved from: https://knowledge.autodesk.com/support/ecotect-analysis/learn-explore/caas/video/youtube/watch-v-BKZ35xh4ofw.html
Eder, G.C., Knöbl, K., Maul, L., Aichinger, M., Peharz, G., Berger, K.A., 2017. Designed BIPV-elements with printed front-glass: Simulation and experimental evaluation of the effect of print, in: 12th Conference on Advanced Building Skins. Bern, Switzerland, pp. 1255–1262.
Egger, S., 2016. Solar Access with Insight Revit 2017 plugin . Insight blog. Retrieved from: http://blogs.autodesk.com/insight/solar-access-with-insight-revit-2017-plugin/
Eisenlohr, J., Wilson, H.R., Kuhn, T.E., 2017. Detailed modeling of building-integrated photovoltaics - from component and environmental data to the system output, in: 33rd EUPVSEC. Amesterdam, The Nederlands.
Elarga, H., Zarrella, A., De Carli, M., 2016. Dynamic energy evaluation and glazing layers optimization of façade building with innovative integration of PV modules. Energy and Buildings 111, 468–478.
Eltawil, M.A., Zhao, Z., 2010. Grid-connected photovoltaic power systems: Technical and potential problems—A review. Renewable and Sustainable Energy Reviews 14, 112–129.
Energy Matters, 2014. Fronius IG. Retrieved from: http://store.energymatters.com.au/brand/fronius/products/inverters?show=48
Erdélyi, R., Wang, Y., Guo, W., Hanna, E., Colantuono, G., 2014. Three-dimensional SOlar RAdiation Model (SORAM) and its application to 3-D urban planning. Solar Energy 101, 63–73.
Erin Takata, 2017. Analysis of Solar Community Energy Storage for Supporting Hawaii's 100% Renewable Energy Goals. University of San Francisco.
ERSE, 2016a. Preços de referência no mercado liberalizado de energia elétrica e gás natural em Portugal continental. Retrieved from: http://www.erse.pt/pt/Simuladores/Documents/PreçosRef_BTN.pdf
ERSE, 2016b. Perfis de perdas, perfis de consumo e de autoconsumo, e perfis de produção. Retrieved from: http://www.erse.pt/pt/electricidade/regulamentos/acessoasredesaasinterligacoes/Paginas/PerfishorariosdeperdasedeconsumoemBTEBTNeIP.aspx?master=ErsePrint.master
Esclapés, J., Ferreiro, I., Piera, J., Teller, J., 2014. A method to evaluate the adaptability of photovoltaic energy on urban façades. Solar Energy 105, 414–427.
European Commission, 2014. HORIZON 2020 in brief. The EU Framework Programme for Research & Innovation. Retrieved from: http://ec.europa.eu/programmes/horizon2020/en/news/horizon-2020-brief-eu-framework-programme-research-innovation
Evseev, E.G., Kudish, A.I., 2009. The assessment of different models to predict the global solar radiation on a surface tilted to the south. Solar Energy 83, 377–388.
Faessler, J., 2010. Evaluation du potentiel solaire en milieu urbain: essais d'application aux toitures du canton de Genève. Retrieved from: https://archive-ouverte.unige.ch/unige:33155
Fath, K., Stengel, J., Sprenger, W., Wilson, H.R., Schultmann, F., Kuhn, T.E., 2015. A method for predicting the economic potential of (building-integrated) photovoltaics in urban areas based on hourly Radiance simulations. Solar Energy 116, 357–370.

Favoino, F., Fiorito, F., Cannavale, A., Ranzi, G., Overend, M., 2016. Optimal control and performance of photovoltachromic switchable glazing for building integration in temperate climates. Applied Energy 178, 943–961.

Fish, C.S., Calvert, K., 2017. An Analysis of Interactive Solar Energy Web Maps for Urban Energy Sustainability. Cartographic Perspectives 5–22.

Fonseca, C., 1995. Multiobjective Genetic Algorithms with Application to Control Engineering Problems. Systems Engineering 172.

Frearson, A., 2013. UNStudio's Chinese shopping centre is covered in silver balls. Retrieved from: https://www.dezeen.com/2013/11/27/shopping-centre-covered-in-silver-balls-by-unstudio/

Freitas, S., Brito, M.C., 2015. Maximizing the solar photovoltaic yield in different building facade layouts, in: 31st European Photovoltaic Solar Energy Conference and Exhibition. Hamburg, pp. 2862–2866.

Freitas, S., Brito, M.C., 2016. Bifacial PV integrated on building balconies, in: 32nd European Photovoltaic Solar Energy Conference and Exhibition. Munich, Germany.

Freitas, S., Brito, M.C., 2017a. Validation of a façade PV potential model based on LiDAR data, in: 33rd EUPVSEC. Amesterdam, The Nederlands.

Freitas, S., Brito, M.C., 2017b. The contribution of façades to the PV potential for sites with high diffuse fraction, in: 33rd EUPVSEC. Amesterdam, The Nederlands.

Freitas, S., Cristóvão, A., Amaro e Silva, R., Brito, M.C., 2016a. Obstruction surveying methods for PV application in urban environments, in: Proceedings of the 32nd European Photovoltaic Solar Energy Conference and Exhibition. Munich, Germany, pp. 2759–2764.

Freitas, S., Redweik, P., Catita, C., Brito, M.C., 2016b. Potencial solar nas cidades, in: VI Congresso Brasileiro de Energia Solar. Belo Horizonte, Brazil.

Freitas, S., Reinhart, C., Brito, M.C., 2018. Minimizing storage needs for large scale photovoltaics in the urban environment. Solar Energy 159, 375–389.

Freitas, S., Santos, T., Brito, M.C., 2017a. Impact of large scale PV deployment in the sizing of urban distribution transformers. Renewable Energy 1–10.

Freitas, S., Santos, T., Brito, M.C., 2017b. Sizing of urban distribution transformers in a neighbourhood with PV generation and energy storage, in: 33rd EUPVSEC. Amesterdam, The Nederlands.

Freitas, S., Serra, F., Brito, M.C., 2015a. Pv layout optimization: String tiling using a multi-objective genetic algorithm. Solar Energy 118, 562–574.

Freitas, S., Serra, F., Brito, M.C., 2015b. Multi-Objective Genetic Algorithm for the Optimization of a PV System Arrangement, in: Proceedings of the ISES Solar World Congress 2015. International Solar Energy Society, Daegu, South Korea.

Frontini, F., Bonomo, P., Saretta, E., Weber, T., Berghold, J., 2016. Indoor and Outdoor Characterization of Innovative Colored BIPV Modules for Façade Application, in: 32nd European Photovoltaic Solar Energy Conference and Exhibition. Munich, Germany.

Frontini, F., Friesen, T., Von Ballmoos, C., Di Gregorio, S., 2014. Palazzo Positivo: Renovation of a Residential Building in Switzerland with BIPV Facades, in: 29th European Photovoltaic Solar Energy Conference and Exhibition. WIP, Amsterdam, The Netherlands, pp. 3733–3737.

Fu, P., Rich, P.M., 1999. Design and implementation of the solar analyst: an arcview extension for modeling solar radiation at landscape scales, in: 19th Annual ESRI User Conference. San Diego, USA, USA, pp. 1–24.

Gaillard, L., Giroux-Julien, S., Ménézo, C., Pabiou, H., 2014. Experimental evaluation of a naturally ventilated PV double-skin building envelope in real operating conditions. Solar Energy 103, 223–241.

Gallant, J.C., Wilson, J.P., 2000. Secondary topographic attributes, in: Terrain Analysis: Principles and Applications. ISBN 0-471-32188-5, pp. 87–131.

Global Solar Inc., 2017. Flexible Solar Panels. Retrieved from: http://www.globalsolar.com/

Goldberg, D.E., 1989. Genetic algorithms in search, optimization, and machine learning. Addison-Wesley Longman Publishing Co., Inc., ISBN 0201157675.

Golden, R., Paulos, B., 2015. Curtailment of Renewable Energy in California and Beyond. The Electricity Journal 28, 36–50.

Gomes, N.M.P., 2011. Integração de dados LIDAR com imagens de muito alta resolução espacial para determinação de áreas urbanas com potencial solar. MSc thesis, Faculdade de Ciências Sociais e Humanas, Universidade Nova de Lisboa.

Gómez-Lorente, D., Triguero, I., Gil, C., Espín Estrella, A., 2012. Evolutionary algorithms for the design of grid-connected PV-systems. Expert Systems with Applications 39, 8086–8094.

Google, 2017. Project Sunroof. Retrieved from: https://www.google.com/get/sunroof#p=0

Goretzki, P., 2013. GOSOL - Solarbüro für energieeffiziente Stadtplanung. Retrieved from: http://www.gosol.de/gosol.htm

Gouveia, J.P., Seixas, J., 2016. Unraveling electricity consumption profiles in households through clusters: Combining smart meters and door-to-door surveys. Energy and Buildings 116, 666–676.

Grandjean, A., Adnot, J., Binet, G., 2012. A review and an analysis of the residential electric load curve models. Renewable and Sustainable Energy Reviews 16, 6539–6565.

Green, J., Newman, P., 2017. Citizen utilities: The emerging power paradigm. Energy Policy 105, 283–293.

Green, M.A., 1982. Solar cells: operating principles, technology, and system applications. OSTI Identifier 6051511, Prentice-Hall Inc., Englewood Cliffs, NJ, USA.

Grigiante, M., Mottes, F., Zardi, D., de Franceschi, M., 2011. Experimental solar radiation measurements and their effectiveness in setting up a real-sky irradiance model. Renewable Energy 36, 1–8.

Grimmond, C.S.B., Potter, S.K., Zutter, H.N., Souch, C., 2001. Rapid methods to estimate sky-view factors applied to urban areas. International Journal of Climatology 21, 903–913.

Grueneich, D.M., 2015. The Next Level of Energy Efficiency: The Five Challenges Ahead. The Electricity Journal 28, 44–56.

Gueymard, C., 1987. An anisotropic solar irradiance model for tilted surfaces and its comparison with selected engineering algorithms. Solar Energy 38, 367–386.

Gueymard, C.A., 2009. Direct and indirect uncertainties in the prediction of tilted irradiance for solar engineering applications. Solar Energy 83, 432–444.

Habibi, S., 2017. The promise of BIM for improving building performance. Energy and Buildings 153, 525–548.

Hachem, C., Athienitis, A., Fazio, P., 2011. Investigation of solar potential of housing units in different neighborhood designs. Energy and Buildings 43, 2262–2273.

Hachem, C., Elsayed, M., 2016. Patterns of façade system design for enhanced energy performance of multistory buildings. Energy and Buildings 130, 366–377.

Hagemann, I.B., 2011. Perspectives and challenge of BIPV product design, in: 26th European Photovoltaic Solar Energy Conference and Exhibition. Hamburg.

Harden, K.D., 2011. Optimizing energy efficiency standards for low voltage distribution transformers. MSc thesis, Fort Wayne, Indiana: Purdue University.

Harrington, R., 2015. How many solar panels would we need to power the Earth? . Business Insider. Retrieved from: http://www.businessinsider.com/map-shows-solar-panels-to-power-the-earth-2015-9

Hartner, M., Ortner, A., Hiesl, A., Haas, R., 2015. East to west – The optimal tilt angle and orientation of photovoltaic panels from an electricity system perspective. Applied Energy 160, 94–107.

Hay, J.E., 1979. Calculation of monthly mean solar radiation for horizontal and inclined surfaces. Solar Energy 23, 301–307.

Hetrick, W. a., Rich, P.M., Weis, S.B., Weiss, S.B., 1993. Modeling insolation on complex surfaces. Thirteen Annual ESRI User Conference 2, 447–458.

Hezel, R., 2003. Novel applications of bifacial solar cells. Progress in Photovoltaics: Research and Applications 11, 549–556.

Ho, C.K., Sims, C.A., Yellowhair, J., Bush, E., 2015. Solar Glare Hazard Analysis Tool (SGHAT). Retrieved

from: www.sandia.gov/glare
Hofer, J., Groenewolt, A., Jayathissa, P., Nagy, Z., Schlueter, A., 2016. Parametric analysis and systems design of dynamic photovoltaic shading modules. Energy Science & Engineering 4, 134–152.
Hofierka, J., 1997. Direct Solar radiation within an open GIS environment, in: Proceedings of JEC-GI'97 Conference. pp. 575–584.
Hofierka, J., Kaňuk, J., 2009. Assessment of photovoltaic potential in urban areas using open-source solar radiation tools. Renewable Energy 34, 2206–2214.
Hofierka, J., Suri, M., Šúri, M., 2002. The solar radiation model for Open source GIS: implementation and applications, in: Proceedings of the Open Source GIS-GRASS Users Conference. pp. 11–13.
Hofierka, J., Zlocha, M., 2012. A New 3-D Solar Radiation Model for 3-D City Models. Transactions in GIS 16, 681–690.
Holmer, B., Postgård, U., Eriksson, M., 2001. Sky view factors in forest canopies calculated with IDRISI. Theoretical and Applied Climatology 68, 33–40.
Horisun, 2000. PVdatabase Project BP Solar Skin. Retrieved from: http://www.pvdatabase.org/projects_view_detailsmore.php?ID=86
Huld, T., Müller, R., Gambardella, A., 2012. A new solar radiation database for estimating PV performance in Europe and Africa. Solar Energy 86, 1803–1815.
Huld, T., Suri, M., Kenny, R.P., Dunlop, E.D., 2005. Estimating PV performance over large geographical regions, in: Conference Record of the 31st IEEE Photovoltaic Specialists Conference. IEEE, pp. 1679–1682.
Hummon, M., Denholm, P., Margolis, R., 2013. Impact of photovoltaic orientation on its relative economic value in wholesale energy markets. Progress in Photovoltaics: Research and Applications 21, 1531–1540.
IBA Technics, 2015. Bio-gerador. Retrieved from: http://www.ibatechnics.be/portfolio-item/bio-generator/
IEA, 2014. Technology Roadmap: Solar Photovoltaic Energy - 2014 edition. Retrieved from: https://www.iea.org/publications/freepublications/publication/technology-roadmap-solar-photovoltaic-energy---2014-edition.html
IMBY, 2013. In My Backyard. Retrieved from: http://www.nrel.gov/eis/imby/
INE, 2011. Censos - Resultados definitivos. Portugal - 2011. Retrieved from: http://censos.ine.pt/xportal/xmain?xpid=CENSOS&xpgid=ine_censos_publicacao_det&context o=pu&PUBLICACOESpub_boui=73212469&PUBLICACOESmodo=2&selTab=tab1&pcensos=61969554
Inman, R.H., Shcherbatyuk, G. V., Medvedko, D., Gopinathan, A., Ghosh, S., 2011. Cylindrical luminescent solar concentrators with near-infrared quantum dots. Optics Express 19, 24308.
Iqbal, M., 1983. An Introduction to Solar Radiation. Academic Press Canada, ISBN 9780323151818.
Issol, 2015. Union Eiendomsutvikling AS. Retrieved from: http://www.issol.eu/es/galerias/?album=6412970410205715057
Ivanova, S., 2015. Using cumulative sky approach for variant analysis of the seasonal vertical solar radiation for different types of urban street canyons, in: WREC XIV. Bucharest, Romania.
Ivanova, S.M., 2013. Estimation of background diffuse irradiance on orthogonal surfaces under partially obstructed anisotropic sky. Part I – Vertical surfaces. Solar Energy 95, 376–391.
Izquierdo, S., Rodrigues, M., Fueyo, N., 2008. A method for estimating the geographical distribution of the available roof surface area for large-scale photovoltaic energy-potential evaluations. Solar Energy 82, 929–939.
Jakica, N., 2017. State-of-the-art review of solar design tools and methods for assessing daylighting and solar potential for building-integrated photovoltaics. Renewable and Sustainable Energy Reviews In Press,.
Jakubiec, J.A., Balakrishnan, P., 2015. Quantifying Materials in Lighting Simulations, in: 14th International Radiance Workshop. Philadelphia.
Jakubiec, J.A., Reinhart, C.F., 2011. DIVA 2.0: Integrating daylight and thermal simulations using

rhinoceros 3D, DAYSIM and EnergyPlus. Proceedings of Building Simulation 2011: 12th Conference of International Building Performance Simulation Association 2202–2209.
Jakubiec, J.A., Reinhart, C.F., 2013. A method for predicting city-wide electricity gains from photovoltaic panels based on LiDAR and GIS data combined with hourly Daysim simulations. Solar Energy 93, 127–143.
Jardini, J.A., Tahan, C.M.V., Gouvea, M.R., Ahn, S.U., Figueiredo, F.M., 2000. Daily load profiles for residential, commercial and industrial low voltage consumers. IEEE Transactions on Power Delivery 15, 375–380.
Jochem, A., Höfle, B., Rutzinger, M., 2011. Extraction of Vertical Walls from Mobile Laser Scanning Data for Solar Potential Assessment. Remote Sensing 3, 650–667.
John Fitzgerald Weaver, 2017. Solar panel bling – custom coloring at an affordable price meeting modern efficiency expectations . Electrek. Retrieved from: https://electrek.co/2017/10/30/solar-panel-bling-custom-coloring-at-an-affordable-price-meeting-modern-efficiency-expectations/
Johnson, G.T., Watson, I.D., 1984. The Determination of View-Factors in Urban Canyons. Journal of Climate and Applied Meteorology 23, 329–335.
Joshi, H., 2008. Residential, Commercial and Industrial Electrical Systems: Equipment and Selection, Vol.1. ed. Tata McGraw-Hill Publishing company Limited, ISBN 9780070620964.
JRC EC, 2014. Photovoltaic Geographical Information System (PVGIS) . Joint Research Centre - Institute for Energy and Transport. Retrieved from: http://re.jrc.ec.europa.eu/
Juutilainen, L.T., Thorsteinsson, S., Poulsen, P.B., Thorseth, A., Amdemeskel, M.W., Canulescu, S., Rødderb, P.M., Rødderb, K., 2016. Angle resolved performance meausrements on PV glass and modules, in: 32nd European Photovoltaic Solar Energy Conference and Exhibition. Munich, Germany.
Kang, J.-G., Kim, J.-H., Kim, J.-T., 2013. Performance Evaluation of DSC Windows for Buildings. International Journal of Photoenergy 2013, 1–6.
Kanters, J., Wall, M., Dubois, M.-C., 2014. Development of a Façade Assessment and Design Tool for Solar Energy (FASSADES). Buildings 4, 43–59.
Karimi, M., Mokhlis, H., Naidu, K., Uddin, S., Bakar, A.H.A., 2016. Photovoltaic penetration issues and impacts in distribution network – A review. Renewable and Sustainable Energy Reviews 53, 594–605.
Karlessi, T., Kampelis, N., Kolokotsa, D., Santamouris, M., Standardi, L., Isidori, D., Cristalli, C., 2017. The concept of smart and NZEB buildings and the integrated design approach. Procedia Engineering 180, 1316–1325.
Koehl, M., Hamperl, S., Heck, M., 2016. Effect of thermal insulation of the back side of PV modules on the module temperature. Progress in Photovoltaics: Research and Applications 24, 1194–1199.
Koo, C., Hong, T., Jeong, K., Ban, C., Oh, J., 2017. Development of the smart photovoltaic system blind and its impact on net-zero energy solar buildings using technical-economic-political analyses. Energy 124, 382–396.
Koo, C., Hong, T., Park, H.S., Yun, G., 2014. Framework for the analysis of the potential of the rooftop photovoltaic system to achieve the net-zero energy solar buildings. Progress in Photovoltaics: Research and Applications 22, 462–478.
Kornelakis, A., Koutroulis, E., 2009. Methodology for the design optimisation and the economic analysis of grid-connected photovoltaic systems. IET Renewable Power Generation 3, 476.
Kuo, H.-J., Hsieh, S.-H., Guo, R.-C., Chan, C.-C., 2016. A verification study for energy analysis of BIPV buildings with BIM. Energy and Buildings 130, 676–691.
Kwon, H.-K., Lee, K.-T., Hur, K., Moon, S.H., Quasim, M.M., Wilkinson, T.D., Han, J.-Y., Ko, H., Han, I.-K., Park, B., Min, B.K., Ju, B.-K., Morris, S.M., Friend, R.H., Ko, D.-H., 2015. Optically Switchable Smart Windows with Integrated Photovoltaic Devices. Advanced Energy Materials 5.
La Manna, D., Li Vigni, V., Riva Sanseverino, E., Di Dio, V., Romano, P., 2014. Reconfigurable electrical interconnection strategies for photovoltaic arrays: A review. Renewable and Sustainable Energy

Reviews 33, 412–426.
Lai, C.-M., Hokoi, S., 2015. Solar façades: A review. Building and Environment 91, 152–165.
Lazard, 2017. Lazard's Levelized Cost of Energy analysis - version 11.0. Retrieved from: https://www.lazard.com/media/450337/lazard-levelized-cost-of-energy-version-110.pdf
Lee, J.Y., Lee, K.-T., Seo, S., Guo, L.J., 2015. Decorative power generating panels creating angle insensitive transmissive colors. Scientific Reports 4, 4192.
Lee, T.D., Ebong, A.U., 2017. A review of thin film solar cell technologies and challenges. Renewable and Sustainable Energy Reviews 70, 1286–1297.
Li, D.H.W., Chau, N.T.C., Wan, K.K.W., 2013. Predicting daylight illuminance and solar irradiance on vertical surfaces based on classified standard skies. Energy 53, 252–258.
Liang, J., Gong, J., Zhou, J., Ibrahim, A.N., Li, M., 2015. An open-source 3D solar radiation model integrated with a 3D Geographic Information System. Environmental Modelling and Software 64, 94–101.
Liebreich, M., 2017. Bloomberg New Energy Finance Summit. Retrieved from: https://data.bloomberglp.com/bnef/sites/14/2017/04/2017-04-25-Michael-Liebreich-BNEFSummit-Keynote.pdf
Lindberg, F., Holmer, B., 2010. Sky View Factor Calculator User Manual -Version 1.1.
Lindberg, F., Jonsson, P., Honjo, T., Wästberg, D., 2015. Solar energy on building envelopes – 3D modelling in a 2D environment. Solar Energy 115, 369–378.
Lindsay, A., Chiodetti, M., Dupeyrat, P., Binesti, D., Lutun, E., Radouane, K., 2015. Key Elements in the Design of Bifacial PV Power Plants. 31st European Photovoltaic Solar Energy Conference and Exhibition.
Lingel, R., Nordmann, T., Vontobel, T., 2016. Balance of system components performance of recent inverter systems under partial shading conditions results from side-by-side comparison in a field test, in: 32nd European Photovoltaic Solar Energy Conference and Exhibition. Munich, Germany, pp. 1512–1515.
Littlefair, P., 1998. Passive solar urban design : ensuring the penetration of solar energy into the city. Renewable and Sustainable Energy Reviews 2, 303–326.
Liu, B.Y.H., Jordan, R.C., 1960. The interrelationship and characteristic distribution of direct, diffuse and total solar radiation. Solar Energy 4, 1–19.
Lloret, A., Andreu, J., Merten, J., Chantant, M., Servant, J.M., Aceves, O., Sabata, L., Sen, F., Puigdollers, J., Person, C., Eicker, U., 1995. The Mataro public library: a 53 kWp grid connected building with integrated PV-thermal multifunctional modules, in: Proceedings of the 13th European Photovoltaic Solar Energy Conference. Nice, France, pp. 490–493.
LOF Solar Corporation, 2010. Germany Black Forest. Retrieved from: http://www.lofsolar.com/LofsolarPerformance/germanyblackforest-18.html
LOF Solar Corporation, 2014. London Kingsgate House. Retrieved from: http://www.lofsolar.com/LofsolarPerformance/londonkingsgatehouse-sustainablehomeslevel4-69.html
Lopes, R.A., Martins, J., Aelenei, D., Lima, C.P., 2016. A cooperative net zero energy community to improve load matching. Renewable Energy 93, 1–13.
Lowe, N., 2015. Merkat GIS. Retrieved from: http://www.food4rhino.com/app/meerkat-gis
Lunt, R.R., Bulovic, V., 2011. Transparent, near-infrared organic photovoltaic solar cells for window and energy-scavenging applications. Applied Physics Letters 98.
Luthander, R., Widén, J., Nilsson, D., Palm, J., 2015. Photovoltaic self-consumption in buildings: A review. Applied Energy 142, 80–94.
LXI, 2012. Online SIG Platform of the Lisbon Council. Retrieved from: http://lxi.cm-lisboa.pt/lxi/
Ma, C.C.Y., Iqbal, M., 1983. Statistical comparison of models for estimating solar radiation on inclined surgaces. Solar Energy 31, 313–317.
Magarreiro, C., Freitas, S., Brito, M.C., 2016. Radiação e energia solar. Gazeta de Física 39, 57–59.
Mallick, T., Eames, P., 2007. Design and fabrication of low concentrating second generation PRIDE concentrator. Solar Energy Materials and Solar Cells 91, 597–608.

Manasc Isaac, 2005. Greenstone Government of Canada Building. Retrieved from: https://apps.manascisaac.com/projects/greenstone_building/recognition

Manito, A.R.A., Pinto, A., Zilles, R., 2016. Evaluation of utility transformers' lifespan with different levels of grid-connected photovoltaic systems penetration. Renewable Energy 96, 700–714.

Manz AG, 2017. Application examples. Retrieved from: https://www.manz.com/markets/solar/system-solutions-for-bipv/application-examples/

Mapdwell, 2017. Cambridge, MA Solar Map. Retrieved from: https://www.mapdwell.com/en/solar/cambridge

Mardaljevic, J., 2000. Simulation of annual daylighting profiles for internal illuminance. Lighting Research and Technology 32, 111–118.

Marion, B., 2002. A method for modeling the current-voltage curve of a PV module for outdoor conditions. Progress in Photovoltaics: Research and Applications 10, 205–214.

Marion, B., 2017. Numerical method for angle-of-incidence correction factors for diffuse radiation incident photovoltaic modules. Solar Energy 147, 344–348.

Marion, B., Anderberg, M., George, R., Gray-Hann, P., Heimiller, D., 2001. PVWATTS version 2 – enhanced spatial resolution for calculating grid-connected PV performance. NCPV Program Review Meeting.

Marsh, A.J., 2011. Sky Subdivision . Natural Frequency. Retrieved from: http://naturalfrequency.com/wiki/sky-subdivision

Marszal, A.J., Heiselberg, P., Bourrelle, J.S., Musall, E., Voss, K., Sartori, I., Napolitano, A., 2011. Zero Energy Building – A review of definitions and calculation methodologies. Energy and Buildings 43, 971–979.

Martín-Chivelet, N., Montero-Gómez, D., 2017. Optimizing photovoltaic self-consumption in office buildings. Energy and Buildings 150, 71–80.

Martin, N., Ruiz, J.M., 2001. Calculation of the PV modules angular losses under field conditions by means of an analytical model. Solar Energy Materials and Solar Cells 70, 25–38.

Martínez-Rubio, A., Sanz-Adan, F., Santamaría-Peña, J., Martínez, A., 2016. Evaluating solar irradiance over facades in high building cities, based on LiDAR technology. Applied Energy 183, 133–147.

Martins, R., Musilek, P., Hesse, H.C., 2016. Optimization of photovoltaic power self-consumption using linear programming, in: 2016 IEEE 16th International Conference on Environment and Electrical Engineering (EEEIC). IEEE, pp. 1–5.

Martins, T.A. de L., Adolphe, L., Bastos, L.E.G., Martins, M.A. de L., 2016. Sensitivity analysis of urban morphology factors regarding solar energy potential of buildings in a Brazilian tropical context. Solar Energy 137, 11–24.

MathWorks, 2014. Traveling Salesman Problem: Solver-Based. Retrieved from: http://www.mathworks.com/help/optim/ug/travelling-salesman-problem.html?requestedDomain=www.mathworks.com

McNeel, 2016. Rhinoceros 5.0. Retrieved from: https://www.rhino3d.com/

McPhail, D., Croker, B., Harvey, B., 2016. A study of solar PV saturation limits for representative low voltage networks, in: 2016 Australasian Universities Power Engineering Conference (AUPEC). IEEE, pp. 1–6.

Mendes, M., 2010. Localização e caracterização de locais com potencial para produção de energia solar-Caso de estudo no nordeste de Portugal. MSc Thesis, Universidade de Trás-os-Montes e Alto Douro.

Menicucci, D.F., Fernandez, J.P., 1989. User's manual for PVFORM: A photovoltaic system simulation program for stand-alone and grid-interactive applications. Retrieved from: https://www.osti.gov/scitech/biblio/5964340

Merei, G., Moshövel, J., Magnor, D., Sauer, D.U., 2016. Optimization of self-consumption and techno-economic analysis of PV-battery systems in commercial applications. Applied Energy 168, 171–178.

Mészáros, I., Miklánek, P., Parajka, J., 2002. Solar energy income modelling in mountainous areas, in:

Interdisciplinary Approaches in Small Catchment Hydrology: Monitoring and Research - Proceedings of the 9th Conference of the European Network of Experimental and Representative Basins. pp. 127–135.
Meza, E., 2016. IHS examines 22% price gap between modules from China and global rivals . pv magazine. Retrieved from: https://www.pv-magazine.com/2016/04/19/ihs-examines-22-price-gap-between-modules-from-china-and-global-rivals_100024204/
MG Solar, 2014. Fronius IG Plus. Retrieved from: http://mg-solar-shop.com/fronius_ig_plus_150_v_3.html
Miguet, F., 2007. A further step in environment and bioclimatic analysis: the software tool SOLENE. Proceedings: Building Simulation 1630–1637.
Miguet, F., Groleau, D., 2001. Simulation tool including transmitted direct and diffuse light: application to the evaluation of daylighting inside glazed intermediate spaces, in: Proceedings of the 7th IBPSA. pp. 907–914.
Mills, D.R., Giutronich, J.E., 1978. Ideal prism solar concentrators. Solar Energy 21, 423–430.
Mohajeri, N., Upadhyay, G., Gudmundsson, A., Assouline, D., Kämpf, J., Scartezzini, J.-L., 2016. Effects of urban compactness on solar energy potential. Renewable Energy 93, 469–482.
Mondol, J.D., Yohanis, Y.G., Norton, B., 2008. Solar radiation modelling for the simulation of photovoltaic systems. Renewable Energy 33, 1109–1120.
Morille, B., Lauzet, N., Musy, M., 2015. SOLENE-microclimate: A Tool to Evaluate Envelopes Efficiency on Energy Consumption at District Scale. Energy Procedia 78, 1165–1170.
Muneer, T., 2004. Solar Radiation and Daylight Models.
Muneer, T., Gueymard, C., Kambezidis, H., 2004. Psychrometrics, in: Solar Radiation and Daylight Models. Elsevier, pp. 317–322.
N.C. Clean Energy Technology Center, 2017. DSIRE - Database of State Incentives for Renewables & Efficiency. Retrieved from: http://www.dsireusa.org/
Naumann, M., Karl, R.C., Truong, C.N., Jossen, A., Hesse, H.C., 2015. Lithium-ion Battery Cost Analysis in PV-household Application. Energy Procedia 73, 37–47.
Nelson, T., 2017. Building the future of energy generation . University of Exeter. Retrieved from: http://www.exeter.ac.uk/business/expertise/aedm/engineering/solar/
NFPA, 2014. National Electrical Code. Retrieved from: https://archive.org/download/nfpa.nec.2014/nfpa.nec.2014.pdf
Ning, G., Junnan, L., Yansong, D., Zhifeng, Q., Qingshan, J., Weihua, G., Geert, D., 2017. BIM-based PV system optimization and deployment. Energy and Buildings 150, 13–22.
Ning, G., Kan, H., Zhifeng, Q., Weihua, G., Geert, D., 2018. e-BIM: a BIM-centric design and analysis software for Building Integrated Photovoltaics. Automation in Construction 87, 127–137.
Noorian, A.M., Moradi, I., Kamali, G.A., 2008. Evaluation of 12 models to estimate hourly diffuse irradiation on inclined surfaces. Renewable Energy 33, 1406–1412.
Norton, B., Eames, P.C., Mallick, T.K., Huang, M.J., McCormack, S.J., Mondol, J.D., Yohanis, Y.G., 2011. Enhancing the performance of building integrated photovoltaics. Solar Energy 85, 1629–1664.
Nouvel, R., Brassel, K.-H., Bruse, Duminil, E., Coors, V., Eicker, U., Robinson, D., 2015. Simstadt, a new workflow-driven urban energy simulation platform for citygml city models, in: CISBAT 2015. Lausanne, Switzerland.
Nouvel, R., Schulte, C., Eicker, U., Pietruschka, D., Coors, V., 2013. CityGML-Based 3D City Model for Energy Diagnostics and Urban Energy Policy Support. Proceedings of BS2013: 13th Conference of International Building Performance Simulation Association 218–225.
NREL, 2017. PVWatts Calculator. Retrieved from: http://pvwatts.nrel.gov/
Nyholm, E., Goop, J., Odenberger, M., Johnsson, F., 2016. Solar photovoltaic-battery systems in Swedish households – Self-consumption and self-sufficiency. Applied Energy 183, 148–159.
Obi, M., Bass, R., 2016. Trends and challenges of grid-connected photovoltaic systems – A review. Renewable and Sustainable Energy Reviews 58, 1082–1094.
OpenStreetMap contributors, 2017. OpenStreetMap. Retrieved from: https://www.openstreetmap.org/

OPVIUS, 2017. Applications and projects powered by Organic PV. Retrieved from: http://www.opvius.com/en/applications.html

Oslandia, 2014. OslandiaTechnos. Retrieved from: http://www.oslandia.com/pages/technos.html

Pandey, A.K., Tyagi, V.V., Selvaraj, J.A., Rahim, N.A., Tyagi, S.K., 2016. Recent advances in solar photovoltaic systems for emerging trends and advanced applications. Renewable and Sustainable Energy Reviews 53, 859–884.

Parra, D., Gillott, M., Norman, S.A., Walker, G.S., 2015. Optimum community energy storage system for PV energy time-shift. Applied Energy 137, 576–587.

Parra, D., Norman, S.A., Walker, G.S., Gillott, M., 2017. Optimum community energy storage for renewable energy and demand load management. Applied Energy 200, 358–369.

Passey, R., Spooner, T., MacGill, I., Watt, M., Syngellakis, K., 2011. The potential impacts of grid-connected distributed generation and how to address them: A review of technical and non-technical factors. Energy Policy 39, 6280–6290.

Peckham, R.J., 1990. Shadowpack - P.C. Version 2-0 User's Guide.

Perez, R., Ineichen, P., Seals, R., Michalsky, J., Stewart, R., 1990. Modeling daylight availability and irradiance components from direct and global irradiance. Solar Energy 44, 271–289.

Perez, R., Seals, R., Ineichen, P., Stewart, R., Menicucci, D., 1987. A new simplified version of the perez diffuse irradiance model for tilted surfaces. Solar Energy 39, 221–231.

Perez, R., Seals, R., Michalsky, J., 1993. To all-weather model for sky luminance distribution—preliminary configuration and validation. Solar Energy 51, 423.

Perez, R., Stewart, R., Arbogast, C., Seals, R., Scott, J., 1986. An anisotropic hourly diffuse radiation model for sloping surfaces: Description, performance validation, site dependency evaluation. Solar Energy 36, 481–497.

Physee, 2017. PowerWindow. Retrieved from: http://www.physee.eu/products/

Piccolo, A., Siano, P., 2009. Evaluating the Impact of Network Investment Deferral on Distributed Generation Expansion. IEEE Transactions on Power Systems 24, 1559–1567.

Polo Lopez, C., Frontini, F., Bonomo, P., Scognamiglio, A., 2014. PV and Façade Systems for the Building Skin. Analysis of Design Effectiveness and Technological Features, in: 29th European Photovoltaic Solar Energy Conference and Exhibition.

PORDATA, 2013. Consumo de energia eléctrica: total e por tipo de consumo. Retrieved from: http://www.pordata.pt/

Primsolar, 2016. Bifacial module Bi60-343BSTC. Retrieved from: http://www.solcentral.com.br/wp-content/uploads/2016/06/PrismSolar_Bi60-343W-Bifacial_en.pdf

PVsites, 2017. PVSITES software. Retrieved from: http://www.pvsites.eu/software/

Quiquerez, L., 2012. Evaluation du potentiel solaire photovoltaïque et thermique dans un environnement urbain - Etude de cas de deux territoires genevois : Les Pâquis et Veyrier. Retrieved from: http://www.cuepe.ch/html/enseigne/pdf/trp-rech-2013-01.pdf

Rakovec, J., Zakšek, K., 2012. On the proper analytical expression for the sky-view factor and the diffuse irradiation of a slope for an isotropic sky. Renewable Energy 37, 440–444.

Ramachandra, T., Shruthi, B., 2007. Spatial mapping of renewable energy potential. Renewable and Sustainable Energy Reviews 11, 1460–1480.

Ramaswamy, P.C., Leyder, S., Rapoport, S., Picart, B., De Greve, Z., Vangulick, D., 2016. Impact of load and generation flexibility on the long term planning of YLPIC distribution network, in: CIRED Workshop 2016. Institution of Engineering and Technology.

Ramírez-Faz, J., López-Luque, R., Casares, F.J., 2015. Development of synthetic hemispheric projections suitable for assessing the sky view factor on vertical planes. Renewable Energy 74, 279–286.

Ratti, C., Richens, P., 2004. Raster Analysis of Urban Form. Environment and Planning B: Planning and Design 31, 297–309.

Redweik, P., Catita, C., Brito, M., 2013. Solar energy potential on roofs and facades in an urban landscape. Solar Energy 97, 332–341.

Redweik, P., Catita, C., Brito, M.C., 2011. PV Potential Estimation Using 3D Local Scale Solar Radiation

Model Based on Urban Lidar Data. 26th European Photovoltaic Solar Energy Conference and Exhibition 4081–4083.
Reich, N.H., Mueller, B., Armbruster, A., van Sark, W.G.J.H.M., Kiefer, K., Reise, C., 2012. Performance ratio revisited: is PR > 90% realistic? Progress in Photovoltaics: Research and Applications 20, 717–726.
Reindl, D.T., Beckman, W.A., Duffie, J.A., 1990a. Evaluation of hourly tilted surface radiation models. Solar Energy 45, 9–17.
Reindl, D.T., Beckman, W.A., Duffie, J.A., 1990b. Diffuse fraction correlations. Solar Energy 45, 1–7.
Reinhart, C., 2011. Simulation-based Daylight Performance Predictions, in: Building Performance Simulation for Design and Operation. Taylor & Francis, ISBN 9780415474146.
Reinhart, C.F., Cerezo Davila, C., 2016. Urban building energy modeling – A review of a nascent field. Building and Environment 97, 196–202.
Reinhart, C.F., Walkenhorst, O., 2001. Validation of dynamic RADIANCE-based daylight simulations for a test office with external blinds. Energy and Buildings 33, 683–697.
Reise, C., Schmid, A., 2015. Realistic Yield Expectations for Bifacial PV Systems – An Assessment of Announced, Predicted and Observed Benefits. 31st European Photovoltaic Solar Energy Conference and Exhibition.
REN, 2011. Electricity - Real Time Information. Retrieved from: http://www.centrodeinformacao.ren.pt/EN/Pages/CIHomePage.aspx
Rich, P., Hetrick, W., Saving, S., 1995. Modeling topographic influences on solar radiation: A manual for the SOLARFLUX Model. Los Alamos, NM.
Rigollier, C., Bauer, O., Wald, L., 2000. On the clear sky model of the ESRA — European Solar Radiation Atlas — with respect to the heliosat method. Solar Energy 68, 33–48.
Roberts, S., Guariento, N., 2009. Building Integrated Photovoltaics: A Handbook. ISBN 9783764399481.
Robinson, D., 2006. Urban morphology and indicators of radiation availability. Solar Energy 80, 1643–1648.
Robinson, D., Haldi, F., Kämpf, J.H., Leroux, P., Perez, D., Rasheed, A., Wilke, U., 2009. CITYSIM: Comprehensive Micro-Simulation Of Resource Flows For Sustainable Urban Planning. 11th International IBPSA Conference 1083–1090.
Robinson, D., Stone, A., 2004. Irradiation modelling made simple: the cumulative sky approach and its applications, in: 21st PLEA. Eindhoven.
Robinson, D., Stone, A., 2005. A simplified radiosity algorithm for general urban radiation exchange. Building Services Engineering Research and Technology 26, 271–284.
Rodrigues, C., 2008. Centrais solares fotovoltaicas ligadas à rede eléctrica. Provas de acesso à categoria de investigador auxiliar, INETI.
Rodríguez San Segundo, H.J., et al, 2016. Integration of Trackless Holographic CPV Modules in Buildings and Urban Furniture, in: 32nd European Photovoltaic Solar Energy Conference and Exhibition. Munich, Germany.
Romero Rodríguez, L., Duminil, E., Sánchez Ramos, J., Eicker, U., 2017a. Assessment of the photovoltaic potential at urban level based on 3D city models: A case study and new methodological approach. Solar Energy 146, 264–275.
Romero Rodríguez, L., Nouvel, R., Duminil, E., Eicker, U., 2017b. Setting intelligent city tiling strategies for urban shading simulations. Solar Energy 157, 880–894.
Roudsari, M., 2017. Ladybug Tools, food4rhino Apps for Rhino and Grasshopper. Retrieved from: http://www.food4rhino.com/app/ladybug-tools
Roudsari, M.S., Pak, M., 2013. Ladybug: a Parametric Environmental Plugin for Grasshopper To Help Designers Create an Environmentally-Conscious Design. 13th Conference of International building Performance Simulation Association 3129–3135.
SADEV, 2015. Hikari Lyon – France. Retrieved from: http://www.sadev.com/blog/vea-hikari-lyon-france/?lang=en
Sánchez, E., Izard, J., 2015. Performance of photovoltaics in non-optimal orientations: An

experimental study. Energy and Buildings 87, 211–219.
Santos-Martin, D., Lemon, S., Watson, J.D., Wood, A.R., Miller, A.J.V., Watson, N.R., 2016. Impact of solar photovoltaics on the low-voltage distribution network in New Zealand. IET Generation, Transmission & Distribution 10, 1–9.
Santos, J.M., Moura, P.S., Almeida, A.T. de, 2014. Technical and economic impact of residential electricity storage at local and grid level for Portugal. Applied Energy 128, 254–264.
Santos, T., Gomes, N., Freire, S., Brito, M.C., Santos, L., Tenedório, J.A., 2014. Applications of solar mapping in the urban environment. Applied Geography 51, 48–57.
Sark, W.G.J.H.M. van, Barnham, K.W.J., Slooff, L.H., Chatten, A.J., Büchtemann, A., Meyer, A., McCormack, S.J., Koole, R., Farrell, D.J., Bose, R., Bende, E.E., Burgers, A.R., Budel, T., Quilitz, J., Kennedy, M., Meyer, T., Donegá, C.D.M., Meijerink, A., Vanmaekelbergh, D., 2008. Luminescent Solar Concentrators - A review of recent results. Optics Express 16, 21773–21792.
Sarralde, J.J., Quinn, D.J., Wiesmann, D., Steemers, K., 2015. Solar energy and urban morphology: Scenarios for increasing the renewable energy potential of neighbourhoods in London. Renewable Energy 73, 10–17.
Scognamiglio, A., Røstvik, H.N., 2013. Photovoltaics and zero energy buildings: a new opportunity and challenge for design. Progress in Photovoltaics: Research and Applications 21, 1319–1336.
Seme, S., Lukač, N., Štumberger, B., Hadžiselimović, M., 2017. Power quality experimental analysis of grid-connected photovoltaic systems in urban distribution networks. Energy 139, 1261–1266.
Shah, A., 2011. Largest Photovoltaic Solar Farms – Are they Advantageous over Distributed Rooftop Solar and Why Utilities Love Them . Green World Investor. Retrieved from: http://www.greenworldinvestor.com/2011/03/05/largest-photovoltaic-solar-farms-are-they-advantageous-over-distributed-rooftop-solar-and-why-utilities-love-them/
Shahrestani, M., Yao, R., Essah, E., Shao, L., Oliveira, A.C., Hepbasli, A., Biyik, E., Caño, T. del, Rico, E., Lechón, J.L., 2017. Experimental and numerical studies to assess the energy performance of naturally ventilated PV façade systems. Solar Energy 147, 37–51.
Shih, N.-J., Huang, Y.-S., 2001. A study of reflection glare in Taipei. Building Research & Information 29, 30–39.
Shirzadi, S., Hizam, H., Wahab, N.I.A., 2014. Mismatch losses minimization in photovoltaic arrays by arranging modules applying a genetic algorithm. Solar Energy 108, 467–478.
Shukla, A.K., Sudhakar, K., Baredar, P., 2017. Recent advancement in BIPV product technologies: A review. Energy and Buildings 140, 188–195.
Skartveit, A., Asle Olseth, J., 1986. Modelling slope irradiance at high latitudes. Solar Energy 36, 333–344.
Skelion, 2013. Skelion 5.0.7 User's guide. Retrieved from: https://extensions.sketchup.com/en/content/skelion
Slooff, L.H., et al., 2016. Luminescent solar noise barrier - large scale testing and modeling, in: 32nd European Photovoltaic Solar Energy Conference and Exhibition. Munich, Germany.
Slooff, L.H., et al., 2017. An architectual approach for improving aesthetics of PV, in: 33rd EUPVSEC. Amesterdam.
Söderström, K., Musolino, V., Perret-Aebi, L.E., 2017. Temperature and performance monitoring of white panels in facade configuration, in: 33rd EUPVSEC. Amesterdam.
Solar Window Technologies, I., 2017. SolarWindow. Retrieved from: https://solarwindow.com/
SolarGaps Inc., 2017. SolarGaps. Retrieved from: https://solargaps.com/
SolarGIS, 2017. Global horizontal irradiation - Portugal. Retrieved from: http://solargis.com/assets/graphic/free-map/GHI/Solargis-Portugal-GHI-solar-resource-map-en.png
Solaria, 2016. Solaria PowerView. Retrieved from: http://www.solaria.com/buildings
Solaronix, 2014. Solar cells - Technology. Retrieved from: https://www.solaronix.com/solarcells/technology/
Solaxess, 2017. Image gallery. Retrieved from: http://www.solaxess.ch/default.asp?Language=EN
SolemmaLLC, 2016. DIVA. Retrieved from: http://www.solemma.net/

Solpros, 2003. Ekoviikki Solar Project. Retrieved from: http://www.kolumbus.fi/solpros/ekoviikki.htm
Soria, B., Gerritsen, E., 2013. Vertical Facade Integration of Bifacial PV Modules: Outdoor Testing & Optical Modelling. 28th EUPVSEC.
Stamatakis, A., Mandalaki, M., Tsoutsos, T., 2016. Multi-criteria analysis for PV integrated in shading devices for Mediterranean region. Energy and Buildings 117, 128–137.
Stamenic, L., Smiley, E., Karim, K., 2004. Low light conditions modelling for building integrated photovoltaic (BIPV) systems. Solar Energy 77, 37–45.
Stein, M., 2000. When Technology Fails. Chelsea Green Publishing Company, ISBN 978-1-933392-45-5, White River Junction, Vermont.
Struth, J., Leuthold, M., Aretz, A., Bost, M., 2013. PV-Benefit: a critical review of the effect of grid integrated PV-storage-systems, in: 8th International Renewable Energy Storage Conference and Exhibition.
Stylepark, 2016. Shadovoltaic Merck-Group Darmstadt. Retrieved from: https://www.stylepark.com/en/colt/shadovoltaic-merck-group-darmstadt
Sulaiman, S.I., Rahman, T.K.A., Musirin, I., Shaari, S., Sopian, K., 2012. An intelligent method for sizing optimization in grid-connected photovoltaic system. Solar Energy 86, 2067–2082.
Sunaitec, 2014. Smart Solar energy | Sunaitec. Retrieved from: http://www.sunaitec.pt/
Suri, M., Huld, T. a., Dunlop, E.D., 2005. PV-GIS: a web-based solar radiation database for the calculation of PV potential in Europe. International Journal of Sustainable Energy 24, 55–67.
Suri, M., Huld, T., Cebecauer, T., Dunlop, E.D., 2008. Geographic Aspects of Photovoltaics in Europe: Contribution of the PVGIS Website. IEEE Journal of Selected Topics in Applied Earth Observations and Remote Sensing 1, 34–41.
Swan, L.G., Ugursal, V.I., 2009. Modeling of end-use energy consumption in the residential sector: A review of modeling techniques. Renewable and Sustainable Energy Reviews 13, 1819–1835.
Taha, H., 2013. The potential for air-temperature impact from large-scale deployment of solar photovoltaic arrays in urban areas. Solar Energy 91, 358–367.
Taste of Nova Scotia, 2015. Just Us! Coffee Roastery and Museum. Retrieved from: http://tasteofnovascotia.com/members/just-us-coffee-roastery-museum/
Teller, J., Azar, S., 2001. Townscope II—A computer system to support solar access decision-making. Solar Energy 70, 187–200.
Tesla Motors, 2017. Powerwall | The Tesla Home Battery. Retrieved from: https://www.tesla.com/powerwall
The Core Studio Team, 2017. TT Tolboox. Retrieved from: http://www.food4rhino.com/app/tt-toolbox
The World Bank, 2017. Urban population (% of total) | Data. Retrieved from: http://data.worldbank.org/indicator/SP.URB.TOTL.IN.ZS
Tian, W., Wang, Y., Xie, Y., Wu, D., Zhu, L., Ren, J., 2007. Effect of building integrated photovoltaics on microclimate of urban canopy layer. Building and Environment 42, 1891–1901.
Tooke, T.R., 2014. Building energy modelling and mapping using airborne LiDAR. PhD thesis, University of British Columbia.
Tooke, T.R., Coops, N.C., Christen, A., Gurtuna, O., Prévot, A., 2012. Integrated irradiance modelling in the urban environment based on remotely sensed data. Solar Energy 86, 2923–2934.
Torcellini, P., Pless, S., Deru, M., Crawley, D., 2006. Zero Energy Buildings: A Critical Look at the Definition, in: ACEEE Summer Study on Energy Efficiency in Buildings. Pacific Grove, CA, USA.
Torriti, J., 2014. A review of time use models of residential electricity demand. Renewable and Sustainable Energy Reviews 37, 265–272.
Trabish, H.K., 2017. As solar booms, utilities look to build new business models with strategic investments . Utility Dive. Retrieved from: http://www.utilitydive.com/news/as-solar-booms-utilities-look-to-build-new-business-models-with-strategic/437899/
Tregenza, P.R., 1987. Subdivision of the sky hemisphere for luminance measurements. Lighting Research & Technology 19, 13–14.
Trimble, 2016. Archelios PRO | SketchUp Extension Warehouse. Retrieved from:

http://extensions.sketchup.com/pt-BR/content/archelios-pro
Unger, J., 2009. Connection between urban heat island and sky view factor approximated by a software tool on a 3D urban database. International Journal of Environment and Pollution 36, 59.
Ural, S., Hussain, E., Shan, J., 2011. Building population mapping with aerial imagery and GIS data. International Journal of Applied Earth Observation and Geoinformation 13, 841–852.
Valckenborg, R.M.E., et al., 2016. ZigZag Structure in Façade Optimizes PV Yield While Aesthetics Are Preserved, in: 32nd European Photovoltaic Solar Energy Conference and Exhibition. Munich, Germany.
Valley, S.L., 1965. Handbook of Geophysics and Space Environments. Retrieved from: http://www.dtic.mil/docs/citations/ADA056800
Vangimalla, P.R., Olbina, S.J., Issa, R.R., Hinze, J., 2011. Validation of Autodesk Ecotect; accuracy for thermal and daylighting simulations, in: Proceedings of the 2011 Winter Simulation Conference (WSC). IEEE, pp. 3383–3394.
Vartiainen, E., 2001. Electricity benefits of daylighting and photovoltaics for various solar facade layouts in office buildings. Energy and Buildings 33, 113–120.
Vera, L.H., Cáceres, M., Busso, A., 2014. Grid Connected Photovoltaic Systems to the Urban Environment of Argentinian Northeast. Energy Procedia 57, 3171–3180.
Verberne, G., Bonomo, P., Frontini, F., van den Donker, M.N., 2014. BIPV products for façades and roofs: a market analysis, in: 29th European Photovoltaic Solar Energy Conference and Exhibition. Amesterdam, pp. 3630–3636.
Vergne, A., 2011. Façade plissée avec cellules photovoltaïques: une double peau innovante . Le Moniteur.fr. Retrieved from: https://www.lemoniteur.fr/article/facade-plissee-avec-cellules-photovoltaiques-une-double-peau-innovante-15832927
Vermeulen, T., Knopf-Lenoir, C., Villon, P., Beckers, B., 2015. Urban layout optimization framework to maximize direct solar irradiation. Computers, Environment and Urban Systems 51, 1–12.
Verso, A., Martin, A., Amador, J., Dominguez, J., 2015. GIS-based method to evaluate the photovoltaic potential in the urban environments: The particular case of Miraflores de la Sierra. Solar Energy 117, 236–245.
ViaSolis, 2017. BIPV. Retrieved from: http://www.viasolis.eu/ru/page/bipv.125/
Vieira, F.M., Moura, P.S., de Almeida, A.T., 2017. Energy storage system for self-consumption of photovoltaic energy in residential zero energy buildings. Renewable Energy 103, 308–320.
Vincent Fillon, 2009. Photographie d'architecture: Cité du Design, Saint Etienne. Retrieved from: http://vincent-fillon.fr/photographie-architecture/lin-a-cite-design-st-etienne/photo-architecture-finn-geipel.php
Vishwanathan, B., Reinders, A.H.M.E., De Boer, D.K.G., Desmet, L., Ras, A.J.M., Zahn, F.H., Debije, M.G., 2015. A comparison of performance of flat and bent photovoltaic luminescent solar concentrators. Solar Energy 112, 120–127.
Vrhel, M., 2015. Lighting Materials of Simulation: dark blue jeans. Retrieved from: http://www.lighting-materials.com/materials/1690
Ward, G., 1994. The RADIANCE Lighting Simulation and Rendering System, in: 4 SIGGRAPH Conference. pp. 459–72.
Weber, W.H., Lambe, J., 1976. Luminescent greenhouse collector for solar radiation. Applied Optics 15, 2299.
Weniger, J., Tjaden, T., Quaschning, V., 2014. Sizing of Residential PV Battery Systems. Energy Procedia 46, 78–87.
Wesslund, T., Kreutzer, S., 2015. Villa Circuitus. Retrieved from: http://circuitus.se/
Wholesale Solar, 2015. SMA Sunny Boy 240-US-99-10 Inverter. Retrieved from: https://www.wholesalesolar.com/2960055/sma/inverters/sma-sunny-boy-240-us-99-10-inverter
Wieland, M., Wendel, J., 2015. Computing Solar Radiation on CityGML Building Data. Proceedings of the 18th AGILE conference on Geographic Information Science. 2–5.

Wiginton, L.K., Nguyen, H.T., Pearce, J.M., 2010. Quantifying rooftop solar photovoltaic potential for regional renewable energy policy. Computers, Environment and Urban Systems 34, 345–357.

Wirth, H., 2017. Recent Facts about Photovoltaics in Germany . Fraunhofer ISE. Retrieved from: https://www.ise.fraunhofer.de/content/dam/ise/en/documents/publications/studies/recent-facts-about-photovoltaics-in-germany.pdf

Yang, D., 2016. Solar radiation on inclined surfaces: Corrections and benchmarks. Solar Energy 136, 288–302.

Yang, X., Grobe, L., Stephen, W., 2013. Simulation of reflected daylight from building envelopes, in: 13th Conference of International Building Performance Simulation Association. Chambéry, France.

Yao, W., Li, Z., Wang, X., Zhao, Q., Zhang, Z., Lin, L., 2016. A simplified model exploration research of new anisotropic diffuse radiation model. Energy Conversion and Management 126, 724–735.

Zhang, X., Lv, Y., Tian, J., Pan, Y., 2015. An Integrative Approach for Solar Energy Potential Estimation Through 3D Modeling of Buildings and Trees. Canadian Journal of Remote Sensing 41, 126–134.

Zhao, Y., Lunt, R.R., 2013. Transparent Luminescent Solar Concentrators for Large-Area Solar Windows Enabled by Massive Stokes-Shift Nanocluster Phosphors. Advanced Energy Materials 3, 1143–1148.

Zhu, L., Shao, Z., Sun, Y., Soebarto, V., Gao, F., Zillante, G., Zuo, J., 2018. Indoor daylight distribution in a room with integrated dynamic solar concentrating facade. Energy and Buildings 158, 1–13.